LBL-23776
c.2

Lawrence Berkeley Laboratory

UNIVERSITY OF CALIFORNIA

Materials & Chemical Sciences Division

RECEIVED
LAWRENCE
BERKELEY LABORATORY

SEP 1 8 1987

LIBRARY AND
DOCUMENTS SECTION

THE CORROSION OF IRON ROTATING HEMISPHERES IN 1 M SULFURIC ACID: AN ELECTROCHEMICAL IMPEDANCE STUDY

C. Haili
(M.S. Thesis)

June 1987

TWO-WEEK LOAN COPY
This is a Library Circulating Copy
which may be borrowed for two weeks.

LBL-23776
c.2

Prepared for the U.S. Department of Energy under Contract DE-AC03-76SF00098

DISCLAIMER

This document was prepared as an account of work sponsored by the United States Government. While this document is believed to contain correct information, neither the United States Government nor any agency thereof, nor the Regents of the University of California, nor any of their employees, makes any warranty, express or implied, or assumes any legal responsibility for the accuracy, completeness, or usefulness of any information, apparatus, product, or process disclosed, or represents that its use would not infringe privately owned rights. Reference herein to any specific commercial product, process, or service by its trade name, trademark, manufacturer, or otherwise, does not necessarily constitute or imply its endorsement, recommendation, or favoring by the United States Government or any agency thereof, or the Regents of the University of California. The views and opinions of authors expressed herein do not necessarily state or reflect those of the United States Government or any agency thereof or the Regents of the University of California.

The Corrosion of Iron Rotating Hemispheres in 1 M Sulfuric Acid: An Electrochemical Impedance Study

Chrystalla C. Haili

M.S. Thesis

Lawrence Berkeley Laboratory
University of California
Berkeley, California 94720

June 1987

The Corrosion of Iron Rotating Hemispheres in 1 M Sulfuric Acid: An Electrochemical Impedance Study

Chrystalla Haili

Abstract

This research project consists of experimental investigation and theoretical analysis of the corrosion of iron in sulfuric acid. The main objectives of the project are: to elucidate the processes governing the complex behavior of the iron-sulfuric acid system, particularly the reaction mechanism, the passivation process, and the observed limiting current and electrochemical oscillations; to improve our fundamental understanding of metal corrosion and passivation phenomena; and to demonstrate the application of the electrochemical impedance method as a tool for the study of electrochemical systems.

Three different types of experiments are carried out: (I) potentiodynamic experiments to determine the anodic polarization curve, especially the passivation curve; (II) potentiostatic experiments recording the sustained current oscillations that occur within a certain potential range on the limiting current plateau; (III) measurement of the AC (alternating current) impedance of the system at several points along the anodic polarization curve, using a frequency response analyser. Rotating hemispherical iron electrodes are used in most of these experiments, because they have the advantage of a uniform primary current distribution, in contrast to the more commonly used rotating disk electrodes.

Comparing the experimental results for the passivation and current oscillations for hemispheres with results for disks obtained by other investigators, we observe no dramatic difference. Some differences are observed, and they may be attributed to differences between the current, potential, and concentration distributions of the two electrode geometries. The hemispherical electrodes are observed to passivate first near the pole, and then the passivated area increases toward the equator, at the conditions tested.

Rotating disk electrodes are used in some of the impedance measurement experiments, and the results for the disks are compared with the results for the hemispheres. Significant differences are observed at high perturbation frequencies, where the electrodes approach the primary current distribution. Specifically at high frequencies, the impedance of the hemispherical electrodes exhibits an additional time constant, which might be related to the reaction mechanism for iron dissolution.

The Kramers-Kronig relations can be applied to the electrochemical impedance, and they provide a means of testing the accuracy and consistency of experimental impedance data, or the validity of theoretical results. The test consists of calculation of the real part of the impedance from the imaginary part, and *vice versa*, through the Kramers-Kronig relations and comparison of the calculated results with the experimental or theoretical values. A general method of calculation is developed and is applied to test the consistency of some of the experimental impedance data exhibiting inductive loops. The data tested are found to be consistent with the Kramers-Kronig relations.

The experimental results are then compared with theoretical predictions in order to elucidate the behavior of the iron-sulfuric acid system. A concentrated-solution model developed recently in this laboratory is used to calculate the impedance, in addition to analytic calculations using infinitely-dilute-solution theory. The concentrated-solution model has provision for multicomponent diffusion, heterogeneous electron-transfer reactions, homogeneous reactions, hydrodynamics, and migration, but it has no provision for adsorbed intermediate species, the microscopic structure of the electrochemical interface, or porous films covering the electrode surface. The calculated results for the reaction mechanism and conditions tested do not agree with the experimental results. The analysis indicates further research directions that could give an agreement between theory and experiment, completing the characterization of the iron-sulfuric acid system.

Acknowledgements

I would like to thank Professor John Newman for providing an excellent working environment and sharing his expertise and methodological approach with his students. His suggestions and criticisms have been very helpful for doing the research work and also for writing this thesis.

I would also like to thank my committee members Jim Michaels and Fiona Doyle for their review of the manuscript.

The days and nights I have spent in the laboratory have been pleasant ones, and I would like to thank my colleagues (labmates). I would like to thank particularly Alan Hauser and Alan West for many beneficial discussions, John Sukamto, Paul Shain for his help with some technical computer problems, and Gina Whitney.

I also wish to acknowledge the electronic-shop and machine-shop personnel for providing some parts of the experimental apparatus and Flavio Robles for drawing some of the figures.

Finally, I would like to thank Paul and Alan for their help during the final stages of the preparation of this thesis.

This work was supported by the Assistant Secretary of Conservation and Renewable Energy, Office of Energy Systems Research, Energy Storage Division of the U.S. Department of Energy under Contract DE-AC03-76SF00098.

A 'typical' electrochemical impedance diagram

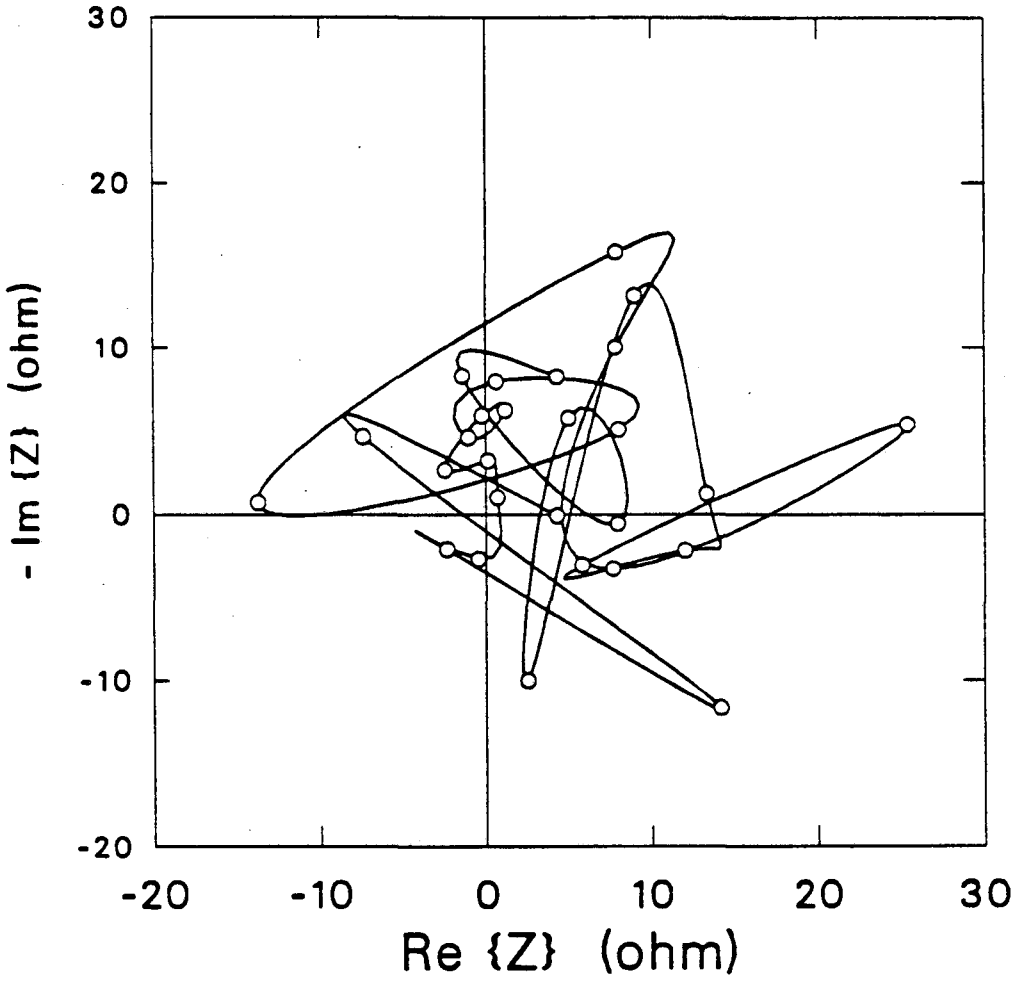

Chapter 1. Introduction 1

1.1 Motivation 1

1.2 In Search for a Method 4

1.3 A History of the Iron - Sulfuric Acid System 6

1.3.1 Reaction Mechanism for Iron Dissolution 6

1.3.2 Limiting Current and Passivation 20

1.3.3 Sustained Current Oscillations 42

1.4 Outline of This Work 49

1.5 The Rotating Hemispherical Electrode 52

1.6 The Electrochemical Impedance 59

1.6.1 Theoretical Formulation 63

1.6.1.1 General Concepts 63

1.6.1.2 Faradaic Impedance 72

1.6.1.3 Limits as $\omega \longrightarrow \infty$ and $\omega \longrightarrow 0$ 78

1.6.1.4 Convective Warburg Impedance — Dilute Solution Analysis 81

1.6.2 Experimental Measurement 89

1.6.3 Presentation and Analysis of Experimental Results 96

1.6.3.1 Graphical Presentation 96

1.6.3.2 Determination of Parameters 98

1.6.3.3 Equivalent Circuits 103

List of Symbols 110

References 117

Chapter 2. Anodic Polarization Curve, Passivation, and Current Oscillations: Experimental Results 139

2.1 Introduction 139

2.2 Principles of Polarization Control 141

2.3 Experimental Apparatus and Procedure 143

2.4 Anodic Polarization Curve — Discontinous Active - Passive Transitions 151

2.5 Anodic Polarization Curve — Continous Passivation 155

2.5.1 Experimental Curves 155

2.5.2 Probable Passivation Configurations 163

2.6 Current Oscillations 167

2.7 Conclusions 177

References 179

Chapter 3. AC Impedance: Experimental Results 181

3.1 Introduction 181

3.2 Experimental Apparatus and Procedure 183

3.3 Corrosion at $\bar{I} = 0$ (Open Circuit Potential) 188

3.4 Anodic Dissolution at Low Currents 201

3.5 Anodic Dissolution at High Currents — Limiting Current Plateau 219

3.6 Passivation 225

3.6.1 Experimental 225

3.6.2 Electrode Dissolution Profiles 227

3.6.3 Results 229

3.7 Summary 234

References 239

Chapter 4. Application of the Kramers-Kronig Relation to Test the Consistency of Electrochemical Impedance Data 242

4.1 Introduction 242

4.1.1 The Kramers-Kronig Relations for the Impedance 243

4.1.2 Literature Review 246

4.1.3 Significance of the Kramers-Kronig Relations for the Electrochemical Impedance 248

4.1.4 Some Questions 249

4.2 Integration Scheme 251

4.2.1 Integrals 251

4.2.2 Fitting / Interpolation Functions 259

4.3 Extrapolation to Zero and Infinite Frequency 272

4.3.1 Extrapolation to $\omega = 0$ 272

4.3.2 Extrapolation to $\omega \longrightarrow \infty$ 276

4.3.3 Concluding Remarks 280

4.4 Results 281

References 297

Chapter 5. Theoretical Models of the Electrochemical Impedance: Application to the Fe/H_2SO_4 System 300

5.1 Introduction 300

5.2 Reaction Kinetics — Charge-Transfer Resistance 302

5.3 Infinitely-Dilute-Solution Calculations 304

5.4 Concentrated Solution Model 305

5.5 Parameter Values Used in Calculations 309

5.6 Results and Discussion 312

References 323

Appendix A. Computer Programs Used for the Application of the Kramers-Kronig Relations 326

CHAPTER 1

Introduction

1.1. Motivation

Most metals spontaneously corrode in the environments in which they are used. Given the constraints imposed by scarcity and as metal resources are extensively utilized, metal corrosion is an important problem. For example, the cost of metal corrosion in the United States in 1982 was estimated to be $122 billion, about 4% of the Gross National Product (1).

A knowledge and understanding of corrosion phenomena is necessary in an effort to solve the problem of corrosion. Indeed lack of such knowledge has been a main cause for the persistence of the problem. Since corrosion phenomena are electrochemical in nature, fundamental electrochemical research is essential for providing an understanding of corrosion, so that we can predict the behavior of corrosion systems and ultimately so that we can control and prevent metal corrosion. The electrochemical impedance technique can be a powerful tool for the study of complex electrochemical processes such as corrosion.

This thesis is a study of a specific metal corrosion system using the electrochemical impedance technique. The system studied is the corrosion of iron in de-aerated one molar sulfuric acid solution. Generally in a corrosion system, an overall anodic reaction and an overall cathodic reaction occur simultaneously. In the system studied, anodic

iron dissolution and cathodic hydrogen evolution,

$$Fe \rightleftarrows Fe^{++} + 2e^{-} \qquad [1\text{-}1]$$

$$2H^{+} + 2e^{-} \rightleftarrows H_2 \ , \qquad [1\text{-}2]$$

take place. In addition iron passivates in sulfuric acid under certain conditions through a mechanism that has not yet been established. This work considers mainly the iron dissolution reaction. The study of the anodic process itself is a useful approach to the study of corrosion systems, especially systems exhibiting passivation. The complexity and the practical importance of iron corrosion make the study of this system a challenging project.

Figure 1-1 summarizes the background for this work. A typical anodic polarization curve determined in potentiodynamic experiments for the iron-sulfuric acid system exhibits two different shapes for the passivation curve (active-passive transition), depending on the polarization control device being used. In addition the polarization curve displays a limiting current plateau and a region of sustained current oscillations. The presence of these characteristics of the system is well established, but the processes generating these characteristics have not been unequivocally established. Even in the low-current range where the behavior of the system appears less complex and reproducible experimental results exist, several conflicting theories for the reaction mechanism have been postulated.

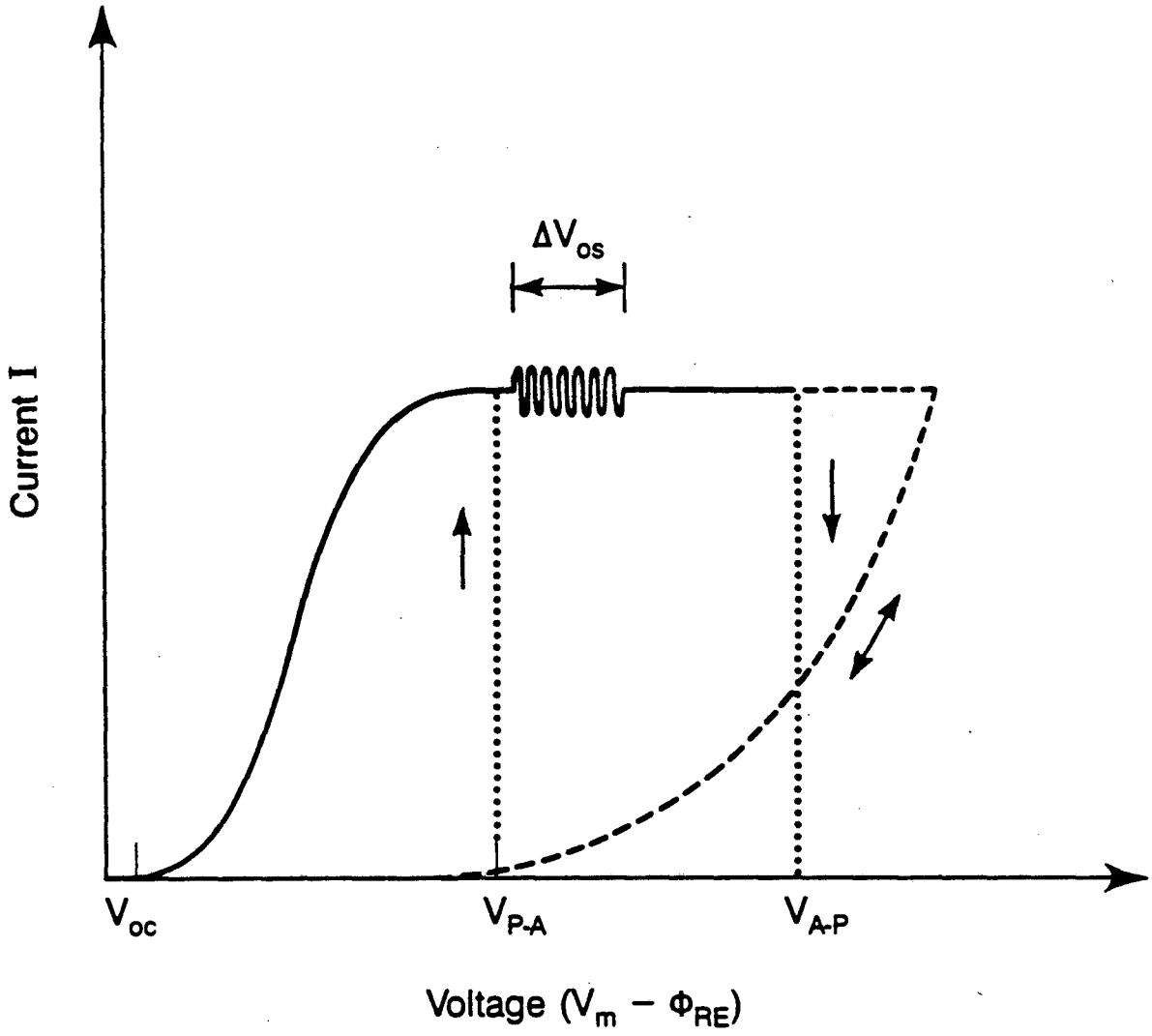

XBL 876-6324

Figure 1-1. Schematic diagram of a typical anodic polarization curve determined in potentiodynamic experiments for the iron-sulfuric acid system. The dotted lines illustrate the transitions between the active and the passive states obtained with a normal potentiostat. The dashed line illustrates the active-passive transition curve obtained with an alternative polarization control device. ΔV_{os} indicates the potential region where current oscillations are observed.

1.2. In Search for a Method

Figure 1-1 illustrates a fundamental problem in scientific research: the experimenter may change the system under study in such a way that the true behavior of the system is not observed, or an artificial and hence misleading behavior is observed. Thus the value of any experimental results becomes questionable, and identification of the characteristics of an inherently complex system becomes very difficult.

In any event, experimental observations and measurements provide the foundation for the development of a theoretical model which is an abstract description of the physical system, based on already established principles (laws) or new postulates. To obtain quantitative results, the theoretical model is formulated into a mathematical model and calculations are made. Subsequent comparison of theoretically calculated and experimentally measured results is necessary to characterize the system under study, but the comparison is primarily a test of both theory and experiment.

If theory and experiment are found to be in agreement, further experiments are usually needed to check and verify the theory and to determine the values of relevant parameters. Then we may be confident that we have a satisfactory knowledge and understanding of the system. If theory and experiment are found to be in disagreement, we need to consider whether the theory or the experiment is in error. Changes in the experimental apparatus and procedure or the theoretical principles and calculations are necessary to reach an agreement.

And there is always the question when can we say that experimental and theoretical results are in agreement, or what is the maximum acceptable discrepancy, given the existing experimental and theoretical uncertainties. Moreover experimental and theoretical results may not be directly comparable. An experimental system is normally a simplified or idealized representation of the real system whose characteristics we seek to determine, and a theoretical model is an abstract idealized representation of the real system, but the assumptions (idealizations) used in representing the system theoretically may be different from those used in representing the system experimentally.

Independent methods (means) to test the experimental data can be useful for determining whether the experiment is in error, but similar questions and uncertainties will inevitably arise during the application of the testing methods.

Often research gives useful insight into the questions it seeks to answer about a system, but no definitive answers or conclusions. Repeating experiments many times and under many different conditions, performing many different types of experiments, as well as performing numerous calculations and continuing the development of theoretical models, including possibly a radical reshaping of theoretical laws, are all necessary to bridge the gap between theory and experiment and complete a research study determining the characteristics of a system. One hopes that the interaction of theory and experiment will at last reveal the truth.

1.3. A History of the Iron - Sulfuric Acid System

A complete research study to determine the characteristics of a complex system requires a great amount of work, and often several researchers may work on the same system over a period of time. The determination of the characteristics of the system may therefore be considered to be a collective effort, in which many investigators take part and each investigator needs to be aware of the others' work. This section then is an overview of work that has been done on the iron-sulfuric acid system.

The iron-sulfuric acid system has been studied for many years by many investigators, but the behavior of the system has not yet been completely determined. Some authors have claimed that they have proved or established some characteristics of the system, but their work is generally limited to a certain range of the system, or their analysis is not rigorous enough to account for the complexity of the system, and their conclusions are therefore questionable, or leave unanswered questions.

Specifically in this section we consider the reaction mechanism for iron dissolution, the limiting-current and passivation phenomena, and the sustained current oscillations.

1.3.1. Reaction Mechanism for Iron Dissolution

The reaction mechanism for iron dissolution in acidic sulfate solutions has been very controversial, and a variety of conflicting experimental results have been reported about it. The controversy has most

frequently centered on two basic mechanisms: the Heusler or catalytic mechanism and the Bockris or consecutive mechanism.

Heusler (2) proposed the following mechanism, in the 1950's:

$$Fe + OH^- \rightleftarrows (FeOH)_{ads} + e^- \qquad [1\text{-}3a]$$

or

$$Fe + H_2O \rightleftarrows (FeOH)_{ads} + H^+ + e^- \qquad [1\text{-}3b]$$

and

$$Fe + (FeOH)_{ads} + OH^- \longrightarrow (FeOH)^+ + (FeOH)_{ads} + 2e^- \qquad \text{(rds)} \qquad [1\text{-}4]$$

$$(FeOH)^+ + H^+ \rightleftarrows Fe^{++} + H_2O \quad . \qquad [1\text{-}5]$$

In 1961, Bockris and coworkers (3) proposed a different mechanism:

$$Fe + OH^- \rightleftarrows (FeOH)_{ads} + e^- \qquad [1\text{-}3a]$$

or

$$Fe + H_2O \rightleftarrows (FeOH)_{ads} + H^+ + e^- \qquad [1\text{-}3b]$$

and

$$(FeOH)_{ads} \longrightarrow (FeOH)^+ + e^- \qquad \text{(rds)} \qquad [1\text{-}6]$$

$$(FeOH)^+ + H^+ \rightleftarrows Fe^{++} + H_2O \quad . \qquad [1\text{-}5]$$

The subscript ads indicates that the species is adsorbed at the electrode surface; an ion with no subscript is present in the electrolytic solution. (rds) indicates that the reaction was assumed to be the rate determining step.

Both of these mechanisms assume the formation of $(FeOH)_{ads}$, but in the Heusler mechanism $(FeOH)_{ads}$ acts as a catalyst, whereas in the Bockris mechanism $(FeOH)_{ads}$ is an intermediate consumed by the reaction.

Note that no physical picture of the catalytic action of $(FeOH)_{ads}$ is given by Heusler and that the catalytic mechanism assumes a two-electron transfer in a single reaction step, which is considered energetically unfavorable (3-5).

In the original formulation of the two mechanisms, reaction 1-3a, where OH^- ions react directly with iron atoms, was assumed. However in a strong-acid solution, the OH^- concentration is evidently too small to participate in the reaction.† To avoid this problem, reaction 1-3a was subsequently (4, 5) replaced by reaction 1-3b which involves reaction of H_2O molecules rather than OH^- ions from the solution to produce $(FeOH)_{ads}$. Reaction 1-3b can be considered as the sum of a series of elementary steps in equilibrium (4, 5). Proponents of the Heusler mechanism (*e.g.*, 6) have continued to write the catalytic step (equation 1-4) with OH^- as a reactant.

Both the Heusler and the Bockris mechanisms are for the range of low anodic overpotentials and very small surface coverage by $(FeOH)_{ads}$. The adsorption process was not explicitly treated in these early models (2, 3), and mass-transfer limitations were not considered. Extensions of the mechanisms to describe the entire anodic dissolution and passivation range were proposed later by several investigators, and we will discuss these models later in this section.

The Heusler and Bockris mechanisms were introduced mainly on the basis of experimental results for the value of the steady-state anodic

---

† Note that in their original work, Bockris and coworkers (3) used electrolytes with pH between 1 and 5. In this work we use 1 M H_2SO_4 with pH ≈ 0 and hence much smaller OH^- concentration.

Tafel slope

$$b_a = \frac{1}{\alpha_{a,Fe}} \frac{RT}{F} \qquad [1\text{-}7]$$

and for the apparent value of the reaction order with respect to the bulk solution pH or equivalently the OH^- concentration,

$$p_H = \frac{\partial \log i_{a,Fe}}{\partial \text{ pH}} = \frac{\partial \log i_{a,Fe}}{\partial \log [OH^-]} \; . \qquad [1\text{-}8]$$

Assuming the symmetry factor for each elementary reaction-step is 1/2 (see equation 1-34), the Heusler mechanism is consistent with b_a = 30 mV/decade (*i.e.*, $\alpha_{a,Fe}$ = 2) for a steady-state experiment, b_a = 60 mV/decade for a transient experiment, and p_H = 2, while the Bockris mechanism is consistent with b_a = 40 mV/decade (*i.e.*, $\alpha_{a,Fe}$ = 3/2) and p_H = 1. (4)

Since the introduction of the two mechanisms, much work has been done measuring the parameters b_a and p_H and thus providing support for either of the two mechanisms. In most of these studies, acidic sulfate solutions of pH above 0.5 or 1 were used. Reported values of the Tafel slope have ranged from 30 to 100 mV/decade, and values of the reaction order have ranged from 0 to 2. (4-11)

This wide range of experimental values may be due to deviations from Tafel behavior, or due to impurities in the iron electrode, impurities in the electrolytic solution, or defects of the electrode surface structure (3-5). Again we see how questionable experimental results can be, in this case, due to experimental conditions that are not strictly set up, rather than due to a fundamental problem.

Useful studies and reviews comparing the two types of mechanisms for iron dissolution from theoretical and experimental viewpoints are given by Kelly (4) and Hilbert, Lorenz, and coworkers (5). Kelly's analysis concluded in favor of the Bockris mechanism, which Kelly presented in a more elaborate form. Hilbert, Lorenz, and coworkers (5) concluded hoping "to have proved, beyond doubt, that the anodic dissolution [of iron] in aqueous solutions can follow two different mechanisms." They gave a synopsis of experimental results consistent with either the Bockris or the Heusler mechanism, depending on the morphology (crystallographic substructure) of the electrode surface.

According to Lorenz and coworkers (5), highly pure iron having a relatively low density of crystal imperfections gives results in agreement with the Bockris mechanism, whereas iron with many crystal imperfections[††] and hence high surface activity gives results in agreement with the Heusler mechanism, presumably because the catalytic action of $(FeOH)_{ads}$ takes place at imperfection sites. They believe that the catalytic mechanism is energetically rather improbable, but possible under certain conditions, since they cannot explain some experimental results in another way. Bech-Nielsen and coworkers (12) have also found results in agreement with either mechanism, depending on the electrode surface morphology. Allgaier and Heusler (13) presented a quantitative statistical analysis of the morphology of iron electrodes during dissolution, emphasizing that according to the catalytic mechanism, charge transfer occurs at sites of crystal imperfections.

[††] iron produced by cold-working processes

According to a more recent experimental study (11) of iron corrosion in sulfate solutions ($0 \leq pH \leq 2$), iron dissolution can follow three different mechanisms, depending on the solution pH. On the basis of measured b_a and p_H values, this study concluded that iron dissolves according to the Bockris mechanism at pH ~ 1, according to the Heusler mechanism at pH ~ 2, and according to a different mechanism at pH ~ 0. A significant conclusion of this study, which included solutions more acidic than most other studies, was that for pH ~ 0 ($pH < 0.2$) solutions, the rate of the anodic reaction is independent of the pH ($p_H = 0$), indicating that in this pH-range, H^+, OH^-, or H_2O species are probably not involved in the dissolution reaction. Hurlen (10) had earlier proposed a "double metal ion mechanism," according to which, half of the iron atoms undergo dissolution through reaction with (OH) species, and the other half of the iron atoms dissolve without interaction with (OH).

Experimental results were often consistent with a Bockris-type consecutive mechanism. Thus the Bockris mechanism has become the most widely accepted mechanism for the anodic iron dissolution in acidic sulfate solutions, at least at low overpotentials, but the controversy is not completely resolved.

Generally, two different sets of b_a and p_H values were often found experimentally and were usually interpreted by two different mechanisms, the Bockris or the Heusler mechanism. Dražić and Vorkapić (14) proposed an alternative mechanism which can account for both sets of experimental data depending on the effect of "internal strains" (the state of the electrode surface, concentration of active sites). The proposed mechan-

ism was basically the Bockris mechanism with an additional parallel dissolution-path, where $(FeOH)_{ads}$ can be transformed into $[Fe(OH)_2]_{ads}$ and then Fe^{++}. Such a general mechanism seems more likely than a change from one mechanism to a completely different mechanism to account for the experimental data.

So far we have considered work limited to low anodic overpotentials. Let us now consider work that has been done to determine the reaction mechanism for iron dissolution over the entire active and passivation range.

Proposed models have been based on the mechanisms described earlier in this section, predominantly the Bockris mechanism. These models are more complex than the earlier models in order to account for the more complex behavior of the system. They include more reaction steps and more intermediate adsorbed species. The models discussed next, in this section, generally derive kinetic equations using the Langmuir adsorption isotherm for the surface coverage by adsorbed intermediates, and they neglect mass-transfer limitations.

Lorenz and coworkers (15-17) measured steady-state polarization curves for iron in weak-acid sulfate solutions ($3.5 \leq pH \leq 5.5$). To interpret the experimental results, they proposed a mechanism with eight reaction steps including explicitly three adsorbed intermediates as well as H^+ ions. (See table 1-1.) They calculated kinetic parameters and current-potential curves which were similar to the experimental results. Bech-Nielsen (12, 18) proposed an even more complex mechanistic model, including H^+ ions, the activity of certain anions (*e.g.*, Cl^-) or

Table 1-1. Reaction Mechanism for Iron Dissolution and Passivation proposed by Lorenz and coworkers (15-17) (Based on experimental results for weak-acid sulfate solutions, $4 < pH < 6$)

$$Fe + H_2O \rightleftarrows (FeOH)_{ads} + H^+ + e^- \qquad [I]$$

$$(FeOH)_{ads} \rightarrow (FeOH)^+ + e^- \qquad \text{(rds)} \qquad [II]$$

$$(FeOH)^+ + H^+ \rightleftarrows Fe^{++} + H_2O \qquad [III]$$

$$(FeOH)_{ads} + H_2O \rightleftarrows [Fe(OH)_2]_{ads} + H^+ + e^- \qquad [IV]$$

$$Fe_s[Fe(OH)_2]_{ads} \rightarrow (FeOH)^+ + (FeOH)_{ads} + e^- \qquad \text{(rds)} \qquad [V]$$

$$Fe_s[Fe(OH)_2]_{ads} + H_2O \rightleftarrows Fe_s[Fe(OH)_3]_{ads}\text{-oxide phase} + H^+ + e^- \qquad [VI]$$

Passive (nonporous) layer formation:

$$2\ [Fe(OH)_3]_{ads}\text{-oxide phase} \rightleftarrows \gamma\text{-}Fe_2O_3 + 3\ H_2O \qquad [VII]$$

$$Fe_s[Fe(OH)_3]_{ads}\text{-oxide phase} \rightleftarrows Fe_2O_3 + 3H^+ + 3e^- \qquad [VII^*]$$

$$Fe_2O_3 + [Fe(OH)_2]_{ads} \rightleftarrows Fe_3O_4 + H_2O \qquad [VIII]$$

Fe_s is an iron atom of the metallic substrate on which a species is adsorbed.

* This alternative reaction for the formation of ferric oxide was proposed earlier (15), but was later (16) replaced by reaction VII. (See discussion of passivation in section 1.3.2.)

molecules of the electrolytic solution, and the density of defects on the metal surface and using Langmuir, Freundlich, and Temkin isotherms for the adsorbed intermediates.

Considering the complexity of the reaction mechanisms proposed by Lorenz and coworkers (15-17) and by Bech-Nielsen (12, 18), it becomes evident that steady-state techniques examining current-potential curves may be inadequate for elucidating such complex processes and establishing their characteristics. Transient techniques such as the electrochemical impedance technique can be much more powerful than steady-state techniques for investigating complex electrochemical systems. Let us then consider impedance studies of the iron-sulfuric acid system.

Epelboin and coworkers at the French *Centre National de la Recherche Scientifique* have done much work developing and applying the electrochemical impedance method for the study of the kinetics of metal dissolution and passivation as well as electrodeposition. Epelboin and Keddam (19, 20) first investigated steady-state polarization curves and concluded, on the basis of the corresponding reaction-order (p_H) values, that these curves strongly supported the Bockris type of mechanism. After the steady-state analysis, they performed an electrochemical impedance analysis which "confirmed" that conclusion.

Bechet, Epelboin, and Keddam (21) later stated that their previous impedance measurements were not sufficiently accurate at low frequencies and that the current-density range was limited. They therefore performed more impedance measurements over a larger current-density range and with better accuracy, made possible by the development of improved

instrumentation. These impedance measurements showed two inductive loops at low frequencies, at current densities of 50 to 100 mA/cm^2. To explain these results they added a parallel dissolution-path to the Bockris mechanism. The additional dissolution path involved another adsorbed intermediate species, $[Fe(OH)_2]^-_{ads}$. The additional dissolution reaction-step was assumed to be catalytic, similar to reaction 1-4 of the Heusler mechanism, but catalyzed by $[Fe(OH)_2]^-_{ads}$ instead of $(FeOH)_{ads}$. According to Bechet *et al.* (21), the Bockris mechanism is dominant at low pH, but the contribution of the parallel dissolution path to the overall current increases as the current density increases.

More recently Keddam *et al.* (22) presented the results of impedance measurements for iron dissolution in acidic sulfate electrolytes (H_2SO_4 + Na_2SO_4) with $0 \leq pH \leq 5$, at current densities well below the mass-transfer-limited current. At pH = 0 (1 M H_2SO_4) they observed two inductive loops in addition to the high-frequency capacitive loop attributed to the double layer. At higher pH they sometimes observed three time constants, inductive or capacitive, in addition to the one for the double layer, and they assumed that the presence of three additional time constants implies three adsorbed intermediate species in the reaction mechanism.

Keddam *et al.* (22, 23) then considered forty different reaction mechanisms having three adsorbed intermediates and finally concluded that, among the mechanisms considered, only one mechanism is able to interpret the experimental results over the range investigated. This mechanism is given in table 1-2 (reactions [A] through [G]). Reactions

Table 1-2. Reaction Mechanism for Iron Dissolution proposed by Keddam *et al.* (22, 23)

$Fe \longrightarrow (Fe^{+})_{ads} + e^{-}$	[A]
$(Fe^{+})_{ads} \longrightarrow Fe^{++} + e^{-}$	[B]
$(Fe^{+})_{ads} \rightleftarrows (Fe^{+})^{*}_{ads}$	[C]
$(Fe^{+})_{ads} \rightleftarrows (Fe^{++})^{*}_{ads} + e^{-}$	[D]
$(Fe^{+})^{*}_{ads} + Fe \longrightarrow (Fe^{+})^{*}_{ads} + Fe^{++} + 2e^{-}$	[E]
$(Fe^{++})^{*}_{ads} + Fe \longrightarrow (Fe^{++})^{*}_{ads} + Fe^{++} + 2e^{-}$	[F]
$(Fe^{++})^{*}_{ads} \rightleftarrows (Fe^{++})_{ads}$ (passivation)	[G]

[A] and [B] represent a Bockris-type dissolution path, which Keddam *et al.* (22) found to be dominant at low currents. Note that reactions [E] and [F] are "self-catalytic," similar to reaction 1-4 of the Heusler mechanism. The last reaction was introduced to account for passivation, and it can be ignored at low current and low pH. Keddam *et al.* obtained a theoretical expression for the faradaic impedance based on the proposed reaction mechanism. To obtain the (total) electrochemical impedance they subsequently assumed a constant double-layer capacity of 100 $\mu F/cm^2$ connected in parallel with the faradaic impedance.

Keddam *et al.* (22) state that the proposed reactions may not strictly be related to the true elementary steps, but were introduced as possible overall steps manifested in the electrochemical impedance. We note that elucidating the true elementary steps is limited by the sensitivity of available analytical methods and the stability of intermediate species. The chemical composition and nature of the intermediate species were not considered by Keddam *et al.* (22, 23). More direct analytical methods may be necessary to determine what species are actually present in the system and hence establish a detailed mechanism.

Neither OH^- nor H_2O was explicitly included in the reaction mechanism, but Keddam *et al.* (22) believe that the OH^- concentration can be considered to be implicitly contained in the value of the reaction rate constants. The rate constants were adjustable parameters in the theoretical model, and their values, which were chosen so that the model would reproduce as closely as possible the experimental results, were different for solutions with different pH.

(a)

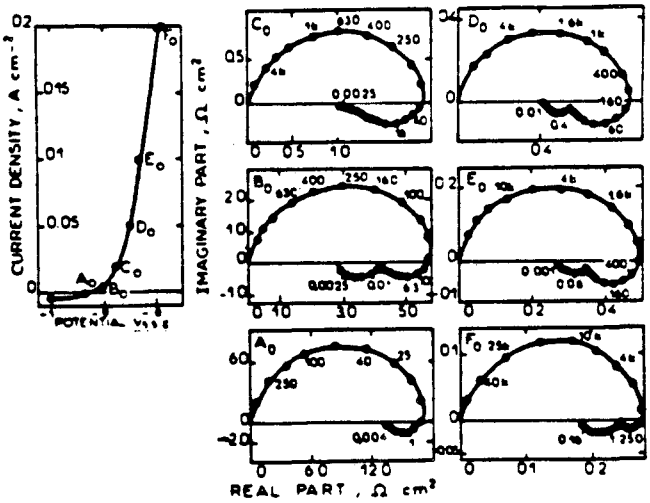

(b)

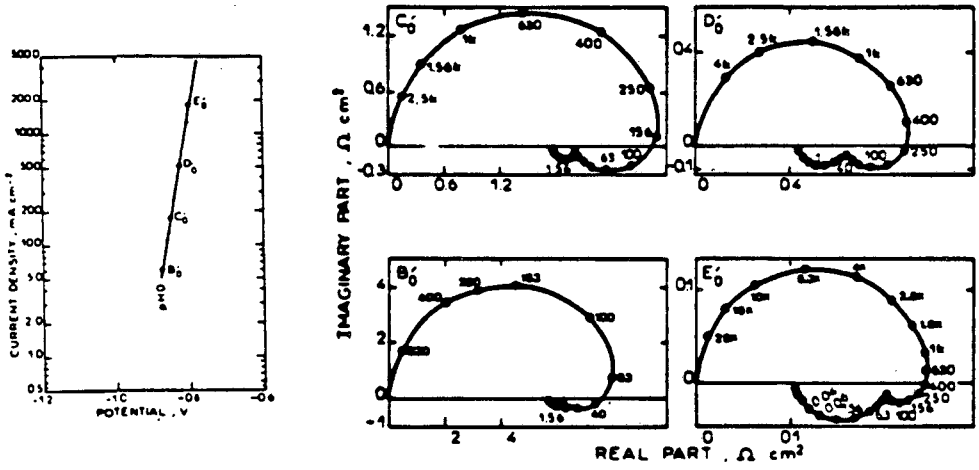

Figure 1-2. Comparison of measured and calculated impedance results of Keddam *et al.* (22) for an iron rotating disk electrode (d = 3 mm, Ω = 1600 rpm) in sulfuric acid solution (pH = 0). The parameter is frequency in Hz. Measured and simulated steady-state polarization curves are also shown. Polarization points about which the impedance was measured or calculated are marked on the corresponding polarization curve. (a) Measured results (Fig. 2 in Reference 22). (b) Calculated results (Fig. 8 and 7 in Ref. 22).

The calculated impedance results (22, 23) were generally in agreement with the experimental results over the range studied. Figure 1-2 shows the experimental and calculated impedance results for pH = 0. However the slope of the simulated steady-state polarization curves was different from that of the experimental curves, and Keddam *et al.* (22) state that the discrepancy in the steady-state results was "the price to be paid for better agreement of the impedance diagrams."

Schweickert *et al.* (6) also presented an impedance study to elucidate the iron dissolution mechanism, and proposed a mechanism quite different from those proposed by Epelboin, Keddam, and coworkers (19-25). Schweickert *et al.* argued that a dominant Bockris mechanism is not appropriate for explaining both the steady-state and the impedance experimental results, and they proposed a catalytic mechanism with seven reaction steps.

Schweickert *et al.* (6) emphasized the influence of the electrode surface state, which they modeled using potential-dependent coefficients. They used several fitting parameters to simulate the current-potential curves and the faradaic impedance, and they concluded that, because of the use of many fitting parameters, the agreement between simulation and experiment for the current-potential curves was only qualitative in nature. Schweickert *et al.* did not directly compare theoretical and experimental results for the electrochemical impedance; they only showed that their model yields a faradaic impedance with three time constants, two inductive and one capacitive.

In conclusion, this review of previous work investigating the reaction mechanism for iron dissolution in sulfuric acid solutions shows that there has been no complete and definitive study of the subject and thus the question of determining the reaction mechanism is still open.

In view of the complexity of the proposed reaction mechanisms for iron dissolution and the several simplifying assumptions that have been employed to develop mathematical expressions describing these mechanisms, it is evident that the development of more rigorous theoretical models taking into account most of the occurring phenomena and the interactions among them is necessary to characterize the system. These phenomena include multiple reactions, mass transfer, nonuniform current and potential distributions, and the role of the double layer.

Accounting for these phenomena becomes more important in the range of higher overpotentials, at the limiting current plateau, and along the active-passive transition. We consider this range in the following section.

1.3.2. Limiting Current and Passivation

As the overpotential is increased, the current increases until a limiting current plateau is reached, and subsequently the electrode passivates. Let us consider first the physical phenomena that underlie the limiting current and passivation behavior and then theoretical models that have been proposed to describe the phenomena.

Limiting currents are generally due to limitations in the transfer of a reactant from the solution to the electrode, or in the removal of a

product from the electrode into the solution. Anodic limiting currents are often associated with more complex phenomena such as formation of films covering the electrode surface and resulting in additional concentration and potential gradients in the system. For the iron-sulfuric acid system, the formation of a ferrous sulfate film is also thought to be a necessary precursor to passivation due to subsequent formation of an iron oxide film.

Several authors (26-31) have reported formation of ferrous sulfate films on iron electrodes in sulfuric acid solutions, at the limiting current and during the onset of passivation. In a microscopic investigation Beck (31) observed that salt crystals would often start at the periphery of a shielded electrode (where the current density was a little higher) and then propagate part way toward the center. Another study (32) using microscopic observations of iron in 1 N sulfuric acid solution suggested the precipitation of colloidal ferrous hydroxide particles rather than ferrous sulfate crystals as a precursor to passivation.

At a high current density, rapid dissolution of the iron electrode results in a high concentration of ferrous ions near the electrode. If the ferrous ion concentration exceeds the saturation concentration in the solution, or a critical supersaturation concentration, then ferrous salt crystals can precipitate on the electrode surface. Serra and Feliu (27) and Beck (31) calculated supersaturation factors of about 2 for ferrous sulfate precipitation to begin.

As iron dissolution continues, a porous salt film grows on the electrode surface. Alkire *et al.* (30) calculated maximum salt film thicknesses between 2 and 25 μm using a simple theoretical model for film growth and experimental data for iron in 6 N H_2SO_4. Beck (31) measured potentiostatic current transients for iron in acid solutions, while observing the electrode surface with a microscope. He calculated a salt film thickness of about 10 μm for iron in 5 N $HClO_4$, using the model of Ref. (30) and his experimental data. He also calculated an approximate porosity value of 1% for the $Fe(ClO_4)_2$ salt film.

The thickness (δ_f) and porosity (ϵ_f) of the salt film are key parameters for the behavior of a system that contains a salt film, but there is little knowledge about their values. The ohmic potential drop in the pores of the salt film depends on these parameters and is approximately given by (31)

$$\Delta\Phi_{\Omega,f} = \frac{i}{\kappa_f}\left(\frac{\delta_f}{\epsilon_f}\right) , \qquad [1\text{-}9]$$

where κ_f is the conductivity of the solution in the pores. The potential drop in the salt film produces concentration changes through the film. Changes in the H^+ concentration are particularly important, because they determine the tendency of the iron electrode to passivate, as we describe later. It appears that more sophisticated experimental techniques and theoretical models are necessary in order to obtain accurate and reliable values for the porosity and thickness of the salt film on iron (and other corroding metals) and therefore be able to characterize the system.

Faraday (33, 34) discussed the passivation of iron in 1836 and attributed passivation to coverage of the iron surface by an insoluble oxide film. Almost 100 years later, the oxide passivation theory was initially verified by Evans *et al.* (35), who isolated oxides from passivated iron. Flade (36) studied the passivation of iron in sulfuric acid and observed a potential characteristic of the passive-active transition. Pourbaix (37) presented data for the theoretical equilibrium between iron and iron oxides as well as experimental data for the conditions where iron was observed to passivate. The experimental conditions for passivation were described by

$$(V_m - \Phi_o)_{NHE} \geq 0.40 - 0.085\ pH \qquad (\text{for } pH < 12). \qquad [1\text{-}10]$$

Passivation therefore requires high potential and/or high pH values. Note that the passivation condition given by equation 1-10 lies above the Fe/Fe_2O_3 equilibrium line in a potential *vs.* pH diagram (37).

Beck (31) demonstrated that, in a strong-acid solution (low pH), condition 1-10 cannot be satisfied and hence oxide passivation is not possible without prior formation of a salt film on the electrode. At the low pH value prevailing in the bulk solution, unrealistically high surface overpotential and hence current-density values would be necessary to satisfy condition 1-10. The high current density would result in a large ohmic potential drop in the solution, which in turn would limit the surface overpotential that can be achieved in a potentiostatic experiment. The formation of a porous salt film can cause two major changes allowing passivation: decrease of the current density, by limiting the transport of Fe^{++} and also by partially covering the active

electrode-surface; increase of the local pH at the electrode surface due to enhanced migration of H^+ away from the electrode through the additional potential drop (equation 1-9) across the porous salt film. The condition for passivation is thus satisfied, and an oxide film begins to form underneath the salt film (31).

Alkire *et al.* (30, 38) have also emphasized the role of a salt film in the corrosion and passivation of iron and other metals. The salt film on the electrode is also associated with the current oscillations in a range of potentials along the limiting current plateau for the iron-sulfuric acid system. We will discuss these oscillatory phenomena in the next section.

The passive state of iron is still controversial. The film covering passive iron is generally recognized as primarily a ferric oxide, about 15 to 40 Å thick, but there is still controversy and incomplete knowledge about the nature of this film, particularly its chemical composition and electrical conduction properties.

There have been numerous studies (39-51) of the passive film on iron, mostly in neutral solution, using a variety of experimental techniques, but the results and proposed models have often contradicted each other. According to a popular model, the passive film is a γ-Fe_2O_3 - Fe_3O_4 film, with the Fe_3O_4 oxide next to the metal and the γ-Fe_2O_3 oxide next to the solution (39, 40). Other models view the film as a single layer of a ferric oxyhydroxide, probably FeOOH, including defects that affect the conductivity of the film (45-47), or a hydrated polymeric ferric oxide (48).

The passivation of iron, *i.e.*, the transition from the active to the passive state, has also been controversial. Various types of passivation are illustrated schematically in figure 1-3 and are discussed in this section. We have already shown in figure 1-1 two different shapes of experimental passivation curves. In potentiodynamic experiments with a conventional potentiostat, sharp vertical transitions between the active and passive states are observed in a current *vs.* potential diagram. The active-passive transition occurs at a potential V_{A-P} and the passive-active transition occurs at V_{P-A}, which is less anodic than V_{A-P}, *i.e.*, there is a hysteresis phenomenon.

Epelboin, Gabrielli, and coworkers (52, 53) suggested that the observed sharp transitions and hysteresis are not fundamental properties of the Fe/H_2SO_4 system, but are due to the inability of the conventional potentiostat to control the system and show its true characteristics. Epelboin and coworkers designed an alternative polarization control device called a Negative Impedance Converter,[‡] with which they recorded a continuous and reversible passivation curve having a parabolic shape (see figures 1-1 and 1-4). The polarization curve obtained with this alternative control device is called a Z-shaped curve, because of its characteristic shape, which is associated with multiple steady states.

Epelboin, Gabrielli, and coworkers (52, 53) observed localized dissolution/passivation of rotating disk electrodes along the passivation curve, and they measured the electrode surface profiles with an

---

[‡] The principles of polarization control are described in more detail in section 2.2.

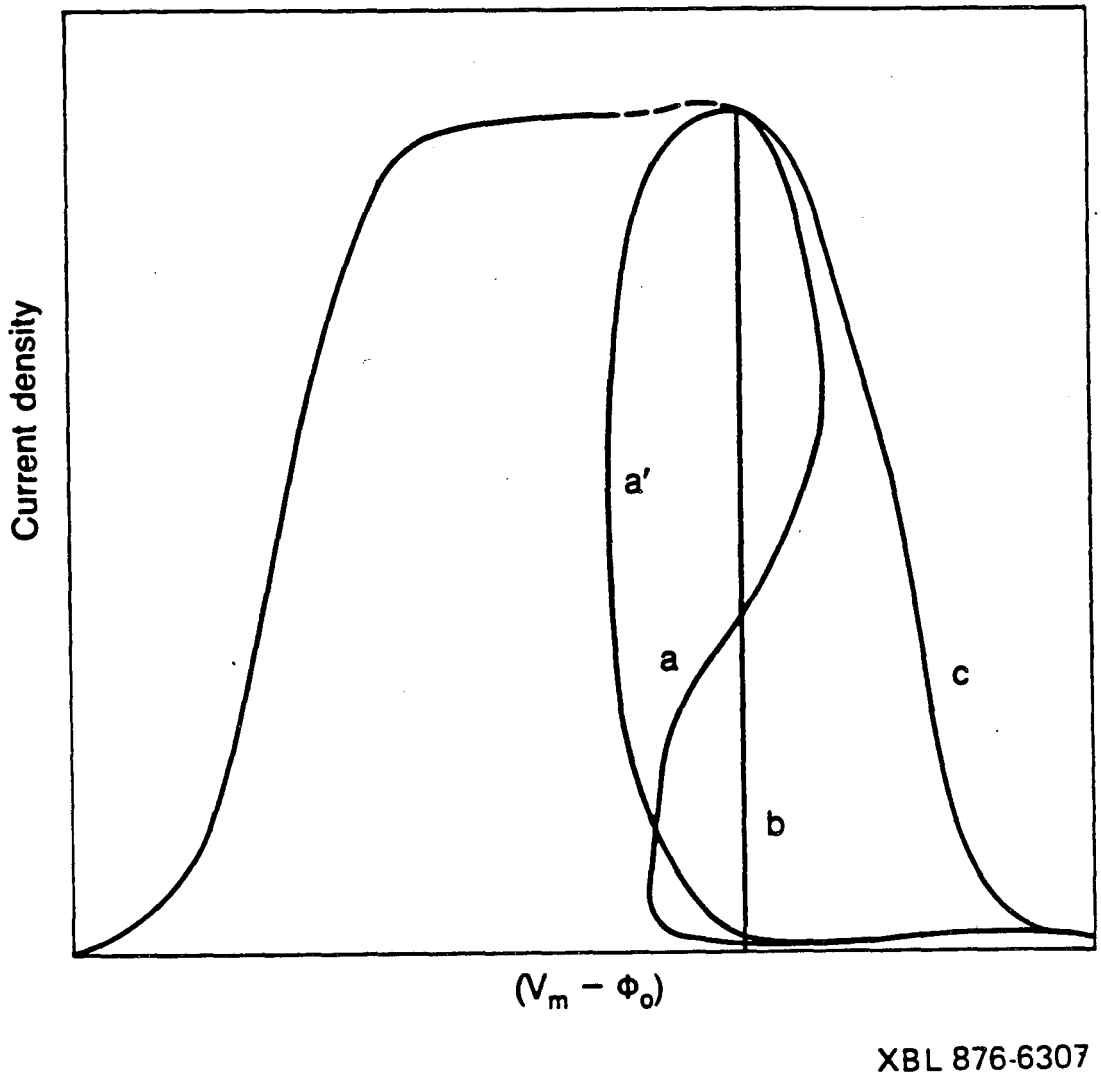

Figure 1-3. Schematic current-overpotential diagram illustrating various types of iron passivation that have been experimentally determined or theoretically proposed. (taken from Ref. 60)
(a) Experimental curve obtained by Epelboin and coworkers (24, 54). (See also figure 1-5.) (a') Theoretical calculated curve by Epelboin and coworkers (24, 25, 54).
(b) Local passivation behavior in the Law and Newman model (59).
(c) Experimental and theoretical curve obtained by Lorenz and coworkers (16, 17).

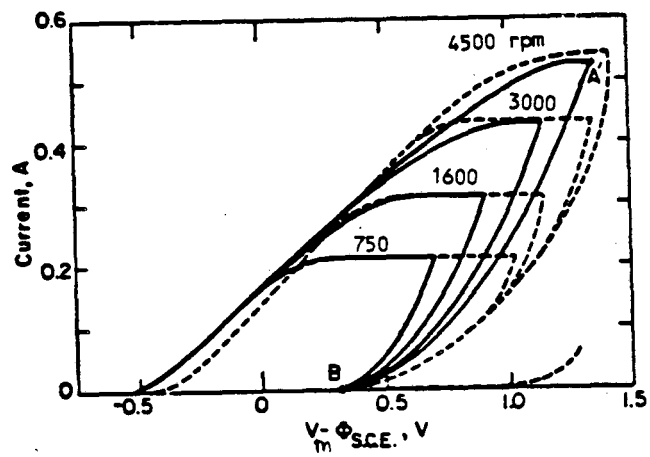

Figure 1-4. Comparison of measured and calculated polarization curves for an iron rotating disk in 1 M sulfuric acid at four rotation speeds (Fig. 6 in Ref. 59).
dashed line - experimental results of Epelboin *et al.* (52)
solid line - calculations of the Law and Newman (59) model, p = 0.01

optical microscope, which had a depth of field small enough to allow measurements within ± 1 μm. The electrodes had three different configurations, depending on the electrode rotation speed: active (dissolving) outer ring and passive center disk, at low or moderate rotation speeds; active ring between an outer passive ring and a passive center disk, at higher rotation speeds; active center disk and passive outer ring, at very high rotation speeds.

Epelboin *et al.* (24, 54, 55) also presented polarization curves recorded with the Negative Impedance Converter and subsequently corrected for ohmic potential drop (curve a in figures 1-3 and 1-5). The ohmic drop was calculated using the theoretical primary resistance for ring-disk electrodes (56) and the experimentally determined dissolving area of the electrode. The polarization curve obtained in this manner had a peculiar shape indicating multiple steady-states without the ohmic drop contribution, and Epelboin *et al.* concluded that the multiplicity of steady states is a fundamental characteristic of the Fe/H_2SO_4 electrochemical system. However one can question the accuracy of the ohmic correction by Epelboin *et al.* and hence the validity of the resulting passivation curve. There could be significant experimental errors and uncertainties in the ohmic drop correction, especially as the electrode is passivating nonuniformly and its ohmic resistance is continuously changing.

According to Lorbeer, Lorenz, and coworkers (16, 17), the sharp transitions between the active and passive states of iron observed with a conventional potentiostat can be due to ohmic potential drop, and the

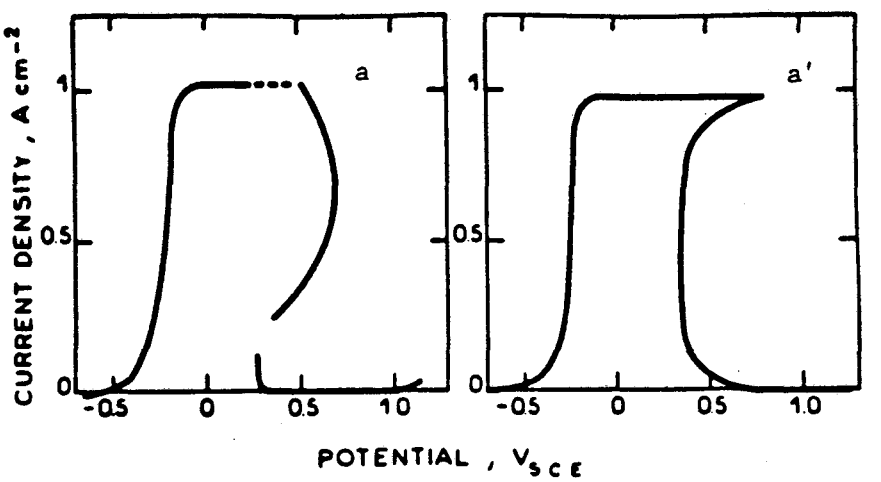

Figure 1-5. Polarization curves for iron in 1 M sulfuric acid obtained by Epelboin *et al.* (Fig. 16 in Ref. 54).
(a) Experimental curve (Ω = 750 rpm) measured using a Negative Impedance Converter and subsequently corrected for ohmic potential drop; plotted in terms of the current density for the actually dissolving area of the electrode.
(a') Calculated curve.

observed hysteresis is due firstly to the high ohmic potential drop included preferentially in the positive potential sweep and secondly to irreversibilities associated with the formation and dissolution of the passive film on the electrode.

Lorenz and coworkers (16) measured current-potential curves (cyclic voltammograms) using electronic feedback compensation of the ohmic resistance for iron in weak-acid sulfate solutions of pH between 4 and 6. They reported polarization curves with a negative slope during passivation (curve c in figure 1-3); *i.e.*, the current decreases gradually with increasing potential over a certain potential range. These negative-slope passivation curves had a Tafel slope of -100 ± 20 mV/decade (16).

Moreover the ohmic-compensated polarization curves presented by Lorenz *et al.* (16) show only a relatively small hysteresis between the positive and negative potential-sweeps compared with the curves obtained with a conventional potentiostat. The small hysteresis, which is related to irreversibilities, is influenced by the potential sweep rate, and according to Lorenz *et al.*, one can assume that measurements under steady-state conditions would lead to a single, continuous curve for the transition between the active and passive states.

Note however that Lorenz *et al.* (16) did not measure current-potential curves with ohmic compensation for iron in anodic sulfate solutions with pH lower than 4, because, as they noted, the maximum current density would reach extremely high values, and in that case exact compensation of the correspondingly high ohmic drop would be

problematical. The polarization curves they presented for sulfate solutions with higher pH have two current local maxima and do not display a limiting current plateau; *i.e.*, those curves show a behavior before passivation which is different from that observed for stronger-acid solution. (See, for example, figures 1-1 and 1-4.) Thus it is not clear whether in sulfate solutions with pH 0 to 3, the iron passivation behavior would be the same as that found by Lorenz *et al.* (16) in solutions with pH 4 to 6. Lorenz (57) later commented that in stronger-acid solutions at very high current densities, coverage of the electrode surface by a porous layer consisting of ferrous salt and iron oxide can be assumed and this layer may act as an inhibitor producing the observed discontinuous passivation behavior.

So far we have considered the shape of experimental passivation curves. Let us then describe and discuss theoretical models that have been proposed for iron passivation. Some of these models also treat the limiting current plateau, which is physically related to the passivation process.

Lorenz and coworkers (15-17) presented a kinetic model for iron dissolution and passivation based on the detailed reaction mechanism shown in table 1-1. The model includes three adsorbed intermediates, $(FeOH)_{ads}$, $[Fe(OH)_2]_{ads}$, and $[Fe(OH)_3]_{ads}$. Gilroy and Conway (58) had already proposed that the iron surface is covered by these three intermediates which inhibit the dissolution reaction, resulting in a negative Tafel slope.

The model of Lorenz *et al.* (16, 17) predicts a negative slope for the passivation curve (curve c in figure 1-3), as a result of the adsorption of the $Fe_s[Fe(OH)_3]$-oxide phase species. This species is transformed into a passive Fe_2O_3 oxide according to the chemical reaction [VII]. The theoretical Tafel slope of the passivation curve is then −120 mV/decade, in agreement with the ohmic-compensated experimental results of Lorenz *et al.* (16). Lorenz *et al.* had previously (15) assumed formation of Fe_2O_3 according to the electrochemical reaction [VII*] involving transfer of $3e^-$. That assumption gives a sharp decrease of current during passivation (−20 mV/decade), which essentially corresponds to curve b in figure 1-3. (See Fig. 5 in Ref. 15) Lorenz *et al.* (16) rejected the latter assumption in order to get better agreement with their ohmic-compensated experimental results.

We consider then the model of Law and Newman (59), which yields a Z-shaped polarization curve very similar to the experimental curves of Epelboin *et al.* (52). Figure 1-4 shows a comparison of the calculated and experimental polarization curves. Law and Newman calculated potential and current distributions for a partially passivated rotating disk electrode. The model uses a modified Butler-Volmer expression to describe the kinetics of active dissolution of a rotating disk electrode and treats the transition from the active to the passive state as a discontinuous change of the local current density to an extremely low value (a specified constant). This discontinuous passivation is assumed to occur at a characteristic value of the local potential $(V_m - \Phi_o)_*$. Curve b in figure 1-3 illustrtates the passivation behavior proposed by

Law and Newman.

The Law and Newman model (59) also includes the effect of mass-transfer limitations in the kinetic expression without explicitly considering the concentration of a limiting reactant. This is accomplished by including the factor $(1 - i/i_{lim})^p$ in the modified Butler-Volmer expression. The model accounts for the nonuniform potential (Φ_o) distribution across the disk electrode. As a result of the nonuniform potential distribution, the electrode is partially passive during passivation. The configuration of the electrode considered by Law and Newman is an active center disk with a passive outer ring, since $(V_m - \Phi_o)$ is higher near the periphery of a rotating disk electrode; as passivation proceeds, the passive state extends towards the center until the entire electrode becomes passive. Note that, as we mentioned earlier, this configuration as well as different configurations were observed by Epelboin *et al.* (52), and thus the assumption of an active disk configuration may limit the applicability of the Law and Newman model.

A main conclusion of the Law and Newman (59) model is that the positive slope of the passivation curve in the observed Z-shaped polarization curve is due entirely to ohmic potential drop for an electrode passivating nonuniformly. In contrast, according to the model of Epelboin and coworkers (24, 25) the positive slope of the passivation curve, indicating multiple steady states, arises mainly from the kinetics and mass-transfer characteristics of the Fe/H_2SO_4 system. The model developed by Epelboin and coworkers yields a passivation curve (curve a′ in figures 1-3 and 1-5) with a different shape from the ohmic-corrected

experimental curve (curve a in figures 1-3 and 1-5) determined by the same workers, while both of these curves show multiple steady-states without the ohmic potential drop contribution. A comparison of the calculated and experimental polarization curves of Epelboin *et al.* (24, 54) is given in figure 1-4.

The model of Epelboin *et al.* (24, 25) assumes the following reaction mechanism:

$$Fe + OH^- \longrightarrow (FeOH)_{ads} + e^- \qquad [1\text{-}3a]$$

$$(FeOH)_{ads} \longrightarrow (FeOH)^+ + e^- \qquad [1\text{-}6]$$

$$(FeOH)^+ = Fe^{++} + OH^- \qquad [1\text{-}11]^{\dagger}$$

$$(FeOH)_{ads} + OH^- \rightleftarrows [Fe(OH)_2]_{ads} + e^- \quad \text{(passivation)}. \qquad [1\text{-}12]$$

$[Fe(OH)_2]_{ads}$ is considered to be the species causing passivation.[‡] The same mechanism for iron dissolution and passivation was proposed by Bockris *et al.* (43).

Epelboin *et al.* (24, 25) write Butler-Volmer type kinetic expressions for the above reaction steps, using the Langmuir isotherm for the adsorbed species. They also consider mass transfer of the reactant OH^-, using the Nernst diffusion-layer approximation. At steady state, they set the rate of change of the surface coverage by each adsorbed species to zero and hence eliminate the coverages from the kinetic expressions.

---

† Reaction 1-11 is assumed to be in fast equilibrium and does not affect the model calculations.

‡ Fe_2O_3 is considered to be the species covering the electrode surface in the completely passive state, after transformation of $[Fe(OH)_2]_{ads}$ into Fe_2O_3 (24, 43).

By equating the current density given by the kinetic relationships to the current density given by the diffusive flux, they obtain an equation which is third order w.r.t. the activity (concentration) of the reactant. This equation can thus have, under certain conditions, three real roots corresponding to three different values of the current density at a given potential value for a range of potentials.

In order to test their model, Epelboin *et al.* (24, 25) also calculated the electrochemical impedance and compared the calculated impedance results with the experimental results. The calculated impedance diagrams appeared to be in qualitative agreement with the experimental diagrams, in terms of the order of magnitude of the impedance and the number and kinds of loops, but a quantitative matching of experimental and theoretical results was not shown.

A critical feature of the reaction mechanism proposed by Epelboin *et al.* (24, 25) which enables the appearance of multiple steady states is that the overall passivation reaction ([1-3a] + [1-12]) has a higher order w.r.t. a reactant species (OH^-) than the dissolution reaction ([1-3a] + [1-6]); this makes the overall mechanism "autocatalytic" (54). The presence of mass-transfer limitations for this reactant species is also an essential feature in the model of Epelboin *et al.* As we mentioned earlier, the presence of a limiting current plateau indicates mass-transfer limitations in the transport of a reactant to the electrode, or in the removal of a product from the electrode surface. Epelboin *et al.* (24) state that if mass transfer of the product $(FeOH)^+$ only is considered, the polarization curve does not show multiple steady

states. They therefore assume in their model that the reactant is the mass-transfer limiting species in order to obtain a limiting current plateau as well as to produce multiple steady states. In terms of the model equations, the diffusion of the reactant together with the reaction orders and the adsorption process gives a third-order equation w.r.t. the activity of the reactant.

Epelboin *et al.* (24, 25) made several simplifying assumptions in their treatment of the diffusion process which may not be valid. First they stated that, for a concentrated medium at high current densities, the infinite-dilution treatment is not appropriate, but then they used the infinite-dilution approximation in their mathematical model. They also stated that it is obvious that the concentration of OH^- in acid solution is far too low to take part directly in the reaction. In their model calculations they chose a value for the bulk activity of OH^- that gives a limiting current value close to the experimental value. The chosen value was about ten orders of magnitude larger than the actual concentration of OH^- in 1 M sulfuric acid (unless one uses a value for the diffusion coefficient even more orders of magnitude larger than its normal value).

To justify using OH^- as the diffusing species, Epelboin *et al.* (24) said that, since the nature of the various species present in the diffusion layer is poorly known and since experimental data showed a dependence of the current on the bulk solution pH, the diffusing species, whatever it is, determines the amount of OH^- at the interface, and therefore they considered OH^- in order to simplify the model. They also

noted that since at the limiting current plateau, the electrolyte close to the electrode is essentially saturated iron sulfate, H_2O is a plausible diffusing and reacting species. (See also the discussion on the role of OH^- in section 1.3.1.) Evidently the reacting and diffusing species in the model of Epelboin *et al.* is a rather arbitrary species without a well-defined physicochemical identity.

It is significant to note here that, the limiting current plateau for the Fe/H_2SO_4 system may be characterized without assuming the presence of a mass-transfer limiting reactant in the solution. Specifically, the presence of a porous $FeSO_4$ film on the electrode can yield a current plateau. Russell and Newman (61) give an analysis of the limiting current showing that the steady-state current value can remain constant while the applied potential changes, if certain conditions are satisfied; these conditions are relationships between the salt film thickness, the film porosity, the fraction of the electrode covered by $FeSO_4$, and the potential.

An alternative explanation of the limiting current plateau is given by a mathematical model for the Fe/H_2SO_4 system developed recently by Gan and Orazem (62). The model does not include a reactant species in the iron dissolution reaction, and it yields limiting current values which are proportional to the square root of the electrode rotation speed and agree with the experimental values obtained by Epelboin *et al.* (52). This one-dimensional model includes the microscopic structure of the double layer, where multiple reactions take place, as well as macroscopic transport in the solution, by migration, diffusion, and con-

vection (still using dilute-solution theory), but it does not include a salt film. At the limiting current plateau, the calculated Fe^{++} concentration near the electrode surface remains constant (independent of potential and rotation speed). According to this model, the limiting current can be attributed to limitations in the removal of corrosion products from the electrode surface coupled with the partial coverage of the surface by a passivating oxide. Specifically in the model, Fe^{++} accumulates near the surface and can be oxidized to Fe^{+++}, which forms Fe_2O_3 reducing the active area of the electrode (62).

Moreover the results of the Law and Newman model (Fig. 4 in Ref. 59) show that the observed parabolic shape of the passivation curve can be partly characterized without considering mass-transfer limitations, since from the viewpoint of the model, the parabolic passivation curve is a result of ohmic potential drop for a partially passive electrode.

The theoretical models of Russell (61), Gan (62), and Law and Newman (59) show that it is possible to characterize two main features of the Fe/H_2SO_4 polarization curve, the limiting current plateau and an approximately parabolic passivation curve, without the assumption of a mass-transfer limiting reactant in the solution. This assumption made by Epelboin *et al.* (24, 25) is essential for predicting multiple steady states without the ohmic potential drop contribution. Therefore, unless one accepts the multiplicity of steady states due to diffusion of a reactant species as a fundamental characteristic of the Fe/H_2SO_4 system, there is no fundamental reason to introduce the assumptions of the model of Epelboin *et al.* which yield the multiplicity of steady states.

Russell (60, 63) performed some experiments to resolve the controversy between the theoretical model of Law and Newman (59) and the model and some experimental results of Epelboin *et al.* (24, 52). He used three rotating disk electrodes with three different diameters. As the disk diameter decreases, the total current is reduced, and the ohmic potential drop in the solution decreases. Therefore the contribution of ohmic effects in the system behavior decreases as the electrode size decreases.

A significant result obtained by Russell and Newman (63) is shown in figure 1-6, which shows that the passivation curve becomes steeper as the disk diameter decreases. Russell also measured the corresponding polarization curves with a normal potentiostat and observed that the width of the hysteresis (difference between V_{P-A} and V_{A-P}) decreases as the disk diameter decreases. These two trends in the experimental polarization curves are considered as an indication that in the limit of zero electrode size (no ohmic potential drop), both the active-passive and passive-active transitions are characterized by a nearly vertical line on a current *vs.* potential graph, in agreement with the Law and Newman (59) model.

Russell and Newman (63) then concluded that, assuming the active part of the rotating disk electrode always has a disk configuration, their experimental results have shown that the Z-shaped polarization curve, obtained with a Negative Impedance Converter, is due only to ohmic potential drop in solution. However Epelboin *et al.* (52) observed that the active part had a ring configuration, and in this work (section

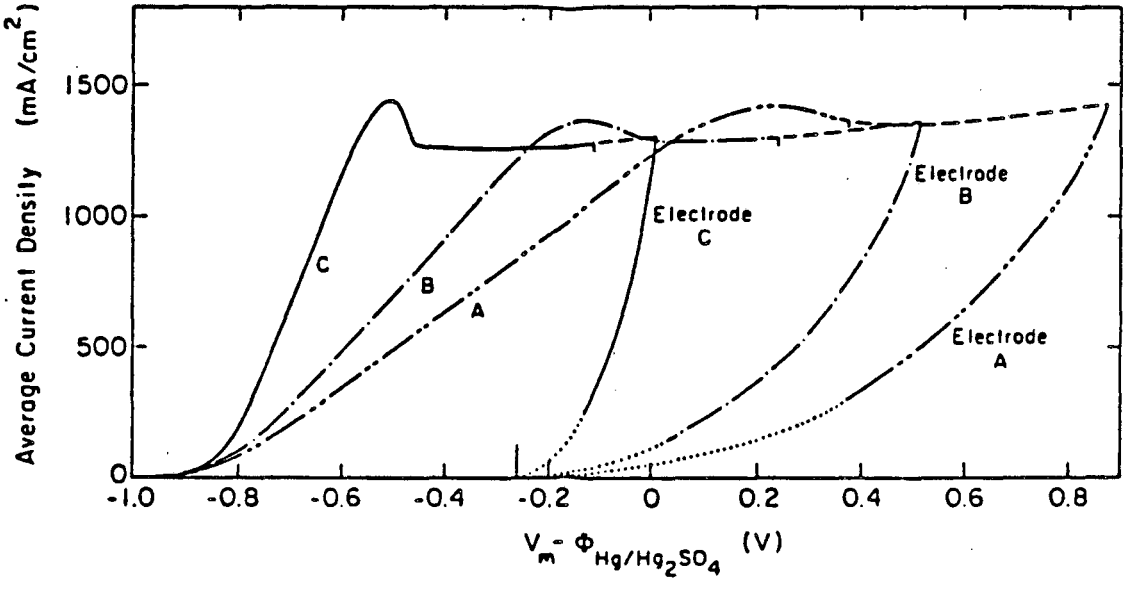

Figure 1-6. Polarization curves for three rotating disk electrodes measured by Russell using a polarization device with a positive-slope load line. Electrode diameters: A - 4.94 mm, B - 2.98 mm, C - 0.986 mm. Electrolyte: 1 M sulfuric acid. Ω = 1600 rpm. (Fig. 6 in Ref. 63)

3.6.2) we have also observed dissolution of the outer ring part of the disk electrode, under the same conditions as the experiments of Russell (60, 63). Therefore the conclusions of Russell and Newman cannot be completely substantiated, even though they support the hypotheses of Law and Newman (59).

A different approach to the modeling of metal passivation kinetics was presented by Griffin (64, 65). Griffin's theoretical passivation model, which may be applied to the Fe/H_2SO_4 system, assumes a two-step reaction mechanism including oxidation of metal atoms to produce adsorbed cations and subsequent dissolution (desorption) of the cations into the electrolyte. The rate of cation desorption is assumed to depend on the (fractional) surface coverage by adsorbed cations, which can be either isolated or incorporated into an oxide layer, and a Temkin-type adsorbed cation interaction parameter, but not on the potential. Griffin (64) calculated steady-state current-potential curves, and for certain values of the interaction parameter, the curves displayed multiple steady states during passivation due to multiple solutions for the surface coverage at certain potentials. Griffin (65) also predicted a hysteresis in potentiodynamic sweep curves around the active-passive transition.

Griffin's passivation model (64) is an example of a simple kinetic model that can give multiple steady states without considering either diffusion or ohmic potential drop effects. The model of Griffin has not been applied to the Fe/H_2SO_4 system, and therefore it is not known whether the model can describe the passivation behavior of this specific

system. Talbot *et al.* (66, 67) applied linear stability and bifurcation analysis to Griffin's passivation model and determined that when three steady states exist, the middle state is unstable and the two outer states are stable; the system moves away from the middle steady state to the outer steady states. For the Fe/H_2SO_4 system, the active state and the passive state may be considered as two stable steady states, and a partly-active partly-passive state may be considered as a middle unstable state.

1.3.3. Sustained Current Oscillations

Sustained current oscillations at constant potential are observed within a certain potential range on the limiting current plateau for the iron-sulfuric acid system (68-72, 31, 60).

Podestá *et al.* (69) studied the effects of the H_2SO_4 concentration, the electrode rotation speed, temperature, and the concentration of iron ions on the current oscillations. They interpreted their results phenomenologically by discussing the reaction mechanism of iron dissolution and passivation together with mass-transfer effects. The oscillations observed by Russell (60, 70) were overall periodic, but in some cases, particularly for larger electrodes and greater rotation speeds, the periods and shapes of the cycles varied significantly. The oscillation frequency was found to be a linear function of the square root of the electrode rotation speed for disk electrodes (69, 70). Oscillations were also observed for a hemispherical electrode, but the oscillation frequency for this electrode was a weaker and nonlinear function of the

rotation speed (70).

Beck (31) observed microscopically an oscillatory growth of salt crystals on a shielded iron electrode during current oscillations in H_2SO_4 and $HClO_4$ solutions. He reported that the salt crystals grew after the current rise and disappeared when the current decayed. Beck then presented a phenomenological description of the processes leading to oscillations. Oscillations were explained by the growth and dissolution of a porous salt film and the associated changes in the potential and concentration profiles in the pores of the film, resulting in cyclic transitions of the electrode between the active and passive states (31).

Oscillations in electrochemical systems are most frequently observed during the anodic dissolution of certain metals which can passivate, *e. g.*, copper in various electrolytes (73-76). These electrochemical oscillations are associated with the instability of porous or non-porous passivating films under certain conditions.

Wojtowicz (77) presented a review of experimental studies and theories proposed to explain oscillatory behavior in electrochemical systems. Several mathematical tools, such as phase-plane analysis and bifurcation, are available for describing oscillatory behavior. Talbot *et al.* (66, 67) recently presented an application of linear stability and bifurcation analysis to the oscillatory model of Franck and FitzHugh (78) for iron dissolution and passivation. These mathematical techniques are useful for determining the conditions for oscillations, multiple steady states, or single steady states. Russell and Newman (61) summarized some of the oscillatory models for the iron-sulfuric acid

system.

An essential feature of the Fe/H_2SO_4 oscillatory system is considered to be a porous ferrous sulfate film covering the electrode surface. We have already discussed the role of the salt film for the limiting current and passivation behavior (section 1.3.2). A qualitative description of the physical process manifested in the current oscillations as proposed by Beck (31) and Russell (61, 70) is given below.

The current values are near a maximum in the oscillatory current-time curve when most or all of the electrode surface is active. When the electrode is in the active dissolution state, the current density is high and therefore there is a high potential gradient across the salt film. This high potential gradient causes migration of H^+ ions away from the electrode through the pores of the salt film and thus facilitates passivation according to condition 1-10. At a sufficiently high pH value at the surface, the electrode passivates locally with an oxide film covering the surface. The current gradually decreases as passivation extends over a larger part of the electrode determined by the potential and pH distributions. The current is at a minimum value when a large part of the electrode is passive. At low current values, the potential gradient in the salt film is substantially reduced, and H^+ ions can diffuse back to the electrode surface. When the pH near the surface decreases sufficiently, the passivating oxide dissolves, and the electrode returns to the active state. One cycle is completed, and the process repeats itself.

Russell and Newman (61, 79) developed a mathematical model based on the above process for the sustained current oscillations in the Fe/H_2SO_4 system. The model is developed on a more fundamental basis than previous models; it includes a porous ferrous sulfate film as an integral part. In the model, the salt film remains on the electrode during the oscillations, and it grows or dissolves following the Fe^{++} concentration. The model uses a modified Butler-Volmer equation to describe the kinetics of the iron dissolution reaction (like the model of Law and Newman, Ref. 59) and the potential-pH condition for passivation given by Pourbaix (equation 1-10). The model also includes mass transfer by convection, diffusion, and migration, and it determines the concentration and potential profiles in the solution in the pores of the salt film and in the diffusion layer. The fundamental equations subject to appropriate boundary conditions are solved numerically.

The model of Russell and Newman (61) is one-dimensional and strictly applies to regions of the electrode undergoing continuous cycling between the active and the passive states. However the observed minimum current density during oscillations is too large to be produced by an entirely passivated electrode, and therefore a portion of the electrode is always undergoing active dissolution. The model then uses a "residual ohmic drop" parameter to correct for the ohmic potential drop due to the dissolution of the portion of the electrode that remains active.

The calculated current-time curve was similar with the experimental curve, specifically the calculated current-density values were in good

agreement with the experimental values, but there were also significant discrepancies between the calculated and experimental results. The calculated frequency was 3 to 5 times higher than the observed frequency, and the shape of the waveform, particularly the ratio of the times the electrode spent in the active and passive states (at high and low currents), did not agree with the observed oscillations (61).

Russell and Newman (61) then suggested several changes in their model as well as experimental studies that could bridge the gap between calculated and experimental results for oscillations. Russell and Newman determined that the discrepancies between the calculated and experimental results were due primarily to a very small calculated value of the salt-film thickness, compared with the expected value and the values reported for certain salt films (see section 1.3.2). They therefore suggested including the kinetics of salt-film dissolution in the mathematical model to obtain a more realistic value for the film thickness. Additional refinements they suggested, for a more accurate description of the physical processes, were including the concentration dependence of the bisulfate-dissociation equilibrium constant and the concentration dependence of the transport properties.

More fundamentally, Russell and Newman (61) indicated that passivation is not necessarily required to achieve oscillations, and they qualitatively outlined two alternative oscillatory mechanisms. In one mechanism, current oscillations are caused by periodic changes in the fraction of the electrode surface covered by ferrous sulfate, and in the other mechanism, current oscillations are caused by periodic changes in

the porosity of the salt film.

To implement the proposed changes in the mathematical model describing the behavior of the Fe/H_2SO_4 system, it is first necessary to have more information about the actual behavior of the system. Information obtained in the proposed experiments may indicate the most appropriate way to proceed with modeling the system behavior (61).

Experiments are needed to determine important parameters, particularly kinetic parameters for the precipitation and dissolution of $FeSO_4$ and also the thickness and porosity of the salt film. Another critical series of experiments for characterizing the oscillatory behavior of the Fe/H_2SO_4 system is determination of the surface dissolution-profile and morphology of the electrode at potentials where oscillations occur and at other potentials on the limiting current plateau where oscillations do not occur. The results of these experiments can indicate whether the electrode is partially active and partially passive and whether there is an important difference between the dissolution profiles of an electrode undergoing oscillations and an electrode at steady state at the limiting current plateau. This information is important for determining the mechanism by which oscillations occur.

Podestá *et al.* (69) observed nonuniform dissolution of iron wire electrodes as well as rotating disk electrodes, after recording the current oscillations for some time. They reported that the dissolution of the rotating disk electrode is characterized by the formation of a central etch.

Miller and Orazem (71, 72) performed some experiments to determine the surface dissolution profile and morphology of an iron disk electrode in 1 M H_2SO_4 subjected to an impinging jet of electrolyte. They used optical microscopy, electron microscopy, and EDX analysis to investigate the electrode surface after potential-step experiments where the electrode was held for three minutes at an anodic potential, before the passivation potential, and particularly in the range of oscillations.

Miller and Orazem (71, 72) observed that at low anodic potentials, the electrode surface was rough and granular and near the limiting current, a smooth region appeared at the periphery of the electrode. Then as the potential was increased, the smooth region was seen over a larger part of the electrode, extending toward the center, and just prior to passivation, the entire surface appeared smooth and uniform. The same trends were observed visually during anodic potential sweep experiments. Miller and Orazem then concluded that the range of potentials where a change of the electrode morphology from a granular to a smooth surface occurs (when smooth and granular regions coexist on the electrode) corresponds to the range of potentials where current oscillations are observed. They attributed the observed smooth dissolution of the outer region of the electrode to formation of a salt film.

Miller and Orazem (71, 72) measured the surface profiles after the potential-step experiments with an optical microscope by a depth of field technique. From these profiles they concluded that the rate of dissolution was higher in the smooth outer region than in the central granular region. and they attributed the higher rate of dissolution

near the periphery to the higher potential driving-force there. However a trend of greater dissolution near the periphery of the electrode during current oscillations was not clearly shown in all the experimental surface profiles presented by Miller and Orazem. For example, in one case (Fig. 5, 0.62 V, in Ref. 72) the profile showed more dissolution near the center, while current oscillations occurred and the electrode surface was mostly smooth with a small granular region at the center; and in another case (Fig. B.1.8, in Ref. 71) the profile showed essentially uniform dissolution, while current oscillations occurred.

The EDX analysis of some electrodes by Miller and Orazem (71, 72) indicated the presence of an iron oxide film in the smooth region of the electrode. An oxide was not detected on the central granular region. The presence of an oxide film may support the hypothesis of preferential passivation of the periphery of the electrode during oscillations. Overall the results of Miller and Orazem do not give a definitive conclusion about the electrode dissolution profile during current oscillations or the mechanism of the oscillations. Further work is needed to elucidate the oscillatory phenomena for the Fe/H_2SO_4 system.

1.4. Outline of This Work

The purpose of this work is to answer some of the questions about the corrosion of iron in sulfuric acid, using mainly the electrochemical impedance technique, and also to develop the impedance technique as a tool for the study of electrochemical systems, using the iron-sulfuric system as an application.

Three different types of experiments are carried out:

I. Potentiodynamic experiments to determine the anodic polarization curve, especially the passivation curve.

II. Potentiostatic experiments recording the sustained current oscillations that occur within a certain potential range on the limiting current plateau.

III. Measurement of the AC (alternating current) impedance of the system at several points along the anodic polarization curve, using a frequency response analyser.

Rotating hemispherical iron electrodes are used in most of these experiments, because they have the advantage of a uniform primary current distribution, in contrast to the commonly used rotating disk electrodes, which have a highly nonuniform primary distribution. The characteristics of the rotating hemispherical electrode are described in section 1.5.

We have already discussed the importance of potential distribution and ohmic potential drop effects for the passivation and oscillatory behavior of the Fe/H_2SO_4 system. Experimental results for electrodes with a uniform primary distribution should therefore provide useful insight into those effects. Results from experiments I and II are presented and compared with results for disk electrodes reported by other investigators, in chapter 2.

Another series of experiments was carried out to determine the surface dissolution profiles of a rotating disk electrode at several potentials in the limiting current plateau, particularly in the range of

current oscillations. An optical microscope was used to measure the profiles, but the results were not sufficiently accurate or definitive and will therefore not be presented. Determination of the electrode surface profile is considered important, and further experiments to determine the surface profile are needed.

This work focuses on the electrochemical impedance technique. The results from experiments III are presented, in chapter 3. Rotating disk electrodes are used in some of the impedance measurement experiments, and the results for the disks are compared with the results for the hemispheres. The nonuniform primary current distribution of the disk electrode may produce serious artifacts in impedance measurements, particularly at high perturbation frequencies. The hemispherical electrode with its uniform primary distribution should be free of this kind of artifacts and is therefore preferable for impedance experiments.

The Kramers-Kronig relations provide a means of testing the accuracy and consistency of experimental impedance data, or the validity of theoretical results. The test consists of calculation of the real part of the impedance from the imaginary part, and *vice versa*, through the Kramers-Kronig relations and comparison of the calculated results with the experimental or theoretical values. A general method of calculation is developed. The method is applied to test the consistency of some of the experimental impedance data exhibiting inductive loops.

The experimental results are then compared with theoretical predictions in order to elucidate the processes and variables governing the behavior of the iron-sulfuric acid system. Theoretical results for the

impedance of the system are calculated using a concentrated-solution model developed recently in this laboratory, as well as analytic expressions from dilute-solution theory, for comparison. The concentrated-solution model uses the Stefan-Maxwell equations for multicomponent diffusion and has provision for heterogeneous electron-transfer reactions, homogeneous chemical reactions, hydrodynamics, and migration. Thus this model can rigorously treat mass-transfer phenomena in solution, which are important for the Fe/H_2SO_4 system. The model in its present form does not include adsorption/desorption reactions, the microscopic structure of the electrochemical interface (double-layer), or a porous salt film on the electrode. This model is therefore not expected to be able to characterize the Fe/H_2SO_4 system completely, but results from the model may indicate whether certain processes are important for determining the system behavior and can indicate directions for further research.

Work is currently being done by researchers in this laboratory to develop a fundamental general model for the electrochemical impedance including the microscopic structure of the interface as well as mass transport for a concentrated solution and a porous film on the electrode. This general impedance model should be able to describe the corrosion of iron in sulfuric acid.

1.5. The Rotating Hemispherical Electrode

The rotating hemispherical electrode was proposed by Chin (80-82) as a useful tool for studies of reaction kinetics and mass transfer in

electrochemical systems, particularly for metal dissolution or deposition systems. The use of the hemispherical electrode was proposed to overcome an inherent limitation of the rotating disk electrode in such systems. In metal dissolution studies, the disk electrode recedes into the insulator, thereby altering the hydrodynamic conditions at the electrode and rendering the rotating-disk theory no longer rigorously applicable; the hemispherical electrode maintains its shape and hydrodynamic characteristics relatively unchanged.

A major advantage of the hemispherical electrode is that it has a uniform primary current distribution, whereas the rotating disk electrode has a very nonuniform primary current distribution (83). A nonuniform primary distribution may result in significant errors in the evaluation of kinetic parameters such as exchange current densities in investigations of electrode kinetics (84). In electrochemical impedance measurements, problems due to a nonuniform primary current distribution may be even more serious.†

On the other hand, the rotating disk electrode has a uniform limiting current distribution, which makes it attractive for mass-transfer studies. The hemispherical electrode has a nonuniform limiting current distribution (85, 80). Below the limiting current, the disk electrode always has a nonuniform current distribution, due to the nonuniform ohmic potential drop in the solution (nonuniform primary distribution) (86). In contrast, the current distribution on a rotating hemispherical electrode is uniform at low current densities and becomes less uniform

† See discussion in section 1.6.2.

as the limiting current is approached (87). In the absence of concentration gradients, the hemisphere maintains a uniform current distribution. Nişancioğlu and Newman (87) showed that it is possible, in principle, to attain a uniform current distribution on a rotating sphere below the limiting current, even in the presence of concentration variations at the surface. In general, the rotating hemisphere and disk electrodes have some complementary aspects for electrochemical studies (87). The rotating disk electrode is uniformly accessible from a mass-transfer viewpoint, and the hemispherical electrode is uniformly accessible from an ohmic viewpoint.

Chin (80, 88) and Newman (85) have solved the convective diffusion equation for a rotating sphere at limiting current conditions and predicted that the average limiting current is proportional to the square root of the electrode rotation speed. The mass transfer rate near the poles of the sphere was found to be essentially identical to a rotating disk, but then decreasing in the direction toward the equator. The analysis for a sphere also applies to a hemispherical electrode on an insulating plane (80). Experimental data for the limiting current for rotating hemispherical electrodes agreed with the calculated results (81).

Nişancioğlu and Newman (87) calculated the current distribution on a rotating (hemi)spherical electrode at appreciable fractions of the limiting current, assuming Tafel kinetics and no migration effects. They showed that at high rotation speeds, the current distribution is uniform when the current level is below 68% of the limiting current.

Figure 1-7 shows the current and potential distributions at the limiting current on a hemispherical electrode (87). Figure 1-8 shows an analogous plot for a rotating disk electrode (86). The maximum potential variations near the surface of a hemisphere occur at the limiting current, and the maximum potential difference between the pole and the equator is then (87)

$$(\Delta\Phi_o')_{max} = 0.546 \left(\frac{r_o i_{avg}}{\kappa}\right) . \qquad [1\text{-}13]$$

The rotating disk electrode at the limiting current follows the same formula except with a coefficient 0.363. (89) The ohmic resistance of a hemispherical electrode of radius r_o on an insulating plane is

$$R_\Omega = \frac{1}{2\pi\kappa r_o} ; \qquad [1\text{-}14]$$

the ohmic resistance of a disk electrode is

$$R_\Omega = \frac{1}{4\kappa r_o} , \qquad [1\text{-}15]$$

which is a factor of $\pi/2$ greater than that of a hemisphere (83).

Chin (90) recently calculated the convective Warburg impedance of a rotating hemispherical electrode using a series expansion of the concentration for small values of θ, the angle from the pole. His results showed that for values of a dimensionless perturbation frequency K' greater than 10, where K' is defined as $\frac{\omega}{\Omega} Sc^{1/3}$, the convective Warburg behavior of the hemispherical electrode becomes the same as that of a rotating disk electrode.

The hemispherical geometry also has certain limitations. For example, mechanical polishing of the hemispherical electrode without

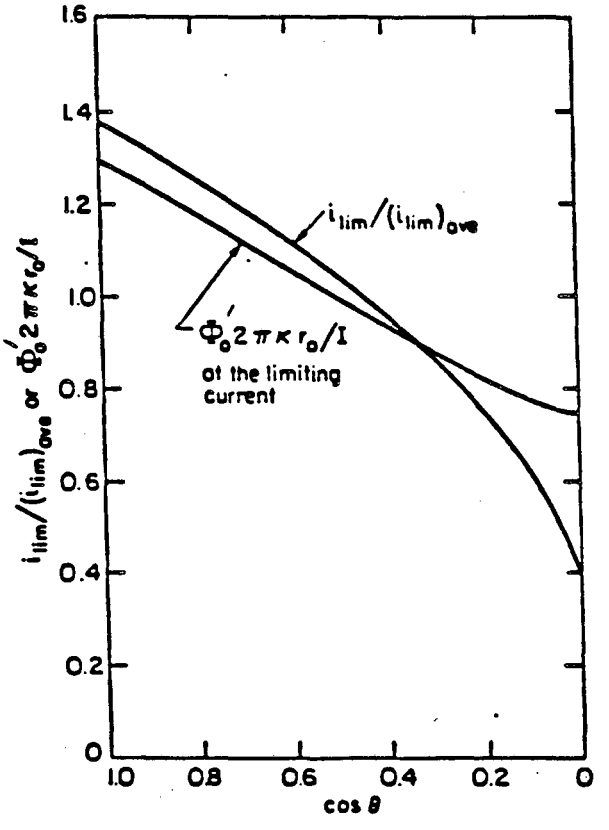

Figure 1-7. Current and potential distributions at the limiting current on a rotating (hemi)spherical electrode. θ is the angle from the pole. Φ_o' is the potential in the solution just outside the diffusion layer; more precisely Φ_o' is the solution of Laplace's equation in the bulk solution extrapolated to the electrode surface. (Fig. 8 in Ref. 87)

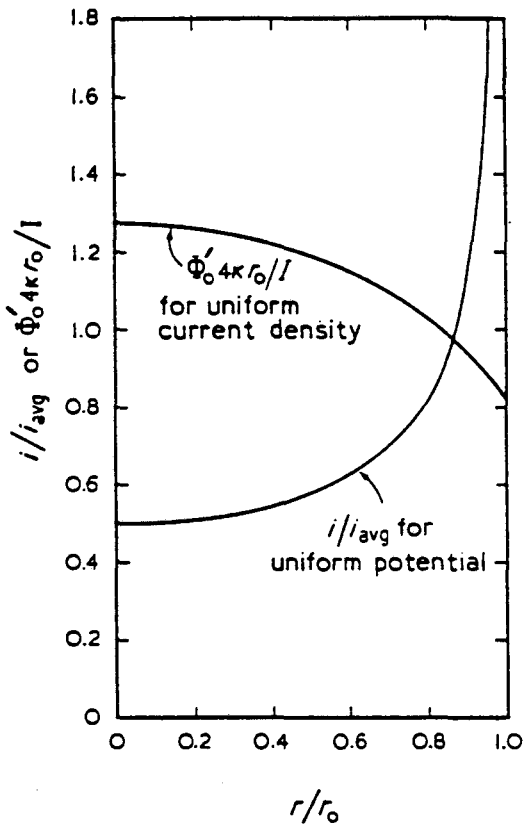

Figure 1-8. Primary current distribution and potential distribution for a uniform current density (at the limiting current) on a rotating disk electrode (Fig. 1 in Ref. 86).

slightly deforming its shape seems difficult. It has been found that a slight deviation from a spherical shape does not change the flow characteristics appreciably. However in the case of severe etching of a hemispherical electrode, localized disturbances in the flow or an early transition to turbulent flow may occur (82). For a smooth rotating hemispherical electrode, the transition from laminar to turbulent flow was experimentally found to occur at a Reynolds number of 1.5×10^4 (81). This value is lower than the value of the transition Reynolds number for a rotating disk, which is about 2×10^5 (89, 91). The influence of surface roughness on the transition to turbulence is discussed by Schlichting (91).

Changes in the flow characteristics of a rotating hemispherical or disk electrode are sometimes manifested as the formation of spiral markings (vortices) on the surface of the electrode. Kim and Jorné (92) used a rotating zinc hemisphere to study zinc dissolution in chloride solution. They observed spiral markings on the surface of the hemisphere at Reynolds numbers of about 7×10^3, and they attributed the markings to a transition to turbulent flow earlier than expected, as a result of increasing surface roughness. Kim and Jorné (93) observed spiral markings on a rotating hemispherical zinc electrode after zinc deposition, under certain conditions. Several other investigators (*e.g.*, 94-96) have also found spiral patterns on rotating disk electrodes in the process of metal dissolution or deposition. Rogers and Taylor (94) concluded that the spirals observed in their investigation were traces of wakes (flow disturbances) produced from small protrusions

such as evolved hydrogen bubbles and burrs on the electrode surface, while the flow appeared to remain laminar.

1.6. The Electrochemical Impedance

This section is an introduction to the electrochemical impedance method, providing the background for the application of the method to the Fe/H_2SO_4 system. Many treatments of the method are found in the literature, but only few comprehensive theoretical treatments are available, and the analysis and interpretation of electrochemical impedance results are controversial. This section then presents our perspective on the method. In addition the definitions of some terms used in the electrochemical impedance literature are often confusing or not universally recognized. Another objective of this section is therefore to clarify those definitions.

The electrochemical impedance technique consists of applying a small perturbation to the electrochemical system under study and measuring the response of the system. By analyzing the response, one can then obtain information about the system. The perturbation can be either a small-amplitude alternating voltage (ΔV) or a small-amplitude alternating current (Δi) and is superimposed on the steady-state polarization ($\bar{V}$, $\bar{i}$) of the system. The response of the systen can be expressed in terms of an impedance (Z) defined as the ratio (transfer function) of the applied (resulting) alternating voltage to the resulting (applied) alternating current. The technique is illustrated in figure 1-9 for the case of a sinusoidal current perturbation of a particular frequency (ω).

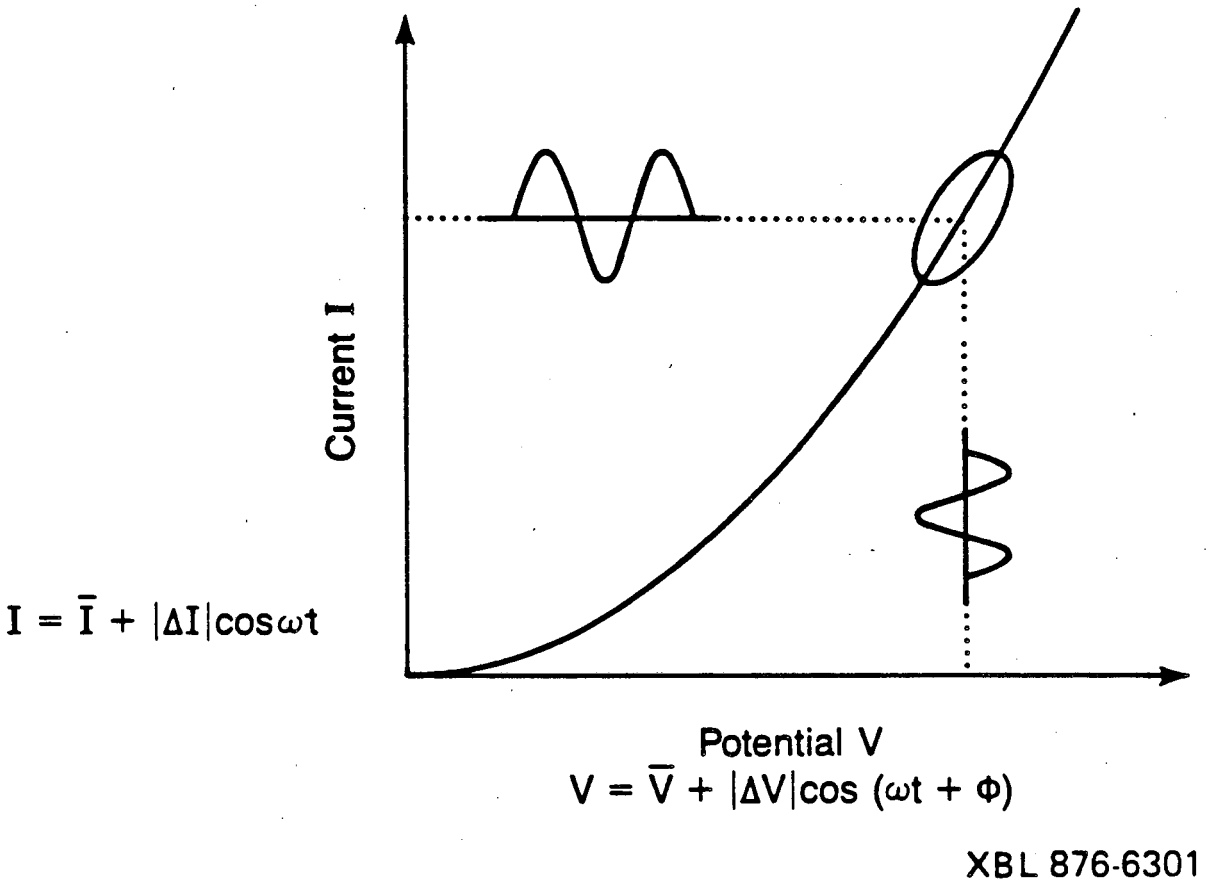

Figure 1-9. Illustration of the electrochemical impedance technique. A small-amplitude sinusoidal current perturbation is superimposed on the steady-state (DC) polarization curve and an alternating voltage results. (Fig. 1.2 in Ref. 110). The measured impedance (in ohm) is

$$Z = \frac{|\Delta V|}{|\Delta I|} \exp(j\phi).$$

The origins of the electrochemical impedance method are found in the works of Kohlrausch (97), Warburg (98), and Krüger (99), about a hundred years ago and later in the works of Randles (100), Ershler (101), Gerischer (102), Grahame (103), and others. Treatises and reviews of the method are given in References (104-111). A helpful introduction to the theoretical aspects, experimental aspects, and applications of the method is given by Gabrielli (110).

The electrochemical impedance technique is a powerful tool for the study of electrochemical systems. The power of the impedance technique lies mainly in its ability to discern the different elementary processes occurring in complex electrochemical systems. As the different elementary processes change at different rates (have different characteristic time constants), certain processes dominate the response of the system at certain perturbation frequencies. Measurement and analysis of the impedance over a wide range of frequencies can then elucidate the different processes.

More specifically, the electrolytic solution resistance is manifested in the electrochemical impedance at very high frequencies, while mass-transfer limitations are manifested in the impedance at low frequencies and electrochemical reactions become evident at frequencies corresponding to the reaction rate constants. Experimental measurement together with theoretical calculation of the impedance as a function of frequency at several points all along the polarization curve allows a complete* description of the electrochemical system. Figure 1-10

* From the viewpoint of purely electrochemical experimental techniques.

(a) charge-transfer resistance: $R_t = \left(\frac{\partial i_F}{\partial V_o}\right)_{ss}$

classical Warburg impedance for semi-infinite diffusion: $Z_D^o = \frac{R_t \lambda}{\sqrt{j\omega}}$

(total) electrochemical impedance: $Z = \left[\left(R_t + Z_D^o\right)^{-1} + j\omega C_d\right]^{-1} + R_s$

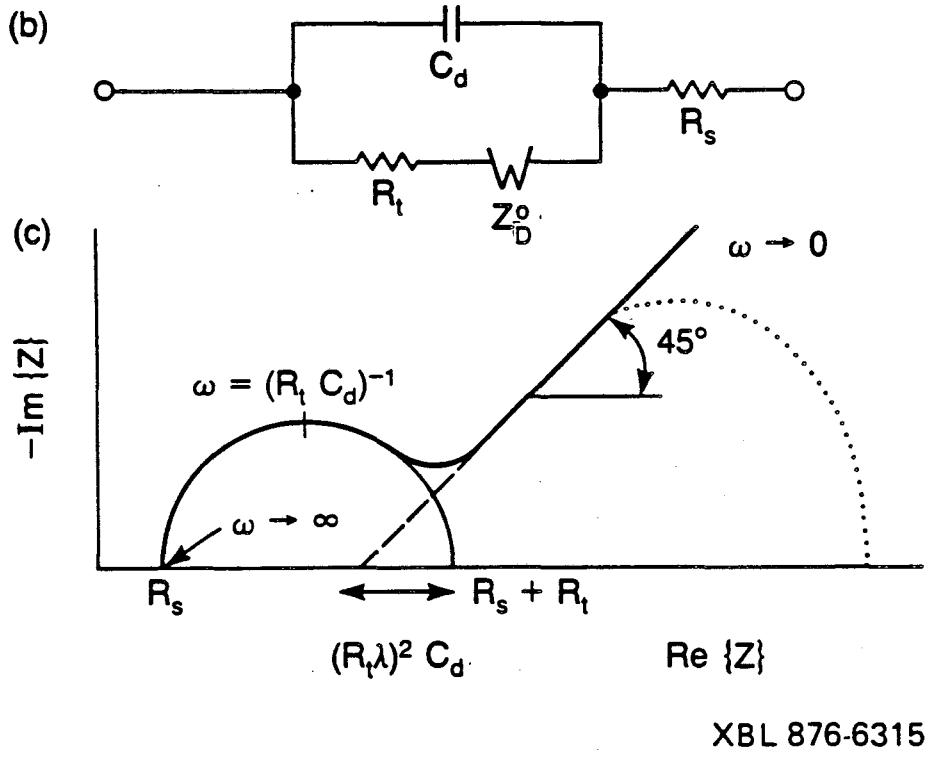

XBL 876-6315

Figure 1-10. A classical model of the electrochemical impedance (103, 98, 105).
(a) Summary of model expressions for the impedance (λ is given by equation 1-47).
(b) Illustration of the model by an equivalent circuit (Fig. 1 in Ref. 103).
(c) Complex-plane plot of the impedance (Fig. 4 in Ref. 105). Thick solid line: general behavior predicted by the model. Thin solid line: limiting behavior predicted by the model for $\lambda = 0$, *i.e.*, no mass-transfer effects (see also figure 1-12). Dotted line: behavior expected in the presence of convection (not included in the classical model).

summarizes a classical model of the electrochemical impedance (103, 98, 105), showing what information can be obtained through the electrochemical impedance method.

The use of the electrochemical impedance technique has been increasing rapidly over the past one or two decades, mainly due to the development of instrumentation that allows experimental measurement of the impedance relatively easily. The impedance technique is finding increasing application for the study and *in situ* monitoring of electrochemical corrosion systems, which always involve multiple phenomena. Epelboin, Keddam, Gabrielli, and coworkers (19-25, 53, 54) have applied the electrochemical impedance method to elucidate the reaction mechanism and mass-transfer effects for metal dissolution and passivation systems and to determine the corrosion rate (112). The application of electrochemical impedance analysis to corrosion systems, particularly for the measurement of corrosion rates, is discussed in References (110, 112-118). Other important applications of the electrochemical impedance method are biological membranes (119, 120), improving the performance of batteries (121), semiconductor electrochemistry (122), and photoelectrochemical solar cells.

1.6.1. Theoretical Formulation

1.6.1.1. General Concepts

To obtain a theoretical expression for the electrochemical impedance, we need to determine the alternating current response to an imposed alternating potential, or *vice versa*. To determine the

alternating current or potential, it is generally necessary to solve the fundamental equations describing the electrochemical system, specifically equations describing reaction kinetics and other interfacial phenomena, and transport phenomena. These fundamental equations are discussed in detail by Newman (89). The relevant variables (χ) in an electrochemical system include potential differences, partial currents for each electrochemical reaction, species concentrations (mol/cm^3) in the electrolytic solution, surface concentrations (mol/cm^2) of adsorbed species, and charge densities in the electrode-electrolyte interface (double layer). The impedance of the electrochemical system results from the interactions of these variables.

The equations for the electrochemical impedance problem, are generally nonlinear and time-dependent. A steady-state solution is first obtained, and then the transient (alternating) solution is obtained for a small perturbation around the steady state, using a linear analysis. The linearized transient equations are simpler than the nonlinear steady-state equations, but they are still quite complex. In addition the transient problem includes double-layer effects which are not present in the steady problem.

An electrochemical system is inherently nonlinear, but it can be treated using linear analysis, if the amplitude of the applied perturbation is small enough. The response of each variable in a linear system has the same frequency (ω) as the applied perturbation (*i.e.*, higher-frequency harmonics are zero or negligible), but a different phase

angle† (phase shift, ϕ_χ). The response can therefore be expressed in terms of in-phase and out-of-phase components, which are functions of the perturbation frequency. Mathematically, these components are expressed as the real and imaginary parts of complex functions.

Consider now some mathematical notation (123, 124, 110). Each dependent variable χ can be written as

$$\chi = \bar{\chi} + \Delta\chi \ . \qquad [1\text{-}16]$$

$\bar{\chi}$ is the steady-state value, and $\Delta\chi$ is the transient (oscillating) part representing a small perturbation from the steady state. For a small sinusoidal perturbation of frequency ω, all the transient quantities oscillate at the same frequency, and $\Delta\chi$ may be written as

$$\begin{aligned} \Delta\chi &= |\Delta\chi| \cos(\omega t + \phi_\chi) \qquad [1\text{-}17] \\ &= \mathrm{Re}\,\{|\Delta\chi| \exp[j(\omega t + \phi_\chi)]\} \\ &= \mathrm{Re}\,\{\tilde{\chi} \exp(j\omega t)\} \ , \end{aligned}$$

where $j = \sqrt{-1}$ and $e^{j\psi} = \cos\psi + j\sin\psi$. $|\Delta\chi|$ is the magnitude of the oscillating part of χ, and ϕ_χ is the phase angle. Both $|\Delta\chi|$ and ϕ_χ are generally functions of position (distance from the electrode) and are independent of time; their values vary with perturbation frequency. $\tilde{\chi}$ is a complex function, and as such it can be written in two equivalent ways:

$$\tilde{\chi} = |\Delta\chi| \exp(j\phi_\chi) \qquad \text{(polar form)} \qquad [1\text{-}18]$$

† The phase angle may be defined relative to a chosen reference signal.

$$= \mathrm{Re}\,\{\tilde{\chi}\} + j\ \mathrm{Im}\,\{\tilde{\chi}\} \quad \text{(cartesian form)}\ .$$

The time variable is effectively eliminated from the mathematical problem, as $\frac{\partial \chi}{\partial t} = j\omega\tilde{\chi}$ and the exp $(j\omega t)$ terms cancel out. The problem is thus conveniently expressed in the frequency domain.

The electrochemical impedance is defined by a generalized Ohm's law:

$$Z = \frac{\tilde{V}}{\tilde{i}}\ , \qquad [1\text{-}19]$$

where i is the normal component of the total current density at the electrode[††] and V is the total potential, *i.e.*, the potential difference between the working electrode and a reference electrode of a given kind in the bulk solution, which is the potential monitored by the polarization control device in an experiment. The impedance can then be written as

$$Z(j\omega) = |Z|\ \exp\ (j\phi) \qquad [1\text{-}20]$$

$$= \mathrm{Re}\ \{Z\} + j\ \mathrm{Im}\ \{Z\}\ ,$$

where $|Z| = \frac{|\Delta V|}{|\Delta i|}$ (magnitude) and $\phi = (\phi_V - \phi_i)$ (phase angle). [1-21]

For example, the impedance of an ideal electrical condenser C

[††] The measurable impedance is $\tilde{V}/\tilde{I}$ where I is the total current. However theoretical models of electrochemical systems involve primarily current densities. If the electrode has a uniform current distribution (i is constant), then $I = iA$ where A is the electrode surface area. If the electrode has a nonuniform current distribution, then one would have to use an average current density (equal to I/A obtained by integrating the local current density over the electrode surface) in equation 1-19 and in subsequent expressions for Z and the various impedances (or resistances) defined later in this chapter. For convenience in notation, we will use i in the impedance expressions, and the impedance units will be ohm·cm^2. The measurable impedance will be Z/A.

(capacitor, capacitance) is $-j\frac{1}{\omega C}$ ($\phi = -\pi/2$); the impedance of an inductor L is $j\omega L$ ($\phi = \pi/2$), and for a pure resistance $\phi = 0$.

The impedance can equivalently be defined in terms of Laplace transforms. The impedance transfer function is the ratio of the Laplace transform of the voltage to the Laplace transform of the current, where the Laplace transformation variable is $s = j\omega$ (see equation 1-66), or more generally one may choose $s = \sigma + j\omega$.

The total potential V is composed of several potential contributions.

$$V = (V_m - \Phi_o) + \Delta\Phi_c + \Delta\Phi_\Omega \qquad [1\text{-}22]$$

Φ_o is the potential measured with a hypothetical reference electrode of a given kind in the solution just outside the entire double layer, $\Delta\Phi_c$ is the potential difference due to concentration gradients in the solution (diffusion potential), and $\Delta\Phi_\Omega$ is the ohmic potential drop in the solution, assuming the conductivity is constant and equal to its bulk value. $(V_m - \Phi_o)$ is also the potential driving force which is usually included in the kinetic expression for electrochemical reactions. For a rigorous treatment of the electrode-electrolyte interface, the structure of the double layer should be considered, and thus $(V_m - \Phi_o)$ is the sum of potential differences between the double-layer planes (inner Helmhotz plane IHP, outer Helmholtz plane OHP). The potential in the kinetic expression for electron-transfer reactions would then be $(V_m - \Phi_{IHP})$ rather than $(V_m - \Phi_o)$.

The total (measurable) current is also the sum of several contributions. The current can pass from the electrode to the solution either through electron-transfer (faradaic) reactions or by charging the electrical double layer. The current due to electron-transfer (charge-transfer) reactions is known as the faradaic current (i_F), and the current due to accumulation of charge is known as the double-layer charging current. The total current density is thus given by (125, 89)

$$i = i_F + \frac{\partial q}{\partial t} \quad . \qquad [1\text{-}23]$$

For steady-state conditions $\frac{\partial q}{\partial t} = 0$, and thus double-layer charging is not important, but for transient conditions, double-layer charging as well as reactions at the electrode need to be considered. The double layer and electrode reaction theory is presented in References (126, 127, 89).

An elementary electron-transfer reaction is written in symbolic form as (89)

$$\sum_i s_{i,l} M_i^{z_i} \rightleftarrows n_l e^- \quad . \qquad [1\text{-}24]$$

Multiple electron-transfer reactions may occur, and i_F is then the sum of the partial current densities (i_l) due to each electron-transfer reaction:

$$i_F = \sum_l i_l \quad . \qquad [1\text{-}25]$$

The nonlinear character of an electrochemical system arises mainly from the exponential dependence of the partial current densities due to charge-transfer reactions on the potential driving force. This

dependence is given by Butler-Volmer type kinetic expressions. The expression for each partial current density is linearized using a Taylor series expansion about the steady state (ss) to solve the unsteady part of the impedance problem.

$$\text{For} \quad i_1 = f(x_m) \quad \longrightarrow \quad \tilde{i}_1 = \sum_m \left(\frac{\partial i_1}{\partial x_m}\right)_{ss} \tilde{x}_m \quad , \qquad [1\text{-}26]$$

where x_m represent the variables on which i_1 depends, namely the potential driving force for the reaction and the (surface) concentrations of the species involved. The rates of adsorption/desorption reactions at the interface also depend on potential and species concentrations and may be linearized in the same way.

Upon substitution the linearized reaction expressions given by equation 1-26 and the variable form given by equations 1-16 and 1-17, the equations for the unsteady part of the problem become linear. The linearization procedure shown in equation 1-26 requires knowledge of partial derivatives evaluated at steady-state conditions, and that is why the calculation of the electrochemical impedance requires first the solution of the steady-state problem.

The electrode reactions and double-layer charging occurring at the electrode-electrolyte interface are coupled and cannot be separated *a priori* (128-130, 125). The interfacial processes are further coupled to the electrolytic solution outside the interface (diffusion layer and bulk solution). A rigorous determination of the impedance therefore requires solving the transient equations describing the double-layer and the solution simultaneously. More specifically, the equations describ-

ing the interface including the double-layer structure are boundary conditions for the mass-transfer equations for each species in the solution (128-130, 123, 125). The general problem for the electrochemical impedance is thus difficult to solve.

Appel (125) has obtained the most general solution available for the electrochemical impedance of a rotating disk electrode, accounting for the double layer, mass transfer and ohmic potential drop in the electrolytc solution, and radial variations. However Appel's model includes only a simple electron-transfer reaction and no adsorption/desorption reactions, and therefore it cannot be used to test multiple-step reaction mechanisms. In addition Appel's model requires excessive computer time, which limits its application for electrochemical impedance studies.

Other models focus on certain parts of the electrochemical impedance problem, or solve a special case of the general problem. For example, Delahay and coworkers (129) and Levart and Schuhmann (130) have obtained analytic results for the impedance without *a priori* separation of the double-layer charging and faradaic reactions, making other simplifying assumptions. Epelboin, Keddam, and coworkers (131, 20, 22-24, 132) account for multiple electrode reactions including adsorbed intermediates, but without considering the double layer, and they use their impedance model to elucidate reaction mechanisms. A recently developed model (133) includes the microscopic structure of the electrode-electrolyte interface and accounts for multiple electron-transfer and adsorption/desorption reactions, in the absence of mass-transfer limita-

tions. Overall, further theoretical work is needed to develop a general model which can be easily applied for electrochemical impedance studies.

Double Layer — Electrode Reactions Interactions

Let us consider the interactions between the double layer and electrode reactions more specifically.

Consider first the early classical treatments of the electrochemical impedance. Randles (100) did not consider double layer charging in his theory. He measured the total electrochemical impedance and also measured the double-layer capacity in separate experiments in the absence of faradaic reactions. Randles then assumed that the double-layer capacity was the same for the two types of experiments. Grahame (103) discussed the effects of interactions between the faradaic and charging currents on the measured impedance and decided that they were negligible except for the effect of concentration changes produced by the double-layer charging current. Grahame included the latter effect in the equations for the derivation of a faradaic impedance, treating the double-layer as a constant capacity.

The double-layer capacity is a function of composition and potential (134). In general, the capacity and structure of the double layer depend on potential and composition, which depend on the reactions occurring, and electrode reactions are influenced by the double-layer capacity and structure. Interactions between the double layer and electrochemical reactions are greater when ionic species participating in reactions are adsorbed at the interface (128, 129).

A priori separation of the faradaic and double-layer charging currents requires the assumption of a constant double-layer capacity, C_d, independent of frequency. If there are no concentration variations and C_d is independent of frequency, then $C_d \frac{\partial (V_m - \Phi_o)}{\partial t}$ can be substituted for $\frac{\partial q}{\partial t}$, in equation 1-23. However, impedance models in the literature often assume this substitution even when concentration variations are important.

Most impedance models in the literature assume that the faradaic current and the double-layer charging current are separable *a priori* and treat the 'faradaic impedance' in itself. Since the total current is the sum of the faradaic and double-layer charging currents (equation 1-23), the faradaic impedance is considered to be connected in parallel to the 'double-layer impedance,' which is assumed to be an ideal capacitance.

1.6.1.2. Faradaic Impedance

The faradaic impedance is not a rigorously defined concept, since fundamentally the faradaic current cannot be separated from the double-layer charging current and the faradaic impedance is not a measurable quantity. In a theoretical model, one can define a faradaic impedance which is given by expressions in the model, but experimentally, the total electrode impedance is obtained, and it is not generally possible to isolate a faradaic impedance.

A definition for the faradaic impedance consistent with the way the term is most commonly used in the literature is

$$Z_F = \frac{\tilde{V}_o}{\tilde{i}_F} = \left(\frac{\tilde{V}_o}{\sum_1 \tilde{i}_1}\right) , \qquad [1\text{-}27]$$

where V_o is the potential in the kinetic expression for charge-transfer reactions. In most models of the faradaic impedance, V_o is equivalent to $(V_m - \Phi_o)$. Using the definition given by equation 1-27 and linearized expressions for $\tilde{i}_1$, we may then obtain a more explicit expression for the faradaic impedance.

The rate of a charge-transfer reaction is a function of potential and composition.

$$i_1 = f(V_o, c_{i,0}) . \qquad [1\text{-}28]$$

The composition variables $c_{i,0}$ should strictly be the surface concentrations (mol/cm^2) of each species at the inner Helmholtz plane (IHP). to account for the double-layer structure. In his classical theory of the faradaic impedance, Grahame (103) states that, since the surface concentrations are themselves functions of the potential across the interface and the concentrations (mol/cm^3) in the solution just outside the double layer (assuming that the double layer remains in equilibrium with the adjacent solution), i_1 can be written as a function of V_o and the concentrations in the solution just outside the double layer. More precisely, the latter concentrations are extrapolated concentrations representing the expected values at the interface if the double layer were absent (103). Grahame then uses these concentrations in his analysis. Most models of the faradaic impedance also use concentrations in the solution just outside the double layer for the i_1 function (f).

Epelboin and coworkers (25, 110, 20) treat solution concentrations of diffusing reactants and surface concentrations of adsorbed intermediates in a similar way including them all in the function f, without accounting for the double-layer structure. The treatment of Epelboin and coworkers thus yields relatively simple expressions for the faradaic impedance, including multiple reactions and adsorbed intermediate species.

The function f, is used in the linearization procedure, and hence in the expression for the Faradaic impedance. i_l is linearized according to equation 1-26.

$$\tilde{i}_l = \left(\frac{\partial i_l}{\partial V_o}\right)_{ss} \tilde{V}_o + \sum_i \left(\frac{\partial i_l}{\partial c_{i,0}}\right)_{ss} \tilde{c}_{i,0} \quad . \qquad [1\text{-}29]$$

Adding equations 1-29 for each charge-transfer reaction, we obtain the faradaic current.

$$\tilde{i}_F = \sum_l \tilde{i}_l = \left\{ \sum_l \left(\frac{\partial i_l}{\partial V_o}\right)_{ss} \right\} \tilde{V}_o + \sum_l \left\{ \sum_i \left(\frac{\partial i_l}{\partial c_{i,0}}\right)_{ss} \tilde{c}_{i,0} \right\} \qquad [1\text{-}30]$$

Consider now the first term in equation 1-30. A charge-transfer resistance for reaction l is defined as

$$R_{t,l} = \left(\frac{\partial i_l}{\partial V_o}\right)_{ss}^{-1} , \qquad [1\text{-}31]$$

and a total charge-transfer resistance R_t is given by

$$R_t^{-1} = \sum_l \left(\frac{\partial i_l}{\partial V_o}\right)_{ss} = \sum_l R_{t,l}^{-1} = \left(\frac{\partial i_F}{\partial V_o}\right)_{ss} \quad . \qquad [1\text{-}32]$$

Then†

$$Z_F = R_t - \frac{R_t}{\tilde{I}_F} \sum_l \left\{ \sum_i \left(\frac{\partial i_l}{\partial c_{i,0}} \right)_{ss} \tilde{c}_{i,0} \right\} \quad . \qquad [1\text{-}33]$$

The above equation is a general expression for the faradaic impedance. One could use any variable representing species concentration (surface or solution) in the place of $c_{i,0}$ in equation 1-33, since a specific choice was not necessary in the mathematical derivation.

Equation 1-33 shows that the faradaic impedance includes the effects of the kinetics of faradaic reactions (in the first term) and also mass-transfer effects (in the second term). The name 'faradaic impedance' is thus not precise, but it has been adopted in the electrochemical literature.

To proceed further in evaluating the faradaic impedance, it is necessary to determine the partial derivatives $\left(\frac{\partial i_l}{\partial V_o}\right)_{ss}$ and $\left(\frac{\partial i_l}{\partial c_{i,0}}\right)_{ss}$, as well as the alternating concentrations $\tilde{c}_{i,0}$. To determine the derivatives we need a specific model for the reaction kinetics‡ (a specific form of equation 1-28), and to determine the alternating concentrations we need to consider transient mass transfer.

Let us then consider some fundamental kinetic and mass-transfer equations that can be used to determine the faradaic impedance, ignoring

---

† By substituting R_t from equation 1-32 in equation 1-30, multiplying both sides of 1-30 by $(R_t)/(\tilde{I}_F)$, and using the definition of Z_F according to equation 1-27.

‡ For the special case where a single reaction occurs and the steady-state potential is equal to the equilibrium potential, the charge-transfer resistance $R_{t,l}$ defined by equation 1-31 is equal to $RT/(nFi_{o,l})$, where $i_{o,l}$ is the exchange current density (108).

the double layer. The composition variables $c_{i,0}$ in the remaining part of section 1.6 will be the concentrations (mol/cm^3) in the solution adjacent to the interface. More precisely, $c_{i,0}$ will represent the concentration of species i in the electrolytic solution, extrapolated to the interface without considering the presence of the double layer, *i.e.*, $c_{i,0} = c_{i\,|y=0}$ where y is the normal distance from the electrode surface.

The kinetics of an elementary electron-transfer reaction can be expressed by (89)

$$i_l = n_l F k_{a,l} \left(\prod_i c_{i,0}^{s_{i,l}} \right) \exp \left(\frac{(1-\beta_l) n_l F}{RT} V_o \right) - n_l F k_{c,l} \left(\prod_i c_{i,0}^{-s_{i,l}} \right) \exp \left(\frac{-\beta_l n_l F}{RT} V_o \right) \quad . \qquad [1\text{-}34]$$

The first product ($\prod$) is only for anodic reactants ($s_{i,l} > 0$), and the second product is only for cathodic reactants ($s_{i,l} < 0$). For an elementary reaction, the reaction orders in the kinetic expression are presumably given by the stoichiometric coefficients for each species (equation 1-24).

The normal component of the flux ($\underline{N}_i = c_i \underline{v}_i$) of a species at the interface is related to the partial current densities (89, 124)

$$N_{i,0} = - \sum_l \frac{s_{i,l}}{n_l F} i_l \quad . \qquad [1\text{-}35]$$

Note that the above equation ignores the charging current, but it is consistent with most analyses of the faradaic impedance. The flux $N_{i,0}$ is also determined by a material balance

$$\frac{\partial c_i}{\partial t} = - \nabla \cdot \underline{N}_i + R_i \quad , \qquad [1\text{-}36]$$

where R_i is the rate of production by homogeneous chemical reactions.

According to dilute-solution theory, mass transfer of a minor species is due to migration in an electric field, diffusion, and convection, and is described by the following law

$$\underline{N}_i = - z_i u_i F c_i \nabla \Phi - D_i \nabla c_i + c_i \underline{v} \quad . \qquad [1\text{-}37]$$

If migration is negligible and R_i is zero, then insertion of the above transport equation into equation 1-36 gives a simplified material balance

$$\frac{\partial c_i}{\partial t} = D_i \nabla^2 c_i - \underline{v} \cdot \nabla c_i \quad . \qquad [1\text{-}38]$$

This is the convective diffusion equation, which can be used to determine the concentration distribution in an infinitely dilute solution. $N_{i,0}$ is then given by

$$N_{i,0} = - D_i \left(\frac{\partial c_i}{\partial y} \right)_{y=0} \quad . \qquad [1\text{-}39]$$

The dilute-solution theory has been applied successfully to many electrochemical problems, but it may not be applicable for concentrated solutions. A more generally valid description of mass transport in multicomponent solutions is given by the Stefan-Maxwell equation. A modified form of the Stefan-Maxwell equation is (124)

$$c_i \frac{\nabla \mu_i}{RT} = \sum_{k \neq i} \frac{c_i \underline{J}_k - c_k \underline{J}_i}{c D_{ik}} \quad , \qquad [1\text{-}40]$$

where $\underline{J}_i$ is the flux of species i relative to the mass-average velocity, and μ_i is the electrochemical potential, which may be defined by

$$\nabla\mu_i = z_i F \nabla\Phi + RT \nabla(\ln c_i) \quad , \qquad [1\text{-}41]$$

assuming the activity coefficients are equal to one.

The transient mass-transfer problem for the impedance has been treated by many authors using dilute-solution theory. Section 1.6.1.4. considers the dilute-solution analysis and shows the resulting expression for the faradaic impedance. A concentrated solution model for the faradaic impedance has been recently developed (124), and it is used to calculate the impedance for the Fe/H_2SO_4 system (chapter 5).

1.6.1.3. Limits as $\omega \longrightarrow \infty$ and $\omega \longrightarrow 0$

This section considers the limits of the electrochemical impedance at zero and infinite frequencies of perturbation. The existence of these limits is important for obtaining parameters for the electrochemical system from experimental impedance data, for checking the consistency of impedance data with data from other techniques, and also for checking the internal consistency of mathematical impedance models.

At very high frequencies, the impedance due to the capacitive behavior of the double layer approaches zero. The electrochemical impedance then approaches the ohmic resistance of the solution (R_s).

$$\lim_{\omega \longrightarrow \infty} Z = R_s \quad . \qquad [1\text{-}42]$$

R_s should be equal to R_Ω given by equations 1-14 and 1-15 for a hemispherical and a disk electrode respectively. The primary current distribution is approximated at high frequencies (135).

At very low frequencies, steady-state conditions are approached, and the electrochemical impedance approaches the value of the slope of the steady-state (DC) polarization curve.

$$\lim_{\omega \to 0} Z = \left(\frac{dV}{di}\right)_{ss} . \qquad [1\text{-}43]$$

Note that the zero-frequency limit of the electrochemical impedance includes the effects of the kinetics of charge-transfer and adsorption reactions, the effects of mass-transfer,† and the solution ohmic resistance. The slope of the DC polarization curve not including ohmic potential drop is often referred to as the polarization resistance (R_p) and is given by

$$R_p = \lim_{\omega \to 0} Z - \lim_{\omega \to \infty} Z . \qquad [1\text{-}44]$$

When the impedance is measured at the open-circuit potential for a corrosion system, R_p can be correlated to the rate of corrosion, which is expressed as a corrosion current density. Measurements of R_p according to equation 1-44 are often used in corrosion studies to determine the corrosion rate. However there has been some controversy in the literature (112, 116, 110) about the determination of corrosion rates from electrochemical impedance measurements. Epelboin *et al.* (112) and Gabrielli (110) have argued that the parameter most directly correlated with the corrosion rate is the charge transfer resistance (R_t) rather than the polarization resistance (R_p), which is most commonly used. This controversy seems to be due to differences in the interpretation

† See section 1.6.1.4. for the zero-frequency limit of the mass-transfer impedance.

(definition, analysis) of the corrosion rate rather than differences in the interpretation of the electrochemical impedance itself.

The infinite and zero frequency limits of the electrochemical impedance given by equations 1-42 and 1-43 are generally valid, no matter what specific theoretical model one chooses for the impedance. When a specific model is used, further analysis of the high and low frequency limits can be carried out, yielding more useful information (parameter values) about the electrochemical system. For example, modeling the convective diffusion contributions to the impedance indicates that the diffusion coefficient can be obtained from the faradaic impedance at low frequencies (136-138).

Considering the faradaic impedance, the charge-transfer resistance defined by equation 1-32 is also given by

$$R_t = \lim_{\omega \to \infty} Z_F \qquad [1\text{-}45]$$

as the other terms of Z_F tend to zero at infinite frequencies. (See equations 1-33, 1-60, and 1-63.) R_t values according to both equations 1-32 and 1-45 are readily obtained in theoretical models of the faradaic impedance. However direct estimation of R_t according to equation 1-45 from experimental impedance data is not possible without making restrictive assumptions, because in general Z_F cannot be defined from the measured data.

Note that for systems with no mass-transfer effects and no adsorption/desorption processes, R_p (equation 1-44) is equal to R_t, since the double-layer charging current becomes zero as $\omega \rightarrow 0$ and for

such systems $Z_F = R_t$ at all frequencies.

1.6.1.4. Convective Warburg Impedance — Dilute-Solution Analysis

Consider now the impedance due to mass transfer, which is included in the second term of the general expression for the faradaic impedance, equation 1-33. Specifically this section considers the impedance associated with periodic concentration changes induced by an alternating electrode current or potential for species (i) that are involved in electrochemical reactions and can diffuse in the electrolytic solution. This impedance (Z_D) was first analyzed theoretically by Warburg (98) and is known as the (convective) Warburg impedance, or (convective) diffusion impedance, or mass-transfer impedance. Adsorption/desorption processes are not considered in the analysis.

Species in the electrolytic solution which do not participate in reactions affect the value of the mass-transfer impedance only indirectly (since $\left(\frac{\partial i_1}{\partial c_{i,0}}\right)_{ss} = 0$ for such species), by affecting the values of the concentrations of the reactant species. Considering double-layer effects, all ionic species affect the value of the electrochemical impedance, as the double-layer capacity depends on the concentrations of all ionic species. However this section considers only the faradaic impedance analysis, which by definition ignores double-layer effects.

Warburg (98) determined the transient concentration for a reactant species diffusing in a one-dimensional, stagnant, semi-infinite diffu-

sion layer, and not undergoing homogeneous chemical reactions. The surface concentration was found to have a $-\pi/4$ phase angle relative to the current. The faradaic impedance for this case can be written as (110)

$$Z_F = R_t + R_t \lambda (j\omega)^{-\frac{1}{2}}. \qquad [1\text{-}46]$$

$$= R_t + Z_D^o ,$$

where

$$\lambda = \sum_i \left(\frac{\partial i_l}{\partial c_{i,0}}\right)_{ss} \frac{s_{i,l}}{n_l F} D_i^{-\frac{1}{2}} \quad \text{with} \quad l = 1 \text{ and } s_{i,l} = \pm 1 \qquad [1\text{-}47]$$

and $j^{-\frac{1}{2}} = \frac{1}{\sqrt{2}}(1 - j)$. Z_D^o is the classical Warburg impedance, which increases without limit as $\omega \longrightarrow 0$.

Convection results in a finite steady-state diffusion layer; the mass-transfer impedance then reaches a finite limit as $\omega \longrightarrow 0$. The mass-transfer impedance including convection, has been analyzed by several authors (138-144). Approximate analytical expressions as well as exact numerical solutions are available.

Next we consider the convective Warburg problem for a rotating disk electrode, with the following assumptions: application of dilute-solution theory; negligible migration (large excess of supporting electrolyte); no radial variations (one-dimensional problem); large Schmidt number ($Sc_i = \frac{\nu}{D_i}$); no homogeneous chemical reactions; constant transport and thermodynamic properties. Note that solutions of the problem without making certain of these assumptions are available in the literature. The solution considered below can be easily applied to several

electrochemical systems to estimate the mass transfer impedance.

According to the mathematical formulation of Homsy and Newman (140), the concentration distribution of a species i in the solution is given by the convective diffusion equation (equation 1-38), written as

$$\frac{\partial c_i}{\partial t_i^*} - \frac{\partial^2 c_i}{\partial \xi_i^2} - 3\xi_i^2 \frac{\partial c_i}{\partial \xi_i} = 0 \ . \qquad [1\text{-}48]$$

ξ_i and t_i^* are the dimensionless normal distance and time defined by

$$\xi_i = y \left(\frac{\Omega}{\nu}\right)^{1/2} \left(\frac{a\nu}{3D_i}\right)^{1/3} \quad \text{and} \quad t_i^* = t\ \Omega \left(Sc_i\right)^{-1/3} \left(\frac{a}{3}\right)^{2/3} \ , \qquad [1\text{-}49]$$

and $-3\xi_i^2$ is a dimensionless normal velocity for a rotating disk. More generally the normal velocity for a rotating disk is a power series of $y\left(\frac{\Omega}{\nu}\right)^{1/2}$.

For a sinusoidal perturbation, the concentration can be expressed as (140)

$$c_i = \bar{c}_i + \mathrm{Re}\ \{A_i\ \Theta_i\ \exp\ (jK_i t_i^*)\} \ , \qquad [1\text{-}50]$$

where A_i is represents the amplitude of the alternating concentration and K_i is a dimensionless frequency

$$K_i = \frac{\omega}{\Omega} \left(Sc_i\right)^{1/3} \left(\frac{a}{3}\right)^{-2/3} \ . \qquad [1\text{-}51]$$

Θ_i is a dimensionless, complex alternating concentration. In terms of the general notation described in section 1.6.1.1, the dimensionless complex concentration defined by equation 1-50 may also be written as

$$\Theta_i = \frac{\bar{c}_i}{\bar{c}_{i,0}} \ . \qquad [1\text{-}52]$$

Substitution of equation 1-50 into the convective diffusion equation 1-48 yields an equation for $\Theta_i(\xi_i)$, (140)

$$jK_i\ \Theta_i - \frac{d^2\Theta_i}{d\xi_i^2} - 3\xi_i^2\ \frac{d\Theta_i}{dt_i^*} = 0 \qquad [1\text{-}53]$$

subject to the boundary conditions‡

$$\frac{d\Theta_i}{d\xi} = \text{specified constant} \quad \text{at} \quad \xi_i = 0 \quad \text{(at the interface)} \qquad [1\text{-}54]$$

$$\text{or} \qquad \Theta_i = 1 \quad \text{at} \quad \xi_i = 0$$

and

$$\Theta_i \longrightarrow 0 \quad \text{as} \quad \xi_i \longrightarrow \infty \ . \qquad [1\text{-}55]$$

The expression for the impedance involves the alternating concentrations and the alternating faradaic current. Here we shall consider only a simple reaction (l = 1 only). If more than one elementary reactions which include diffusing reactant species occur, then the expression for the faradaic impedance is more complicated, while the derivation procedure is the same. According to equations 1-35 and 1-39, the alternating faradaic current density for a simple reaction is proportional to the flux at the electrode surface, which is proportional to the concentration gradient.

---

‡ The following development for the convective Warburg impedance is not affected by choosing either of the boundary conditions at $\xi_i = 0$, as long as one uses the correct values of $\Theta_i'(0)$ in the final expression. (See Ref. 144)

$$\tilde{i}_F = -\frac{n_1 F}{s_{i,1}} \tilde{N}_{i,0} \qquad [1\text{-}56]$$

$$= \frac{n_1 F}{s_{i,1}} D_i \left(\frac{\partial \tilde{c}_i}{\partial y}\right)_{y=0} .$$

A dimensionless flux is

$$\Theta_i'(0) = \frac{1}{\tilde{c}_{i,0}} \left(\frac{\partial \tilde{c}_i}{\partial \xi_i}\right)_{\xi_i=0} \qquad [1\text{-}57]$$

$$= \frac{1}{\tilde{c}_{i,0}} \left(\frac{\Omega}{\nu}\right)^{-1/2} \left(\frac{a\nu}{3D_i}\right)^{-1/3} \left(\frac{\partial \tilde{c}_i}{\partial y}\right)_{y=0} ,$$

where the prime denotes differentiation w.r.t. ξ_i. Analytic and numerical results for $\Theta_i'(0)$ are available in the literature (*e.g.*, 141, 144). Substituting equation 1-57 into 1-56,

$$\tilde{i}_F = \frac{n_1 F}{s_{i,1}} D_i \tilde{c}_{i,0} \left(\frac{\Omega}{\nu}\right)^{1/2} \left(\frac{a\nu}{3D_i}\right)^{1/3} \Theta_i'(0) . \qquad [1\text{-}58]$$

For convenience in notation, we introduce

$$\delta_i = \left(\frac{\Omega}{\nu}\right)^{-1/2} \left(\frac{a\nu}{3D_i}\right)^{-1/3} \Gamma(4/3) . \qquad [1\text{-}59]$$

δ_i is a steady-state diffusion layer thickness for species i at a rotating disk electrode.

Finally, substituting equation 1-58 into the general expression for the faradaic impedance (equation 1-33), we get a more specific expression, for $l = 1$.

$$Z_F = R_t + R_t \sum_i \left(\frac{\partial i_1}{\partial c_{i,0}}\right)_{ss} \frac{s_{i,1}}{n_1 F} \cdot \frac{1}{D_i} \cdot \frac{\delta_i}{\Gamma(4/3)} \left\{\frac{-1}{\Theta_i'(0)}\right\} . \qquad [1\text{-}60]$$

The second term in the above equation is the convective Warburg impedance (Z_D). The function $\left\{\frac{-1}{\Theta_i'(0)}\right\}$ is called the dimensionless convective Warburg impedance. Figure 1-11 shows a complex-plane plot of this function. If more than one diffusing species i are involved in the kinetic expression for the reaction, equation 1-60 assumes an infinitely dilute solution where the alternating concentrations are so small that the transient convective diffusion equation 1-53 can be solved independently (separately) for each species i; the function $\Theta_i'(0)$ is then identical for each species i.

This section has considered the solution of the transient convective diffusion problem explicitly for a rotating disk electrode, which has been more widely studied. A similar solution procedure is used for a rotating hemispherical electrode (and other rotating electrodes), and a similar solution is obtained (90, 143). The convective diffusion equation and the definitions of the dimensionless variables are modified, and the values of $\left\{\frac{-1}{\Theta_i'(0)}\right\}$ for a rotating hemisphere are different from those for a disk (same order of magnitude).

Consider now the limits of Z_F in equation 1-60 at zero and infinite frequencies. To determine the limits of Z_F, we need to determine the limits of $\left\{\frac{-1}{\Theta_i'(0)}\right\}$. For $\omega = 0$, a limiting solution of equation 1-53 with boundary conditions 1-54 and 1-55 is readily obtained (after setting the first term in 1-53 to zero).

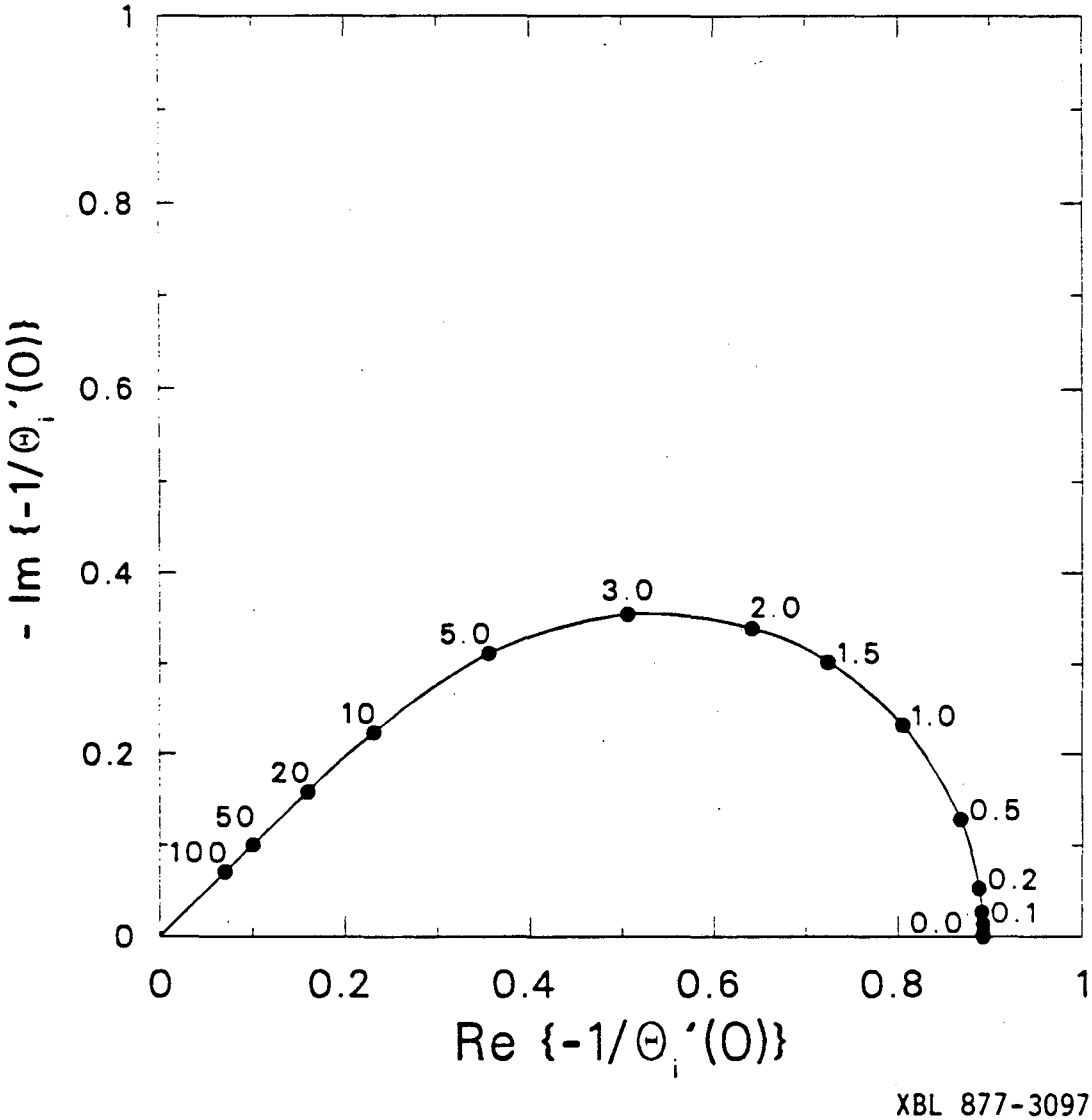

Figure 1-11. Complex-plane plot of the dimensionless convective Warburg impedance $(-1/\Theta_i'(0))$. The parameter is the dimensionless frequency K_i. (Table 1 in Ref. 144)
• exact solution

$$\Theta_i(\xi_i) = 1 - \frac{1}{\Gamma(4/3)} \int_0^{\xi_i} e^{-\psi^3} \, d\psi \qquad [1\text{-}61]$$

Therefore

$$\lim_{\omega \to 0} \left\{ \frac{-1}{\Theta_i'(0)} \right\} = \Gamma(4/3) = 0.89298 \ . \qquad [1\text{-}62]$$

Note that if more terms in the series expansion for the normal velocity are included in the convective diffusion equation and/or if migration is accounted for, the zero-frequency limit of $\{-1/\Theta_i'(0)\}$ is still a number ~ 1. The zero-frequency limit of Z_F is thus equal to the sum of R_t and the zero-frequency limit of Z_D, which may be called a mass-transfer or diffusion resistance.

The infinite-frequency limit is (144)

$$\lim_{K_i \to \infty} \left\{ \frac{-1}{\Theta_i'(0)} \right\} = \left(jK_i \right)^{-1/2} \ , \qquad [1\text{-}63]$$

which agrees asymptotically with the classical Warburg expression (see equation 1-46). Therefore as $\omega \to \infty$ the convective diffusion impedance $Z_D \to 0$, and the faradaic impedance becomes equal to R_t, as already indicated in equation 1-45.

An approximation which is sometimes used in the treatment of mass-transfer problems is a stagnant diffusion layer of finite thickness (Nernst model). An analytic solution for $\Theta_i'(0)$ is obtained for this approximation (145, 142).

$$\left\{\frac{-1}{\Theta_{Ni}'(0)}\right\} = \Gamma(4/3)\ \frac{\tanh\left[j\omega\delta_i^2/D_i\right]^{1/2}}{\left[j\omega\delta_i^2/D_i\right]^{1/2}}\ , \qquad [1\text{-}64]$$

where δ_i is given by equation 1-59 for a rotating disk. This analytical solution gives an approximate account of convective diffusion. Epelboin and coworkers (146, 20, 25) use this solution to treat mass-transfer impedances. The same expression might also be used to estimate the mass-transfer impedance due to a porous film, where a zero velocity and a finite diffusion layer may be a good approximation.

The expression for Z_D given by equation 1-60 can be simplified for the case of a simple reaction where either only the anodic or only the cathodic term is considered and there is a single reactant species. Z_D then becomes

$$Z_D^* = \frac{RT(s_{i,1})^2}{\beta_1^*\ (nF)^2}\cdot\frac{1}{\bar{c}_{i,0}\ D_i}\cdot\frac{\delta_i}{\Gamma(4/3)}\left\{\frac{-1}{\Theta_i'(0)}\right\}\ , \qquad [1\text{-}65]$$

where β_1^* is $(1 - \beta_1)$ for the anodic reaction term or β_1 for the cathodic reaction term. The above expression is the same as that given by Homsy and Newman (140), who set Z_D equal to the ratio of the alternating concentration overpotential to the alternating current density.

1.6.2. Experimental Measurement

The measurement of the impedance of electrochemical systems requires careful design of experimental arrangement and procedure and sophisticated instrumentation. Several techniques have been used to

measure the electrochemical impedance: AC bridges, Lissajous figures, simultaneous plotting of current and voltage, lock-in amplifiers, and more recently, digital frequency response (transfer function) analysers, and fast Fourier transform techniques.

A digital frequency response analyser (FRA) is used in this work to measure the impedance of the iron-sulfuric acid system. The principle of the measurement using a frequency response analyser is briefly described.

A small sinusoidal perturbation of a particular frequency (ω) is applied to the electrochemical system, and the response of the system is measured. The perturbing signal can be either a voltage or a current. The FRA measures both the electrode potential and the cell current simultaneously, and through an integration-correlation process it calculates the real and the imaginary parts (*i.e.*, the in-phase and out-of-phase components relative to the perturbing signal) of the two signals. This correlation process is equivalent to a Laplace transformation of the measured potential and current,

$$F(j\omega) = \int_0^\infty f(t)\, e^{-j\omega t}\, dt \qquad [1\text{-}66]$$

$$= \int_0^\infty f(t) \cos(\omega t)\, dt - j \int_0^\infty f(t) \sin(\omega t)\, dt \ ,$$

where f(t) represents the potential or current, but the integration is carried out over a finite time. The FRA then calculates automatically the impedance as the transfer function between the transformed potential and current signals. A series of measurements is performed, using a

perturbing signal of different frequency for each measurement, to obtain the impedance as a function of frequency.

An alternative to this frequency-by-frequency measurement method is the fast Fourier transform (FFT) method (147-151, 114), which uses a multiple-frequency perturbing signal, consisting of several harmonics superimposed. The FFT algorithm then calculates the impedance at each frequency included in the signal. A potential advantage of the multiple-frequency-FFT method over the frequency-by-frequency-FRA method is savings of measurement time, since data are collected for many frequencies at the same time. This time savings may be significant when the impedance at low frequencies is to be measured.

However a short measurement time can impair the measurement accuracy (152). The FFT technique is inherently less accurate than the FRA technique due to more noise and errors in the multiple-frequency signal processing, and the measurement has to be repeated several times to obtain average results with a reduced error. The FRA technique is generally more accurate and convenient. A thorough comparison between the two methods is not available, but the FFT method may be advantageous for electrochemical systems that change with time, such as corrosion systems (114, 110). The FFT method has been applied to copper corrosion by Smyrl (114, 115, 137).

Some important aspects of electrochemical impedance measurements, which must be considered for any measurement method, are now discussed.

Linearity

Linearity is a requirement for the definition of the impedance according to the generalized Ohm's law (equation 1-19). A system is linear if the measured impedance is independent of the amplitude of the perturbation. An electrochemical system responds as a linear system when the amplitude of the perturbation is small enough.

The maximum amplitude for which the system is in the linear domain depends on the polarization point (steady-state potential) as well as the perturbation frequency (110). A Taylor series expansion of the Butler-Volmer expression for the electrochemical kinetics shows that the magnitude of the nonlinear terms is of the order of $\left(\frac{F|\Delta V_o|}{RT}\right)^2$, and therefore the linearization error will be of the order of 1% for potential perturbations smaller than 5 mV, as a general rule. However one cannot use an arbitrarily small perturbing signal. Noise and the signal-to-noise ratio that can be accepted by the measuring instrument determine the low limit of the applied signal.

Frequency Range

For a complete analysis of complex electrochemical systems, where many processes may occur at different rates, impedance measurements need to be made over a wide frequency range, usually from a few mHz to several kHz. Measurements at very high frequencies are required to obtain the infinite-frequency limit of the electrochemical impedance, which will be equal to the electrolytic solution resistance (R_s) and measurements at very low frequencies are required to obtain the zero-

frequency limit of the impedance, which will be equal to the slope of the polarization curve (polarization resistance R_p). The maximum and minimum frequencies for electrochemical impedance measurements are limited by the experimental arrangement and instrumentation as well as by the electrochemical system itself.

At very high frequencies, the measured data may contain significant errors and artifacts due to extraneous resistive, inductive or capacitive components in the electrical leads or instruments. In particular, the phase-measurement accuracy of the digital frequency response analyser decreases significantly at frequencies above 10 kHz, and phase shifts may arise from the potentiostat (117, 118). One could perhaps avoid some of the problems at high frequencies by making 'four-point' impedance measurements, taking the ratio of quantities measured at the electrochemical cell.

At low frequencies, the stability of the electrochemical system with time may be critical. Low-frequency measurements are generally time consuming, and the steady state of the system may shift during the impedance measurement time. This shift may be particularly important for corrosion systems, which inherently change with time. Specifically, as the metal dissolves, the electrode-surface morphology and geometry as well as the surface or bulk concentrations and hence the thermodynamic equilibrium or open-circuit potential change. An analysis of the effect of these changes on the measured impedance is not available.

Noise

Noise can be a serious problem in electrochemical impedance measurements where small signals are used. Design of the experimental apparatus for impedance measurements therefore becomes more demanding than for steady-state measurements. Digital frequency response analysers can give accurate and precise measurements even in the presence of noise, by integrating the current and voltage signals over a sufficiently large number of signal periods. An infinite integration time would be required for complete elimination of noise, but the measurement time is limited by variations of the electrochemical system with time, especially at low frequencies, as indicated earlier, and one needs to choose an optimum measurement time.

Current Distribution and Frequency Dispersion

A nonuniform current distribution in the experimental system can lead to errors or artifacts in impedance measurements. Newman (135) showed that the nonuniform primary current distribution on a rotating disk electrode causes significant frequency dispersion in capacity measurements, *i.e.*, a variation in the apparent double-layer capacity with perturbation frequency. This frequency dispersion was found to be greater at high frequencies, where the primary current distribution is a good approximation for the distribution on the electrode (135).

Frequency dispersion may appear as distortion in the idealized semicircular shape of complex-plane impedance diagrams. Glarum and Marshall (153) measured the impedance of platinum rotating disk elec-

trodes in sulfuric acid; the data displayed a depressed semicircle in a complex-plane plot. They subsequently corrected the data for the nonuniform current distribution using a variational-approximations method (154). The corrected data displayed a complex-plane plot that was closer to a semicircle than the measured data, illustrating that depressed semicircles, which are often observed for experimental impedance data, can be partly due to a nonuniform current distribution.

Nişancioğlu (155) calculated the error in measurements of the polarization resistance and the double-layer capacity from impedance data for a corroding rotating disk electrode due to the nonuniform primary current distribution, neglecting mass-transfer and adsorption effects and assuming that the faradaic resistance is in parallel with the double-layer capacity. The calculated error R_p/R_{eff} varied from about 1/2 to greater than 10, and the error C_d/C_{eff} varied from about 1 to 20, depending on the magnitude of the impedance, the frequency range, the solution conductivity, and the disk diameter. (R_{eff} and C_{eff} are the effective or apparent polarization resistance and double-layer capacity respectively.)

Errors in the analysis of electrochemical impedance measurements due to a nonuniform current distribution are very difficult or impossible to correct *a posteriori* (46), and the best way to avoid such errors is to use an electrode with a uniform distribution. The rotating hemispherical electrode with its uniform primary distribution is therefore preferable to the rotating disk electrode for impedance measurements. Another useful electrode geometry which has both a uniform primary

current distribution and a uniform mass-transfer-limited current distibution is the rotating cylindrical electrodes (89). An alternative electrode geometry and arrangement for impedance measurements has been used by Cahan and coworkers (46, 156).

Several other factors, besides a nonuniform current distribution, can cause frequency dispersion in capacity measurements. These factors include primarily surface roughness (157), which is hard to eliminate for solid electrodes, and interactions between the double-layer charging and the faradaic processes, especially in systems with specific adsorption (129). Delahay and coworkers (129) showed that the double-layer capacity calculated from analysis of impedance data based on *a posteriori* separation of the electrode impedance into double-layer and faradaic components can vary with frequency.

1.6.3. Presentation and Analysis of Experimental Results

1.6.3.1. Graphical Presentation

Mathematically the impedance Z is a complex function of frequency, and it can therefore be represented in two different forms as shown in equation 1-20. These different forms lead to different ways of graphical presentation of electrochemical impedance results: a complex-plane plot (also known as a Nyquist plot), which is a plot of the imaginary part[††] *vs.* the real part of the impedance, and Bode plots, which are

[††] For electrochemical systems, the imaginary part and the phase angle of the impedance as defined in equations 1-20 and 1-21 are usually negative, indicating a capacitive behavior. Hence $-\mathrm{Im}(Z)$ and $-\phi$ are plotted; impedance diagrams below the horizontal axis (through 0) then

plots of the logarithm of the magnitude and the phase angle[††] *vs.* the logarithm of frequency. Results are sometimes presented as complex-plane plots of the admittance (Z^{-1}). Figure 1-12 shows examples of complex-plane and Bode plots for a simple electrical circuit.

The complex-plane and the Bode plots are equivalent, and they contain the same information if the frequency is indicated in the complex-plane plot; therefore a choice of either form of presentation may be a matter of preference. Complex-plane plots are often more picturesque and are more popular in the electrochemical impedance literature, whereas Bode plots display the frequency dependence of the impedance more clearly. Cahan *et al.* (46, 158) discussed the features of the two types of plots. They showed several illustrative examples and argued in favor of using Bode plots.

A choice of form of presentation becomes important when a particular plot is used as an essential part of data analysis, which is often the case. For example, a graph may be used as a diagnostic tool providing qualitative information about what processes are important in the system and providing estimates of parameter values, or a graph may be used as a criterion of the agreement between experimental and theoretical results.

1.6.3.2. Determination of Parameters

This section summarizes various methods that have been proposed for the determination of parameters from experimental impedance data.

---

indicate an inductive behavior.

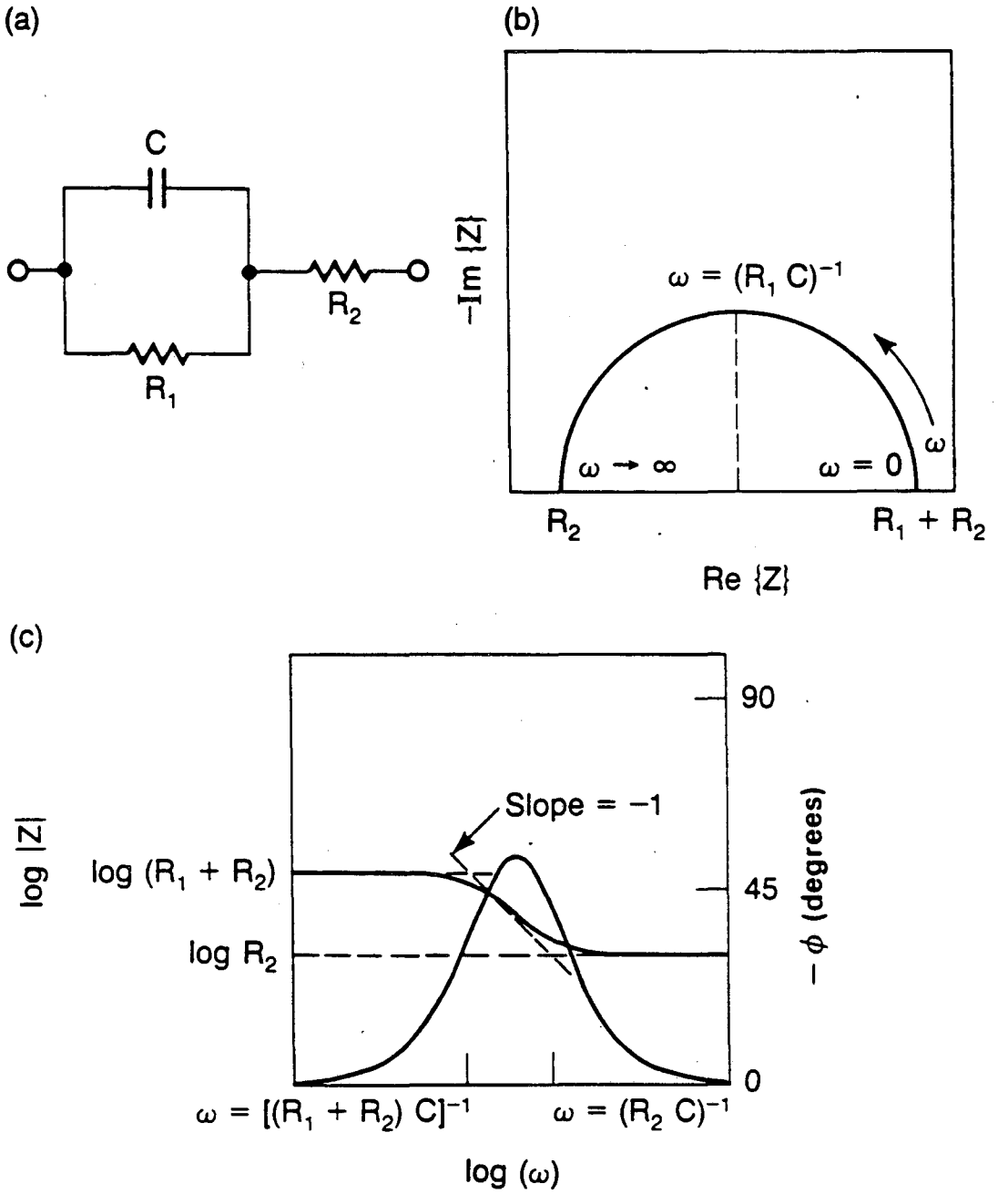

Figure 1-12. (a) Electrical circuit representing an idealization of a simple electrochemical system.
(b) Complex-plane plot of the impedance of circuit (a).
(c) Bode plots of the impedance of circuit (a).

Specifically these parameters are the charge-transfer resistance (R_t) and hence reaction rate constants, the ohmic resistance of the electrolytic solution (R_s), the double-layer capacity (C_d), and diffusion coefficients.

All of the methods of analysis considered in this section assume separation of the electrochemical impedance into a faradaic impedance and a double-layer capacitance connected in parallel. Delahay and coworkers (129) pointed out that for systems where *a priori* separation is not a good approximation, such analyses actually yield composite parameters depending on both kinetic and double-layer characteristics. In addition, these methods do not require independent theoretical modeling for their application, since each method is already based on a certain, relatively simple model. We will then refer to these methods as conventional methods of analysis of experimental impedance data.

Sluyters (105) introduced a method using complex-plane plots for the determination of R_t, R_s, C_d, and the parameter λ in the classical Warburg impedance (equations 1-46 and 1-47) This method is based on the model of the electrochemical impedance shown in figure 1-10; the method is illustrated in figure 1-10(c) and figure 1-12(b) in the absence of mass-transfer effects. Note that Bode plots can also be used to obtain parameter values (R_t, R_s, C_d) as illustrated in figure 1-12(c). Sluyters-Rehbach and Sluyters (106) present additional complex-plane methods for different cases.

Figure 1-13 illustrates another graphical method proposed by Sluyters (105) for the determination of R_t and C_d, also based on the

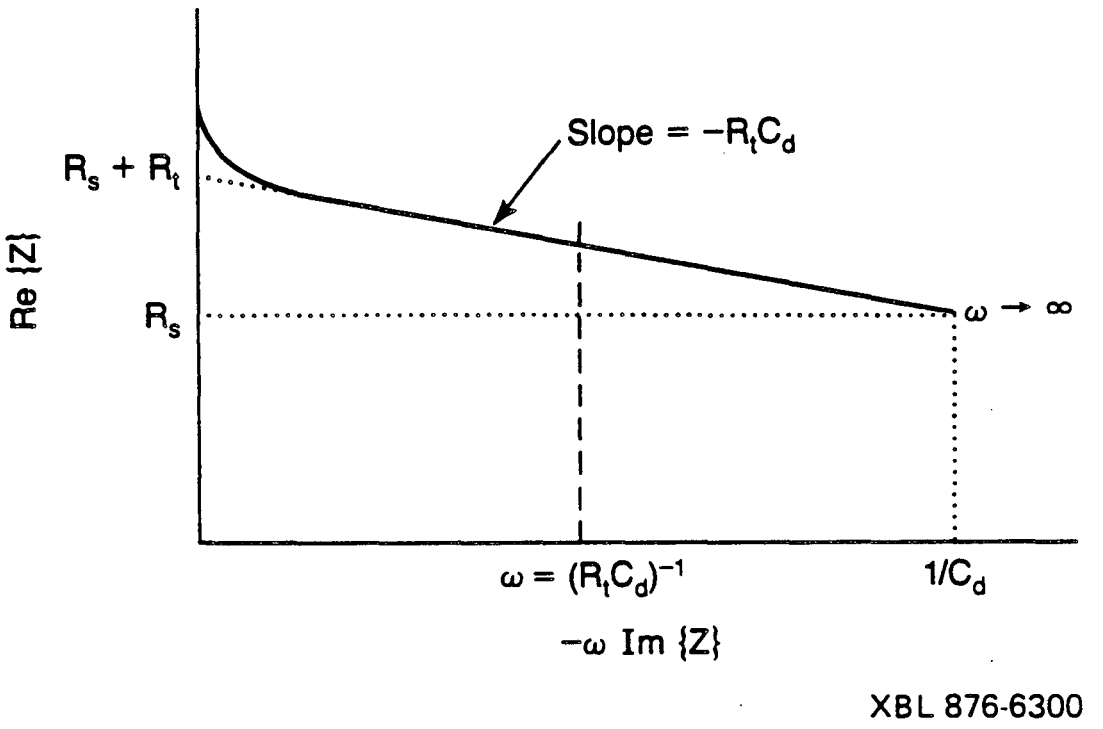

Figure 1-13. Graphical method proposed by Sluyters (105, Fig. 6) for the determination of the charge-transfer resistance and the double-layer capacity based on the impedance model shown in figure 1-10. The point corresponding to $\omega = 1/(R_t \cdot C_d)$ is equidistant from the points corresponding to $\omega = 0$ and $\omega = \infty$.

impedance model shown in figure 1-10. This method uses a plot of Re(Z) *vs.* $-\omega$Im(Z), which is linear with slope $-R_t \cdot C_d$ over a range of frequencies where mass-transfer effects are negligible. Extrapolation of the straight line to $\omega = 0$ gives R_t.

We note here that for systems where equation 1-60 applies and there are significant mass-transfer effects a similar plot of the faradaic impedance, Re(Z_F) *vs.* $-\omega$Im(Z_F), is linear at low frequencies with slope proportional to $Sc^{1/3}$. (137) This linear behavior is expected from the properties of the dimensionless convective Warburg impedance and can be used to obtain diffusion coefficients from impedance measurements (137, 136).

Figure 1-14 shows a method proposed by de Levie (159) for the determination of the double-layer capacitance from electrochemical impedance measurements. C_d is obtained as the extrapolated value of $\mathrm{Im}\left\{\frac{Y_e}{\omega}\right\}$ as $\omega \longrightarrow \infty$. This method is more generally applicable than the other conventional methods of analysis. The only assumption about the electrochemical interface is that the double-layer capacity is constant and connected in parallel to the faradaic impedance. No assumption is made about the faradaic impedance, in contrast to the other methods. However to apply this method, one needs to know the solution ohmic resistance, R_s, and also have impedance measurements at frequencies sufficiently high for a feasible extrapolation to $\omega \longrightarrow \infty$. A small error in the R_s value may result in a larger error in the admittance Y_e obtained by subtraction of R_s from the measured impedance and hence an error in C_d. For systems with a nonuniform current distribution, there is no

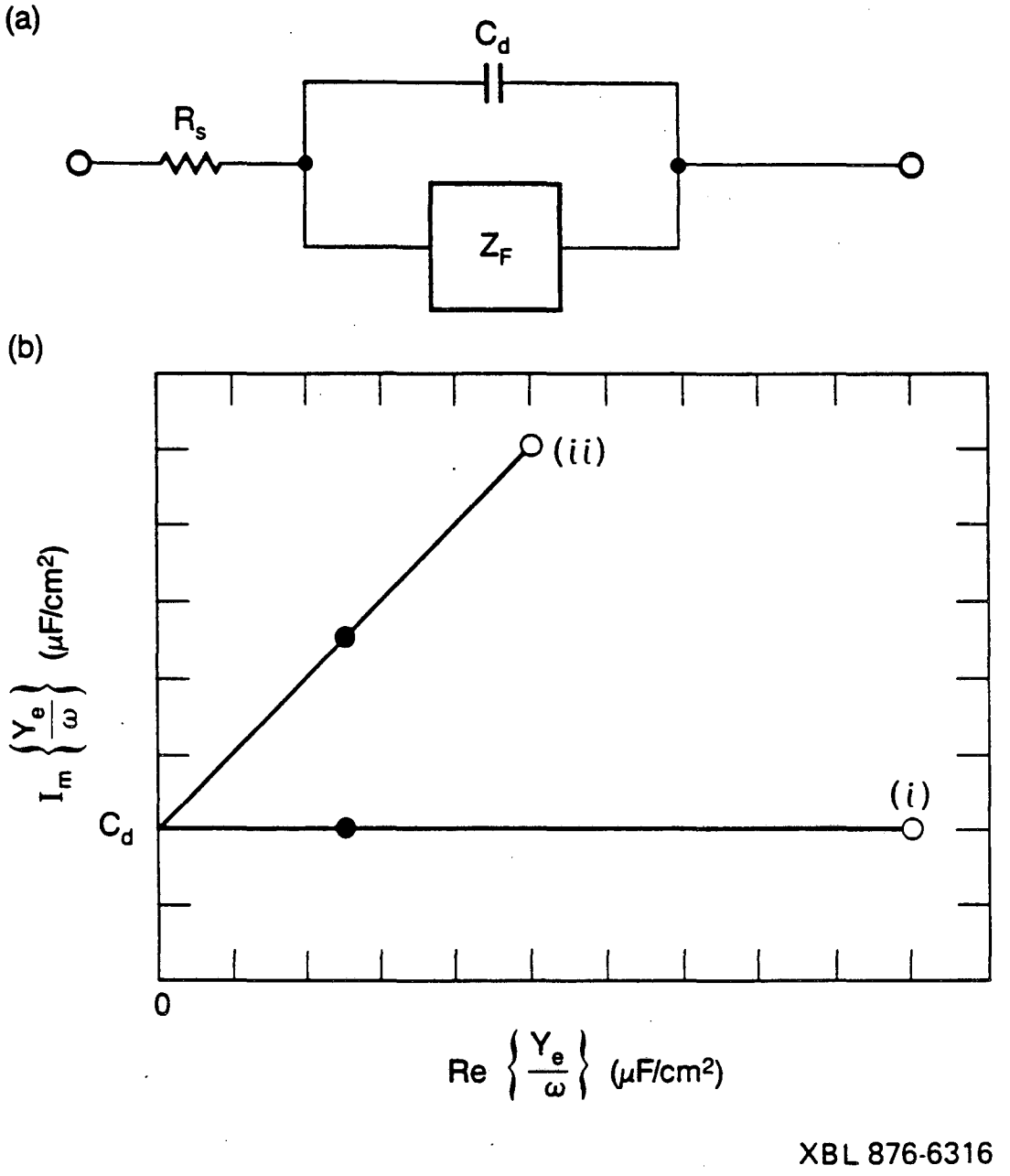

Figure 1-14. Method proposed by de Levie (159) for the determination of the double-layer capacity from electrochemical impedance measurements, assuming the impedance is represented by the equivalent circuit in (a).
(b) Complex-plane admittance plot. $Y_e = (Z - R_s)^{-1}$.
Two limiting cases are shown: (i) $Z_F \approx R_t$ (negligible mass-transfer and adsorption effects).
(ii) $Z_F \approx Z_D^o$ $(R_t \ll Z_D^o)$.

constant R_s value valid for all frequencies, and for such systems this method is practically inapplicable.

Electrochemical impedance data in many cases do not follow the behavior considered by the conventional methods for the determination of parameters, or different methods may give different values for the same parameters. In conclusion, these methods are useful for discerning the important processes in the system and estimating some parameter values, but are not adequate in themselves for a complete characterization of electrochemical systems, which requires further analysis using the approach outlined in section 1.6.1. (See section 1.2.)

Parameter values are often obtained in electrochemical impedance studies by fitting experimental impedance data to an 'equivalent electrical circuit' in which C_d, R_s, R_t, and usually more parameters are considered as circuit components.

1.6.3.3. Equivalent Circuits

In numerous electrochemical impedance studies, the electrochemical system is represented by an 'equivalent circuit' composed of resistors, capacitors, sometimes inductors, and other components. The extensive use of equivalent circuits requires some discussion.

A question that arises first is whether it is possible to represent an electrochemical system by an equivalent electrical circuit. Even if a valid equivalent circuit were found possible, a more important or relevant question would be to ascribe a definite physical meaning to each component of the circuit, or in mathematical terms, to relate the

partial derivatives in the theoretical expression for the electrochemical impedance to the circuit components (130, 129).

Considering the first question, Grahame (103) already indicated in 1952 that in most cases, no finite combination of resistors, condensers, and inductors can represent the frequency variation of the impedance of an electrode-electrolyte interface.

At a given frequency or in a specified limited frequency-range, if *a priori* separation of the faradaic and double-layer charging currents is assumed, it is possible to represent the electrochemical impedance by a simple circuit with resistors, capacitors, and inductors, which are constant only as long as the perturbation frequency is not varied significantly. For some simple cases, specifically when the impedance includes only terms proportional to $(j\omega)^{\pm 1}$ (*e.g.*, when there are no mass-transfer limitations), it is also possible to represent the electrochemical system by an electrical circuit with a finite number of components over the entire frequency range, assuming again *a priori* separation of the faradaic and charging currents. In addition impedance terms proportional to $(j\omega)^{-\frac{1}{2}}$ (classical Warburg impedance) are equivalent to an (infinite) R-C transmission line (130). If the electrochemical impedance involves terms that are not proportional to $(j\omega)^{\pm 1}$ or $(j\omega)^{-\frac{1}{2}}$, which is generally the case (*e.g.*, convective Warburg impedance), then it is not possible to represent the electrochemical system by an equivalent circuit valid over the entire frequency range.

Ascribing a physical meaning to components in an equivalent circuit depends on how an equivalent circuit is used in the analysis of

electrochemical impedance.

More fundamentally, interactions between the double layer and the faradaic processes imply that it is impossible to represent an electrochemical system by a meaningful equivalent circuit, since no independent components can be defined.

An Approach

If separation of faradaic and double-layer impedances is assumed, an equivalent circuit can be useful, having illustrative and pedagogical value, when it is used "as a short-hand (but exact) notation"(119) of a theoretical model consisting of fundamental equations which describe the physical system. Each component in the equivalent circuit then corresponds to a term in the model equations and thus has a defined physical meaning. Such a circuit is indeed equivalent to a theoretical model of the system and contains no assumptions other than those of the theoretical model. The equivalent circuit then is not an essential and independent part of the analysis.

As mentioned earlier, it is possible to represent terms in the theoretical impedance equations by resistors and capacitors (or inductors) only for certain simple cases. If the model considered accounts for more complex cases, one would have to use special symbols, *e.g.*, boxes or letters, for some components in the equivalent circuit (see for example, 103, 102), and the equivalent circuit therefore would not be a normal (electrical) circuit.

The way the various components are connected is also given by the model equations. For example, equation 1-60 for the faradaic impedance shows that Z_F is the sum of a kinetic term (R_t) and a mass-transfer term (Z_D). Therefore if one wanted to illustrate Z_F by an equivalent circuit, R_t and Z_D would be connected in series, and the series combination of R_t and Z_D would be connected in parallel to a double-layer capacitance, since *a priori* separation was assumed in the analysis of Z_F. Without considering the fundamental equations, it is not evident what circuit components may be present and how they are connected.

Examples of this approach of analyzing the electrochemical impedance theoretically and subsequently using an equivalent circuit merely as a convenient notation and illustration, which may also be used to obtain model parameter values, are found in References (131, 120, 103, 160).

Another Approach

A different approach is used by many investigators using the electrochemical impedance technique. In this approach, the equivalent circuit is an essential and independent part of the analysis. Examples of this approach are found in References (161-163).

In this approach an equivalent circuit is assumed, and values of the circuit components are determined by fitting the experimental data to an expression describing the impedance of the circuit. The equivalent circuit is chosen usually by inspection without independent theoretical modeling of the system, sometimes based on previous studies

employing equivalent circuits for similar systems, or at best according to the theory developed for simple electrochemical systems (figure 1-10). (This last choice is more like the previous approach for equivalent circuits.) If the fit with the experimental data is not considered satisfactory, the equivalent circuit may be modified.

When this approach is used, the components of the equivalent circuit have no well-defined physical meaning. For example, a film on the electrode may be assigned a capacitance and a resistance, with little or no discussion of the physical behavior of the film which gives rise to a particular impedance behavior and its variations with frequency. Therefore analysis based on such equivalent circuits offers little insight into the physical processes in the system. Particularly when the electrochemical impedance exhibits behavior more complicated than the simple cases illustrated in figures 1-12 and 1-10, an equivalent circuit would have many not clearly defined components, which would tend to obscure rather than elucidate the physical processes.

Equivalent circuits obtained according to this analysis are sometimes labeled 'theoretical models,' but they are rather a way to avoid a fundamental theoretical analysis. As Grahame (103) pointed out, "The objection to this procedure is that one has no way of knowing whether or not a given equivalent circuit is, in fact, equivalent to the interface under consideration except by carrying out an independent analysis of the problem which it is the objective of those who use this method to avoid."

This method of analysis is often chosen in corrosion applications, presumably because the investigators emphasize determination of parameters such as the polarization resistance (R_p), which is subsequently used to determine the corrosion rate. However the values of parameters obtained in this way are questionable; furthermore for corrosion control, a more complete understanding of the corrosion processes is needed, which this approach avoids.

The Early Classical Approach

The early classical treatments of the electrochemical impedance, which also introduced equivalent circuits, followed an approach similar to the first approach discussed in this section regarding equivalent circuits.

The impedance was analyzed theoretically by solving the fundamental equations for certain cases, particularly Fick's second law of diffusion subject to appropriate boundary conditions. The resulting solution for the (faradaic) impedance was denoted as an equivalent combination of a 'resistance' and a 'capacitance.' The so-called equivalent series or parallel 'resistance' and 'capacitance' were not a resistance and capacitance; they were explicit functions of frequency and also depended explicitly on the electrochemical parameters of the system. The equivalent 'resistance' and 'capacitance' were simply alternative names for the real (in-phase) and imaginary (out-of-phase) parts of the impedance function.

For example, Randles (100), Ershler (101), and Grahame (103) solved the impedance problem and presented expressions for the equivalent series or parallel 'resistance' and 'capacitance', for several cases. Sometimes the expression for the faradaic impedance was illustrated by an equivalent circuit, including resistors, capacitors, and special symbols for terms that did not correspond to an electrical circuit component (103).

The equivalent 'resistance' and 'capacitance' notation for the impedance was used because it was convenient for the experimental measurement of the electrochemical impedance with the instrumentation available at that time, particularly AC bridges (46). Measurement of the electrochemical impedance with an AC bridge consists of applying an alternating signal of a particular frequency and adjusting the values of a variable resistor and a variable capacitor, connected in series or in parallel, until the impedance of the R-C combination balances the impedance of the electrochemical cell. The values of the adjustable resistor and capacitor normally have to be different for different AC frequencies. It was not necessary to express the theoretical electrochemical impedance in terms of an equivalent 'resistance' and 'capacitance' and in terms of an equivalent circuit, but it was a convenient representation, which in a sense seemed natural in relation to the measurement technique. This can be seen for example in the classical paper of Randles (100).

List of Symbols

a	rotating-disk hydrodynamic constant, 0.51023
A	electrode area, cm^2
b_a	anodic Tafel slope for iron dissolution, mV/decade
c	total concentration, mol/cm^3
c_i	concentration of species i, mol/cm^3
$c_{i,0}$	concentration of species i in the electrolytic solution extrapolated to the electrode surface, mol/cm^3; alternatively, surface concentration of species i at IHP, mol/cm^2
C_d	double-layer capacity, F/cm^2
d	electrode diameter, cm or mm
D_i	diffusion coefficient of species i, cm^2/s
D_{ik}	diffusion coefficient for interactions of species i and k, cm^2/s
e^-	symbol for the electron
f	function in the kinetic expression for an electron-transfer reaction
F	Faraday's constant, 96487 C/eq
i	normal component of total current density at the electrode surface, A/cm^2

$i_{a,Fe}$	anodic current density for iron dissolution A/cm^2
i_{avg}	average current density, A/cm^2
i_F	faradaic current density, A/cm^2
i_l	partial current density due to electron-transfer reaction l, A/cm^2
i_{lim}	limiting current density, A/cm^2
I	total current, A
j	$\sqrt{-1}$, imaginary number
$\underline{J}_i$	flux of species i relative to the mass-average velocity, $mol \cdot cm^{-2} \cdot s^{-1}$
$k_{a,l}$	anodic rate constant for reaction l
$k_{c,l}$	cathodic rate constant for reaction l
K_i	dimensionless perturbation frequency based on species i, defined by equation 1-51
M_i	symbol for the chemical formula of species i
n_l	number of electrons transferred in reaction l
$\underline{N}_i$	flux of species i, $mol \cdot cm^{-2} \cdot s^{-1}$
$N_{i,0}$	normal component of flux of species i at the interface, $mol \cdot cm^{-2} \cdot s^{-1}$
p	reaction order for an anodic reactant
p_H	reaction order w.r.t. the solution pH or equivalently the OH^- concentration for anodic iron dissolution (equation 1-8)

q	surface charge density on the metal side of the double layer, C/cm^2
r_o	electrode radius, cm
R	universal gas constant, 8.3143 $J \cdot mol^{-1} \cdot K^{-1}$
R_i	rate of production of species i by homogeneous chemical reactions, $mol \cdot cm^{-3} \cdot s^{-1}$
R_p	polarization resistance, slope of DC-polarization curve not including ohmic potential drop, $\Omega \cdot cm^2$
R_s	ohmic resistance of electrolytic solution, $\Omega \cdot cm^2$
R_t	total charge-transfer resistance, $\Omega \cdot cm^2$
R_t	charge-transfer resistance for reaction 1, $\Omega \cdot cm^2$
R_Ω	ohmic resistance (equations 1-14 and 1-15), Ω
s	Laplace transformation variable, s^{-1}
$s_{i,1}$	stoichiometric coefficient of species i in reaction 1
Sc_i	Schmidt number, ν/D_i
t	time, s
t_i^*	dimensionless time defined by equation 1-49
T	absolute temperature, K
u_i	mobility of species i, $cm^2 \cdot mol \cdot J^{-1} \cdot s^{-1}$
$\underline{v}$	fluid velocity, cm/s

$\underline{v}_i$ velocity of species i, cm/s

V total potential difference between working electrode and reference electrode, V

V_{A-P} potential where the active-passive transition is observed, V

V_m potential of the metal electrode, V

V_o potential driving force for electrochemical reaction, usually equivalent to $(V_m - \Phi_o)$, V

V_{P-A} potential where the passive-active transition is observed, V

y normal distance from the electrode surface, cm

Y_e electrode admittance obtained after subtraction of R_s from the electrochemical impedance, $(Z - R_s)^{-1}$, $\Omega^{-1} \cdot cm^{-2}$

z_i charge number of species i

Z electrochemical impedance, $\Omega \cdot cm^2$

Z_D convective Warburg, or diffusion, or mass-transfer impedance, $\Omega \cdot cm^2$

Z_D^o classical Warburg impedance, $\Omega \cdot cm^2$

Z_F faradaic impedance defined by equation 1-27, $\Omega \cdot cm^2$

Greek letters

$\alpha_{a,Fe}$ anodic transfer coefficient for iron dissolution

β_l symmetry factor for elementary reaction l

$\Gamma(4/3)$	0.89298, the gamma function of 4/3
δ_f	salt-film thickness, cm
δ_i	steady-state diffusion layer thickness for species i at a rotating disk electrode, defined by equation 1-59, cm
$\Delta\chi$	transient (oscillating) part of variable χ
ϵ_f	salt-film porosity
θ	angle from the hemisphere pole
Θ_i	dimensionless, complex alternating concentration of species i defined by equation 1-50
$\Theta_i'(0)$	derivative of Θ w.r.t. ξ_i evaluated at $\xi_i = 0$
$\left\{\frac{-1}{\Theta_i'(0)}\right\}$	dimensionless convective Warburg impedance function for species i
$\left\{\frac{-1}{\Theta_{Ni}'(0)}\right\}$	dimensionless convective Warburg impedance function using the Nernst diffusion layer approximation
κ	conductivity, $\Omega^{-1}\cdot cm^{-1}$
κ_f	conductivity of electrolytic solution in the pores of a salt film, $\Omega^{-1}\cdot cm^{-1}$
λ	parameter in classical Warburg impedance expression, given by equation 1-47, $s^{-1/2}$
μ_i	electrochemical potential of species i, J/mol

ν	kinematic viscosity, cm^2/s
ξ_i	dimensionless normal distance defined by equation 1-49
ϕ	phase angle of the impedance, degrees
ϕ_χ	phase angle of variable χ
Φ	electric potential, V
Φ_o	potential measured with a hypothetical reference electrode of a given kind in the solution just outside the diffuse double-layer, V
Φ_o'	potential in the solution just outside the diffusion layer, solution of Laplace's equation in the bulk solution extrapolated to the electrode surface, V
Φ_{RE}	potential of a reference electrode of a given kind in the bulk solution, V
$\Delta\Phi_c$	potential drop due to concentration gradients in the solution (diffusion potential), V
$\Delta\Phi_\Omega$	ohmic potential drop in the solution, assuming the conductivity is equal to the bulk value, V
$\Delta\Phi_{\Omega,f}$	ohmic potential drop in the in the pores of the salt film
χ	general symbol for a dependent variable in electrochemical impedance problem
$\bar{\chi}$	steady-state value of χ

$\tilde{\chi}$	complex oscillating part of χ
$\Delta\chi$	transient (oscillating) part of χ
ψ	dummy variable
ω	perturbation frequency, rad/s
Ω	electrode rotation speed, rad/s

Subscripts

f	salt film
i	species i
IHP	inner Helmholtz plane
l	elementary reaction l
RE	reference electrode in the bulk solution
ss	steady state
SCE	saturated calomel reference electrode

Supersripts

$-$	(overbar) steady-state value
$\sim$	(tilde) oscillating part

References for Chapter 1

1. *New Horizons in Electrochemical Science and Technology*, Report of the Committee on Electrochemical Aspects of Energy Conservation and Production, National Materials Advisory Board, Commission on Engineering and Technical Systems, National Research Council, Publication NMAB 438-1, National Academy Press, Washington D.C. (1986).

2. K. E. Heusler, "Der Einflub der Wasserstoffionenkonzentration auf das elektrochemische Verhalten des aktiven Eisens in sauren Lösungen. Der Mechanismus der Reaktion $Fe \rightleftarrows Fe^{++} + 2e$," *Zeitschrift für Elektrochemie*, **62**, 582-587 (1958).

3. J. O'M. Bockris, D. Dražić, and A. R. Despić, "The Electrode Kinetics of the Deposition and Dissolution of Iron," *Electrochimica Acta*, **4**, 325-361 (1961).

4. Eugene J. Kelly, "The Active Iron Electrode, I. Iron Dissolution and Hydrogen Evolution Reactions in Acidic Sulfate Solutions," *Journal of the Electrochemical Society*, **112**, 124-131 (1965).

5. F. Hilbert, Y. Miyoshi, G. Eichkorn, and W. J. Lorenz, "Correlations between the Kinetics of Electrolytic Dissolution and Deposition of Iron, I. The Anodic Dissolution of Iron," *Journal of the Electrochemical Society*, **118**, 1919-1926 (1971).

6. H. Schweickert, W. J. Lorenz, and H. Friedburg, "Impedance Measurements of the Anodic Iron Dissolution," *Journal of the Electrochemical Society*, **127**, 1693-1701 (1980).

7. G. Okamoto, M. Nagayama, and N. Sato, *Proceedings of the 8th Meeting of CITCE (International Committee of Electrochemical Thermodynamics and Kinetics)*, Madrid, 1956, p. 72, Butterworths, London (1958).

8. J. J. Podestá and A. J. Arvia, "Kinetics of the Anodic Dissolution of Iron in Concentrated Ionic Media: Galvanostatic and Potentiostatic Measurements," *Electrochimica Acta*, **10**, 171-182 (1965).

9. Tor Hurlen, "Electrochemical Behaviour of Iron," *Acta Chemica Scandinavica*, **14**, 1533-1554 (1960).

10. Tor Hurlen, "Corrosion of Iron, Effect of pH and Ferrous Ion Activity," *Acta Chemica Scandinavica*, **14**, 1555-1563 (1960).

11. H. Bala, "The Corrosion of Iron in Sulphate Solutions at pH = 0-2," *Electrochimica Acta*, **29**, 119-129 (1984).

12. G. Bech-Nielsen, "The Anodic Dissolution of Iron—VII A Detailed Kinetic Model for the Two Coupled, Parallel Anodic Reactions," *Electrochimica Acta*, **21**, 627-636 (1976).

13. W. Allgaier and K. E. Heusler, "Steps and Kinks on {211} Iron Surfaces and the Kinetics of the Iron Electrode," *Journal of Applied Electrochemistry*, **9**, 155-160 (1979).

14. D. M. Dražić, L. Z. Vorkapić, *Bull. Soc. Chim., Beograd*, **46**, 595 (1981)

15. A. A. El Miligy, D. Geana, and W. J. Lorenz, "A Theoretical Treatment of the Kinetics of Iron Dissolution and Passivation," *Electrochimica Acta*, **20**, 273-281 (1975).

16. J. Bessone, L. Karakaya, P. Lorbeer, and W. J. Lorenz, "The Kinetics of Iron Dissolution and Passivation," *Electrochimica Acta*, **22**, 1147-1154 (1977).

17. P. Lorbeer and W. J. Lorenz, "The Kinetics of Iron Dissolution and Passivation," *Passivity of Metals*; *Corrosion Monograph Series*, pp. 607-613, R. P. Frankenthal and J. Kruger, Editors, The Electrochemical Society, Inc., Princeton, New Jersey (1978).

18. G. Bech-Nielsen, "The Anodic Passivation of Iron," *Passivity of Metals*; *Corrosion Monograph Series*, pp. 614-624, R. P. Frankenthal and J. Kruger, Editors, The Electrochemical Society, Inc., Princeton, New Jersey (1978).

19. I. Epelboin and M. Keddam, "Kinetics of Formation of Primary and Secondary Passivity in Sulphuric Aqueous Media," *Electrochimica Acta*, **17**, 177-186 (1972).

20. Israël Epelboin and Michel Keddam, "Faradaic Impedances: Diffusion Impedance and Reaction Impedance," *Journal of the Electrochemical Society*, **117**, 1052-1056 (1970).

21. B. Bechet, I. Epelboin, and M. Keddam, "New Data from Impedance Measurements Concerning the Anodic Dissolution of Iron in Acidic Sulphuric Media," *Journal of Electroanalytical Chemistry and Interfacial Electrochemistry*, **76**, 129-134 (1977).

22. M. Keddam, O. R. Mattos, and H. Takenouti, "Reaction Model for Iron Dissolution Studied by Electrode Impedance, I. Experimental Results and Reaction Model," *Journal of the Electrochemical Society*, **128**,

257-266 (1981).

23. M. Keddam, O. R. Mattos, and H. Takenouti, "Reaction Model for Iron Dissolution Studied by Electrode Impedance, II. Determination of the Reaction Model," *Journal of the Electrochemical Society*, **128**, 266-274 (1981).

24. I. Epelboin, C. Gabrielli, M. Keddam, and H. Takenouti, "A Model of the Anodic Behaviour of Iron in Sulphuric Acid Medium," *Electrochimica Acta*, **20**, 913-916 (1975).

25. I. Epelboin, C. Gabrielli, and M. Keddam, "Rôle de la Diffusion dans les Phénomènes de Passivation et de Corrosion Localisée du Fer en Milieu Acide," *Corrosion Science*, **15**, 155-171 (1975).

26. W. J. Müller, "On the Passivity of Metals," *Transactions of the Faraday Society*, **27**, 737-751 (1931).

27. M. Serra and S. Feliu, *Proceedings of the 6th Meeting of CITCE*, pp. 360-370, Butterworths, London (1955).

28. M. Froment, M. Keddam, and P. Morel, "Sur la Polarization d'une Electrode du Fer et son Etat de Surface," *Comptes Rendus, Acad. Sc. Paris*, **253**, 2529 (1961).

29. K. Schwabe, *Zeitschrift für physikalische Chemie*, **215**, 343 (1960).

30. R. Alkire, D. Ernsberger, and T. R. Beck, "Occurrence of Salt Films during Repassivation of Newly Generated Metal Surfaces," *Journal of the Electrochemical Society*, **125**, 1382-1388 (1978).

31. Theodore R. Beck, "Formation of Salt Films during Passivation of Iron," *Journal of the Electrochemical Society*, **129**, 2412-2418 (1982).

32. A. Pigeaud and H. B. Kirkpatrick, "A Correlated Potentiostatic Microscopic Study of Iron Passivation in Sulfuric Acid," *Corrosion*, **25**, 209-214 (1969).

33. M. Faraday, *Philos. Mag.*, **9**, 57 (1836).

34. M. Faraday, *Experimental Researches in Electricity*, Vol. 2, London (1844); Dover Publishers, New York, Reprinted 1965.

35. Ulick R. Evans, "The Passivity of Metals. Part I. The Isolation of the Protective Film," *Journal of the Chemical Society*, 1020-1040 (1927).

36. Fr. Flade, "Beiträge zur Kenntnis der Passivität," *Zeitschrift für physikalische Chemie* (Leipzig), **76**, 513-559 (1911).

37. Marcel Pourbaix, *Atlas of Electrochemical Equilibria in Aqueous Solutions*, pp. 307-321, National Association of Corrosion Engineers, Houston, Texas (1974).

38. Richard Alkire and Antonia Cangellari, "Formation of Salt Films during Anodic Metal Dissolution in the Presence of Fluid Flow," *Journal of the Electrochemical Society*, **130**, 1252-1259 (1983).

39. Masa-ichi Nagayama and Morris Cohen, "The Anodic Oxidation of Iron in a Neutral Solution, I. The Nature and Composition of the Passive Film," *Journal of the Electrochemical Society*, **109**, 781-790 (1962).

40. Morris Cohen, "The Passivity and Breakdown of Passivity on Iron," *Passivity of Metals; Corrosion Monograph Series*, pp. 521-545, R. P. Frankenthal and J. Kruger, Editors, The Electrochemical Society, Inc., Princeton, New Jersey (1978).

41. K. J. Vetter and F. Gorn, "Kinetics of Layer Formation and Corrosion Processes of Passive Iron in Acid Solutions," *Electrochimica Acta*, **18**, 321-326 (1973).

42. K. J. Vetter, "General Kinetics of Passive Layers on Metals," *Electrochimica Acta*, **16**, 1923-1937 (1971).

43. J. O'M. Bockris, M. A. Genshaw, V. Brusic and H. Wroblowa, "The Mechanism of the Passivation of Iron in Neutral Solutions: An Ellipsometric and Coulometric Investigation," *Electrochimica Acta*, **16**, 1859-1894 (1971).

44. N. Sato, K. Kudo, and R. Nishimura, "Depth Analysis of Passive Films on Iron in Neutral Borate Solution," *Journal of the Electrochemical Society*, **123**, 1419-1423 (1976).

45. Chia-Tien Chen and Boris D. Cahan, "The Nature of the Passive Film on Iron, I. Automatic Ellipsometric Spectroscopy Studies," *Journal of the Electrochemical Society*, **129**, 17-26 (1982).

46. Boris D. Cahan and Chia-Tien Chen, "The Nature of the Passive Film on Iron, II. A-C Impedance Studies," *Journal of the Electrochemical Society*, **129**, 474-480 (1982).

47. B. D. Cahan and Chia-Tien Chen, "The Nature of the Passive Film on Iron, III. The Chemi-Conductor Model and Further Supporting

Evidence," *Journal of the Electrochemical Society*, **129**, 921-925 (1982).

48. O. J. Murphy, T. E. Pou, J. O'M. Bockris, and L. L. Tongson, "Investigation of the Anodically Formed Passive Film on Iron by Secondary Ion Mass Spectroscopy," *Journal of the Electrochemical Society*, **131**, 2785-2790 (1984).

49. M. Keddam, J.-F. Lizee, C. Pallotta, and H. Takenouti, "Electrochemical Behavior of Passive Iron in Acid Medium, I. Impedance Approach," *Journal of the Electrochemical Society*, **131**, 2016-2024 (1984).

50. M. Keddam and C. Pallotta, "Electrochemical Behavior of Passive Iron in Acid Medium, II. The Passive Film/Solution Interface," *Journal of the Electrochemical Society*, **132**, 781-787 (1985).

51. 51. A. Hugot-Le Goff and C. Pallotta, "*In Situ* Raman Spectroscopy for the Study of Iron Passivity in Relation to Solution Composition," *Journal of the Electrochemical Society*, **132**, 2805-2806 (1985).

52. I. Epelboin, C. Gabrielli, M. Keddam, J.-C. Lestrade, and H. Takenouti, "Passivation of Iron in Sulfuric Acid Medium," *Journal of the Electrochemical Society*, **119**, 1632-1637 (1972).

53. Claude Gabrielli, *Régulation et Analyse des Systèmes à Etats Stationnaires Multiples. Application à l'Identification des Processus de Passivation Electrochimique du Fer*, Thèse de Doctorat, Université de Paris, No. C.N.R.S. A.O. 8060 (1973), Editions *Métaux*, *Cor-*

rosion, *Industrie*, No. 573, 574, 577, 578 (1973).

54. I. Epelboin, C. Gabrielli, M. Keddam, and H. Takenouti, "The Study of the Passivation Process by the Electrode Impedance Analysis," *Comprehensive Treatise of Electrochemistry*, Vol. 4, chapter 3, J. O'M. Bockris, B. E. Conway, E. Yeager, and R. E. White, Editors, Plenum Press, New York (1981).

55. M. Keddam, O. R. Mattos and H. Takenouti, "Ohmic Drop and Multiplicity of the Steady States: Case of Fe-5Cr in 1M-H_2SO_4," *Electrochimica Acta*, **24**, 103-105 (1979).

56. Joseph J. Miksis, Jr., and John Newman, "Primary Resistances for Ring-Disk Electrodes," *Journal of the Electrochemical Society*, **123**, 1030-1036 (1976).

57. W. J. Lorenz, Private Communication (1983).

58. D. Gilroy and B. E. Conway, "Kinetic Theory of Inhibition and Passivation in Electrochemical Reactions," *The Journal of Physical Chemistry*, **69**, 1259-1267 (1965).

59. 59. Clarence G. Law, Jr., and John Newman, "A Model for the Anodic Dissolution of Iron in Sulfuric Acid," *Journal of the Electrochemical Society*, **126**, 2150-2155 (1979).

60. Philip P. Russell, *Corrosion of Iron: The Active - Passive Transition and Sustained Electrochemical Oscillations*, Ph. D. Dissertation, University of California, Berkeley, CA (1984).

61. Philip Russell and John Newman, "Anodic Dissolution of Iron in Acidic Sulfate Electrolytes, II. Mathematical Model of Current

Oscillations Observed under Potentiostatic Conditions," *Journal of the Electrochemical Society*, **134**, 1051-1059 (1987).

62. E. C. Gan and Mark E. Orazem, "A Mathematical Model for the Corrosion of Iron in Sulfuric Acid," *Journal of the Electrochemical Society*, **134**, 1357-1366 (1987).

63. Philip P. Russell and John Newman, "Experimental Determination of the Passive-Active Transition for Iron in 1M Sulfuric Acid," *Journal of the Electrochemical Society*, **130**, 547-553 (1983).

64. G. L. Griffin, "A Simple Phase Transition Model for Metal Passivation Kinetics," *Journal of the Electrochemical Society*, **131**, 18-21 (1984).

65. G. L. Griffin, "The Cation Monolayer Model for Metal Passivation, II. Kinetics of the Active-Passive Transition," *Journal of the Electrochemical Society*, **133**, 1315-1320 (1986).

66. Jan B. Talbot, R. A. Oriani, and Mark J. DiCarlo, "Application of Linear Stability and Bifurcation Analysis to Passivation Models," *Journal of the Electrochemical Society*, **132**, 1545-1551 (1985).

67. Jan B. Talbot and R. A. Oriani, "Steady State Multiplicity and Oscillations in Passive Film Formation," *Electrochimica Acta*, **30**, 1277-1284 (1985).

68. J. H. Bartlett, "Transient Anode Phenomena," *Transactions of the Electrochemical Society*, **87**, 521-545 (1945).

69. J. J. Podestá, R. C. V. Piatti, and A. J. Arvia, "The Potentiostatic Current Oscillations at Iron/Sulfuric Acid Solution

Interfaces," *Journal of the Electrochemical Society*, **126**, 1363-1367 (1979).

70. Philip Russell and John Newman, "Current Oscillations Observed within the Limiting Current Plateau for Iron in Sulfuric Acid," *Journal of the Electrochemical Society*, **133**, 2093-2097 (1986).

71. Michael G. Miller, *The Influence of Fluid Velocity on the Corrosion of Iron in 1M Sulfuric Acid*, M. S. Thesis, University of Virginia, Charlottesville, VA, May 1985.

72. Mark E. Orazem and Michael G. Miller, "The Distribution of Current and Formation of a Salt Film on an Iron Disk below the Passivation Potential," *Journal of the Electrochemical Society*, **134**, 392-399 (1987).

73. J. F. Cooper, R. H. Muller, and C. W. Tobias, "Periodic Phenomena during Anodic Dissolution of Copper at High Current Densities," *Journal of the Electrochemical Society*, **127**, 1733-1744 (1980).

74. H. P. Lee, Ken Nobe, and Arne J. Pearlstein, "Film Formation and Current Oscillations in the Electrodissolution of Cu in Acidic Chloride Media, I. Experimental Studies," *Journal of the Electrochemical Society*, **132**, 1031-1037 (1985).

75. Arne J. Pearlstein, H. P. Lee, and Ken Nobe, "Film Formation and Current Oscillations in the Electrodissolution of Cu in Acidic Chloride Media, II. Mathematical Model," *Journal of the Electrochemical Society*, **132**, 2159-2165 (1985).

76. S. H. Glarum and J. H. Marshall, "The Anodic Dissolution of Copper into Phosphoric Acid, I. Voltammetric and Oscillatory Behavior," *Journal of the Electrochemical Society*, **132**, 2872-2878 (1985).

77. J. Wojtowicz, "Oscillatory Behavior in Electrochemical Systems," *Modern Aspects of Electrochemistry*, Vol. 8, chapter 2, J. O'M. Bockris and B. Conway, Editors, Plenum Press, New York (1972).

78. U. F. Franck and R. FitzHugh, "Periodische Elektrodenprozesse und ihre Beschreibung durch ein mathematisches Modell," *Zeitschrift für Elektrochemie*, **65**, 156-168 (1961).

79. Philip Russell and John Newman, "Anodic Dissolution of Iron in Acidic Sulfate Electrolytes, I. Formation and Growth of a Porous Salt Film," *Journal of the Electrochemical Society*, **133**, 59-69 (1986).

80. Der-Tau Chin, "Convective Diffusion on a Rotating Spherical Electrode," *Journal of the Electrochemical Society*, **118**, 1434-1438 (1971).

81. Der-Tau Chin, "An Experimental Study of Mass Transfer on a Rotating Spherical Electrode," *Journal of the Electrochemical Society*, **118**, 1764-1769 (1971).

82. Der-Tau Chin, "A Rotating Ring-Hemispherical Electrode for Electroanalytical Applications," *Journal of the Electrochemical Society*, **120**, 631-635 (1973).

83. John Newman, "Resistance for Flow of Current to a Disk," *Journal of the Electrochemical Society*, **113**, 501-502 (1966).

84. W. H. Tiedemann, J. Newman, and D. N. Bennion, "The Error in Measurements of Electrode Kinetics Caused by Nonuniform Ohmic-Potential Drop to a Disk Electrode," *Journal of the Electrochemical Society*, **120**, 256-258 (1973).

85. John Newman, "Mass Transfer to a Rotating Sphere at High Schmidt Numbers," *Journal of the Electrochemical Society*, **119**, 69-71 (1972).

86. John Newman, "Current Distribution on a Rotating Disk below the Limiting Current," *Journal of the Electrochemical Society*, **113**, 1235-1241 (1966).

87. Kemal Nişancioğlu and John Newman, "Current Distribution on a Rotating Sphere below the Limiting Current," *Journal of the Electrochemical Society*, **121**, 241-246 (1974).

88. Der-Tau Chin, "Rotating Spherical Electrode: A Perturbation Theory for Schmidt Number Corrections," *Journal of the Electrochemical Society*, **119**, 1049-1052 (1972).

89. John Newman, *Electrochemical Systems*, Prentice-Hall, Inc., Englewood Cliffs, New Jersey (1973).

90. Der-Tau Chin, "Sinusoidal A-C Modulation of a Rotating Hemispherical Electrode," *Journal of the Electrochemical Society*, **127**, 2162-2166 (1980).

91. Hermann Schlichting, *Boundary-Layer Theory*, Seventh Edition, McGraw-Hill Series in Mechanical Engineering, New York (1979, 1951).

92. Jung Taek Kim and Jacob Jorné, "Mass Transfer of Dissolved Chlorine to a Rotating-Zinc Hemisphere in $ZnCl_2$ Solution," *Journal of the Electrochemical Society*, **125**, 89-94 (1978).

93. Jung Taek Kim and Jacob Jorné, "The Kinetics and Mass Transfer of Zinc Electrode in Acidic Zn-Chloride Solution," *Journal of the Electrochemical Society*, **127**, 8-15 (1980).

94. G. T. Rogers and K. J. Taylor, "Effect of Small Protrusions on Mass Transport to a Rotating-Disk Electrode," *Nature*, **200**, 1062-1064 (1963).

95. A. C. Riddiford, "The Rotating Disk System," *Advances in Electrochemistry and Electrochemical Engineering*, Vol. 4, pp. 47-116, P. Delahay, Editor, Interscience Publishers, New York (1966).

96. Milan M. Jaksic and Charles W. Tobias, "Effects of Hydrodynamic Flow on the Development of the Morphology of Electrodeposited Zinc," *Extended Abstracts*, *29th ISE Meeting*, pp. 1164-1166, Budapest (1978).

97. F. Kohlrausch, "Ueber die elektromotorisch Kraft sehr dünner Gasschichten auf Metalplatten," *Poggendorf Annalen*, **148**, 143-154 (1873).

98. E. Warburg, "Ueber das Verhalten sogenannter unpolarisirbarer Elektroden gegen Wechselstrom," *Annalen der Physik und Chemie*, **67**, 493-499 (1899); *Annalen der Physik*, **6**, 125-135 (1901).

99. F. Krüger, *Zeitschrift für physikalische Chemie*, **45**, 1 (1903).

100. J. E. B. Randles, "Kinetics of Rapid Electrode Reactions," *Discussions of the Faraday Society*, **1**, 11-19 (1947).

101. B. Ershler, "Investigation of Electrode Reactions by the Method of Charging-Curves and with the Aid of Alternating Currents," *Discussions of the Faraday Society*, **1**, 269-277 (1947); *Journal of Physical Chemistry, U.S.S.R.*, **22**, 683 (1948).

102. Heinz Gerischer, "Wechselstrompolarisation von Elektroden mit einem potentialbestimmenden Schritt beim Gleichgewichtspotential I," *Zeitschrift für physikalische Chemie*, **198**, 286-313 (1951).

103. David C. Grahame, "Mathematical Theory of the Faradaic Admittance (Pseudocapacity and Polarization Resistance)," *Journal of the Electrochemical Society*, **99**, 370C-385C (1952).

104. Paul Delahay, *New Instrumental Methods in Electrochemistry*, chapter 7, Wiley-Interscience, New York (1954).

105. J. H. Sluyters, "On the Impedance of Galvanic Cells, I. Theory" *Recueil des Travaux Chimiques des Pays-Bas*, **79**, 1092 (1960).

106. M. Sluyters-Rehbach and J. H. Sluyters, "Sine Wave Methods in the Study of Electrode Processes," *Electroanalytical Chemistry*, Vol. 4, pp. 1-128, Allen J. Bard, Editor, Marcel Dekker, Inc., New York (1970).

107. D. D. Macdonald, *Transient Techniques in Electrochemistry*, Plenum Press, New York (1977).

108. Klaus J. Vetter, *Electrochemical Kinetics, Theoretical and Experimental Aspects*, Academic Press, New York (1967).

109. Digby D. Macdonald and Michael C. H. McKubre, "Impedance Measurements in Electrochemical Systems," *Modern Aspects of Electrochemistry*, Vol. 14, chapter 2, J. O'M. Bockris, B. E. Conway, and R. E. White, Editors, Plenum Press, New York (1982).

110. Claude Gabrielli, *Identification of Electrochemical Processes by Frequency Response Analysis*, Solartron Instrumentation Group monograph, The Solartron Electronic Group Ltd., Farnborough, England (1980).

111. Allen J. Bard and Larry R. Faulkner, *Electrochemical Methods, Fundamentals and Applications*, chapter 9, John Wiley & Sons, Inc., New York (1980).

112. I. Epelboin, M. Keddam, and H. Takenouti, "Use of Impedance Measurements for the Determination of the Instant Rate of Metal Corrosion," *Journal of Applied Electrochemistry*, 2, 71-79 (1972).

113. D. D. MacDonald and M. C. H. McKubre, in *Electrochemical Techniques for Corrosion Testing*, F. Mansfeld and U. Bertocci, Editors, ASTM, Philadelphia (1980).

114. William H. Smyrl, "Digital Impedance for Faradaic Analysis, I. Introduction to Digital Signal Analysis and Impedance Measurements for Electrochemical and Corrosion Systems," *Journal of the Electrochemical Society*, 132, 1551-1555 (1985).

115. William H. Smyrl and Larry L. Stephenson, "Digital Impedance for Faradaic Analysis, III. Copper Corrosion in Oxygenated 0.1N HCl," *Journal of the Electrochemical Society*, 132, 1563-1567 (1985).

116. W. J. Lorenz and F. Mansfeld, "Determination of Corrosion Rates by Electrochemical DC and AC Methods," *Corrosion Science*, **21**, 647-672 (1981).

117. Florian Mansfeld, "Recording and Analysis of AC Impedance Data for Corrosion Studies, I. Background and Methods of Analysis," *Corrosion*, **36**, 301-307 (1981).

118. F. Mansfeld, M. W. Kendig, and S. Tsai, "Recording and Analysis of AC Impedance Data for Corrosion Studies, II. Experimental Approach and Results," *Corrosion*, **38**, 570-580 (1982).

119. K. S. Cole, *Membranes, Ions and Impulses*, University of California Press, Berkeley (1968).

120. Arthur A. Pilla and Gary S. Margules, "Dynamic Interfacial Electrochemical Phenomena at Living Cell Membranes: Application to the Toad Urinary Bladder Membrane System," *Journal of the Electrochemical Society*, **124**, 1697-1706 (1977).

121. *Proceedings of the Symposium on Advances in Lead-Acid Batteries*, K. Bullock and D. Pavlov, Editors, Battery Division, Proceedings Volume 84-14, The Electrochemical Society, 1984.

122. W. Lorenz and M. Handschuh, "Dynamic Theory of the Alternating Current Response of Semiconductor Electrodes under Illumination," *Journal of Electroanalytical Chemistry and Interfacial Electrochemistry*, **178**, 197-220 (1984).

123. Peter Appel and John Newman, "Radially Dependent Convective Warburg Problem for a Rotating Disk," *Journal of the Electrochemical*

Society, 124, 1864-1868 (1977).

124. Bernard Tribollet and John Newman, "Impedance Model for a Concentrated Solution, Application to the Electrodissolution of Copper in Chloride Solutions," *Journal of the Electrochemical Society*, 131, 2780-2785 (1984).

125. Peter Appel, *Electrochemical Systems: Impedance of a Rotating Disk and Mass Transfer in Packed Beds*, Ph. D. Dissertation, University of California, Berkeley, CA, May 1976.

126. Roger Parsons, "The Structure of the Electrical Double Layer and its Influence on the Rates of Electrode Reactions," *Advances in Electrochemistry and Electrochemical Engineering*, Vol. 1, pp. 1-64, P. Delahay, Editor, Interscience Publishers, New York (1961).

127. Paul Delahay, *Double Layer and Electrode Kinetics*, Interscience Publishers, New York (1965).

128. Paul Delahay, "Electrode Processes without *a Priori* Separation of Double-Layer Charging," *The Journal of Physical Chemistry*, 70, 2373-2379 (1966).

129. Karel Holub, Gino Tessari, and Paul Delahay, "Electrode Impedance without *a Priori* Separation of Double-Layer Charging and Faradaic Process," *The Journal of Physical Chemistry*, 71, 2612-2618 (1967).

130. Eugene Levart and Daniel Schuhmann, "Migration-Diffusion Coupling and the Concept of Electrochemical Impedance," *Journal of Electroanalytical Chemistry and Interfacial Electrochemistry*, 24, 41-52 (1970).

131. I. Epelboin and R. Wiart, "Mechanism of Electrocrystallization of Nickel and Cobalt in Acidic Solution," *Journal of the Electrochemical Society*, **118**, 1577-1582 (1971).

132. M. Keddam, O. R. Mattos, and H. Takenouti, "Mechanism of Anodic Dissolution of Iron-Chromium Alloys Investigated by Electrode Impedances—II. Elaboration of the Reaction Model," *Electrochimica Acta*, **31**, 1159-1165 (1986).

133. Alan K. Hauser and John Newman, "A Microscopic Impedance Model of the Electrode/Electrolyte Interface, I. Adsorption Mechanism for Zinc Dissolution in Acidic Chloride Solutions," to be submitted to *Journal of the Electrochemical Society*.

134. David C. Grahame, "The Electrical Double Layer and the Theory of Electrocapillarity," *Chemical Reviews*, **41**, 441-501 (1947).

135. John Newman, "Frequency Dispersion in Capacity Measurements at a Disk Electrode," *Journal of the Electrochemical Society*, **117**, 198-203 (1970).

136. B. Tribollet, J. Newman, and W. H. Smyrl, "Schmidt Number Determination from Non-Steady Measurements in the Low-Frequency Range," submitted to *Journal of the Electrochemical Society*.

137. William H. Smyrl, "Digital Impedance for Faradaic Analysis, II. Electrodissolution of Cu in HCl," *Journal of the Electrochemical Society*, **132**, 1555-1562 (1985).

138. E. Levart and D. Schuhmann, "Sur la Détermination Générale du Comportement Transitoire d'une Electrode à Disque Tournant Soumise à

une Perturbation Electrique de Faible Amplitude," *Journal of Electroanalytical Chemistry and Interfacial Electrochemistry*, **28**, 45-56 (1970).

139. E. Levart and D. Schuhmann, "Sur la Détermination Générale de l'Impédance de Concentration (Diffusion Convective et Réaction Chimique) Pour une Electrode à Disque Tournant," *Journal of Electroanalytical Chemistry and Interfacial Electrochemistry*, **53**, 77-94 (1974).

140. Robert V. Homsy and John Newman, "An Asymptotic Solution for the Warburg Impedance of a Rotating Disk Electrode," *Journal of the Electrochemical Society*, **122**, 521-523 (1974).

141. E. Levart and D. Schuhmann, "Comparison of Some Solutions for the Warburg Impedance of a Rotating Disk Electrode," *Journal of the Electrochemical Society*, **122**, 1082-1083 (1975).

142. Daniel A. Scherson and John Newman, "The Warburg Impedance in the Presence of Convective Flow," *Journal of the Electrochemical Society*, **127**, 110-113 (1980).

143. C. Deslouis, C. Gabrielli, and B. Tribollet, "An Analytical Solution of the Nonsteady Convective Diffusion Equation for Rotating Electrodes," *Journal of the Electrochemical Society*, **130**, 2044-2046 (1983).

144. Bernard Tribollet and John Newman, "Analytic Expression of the Warburg Impedance for a Rotating Disk Electrode," *Journal of the Electrochemical Society*, **130**, 822-824 (1983).

145. Daniel Schuhmann, *Comptes Rendus Acad. Sci., Paris*, **262C**, 624 (1966).

146. C. Deslouis, I. Epelboin, M. Keddam, and J. C. Lestrade, "Impedance de Diffusion d'un Disque Tournant en Régime Hydrodynamique Laminaire. Etude Expérimentale et Comparaison avec le Modèle de Nernst," *Journal of Electroanalytical Chemistry and Interfacial Electrochemistry*, **28**, 57-63 (1970).

147. S. C. Creason and D. E. Smith, *Journal of Electroanalytical Chemistry and Interfacial Electrochemistry*, **36**, A1 (1972), and **40**, A1 (1972).

148. S. C. Creason, J. W. Hayes, and D. E. Smith, *ibid.*, **47**, 9-46 (1973).

149. D. E. Smith, *Analytical Chemistry*, **48**, 221A, 517A (1976).

150. G. Blanc, I. Epelboin, C. Gabrielli, and M. Keddam, "Measurement of the Electrode Impedance in a Wide Frequency Range Using a Pseudo-Random Noise," *Electrochimica Acta*, **20**, 599-601 (1975).

151. R. de Levie, J. W. Thomas, and K. M. Abbey, *Journal of Electroanalytical Chemistry and Interfacial Electrochemistry*, **62**, 111-125 (1975).

152. C. Gabrielli, F. Huet, M. Keddam, and J.F. Lizee, "Measurement Time Versus Accuracy Trade-Off Analyzed for Electrochemical Impedance Measurements by Means of Sine, White Noise, and Step Signals," *Journal of Electroanalytical Chemistry and Interfacial Electrochemistry*, **138**, 201-208 (1982).

153. S. H. Glarum and J. H. Marshall, "An A-C Admittance Study of the Platinum/Sulfuric Acid Interface," *Journal of the Electrochemical Society*, 126, 424-430 (1979).

154. S. H. Glarum, "Variational Approximations to Current Distribution Problems. The Rotating Disk Electrode," *Journal of the Electrochemical Society*, 124, 518-524 (1977).

155. Kemal Nişancioğlu, "The Error in Polarization Resistance and Capacitance Measurements due to Nonuniform Ohmic Potential Drop to Flush-Mounted Probes," Paper Number 75, Presented in *Corrosion 85*, Annual Conference of the National Association of Corrosion Engineers, Boston, Massachusetts (March 1985).

156. B. D. Cahan, Z. Nagy, and M. A. Genshaw, "Cell Design for Potentiostatic Measuring System," *Journal of the Electrochemical Society*, 119, 64-69 (1972).

157. 157. Robert de Levie, "Electrochemical Response of Porous and Rough Electrodes," in *Advances in Electrochemistry and Electrochemical Engineering*, Vol. 6, pp. 329-397, P. Delahay, Editor, Interscience Publishers, New York (1967).

158. B. D. Cahan, C. T. Chen, D. Radman, and D. A. Scherson, "On the Questions of Presentation and Analysis of Impedance Measurements in Electrochemical Systems," unpublished manuscript.

159. R. de Levie, "On Impedance Measurements: The Determination of the Double Layer Capacitance in the Presence of an Electrode Reaction," *Electrochimica Acta*, 10, 395-402 (1965).

160. J. Hitzig, J. Titz, K. Jüttner, and W. J. Lorenz, "Frequency Response Analysis of the Ag/Ag^+ System: A Partially Active Electrode Approach," *Electrochimica Acta*, **29**, 287-296 (1984).

161. M. W. Kendig, E. M. Meyer, G. Lindberg, and F. Mansfeld, "A Computer Analysis of Electrochemical Impedance Data," *Corrosion Science*, **23**, 1007-1015 (1983).

162. M. W. Kendig, F. Mansfeld, and S. Tsai, "Determination of the Long Term Corrosion Behavior of Coated Steel with A.C. Impedance Measurements," *Corrosion Science*, **23**, 317-329 (1983); *Corrosion*, **38**, 478 (1982).

163. J. Hitzig, K. Jüttner, and W. J. Lorenz, "AC-Impedance Measurements on Corroded Porous Aluminum Oxide Films," *Journal of the Electrochemical Society*, **133**, 887-892 (1986).

CHAPTER 2

Anodic Polarization Curve, Passivation, and Current Oscillations: Experimental Results

2.1. Introduction

This chapter presents experimental polarization curves, particularly passivation curves, and experimentally observed current oscillations for rotating hemispherical iron electrodes.

The purpose of these experiments is to elucidate the passivation and oscillatory behavior of the iron-sulfuric acid system. In particular, the objective of these experiments is to answer questions such as: what is the effect of electrode geometry on the shape of the observed passivation curve? how does a uniform or nonuniform primary current distribution affect the observed behavior of the system? does an iron hemisphere passivate uniformly? do hemispherical electrodes of different sizes undergo sustained current oscillations?

Another objective of these experiments is to determine the anodic polarization curve for the Fe/H_2SO_4 system so that we can then carry out the AC impedance experiments at selected points along the polarization curve. A knowledge of the steady-state behavior of the system, specifically of the polarization curve, is necessary before investigating the dynamic behavior of the system by the electrochemical impedance technique.

The characteristics of the Fe/H_2SO_4 system and the significance of ohmic potential drop and current distribution effects were discussed in section 1.3; the current distribution characteristics of the rotating hemispherical electrode were described in section 1.5. The hemispherical electrode has a uniform primary current distribution, whereas the disk electrode has a highly nonuniform primary distribution. Four rotating hemispherical iron electrodes with different diameters were used in these experiments. The hemisphere diameter affects the degree of uniformity of the current and potential distributions as well as the relative significance of ohmic drop effects. Comparison of the results for hemispheres with results for disks as well as comparison of the results for different hemispheres may therefore elucidate the effects of current distribution and ohmic potential drop on the system behavior.

The diameters of the rotating hemispherical electrodes used in these experiments ranged from 3 to 8.5 mm. The electrode rotation speeds were 400, 900, and 1600 rpm (41.9, 94.2, and 167.6 rad/s). Some representative experimental results are shown in this chapter.

All the potential values in this chapter are relative to the mercury-mercurous sulfate-saturated potassium sulfate (Hg/Hg_2SO_4) reference electrode. The current in the presented results is given as measured (in A units) and is also expressed in terms of an average or apparent current density [i] (A/cm^2), which is defined as the measured current divided by the area of the hemispherical electrode calculated from the measured diameter.

2.2. Principles of Polarization Control

The interaction between the electrochemical system under study and the experimental apparatus and procedure can give rise to phenomena that are not characteristic of the electrochemical system itself. Specifically the Fe/H_2SO_4 system can exhibit different behavior depending on the experimental apparatus, particularly the polarization control device, used to investigate the behavior of the system. (See for example figure 1-1). One therefore needs to consider the principles of polarization control before carrying out an experiment.

Epelboin *et al.* (1) have presented the principles of polarization control necessary to study electrochemical systems such as the Fe/H_2SO_4 system. We will briefly discuss these principles here. The constraint imposed by the polarization device on the electrochemical system can be represented by a relationship between current and potential called a load line.

Consider an electrochemical system with the current-potential characteristics shown in figure 2-1 (1, 2). A conventional (normal) potentiostat provides a vertical (infinite-slope) load line (L_o). An alternative polarization control device, equivalent to a voltage source E in series with a negative internal resistance ρ, provides a load line (L) with a finite positive slope. When a conventional potentiostat is used in a potential sweep experiment, curve a-b-c-d-e is obtained for a positive sweep, while e-d-f-b-a is obtained for a negative sweep. Thus a hysteresis is observed, and curve c-f, which is assumed to be characteristic of the electrochemical system, is obscured. When a

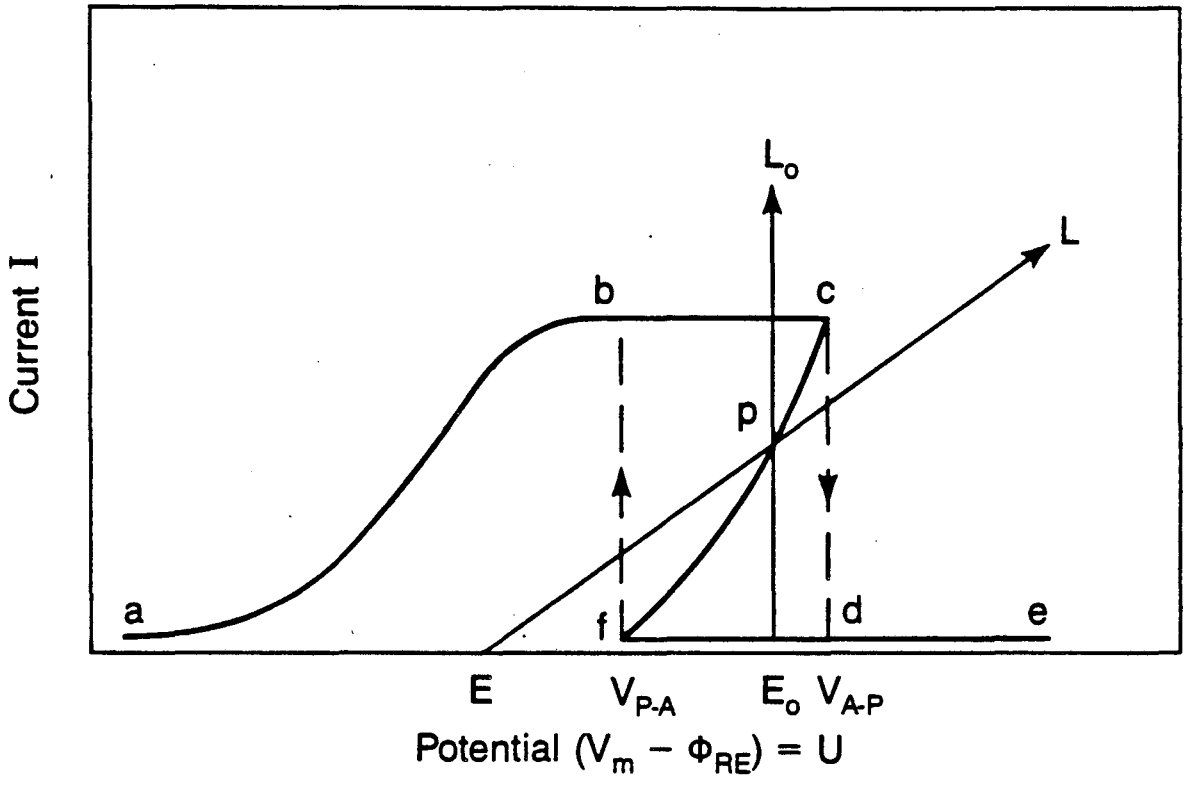

XBL 876-6302

Figure 2-1. Current-potential diagram for a passivating electrochemical system illustrating the principles of polarization control. L_o - vertical load line for a normal potentiostat, $U = E_o$. L - load line for an alternative polarization control device, *e.g.*, a Negative Impedance Converter, $U = E - \rho I$. E_o, E, and ρ are adjustable parameters in the devices. (taken from 1, 2)

polarization control device with a positive-slope load line is used, points such as P along c-f can be reached. Then curve a-b-c-f-d-e is obtained for a positive potential sweep, and the reverse curve is obtained for a negative sweep.

In this study we used a potentiostat (Stonehart BC 1200) that had a positive feedback circuit and was therefore capable of providing either a vertical or a positive-slope load line, and we observed two different types of behavior. For systems including a nonuniform current or potential distribution, localized electrode dissolution, and ohmic potential drop, the question remains — which of the observed types of behavior is closer to the fundamental behavior of the system that we seek to determine?

2.3. Experimental Apparatus and Procedure

The hemispherical electrodes were manufactured by Pine Instrument Company using 99.9985% pure iron shrouded into a Teflon insulating cylinder with a diameter of 1.9 cm. The diameter of the hemispheres decreased slightly during the experiments due to iron dissolution, and probably the hemispherical shape of the electrodes was slightly distorted. The hemisphere diameter at the equator was measured before and after each experiment with a micrometer.

The hemisphere surface was polished before each experiment, using first 600 grit silicon carbide abrasive paper and next polishing cloths with 9, 3, and 1 μm diamond pastes. The electrode was rotating while it was being polished to avoid deformation of the hemispherical shape.

After polishing, the electrode was washed with acetone and rinsed with purified water. Finally the hemisphere was immersed in 1 M H_2SO_4 for ~5 minutes and immediately transferred to the experimental cell.

An analytical rotator (Pine Instrument Model ASR2) was used to rotate the electrode. Electrical connection to the rotating electrode shaft was made by a silver-carbon brush holder assembly (Pine Instrument ACAR917). It was necessary to polish the silver-carbon brush (with abrasive paper, followed by acetone wash) before each experiment to avoid noise in the electrical signals due to the brush. Since a brush is inevitably deformed by contact with the rotating shaft, a better arrangement to avoid noise in rotating electrode experiments would be electrical contact through a liquid mercury chamber. However such an arrangement was not available in the equipment used in this work.

The electrolyte solution consisted of reagent grade sulfuric acid (Fisher Scientific or Mallinckrodt) and purified water with a specific resistance of 17 MΩ-cm, prepared with a Barnstead NANOpure water purification system. The electrolyte solution was sparged with nitrogen (Liquid Carbonic, Hi-Pure) for at least one hour before each experiment. Nitrogen sparging continued during the experiment at a much lower rate so that it would not interfere with the hydrodynamics for a rotating hemisphere.

The glass cell used in these experiments is shown schematically in figure 2-2. The cell had separate compartments for the counterelectrode and the reference electrode. The counterelectrode was a platinum screen with surface area much larger than the working electrode, and the

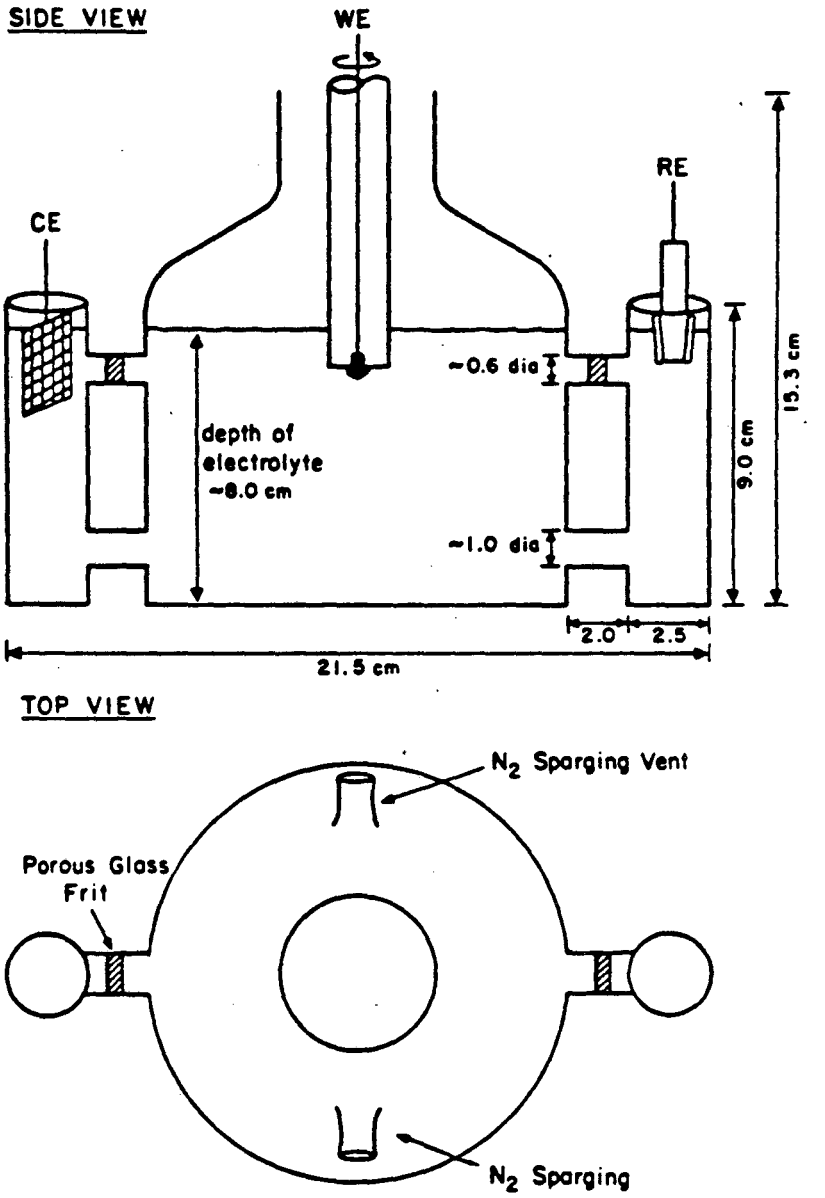

Figure 2-2. Schematic diagram of the experimental cell. Approximate dimensions in cm are given. WE - working electrode, RE - reference electrode, CE - counterelectrode.

reference electrode was a mercury-mercurous sulfate-saturated potassium sulfate electrode, Hg/Hg_2SO_4 (Radiometer, K601 electrode). In this experimental cell arrangement, the reference electrode was located in the bulk solution, essentially at infinity. The cell was placed in a constant temperature bath maintaining the temperature at 25.0 ± 0.5° C.

Polarization of the cell was controlled using a Stonehart potentiostat with the input voltage provided by a universal programmer (Princeton Applied Research Model 175). The current and potential signals were monitored with a digital storage oscilloscope (Nicolet Model 206), and current-potential plots were recorded with an X-Y recorder (Hewlett-Packard Model 7047A). A power-line filter was used to avoid noise from extraneous sources. A schematic diagram of the experimental apparatus is shown in figure 2-3. The apparatus used in this work was nearly the same as that used by Russell (2, 3, 4).

Three types of experiments were carried out:

1. Potentiodynamic sweep experiments in which the load line of the potentiostat was vertical to determine the anodic polarization curve, particularly the region in the limiting current plateau where current oscillations occur and the hysteresis associated with passivation.
2. Potentiodynamic experiments in which the positive-slope load line of the potentiostat was used to determine whether the anodic polarization curve for iron hemispheres is Z-shaped displaying a continuous and reversible passivation curve.
3. Potentiostatic experiments in which the current oscillations were recorded.

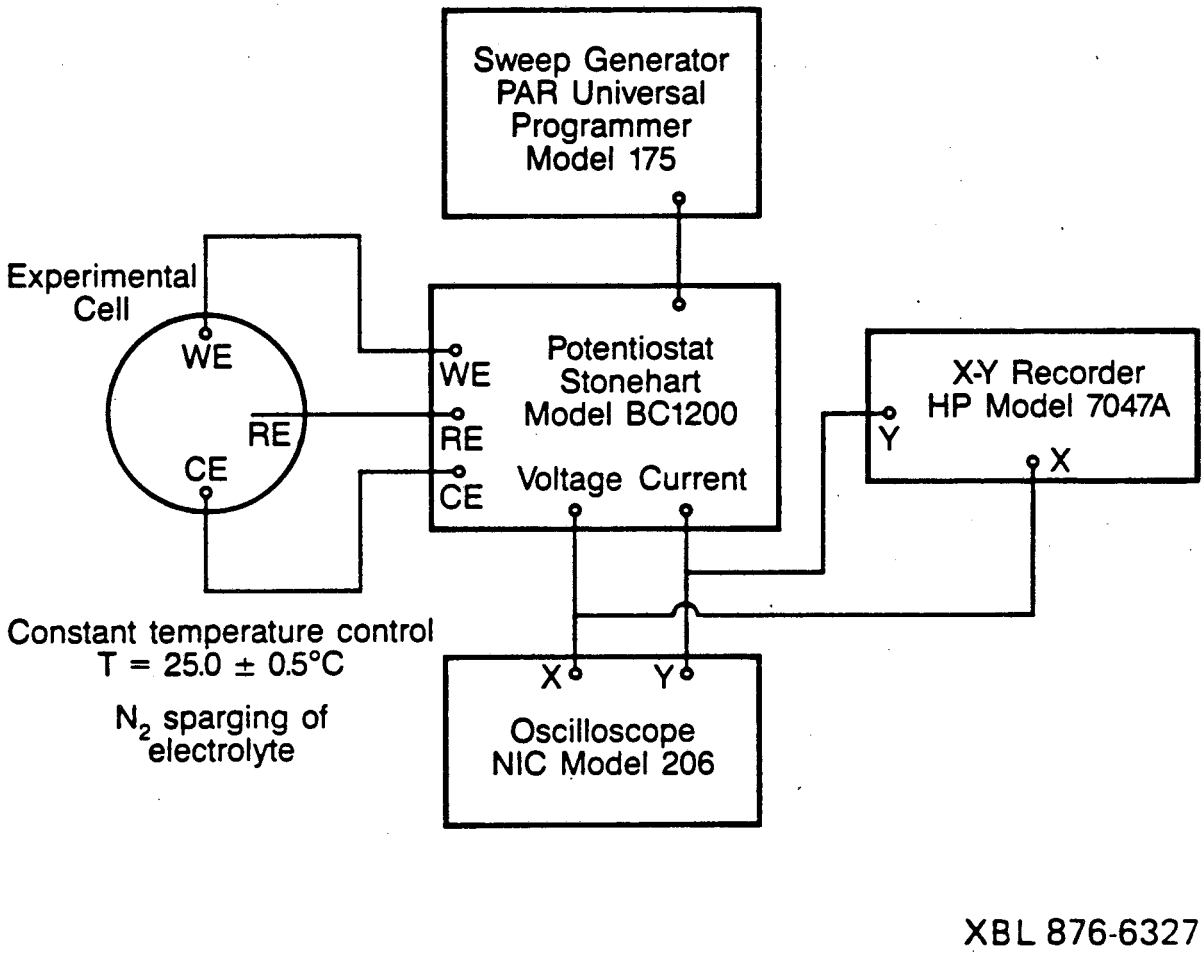

Figure 2-3. Schematic diagram of the experimental apparatus.

In the first type of potentiodynamic experiments, the potential was swept positively from the open-circuit potential to a value within the passive range and *vice versa*. The sweep rates ranged from 2 to 30 mV/s. If the positive potential sweep was carried out continuously from the open-circuit potential to the passive range, the limiting current plateau and the region where oscillations occur could not be clearly obtained. The current would go through a maximum above the limiting current value and then through a minimum below the limiting value; the current would subsequently reach the limiting value, and finally the electrode would passivate. In order to trace out the limiting current plateau, it was therefore necessary to stop the positive sweep 20-50 mV before the active-to-passive transition potential and reverse the direction of the sweep. This procedure was used by Russell (3, 4) to determine the limiting current plateau for rotating disk electrodes. By subsequently sweeping the potential positively, a vertical active-passive transition was observed at V_{A-P}, and by reversing the sweep, a vertical passive-active transition was observed at V_{P-A}, which was less anodic than V_{A-P}, *i.e.*, there was a hysteresis. Some representative results of these potentiodynamic sweep experiments are shown in section 2.4.

In the second type of potentiodynamic experiments, the potential was first swept from the open-circuit value to a value E, which was usually −0.27 V, at a sweep rate of 20 or 30 mV/s. Then the slope of the load line was decreased continuously at a rate slow enough to approach steady-state conditions. Sometimes it was necessary also to vary E in order to trace part of the passivation curve. There was a lower limit

to the slope of the load line provided by the potentiostat, and therefore the lowest-current part of the passivation curve was inaccessible. In some cases the potentiostat overloaded, becoming unable to control the system, perhaps due to violent oxygen evolution at high potentials or high currents. The results of these experiments are discussed in section 2.5.

For the third type of experiments, the electrode was polarized at a potential within the range where oscillations occur at the limiting current plateau. The limiting current plateau was reached following a procedure similar to that for the potentiodynamic sweep experiments. The potential was then held at a value roughly in the middle of the oscillatory region, and the current as a function of time was recorded by the oscilloscope. The results of these experiments are presented in section 2.6.

An interesting phenomenon observed at the end of some experiments was the formation of spiral markings on the surface of the hemispherical electrode as shown in the photograph in figure 2-4. This phenomenon was more often observed at higher rotation speeds and in the experiments recording the current oscillations, when the electrode spent more time at high currents. The formation of spiral markings on rotating electrodes is discussed in section 1.5. Since the Reynolds numbers in our experiments were orders of magnitude lower than that for transition to turbulence, the observed spirals were probably due to hydrodynamic disturbances produced by surface defects, which developed during the dissolution process.

XBB854-3233

Figure 2-4. Photograph of a hemispherical electrode with spiral markings on its surface.

2.4. Anodic Polarization Curve — Discontinuous Active - Passive Transitions

Figure 2-5 shows a polarization curve obtained in a potentiodynamic positive-sweep experiment in which the load line of the potentiostat was vertical. The polarization curve displays a limiting current plateau and a vertical transition from the active to the passive state. The current oscillations are not shown to scale in figure 2-5 (as well as in the other polarization curves presented), because they were beyond the time-response capabilities of the X-Y recorder. Before reaching a plateau, the current went through a maximum above the limiting current value and then through a minimum below the limiting value. This maximum-minimum phenomenon obscured the region where current oscillations would occur, and thus only part of the oscillatory region is evident in figure 2-5.

The maximum-minimum or 'overshoot-undershoot' phenomenon for the Fe/H_2SO_4 system was previously observed by Epelboin *et al.* (1, 5) and Russell and Newman (2, 3), who also discussed the origins of the phenomenon. The appearance of the maximum depends on the potential sweep rate and disappears under steady-state conditions; it may therefore be an experimental artifact due to a fast sweep rate (1). Alternatively, the maximum-minimum phenomenon may be due to the initial precipitation of salt crystals from a supersaturated solution and subsequent growth and rearrangement of the salt crystals, as observed by Beck (6) for iron in perchloric acid.

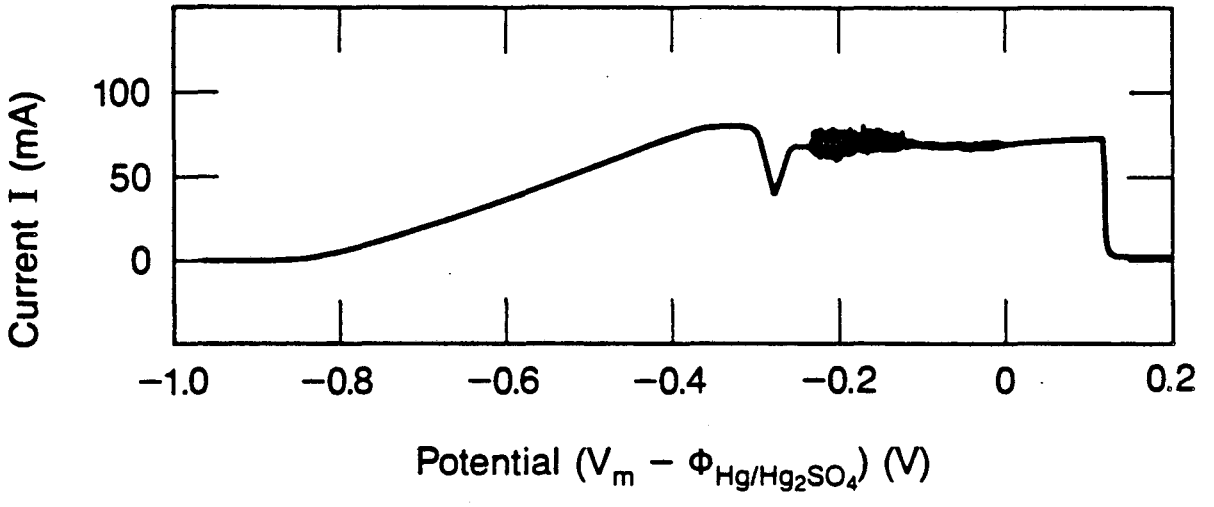

XBL 876-6311

Figure 2-5. Polarization curve obtained in a positive potential sweep experiment in which the load line of the potentiostat was vertical. Rotating hemispherical electrode: d = 3 mm, Ω = 400 rpm. The potential sweep rate was 20 mV/s up to about 60 mA and was then reduced to 5 mV/s.

Figure 2-6 is a typical polarization curve, including the limiting current plateau, the region where current oscillations are observed, and the sharp active-passive and passive-active transitions with the associated hysteresis. The current maximum and minimum behavior around the limiting current plateau is not shown in figure 2-6, for clarity. The limiting current plateau was traced out by following the procedure described in section 2.3.

A peculiarity of the polarization curve shown in figure 2-6 (and less clearly in figure 2-5) is a step increase in the current before passivation. This step increase has also been observed by Russell (4), but its cause is not known.

Figure 2-6 shows that the passive-active transition occurred at $V_{P-A} = -0.14$ V, whereas the active-passive transition occurred at V_{A-P}, which was 0.38 V higher. A rough estimate of the ohmic potential drop included in V_{A-P} is 0.28 V, which is the product of the theoretical ohmic resistance of the hemisphere (equation 1-14 with $\kappa = 0.40\ \Omega^{-1}\cdot cm^{-1}$) and the limiting current value (153 mA). Furthermore the passivation potential according to condition 1-10 would be $(V_m - \Phi_o) = -0.215$ V (w.r.t. Hg/Hg_2SO_4) for pH = 0.

Epelboin *et al.* (7) as well as Russell and Newman (2) obtained a value of $V_{P-A} = -0.17$ V for a 5 mm diameter disk electrode in 1 M H_2SO_4. Russell and Newman (2) observed that V_{P-A} became less negative as the disk electrode size increased, and they rationalized this trend by considering that a bigger disk electrode has greater potential and concentration fluctuations over its surface and such fluctuations may lead to

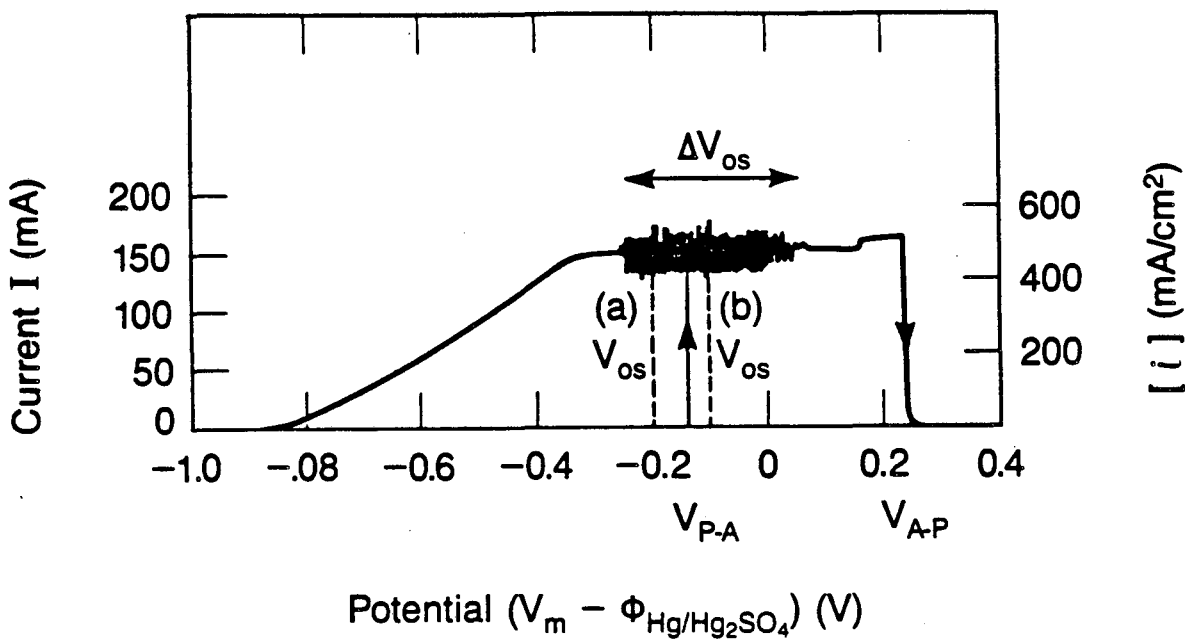

XBL 876-6314

Figure 2-6. Polarization curve from a potentiodynamic sweep experiment for a rotating hemispherical electrode (d = 4.4 mm, Ω = 400 rpm). ΔV_{os} indicates the region of the limiting current plateau where current oscillations are observed. The current maximum-minimum phenomenon is not shown in the figure, for clarity.

earlier breakdown of the passive film covering the electrode. The value $V_{P-A} = -0.14$ V obtained here for a 4.4 mm diameter hemisphere appears consistent with previous results for disk electrodes.

In general the results of potentiodynamic sweep experiments for rotating hemispherical electrodes using a normal potentiostat were very similar to the results for disk electrodes as one might expect.

2.5. Anodic Polarization Curve — Continuous Passivation

2.5.1. Experimental Curves

Experimental results obtained using the positive-slope load line of the potentiostat are discussed in this section.

Figure 2-7 shows an experimental Z-shaped polarization curve for a 3 mm diameter hemispherical electrode. We notice that the minimum below the limiting current plateau reached a quite low value and occurred in the vicinity of the passivation potential given by equation 1-10. Figure 2-8 shows polarization curves for hemispheres of roughly the same diameter at different rotation speeds, and figure 2-9 is a polarization curve for a bigger hemisphere.

Figure 2-7 illustrates that active dissolution around the limiting current plateau extends into potentials higher than V_{A-P} observed with a normal potentiostat, but this extended region is unstable; large-magnitude, uncontrolled current fluctuations occur there. In some experiments, big bubbles, most probably evolved oxygen gas, appeared on the electrode in this region; the system could no longer be controlled,

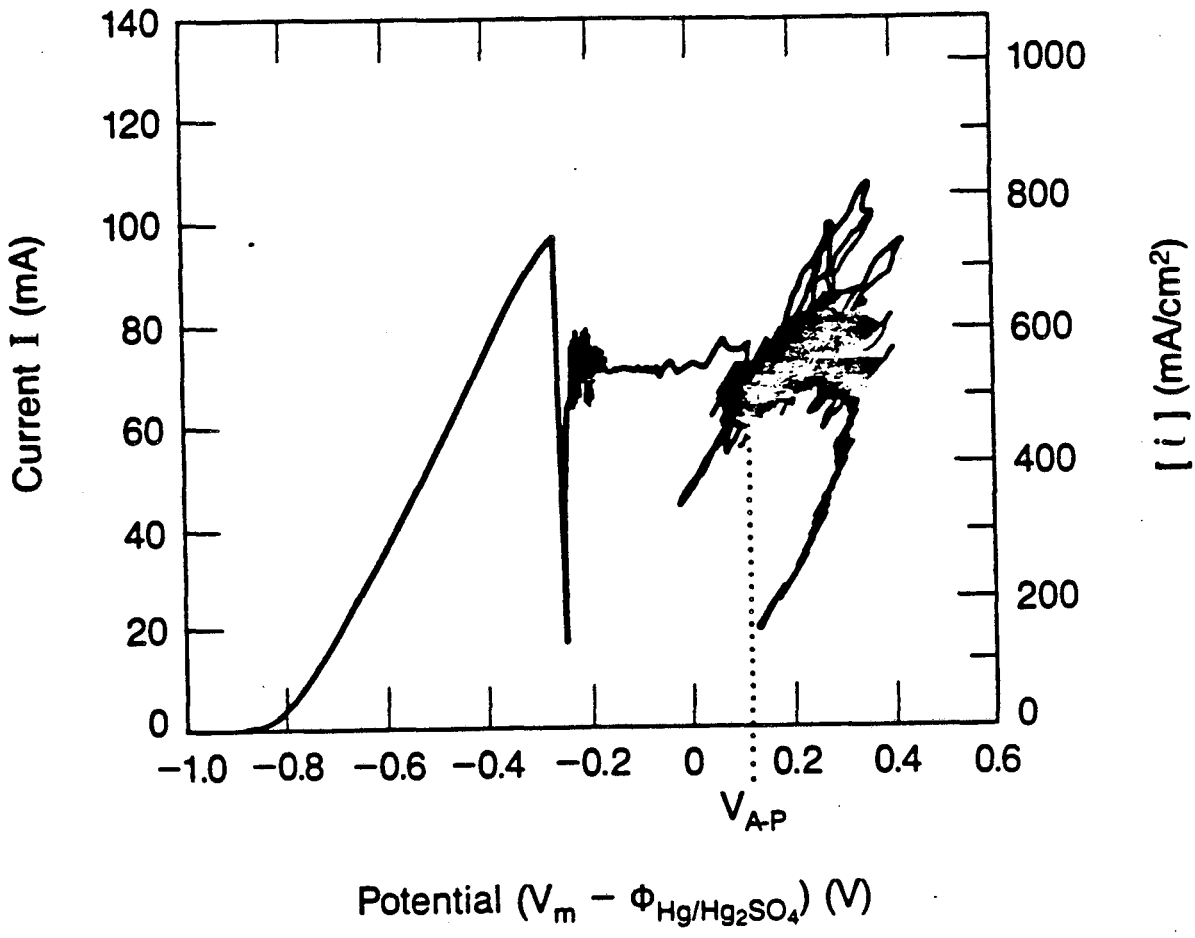

XBL 876-6310

Figure 2-7. Experimental Z-shaped polarization curve for a rotating hemispherical electrode (d = 3 mm, Ω = 400 rpm) obtained using the positive-slope load line of the potentiostat. The corresponding polarization curve obtained using a vertical load line is shown in figure 2-5. The dotted line indicates the active-passive transition observed in the experiment in figure 2-5.

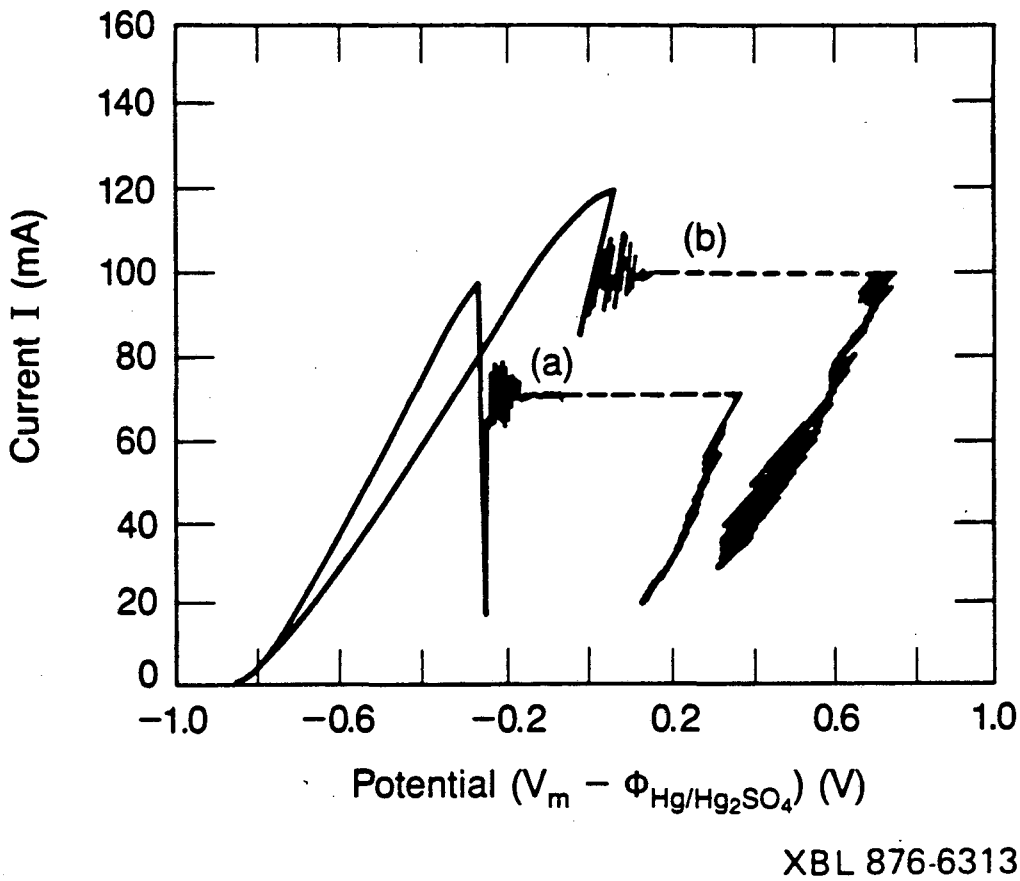

Figure 2-8. Polarization curves for a ~3 mm hemisphere at different rotation speeds: (a) 400 rpm (also shown in figure 2-7), (b) 900 rpm. The dashed lines represent the unstable region of the limiting current plateau.

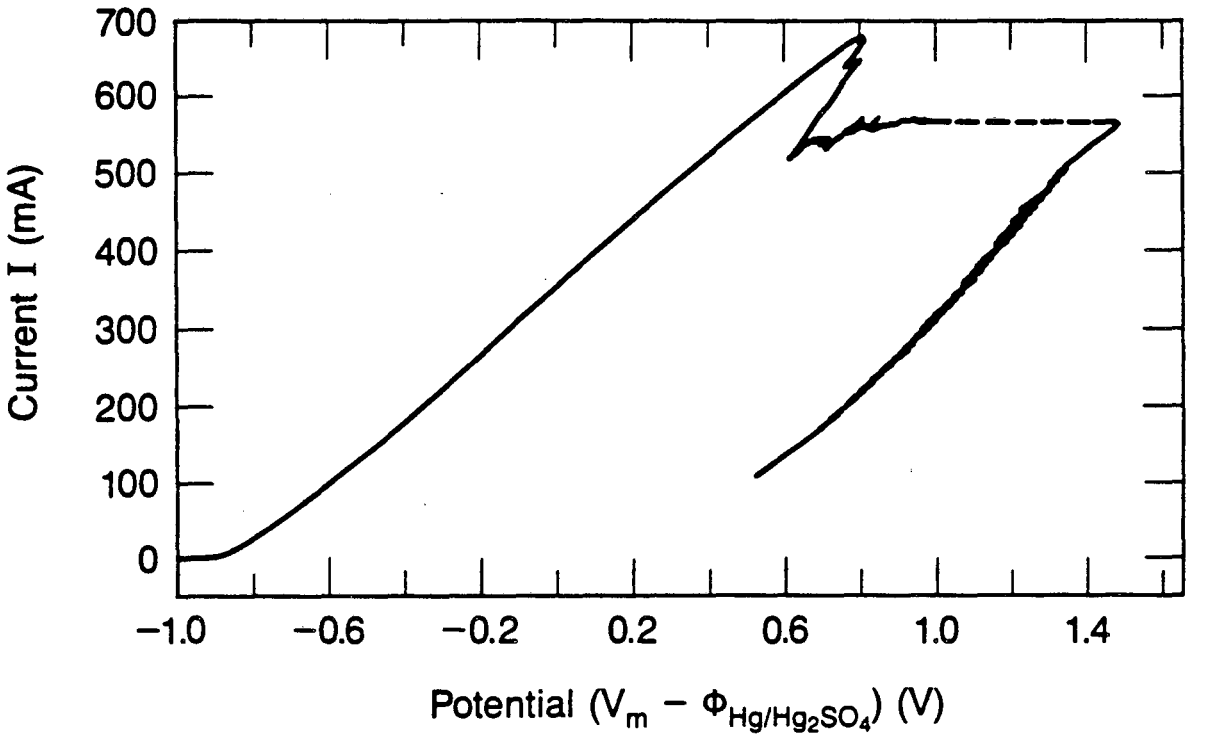

XBL 876-6312

Figure 2-9. Polarization curve for a rotating hemispherical electrode (d = 6.73 mm, Ω = 900 rpm) obtained using a positive-slope load line. The dashed line represents the unstable region of the limiting current plateau.

and those experiments had to be terminated there. Current fluctuations that could not be controlled in the extended limiting current region were also reported by Epelboin *et al.* (1), who used a polarization control device referred to as a Negative Impedance Converter, and by Russell (3, 4).

Small-magnitude fluctuations also occurred along the passivation curve in these experiments. Significant random fluctuations were observed by Russell (4, 3); however Epelboin *et al.* (1) did not report fluctuations during passivation in their experimental Z-shaped curves.

Sometimes we repeated potentiodynamic experiments using the same electrode (with a slightly smaller diameter in each experiment), under the same conditions and observed different magnitude or shape of the fluctuations in the extended limiting current region and during passivation. Overall the fluctuations in the extended region of the limiting current plateau and along the passivation curve appear to be strongly dependent on the experimental electronic equipment, in contrast to the more regular current oscillations observed within the limiting current plateau (section 2.6), which are characteristic of the electrochemical system itself (3).

Recall now figure 1-6 (Fig. 6 in Ref. 2), which shows a trend of steeper passivation curve with decreasing disk electrode diameter and hence decreasing ohmic potential-drop effect. We would like to see whether hemispherical electrodes follow the same trend.

The slope of the passivation curve for an electrode passivating nonuniformly reflects the rate of change of active area with changing potential and therefore the distribution of the potential Φ_o near the electrode surface (see equation 1-10). The passivation curve is expected to be steeper for a more uniform potential distribution. For a rotating disk electrode, which has a nonuniform primary distribution and a uniform mass-transfer distribution, the potential distribution becomes more uniform as the disk size decreases; thus the passivation curve becomes steeper as the disk diameter decreases. A rotating hemispherical electrode has a uniform primary distribution and a nonuniform mass-transfer distribution. At limiting current conditions, the distribution of the ohmic potential Φ_o' becomes more nonuniform as the hemisphere diameter increases, according to equation 1-13, but it is not clear whether at appreciable fractions of the limiting current the potential distribution will be less uniform as the diameter of the passivating hemisphere increases.

Figure 2-10 gives current-potential curves for three hemispherical electrodes, each having a different diameter. The smallest hemispherical electrode (C) has the steepest passivation curve, but there is no clear difference between the slopes of the passivation curves of the two bigger electrodes (A, B). Thus, a monotonic relationship between the slope of the passivation curve and the hemispherical electrode diameter is not evident in figure 2-10, while a monotonic relationship between the magnitude of the ohmic potential drop and the diameter is evident. We tried to measure polarization curves for a much bigger hemispherical

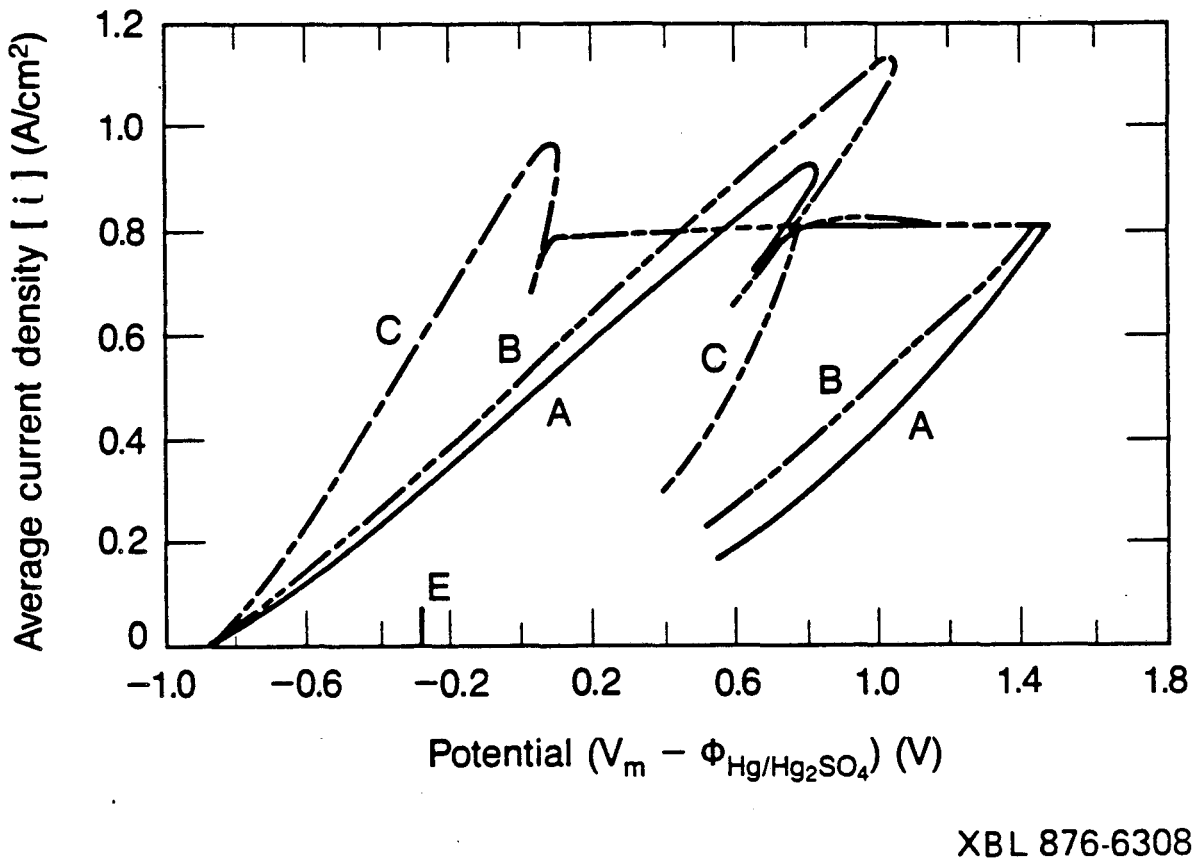

Figure 2-10. Polarization curves for three rotating hemispherical electrodes obtained using a positive-slope load line. Electrode diameters: A - 6.73 mm (also in figure 2-9), B - 4.57 mm, C - 2.85 mm (also in figure 2-8(b)). Rotation speed: Ω = 900 rpm. The unstable region of the limiting current plateau is represented by dashed lines. For clarity, the small-magnitude fluctuations along the passivation curves are not shown; lines representing the average of these fluctuations are given.

electrode (8.5 mm diameter) to clarify (reveal) any possible relationship, but we could not obtain the complete limiting current plateau and the active-passive transition, because the current reached very high values and it was difficult to control the system.

We should note that the average current density $[i] = I/(2\pi r_o^2)$ plotted in figure 2-10 is not a true current density, since the electrode would passivate partially and dissolve nonuniformly in some ranges and also since the electrode diameter decreased slightly during the experiment. Thus $[i]$ is a somewhat arbitrary representation of the current on the electrode and may obscure the comparison of results from different electrodes.

Iron rotating disk electrodes passivate nonuniformly (as discussed in section 1.3.2), and apparently so do hemispherical electrodes. An important question for elucidating iron passivation is: what is the electrode dissolution profile during passivation? In this work, after experiments where hemispherical electrodes were polarized at the passivation curve for a sufficiently long time, we observed much greater dissolution near the equator (see section 3.6.2), *i.e.*, preferential passivation near the pole. An implication of the observed dissolution profile is that along the passivation curve, the effective electrode geometry is not a hemisphere but a different segment of a spherical surface; the potential and concentration distributions for such an electrode geometry are not readily predicted.

Considering the condition for passivation given by equation 1-10 and the potential, current, and concentration distributions for a

rotating hemispherical electrode, how can one explain the observed dissolution-passivation profile?

2.5.2. Probable Passivation Configurations

According to condition 1-10, to determine whether a part of the electrode will passivate, we need to know the values of the potential difference ($V_m - \Phi_o$) and the H^+ concentration near the surface. (Φ_o is the potential in the solution adjacent to the electrode, outside the diffuse double layer.) ($V_m - \Phi_o$) is also the potential driving-force for electrochemical reaction in the Butler-Volmer expression. In addition the electrode may be covered by a porous ferrous-salt film acting as a precursor to oxide passivation.

Consider the case just before passivation starts where the electrode is near limiting current conditions. Figure 2-11 illustrates probable potential distributions for a rotating hemispherical electrode. Nişancioğlu and Newman (8) have calculated the potential (Φ_o', the potential in the bulk solution just outside the diffusion layer) and current distributions for a hemispherical electrode at the limiting current. These distributions are shown in figure 1-7; they are both nonuniform.

Initially, considering the Φ_o' potential distribution, one might expect that as Φ_o' is lower near the equator of the hemisphere, the electrode would passivate preferentially near the equator. But it is Φ_o rather than Φ_o' that is important for passivation. The limiting current density is higher near the pole, and the potential driving force

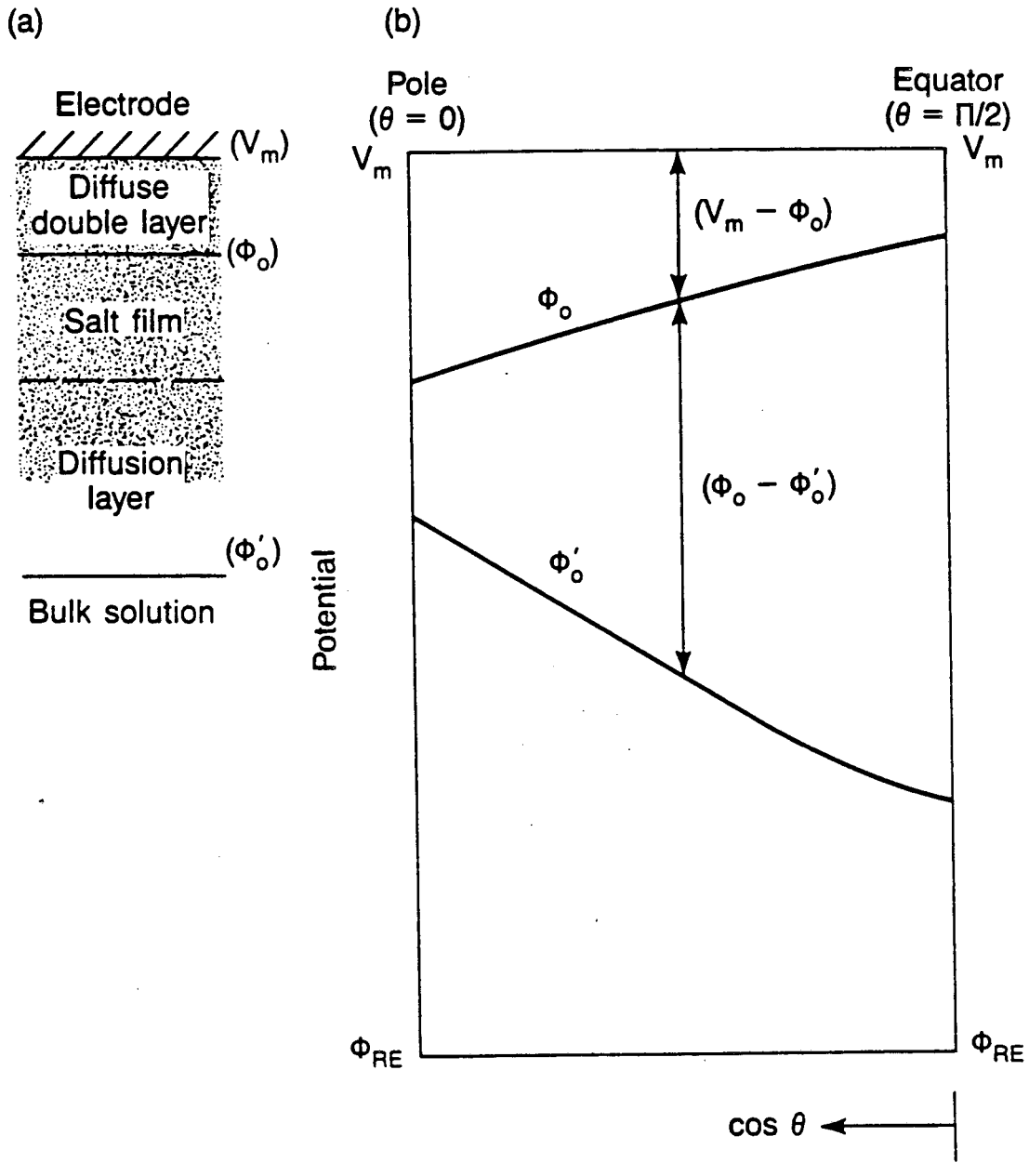

XBL 876-6325

Figure 2-11. (a) Schematic diagram showing the electrode-salt film-solution interfaces. The dots illustrate that these interfaces are not clearly separated (or defined) and the layers may overlap.
(b) Schematic diagram showing probable potential variations for a hemispherical electrode near limiting current conditions.

$(V_m - \Phi_o)$ should therefore be larger near the pole. Larger $(V_m - \Phi_o)$ values then favor passivation near the pole.

However the passivation potential depends on the value of the pH near the electrode surface, and we also need to consider variations of the H^+ concentration along the hemispherical electrode. The H^+ concentration is determined by convective diffusion and electrolytic migration through the solution in the diffusion layer and the salt film (if there is one). The convective diffusion flux is higher near the pole of a hemisphere than near the equator (8, 9), tending to increase the H^+ concentration near the pole, but the flux due to migration through the potential drop $(\Phi_o - \Phi_o')$, illustrated in figure 2-11, would be lower near the pole tending to decrease the H^+ concentration there.

We may also consider whether a salt film forms uniformly over the electrode surface. Since the mass-transfer rate is highest near the pole of the hemisphere and decreases toward the equator, the concentration of Fe^{++}, which is produced by the electrode reaction, may be higher near the equator. Ferrous salt film precipitation would then be greater near the equator, and the salt film thickness might be larger or the porosity smaller near the equator. A higher $\frac{\delta_f}{\epsilon_f}$ value would yield a greater potential gradient and hence a greater pH change across the salt film (see equation 1-9) and would tend to favor passivation near the equator due to a higher pH value. A higher $\frac{\delta_f}{\epsilon_f}$ value is also consistent with a greater potential drop $(\Phi_o - \Phi_o')$ near the equator.

In addition, the electrode surface coverage by a porous salt film and other adsorbed species may be nonuniform, and such nonuniformity would affect the passivation behavior of the electrode. Furthermore, if nonuniform dissolution and passivation proceed over a long-enough period of time, the shape of the electrode will change, and consequently the mass transfer and ohmic potential drop characteristics of the electrode will change in a way that is difficult to determine.

In summary, there are several coupled and sometimes competing effects which tend to favor preferential passivation of a hemispherical electrode either near the pole or near the equator. We have experimentally observed preferential passivation of hemispheres near the pole (more precisely, much greater dissolution near the equator), and this observation may be explained by a dominant effect of the higher $(V - \Phi_o)$ value near the pole, under those experimental conditions. At different conditions there could be more balance between the opposing effects resulting in a more uniform passivation of the hemispherical electrode.

Russell and Newman (10) discussed (qualitatively) the probable radial variations in the potential, the concentrations, and the salt film thickness for a rotating disk electrode at the limiting current plateau and concluded that the disk will preferentially passivate near the periphery. However, experiments sometimes give other results.

The above discussion for the hemispherical electrode is only a qualitative and phenomenological attempt to provide some rationalization of experimental observations. Because multiple interacting phenomena occur in the system, a rigorous quantitative treatment would be required

for a definitive characterization of the system.

2.6. Current Oscillations

Figure 2-12 shows the current oscillations observed for a 3 mm hemisphere rotating at Ω = 400 rpm at a constant potential V_{os} = −0.198 V. The current-time plot (figure 2-12a)) displays uniform cycles repeated at a frequency of 17.0 Hz; the minimum current is lower than the maximum current by a factor of 6. An interesting feature of the current-time waveform is the noise or high-frequency oscillations in the increasing-current part of the overall cycles, near the minimum current. A clearer picture of these high-frequency oscillations is given in figure 2-12(b), which was obtained using a higher recording rate of the digital oscilloscope (more sensitive time scale), during the same experiment. The frequency of the faster oscillations is about 1700 Hz.

Figure 2-13 shows current oscillations for a 3 mm rotating disk electrode at Ω = 400 rpm. The ratio of the minimum to the maximum current is about 3.5 for this case. The values of the limiting current density and the overall oscillation frequency for the disk in this case are close to the values for the hemisphere in figure 2-12 (even though the applied potential V_{os} is quite different), and one may compare the observed oscillations for the two electrodes. The cycles in the oscillations for the disk electrode are also quite uniform. In the rising-current part of the waveform, a feature like a step change is observed for the disk, rather than the high-frequency oscillations observed for the hemisphere.

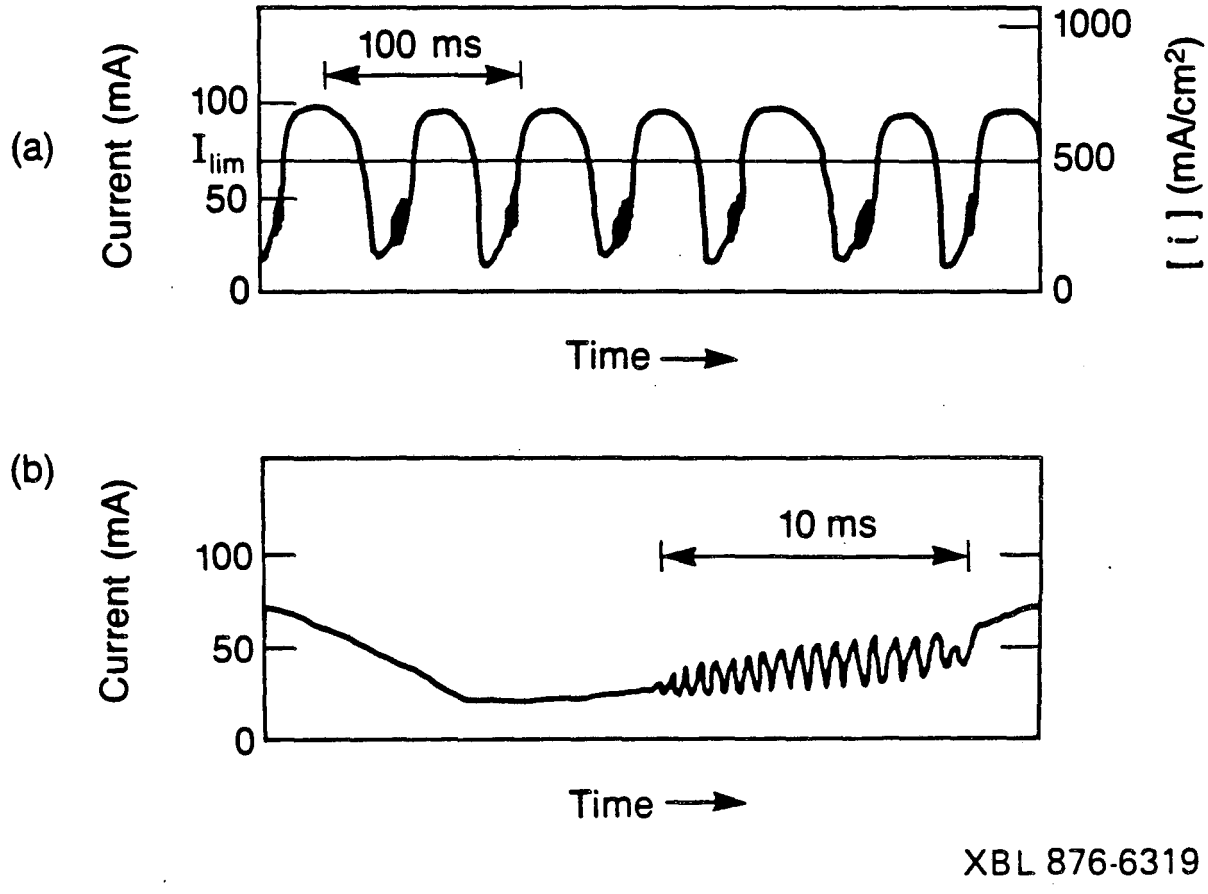

Figure 2-12. Sustained current oscillations observed for a rotating hemispherical electrode, d = 3 mm, Ω = 400 rpm, at a constant potential V_{os} = −0.198 V (indicated on the potentiodynamic sweep curve in figure 2-5).
(a) Overall waveform. Average frequency for 20 cycles: f = 17.0 Hz.
(b) High-frequency oscillations or noise, f = 1700 Hz. This current-time curve was recorded during the same experiment as curve (a), using a higher recording speed of the digital oscilloscope.

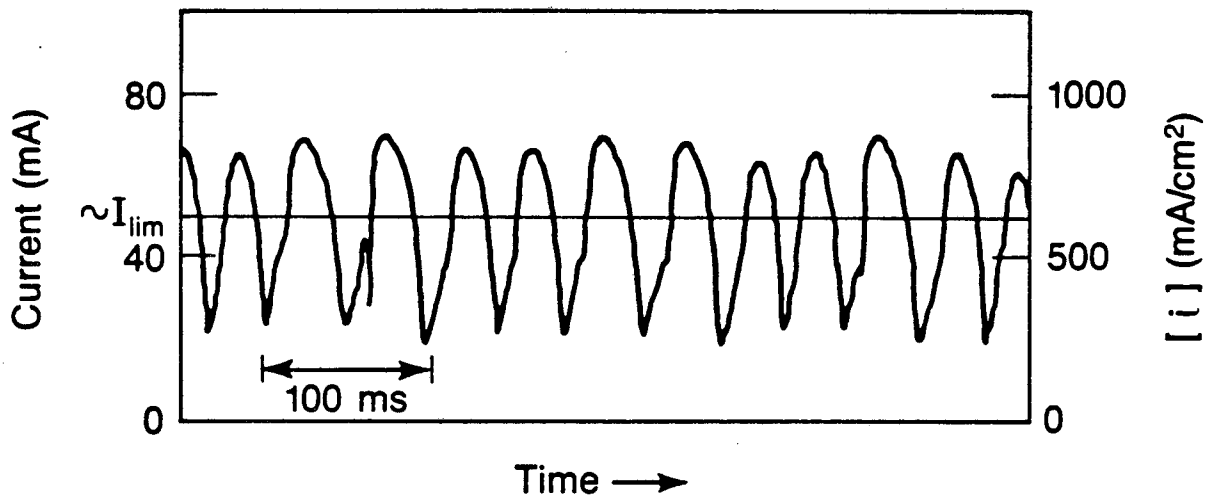

Figure 2-13. Sustained current oscillations observed for a rotating disk electrode. d = 3 mm, Ω = 400 rpm, V_{os} = −0.303 V. Average frequency (11 cycles) f = 23.5 Hz.

Comparing figures 2-12(a) and 2-13, we also notice that the oscillating current density reaches relatively much lower values and the ratio of the maximum to the minimum current is greater for the hemisphere than for the disk. If we assume that the lower current values during the oscillations are associated with a larger part of the electrode surface being passive, this observation may indicate that a larger fraction of the hemispherical electrode becomes passive compared to the disk electrode, and this may imply a more uniform potential distribution on the hemisphere in this range.† However this is not a well established conclusion. Comparing current waveforms for several hemispheres and several disk electrodes, we don't always see lower minimum currents for the hemispheres. Moreover it is not clear when one can directly compare results between hemispherical and disk electrodes; under what conditions of current, potential, electrode size, rotation speed, and oscillation frequency.

Russell (4, 3) has presented several oscillatory current-time curves with a variety of shapes for rotating disk electrodes, and we have observed several oscillatory current-time curves with a variety of shapes for rotating hemispherical electrodes. The oscillations for the hemispherical electrodes are generally similar to those for the disk electrodes. We present some of the observed oscillations for hemispherical electrodes in this section. The waveform in figure 2-12 for the smaller hemisphere at the lower rotation speed was the most uniform

† Using equation 1-13 for the hemisphere and the corresponding equation for the disk electrode, we get an estimate for the maximum potential difference $\Delta\Phi_o'$ of about 100 mV for both cases.

among the observed oscillatory curves for hemispheres.

Before presenting more results, we should note that in many of these experiments, particularly for larger hemispheres, the current kept oscillating for about ½ to 5 minutes and then abruptly decreased to near zero, *i.e.*, the electrode passivated, even though the potential was less than the expected V_{A-P} value. By contrast, we have observed the current for rotating disk electrodes oscillating continuously for more than 15 minutes (until we decided to terminate the experiment) without passivation. Therefore the current oscillations for rotating hemispherical electrodes did not appear to be as 'sustained' as for disk electrodes. Assuming that the current oscillations are due to part of the electrode making continual transitions between the active and passive states, this observed difference in the behavior of hemispherical and disk electrodes indicates that the entire hemispherical surface can passivate more readily than the entire disk surface, perhaps due to a more uniform potential distribution on the hemisphere in the range where current oscillations occur.

Another related phenomenon occurred during an experiment recording the current oscillations for an 8.4 mm hemispherical electrode at Ω = 400 rpm. While the potential was held at a value V_{os} where the current was oscillating, the current suddenly dropped to near zero, and a few moments later the current suddenly rose to a value near the limiting current value and then continued oscillating for some time. This experiment seems to illustrate a bifurcation point where two stable steady states exist, the active state and the passive state, and the system can

be at either of the two states.

The current oscillations for a 4.4 mm diameter hemisphere at different potentials and rotation speeds are illustrated in figure 2-14. The current-time curves in figures 2-14(a) and 2-14(b) were recorded during the same experiment at different potentials within the oscillatory region of the limiting current plateau; they have different shapes and not much different frequencies. A weak dependence of the frequency of oscillations on the potential was also reported by Russell and Newman (3) for a hemispherical electrode. At a higher rotation speed (figure 2-14(c)), the current cycles became more nonuniform and irregular, in a way that it was difficult to assign a frequency to the oscillations. Significant instabilities or noise appeared near the minimum current in the waveforms at both rotation speeds.

Comparing figure 2-14(b) with figure 2-12, we see more high-frequency noise near the minimum current for the bigger hemisphere. Russell and Newman (3, 4) often observed noise near the position of minimum oscillation current for rotating disk electrodes, and they attributed the noise to rapid transitions between the active and passive states, at some parts of the electrode. Increasing the disk electrode size or increasing the rotation speed appeared to promote the occurrence of this noise in their results.

The current oscillations for a bigger hemispherical electrode at three rotation speeds are illustrated in figures 2-15 and 2-16. No significant noise or high-frequency oscillations were observed in these oscillations.

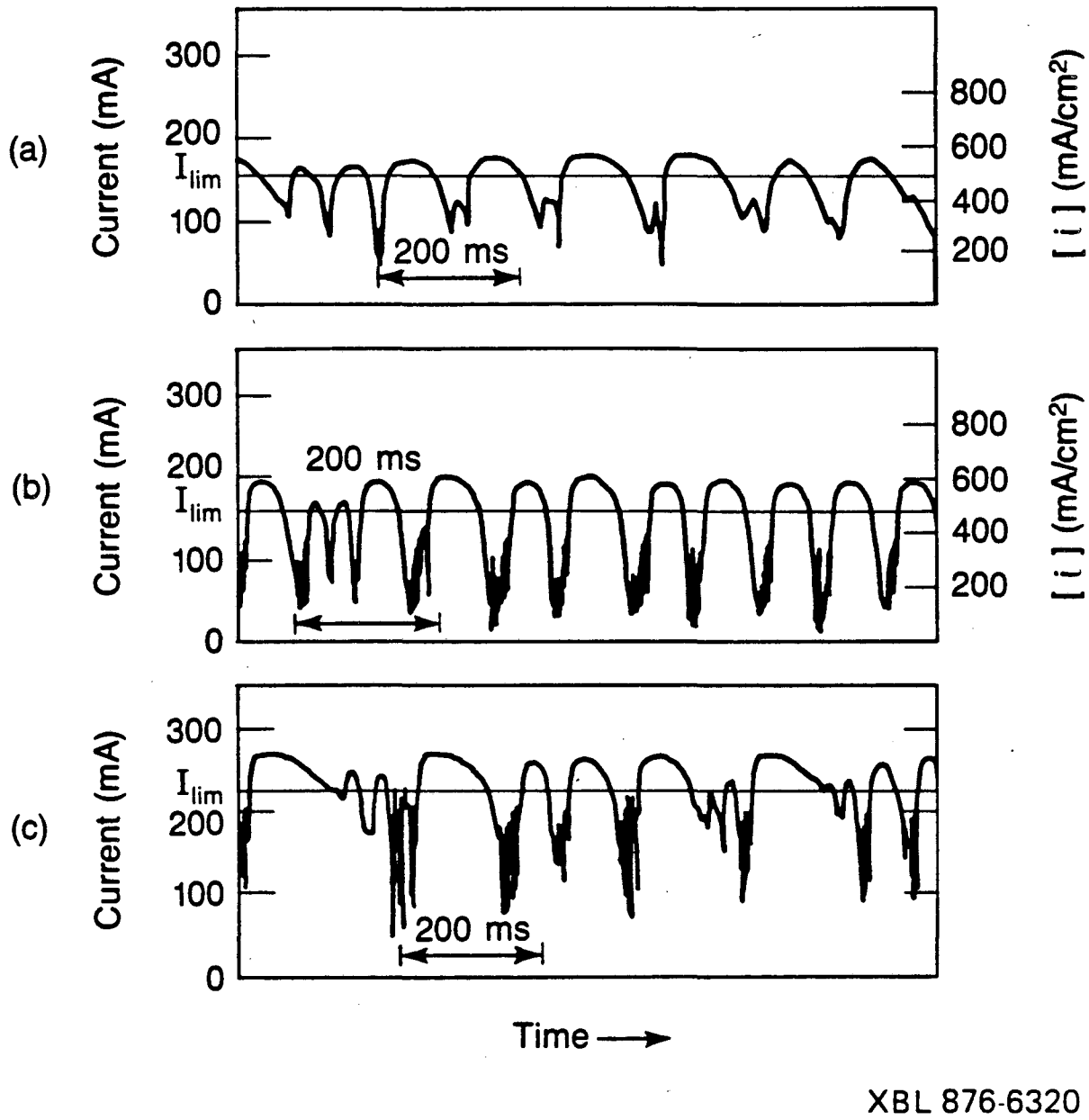

Figure 2-14. Current oscillations observed for a 4.4 mm hemispherical electrode.
(a) Ω = 400 rpm, $V_{os}^{(a)}$ = −0.197 V (marked in figure 2-6). f = 8 Hz.
(b) Ω = 400 rpm, $V_{os}^{(b)}$ = −0.105 V (marked in figure 2-6). f = 11 Hz.
(c) Ω = 900 rpm, V_{os} = 0.174 V. f ≈ 8 Hz.

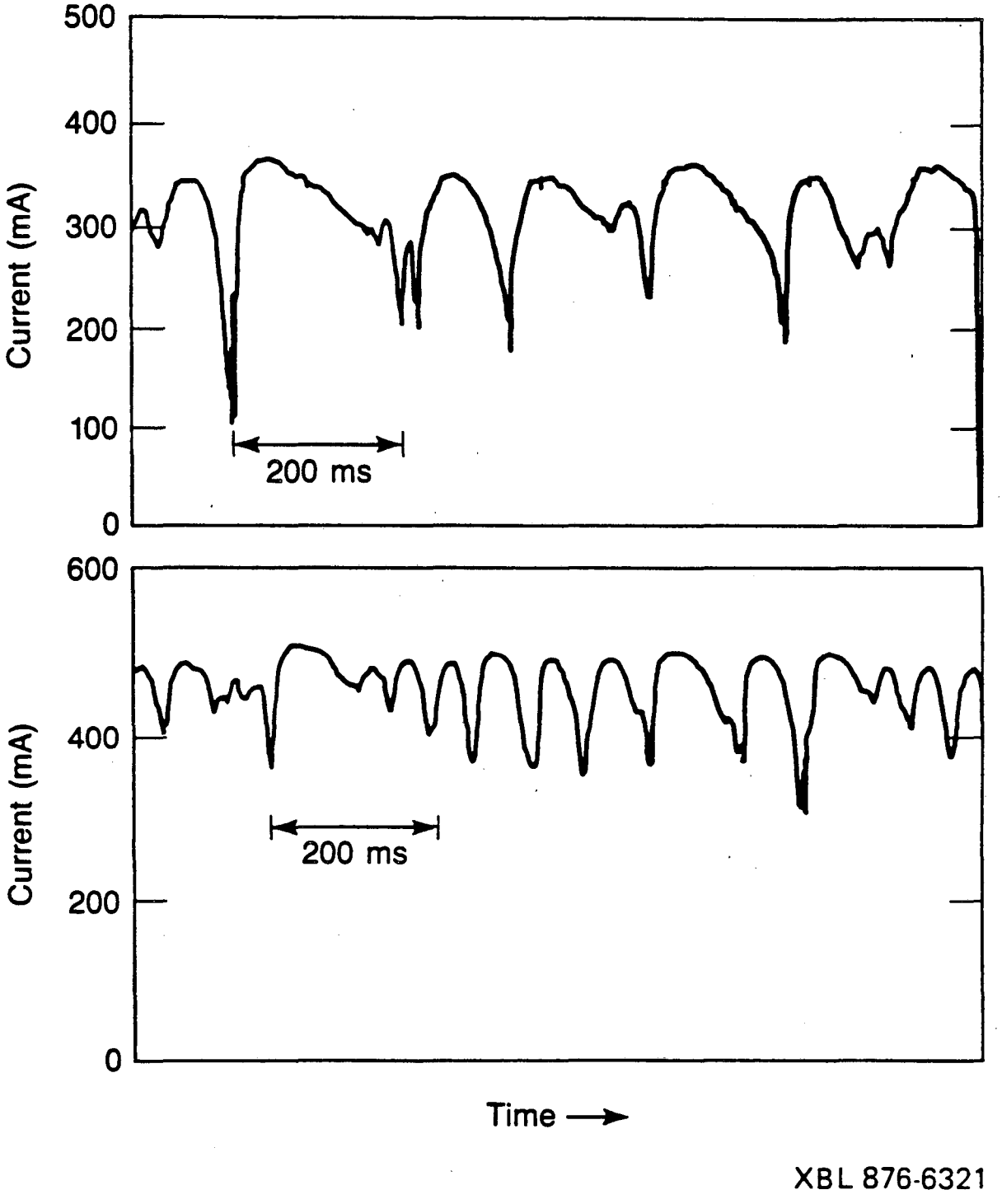

Figure 2-15. Current oscillations observed for a 6.5 mm hemispherical electrode. (a) Ω = 400 rpm, V_{os} = −0.150 V. f ≈ 7 Hz. (b) Ω = 900 rpm, V_{os} = 0.423 V. f ≈ 14 Hz.

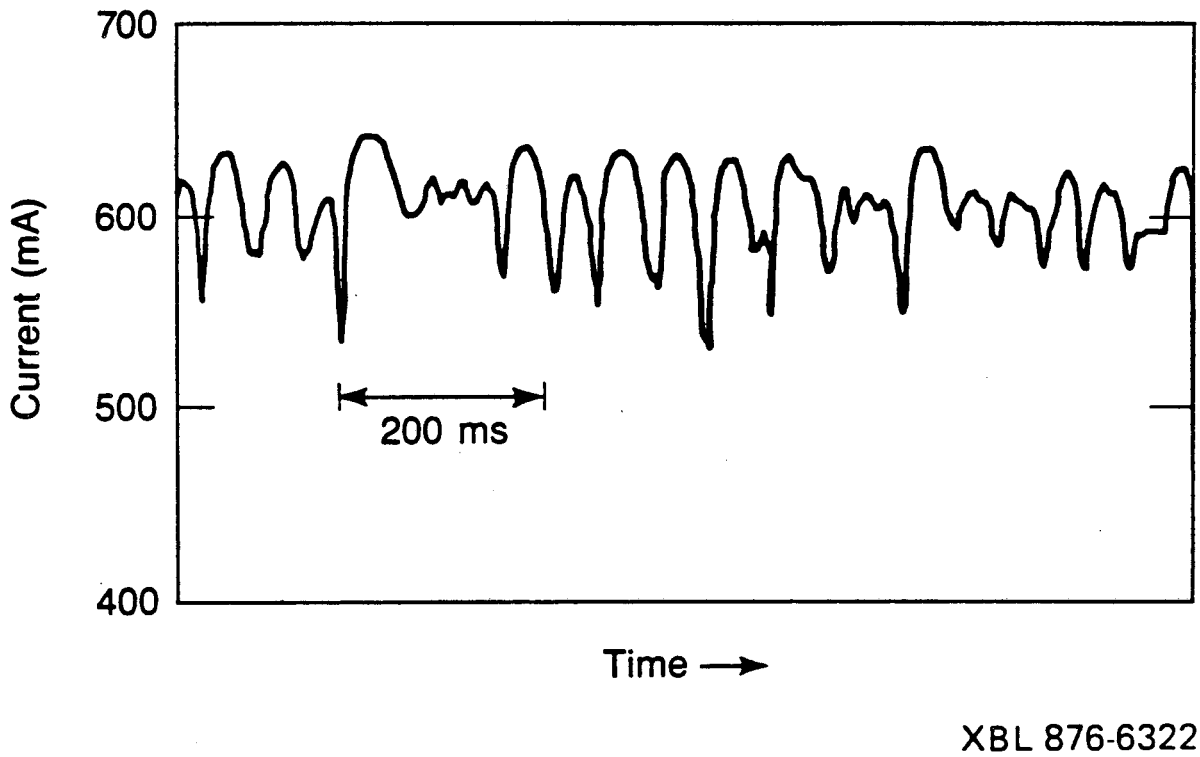

Figure 2-16. Current oscillations observed for a 6.5 mm hemispherical electrode. Ω = 1600 rpm, V_{os} = 0.58 V. f ≈ 18 Hz. Spiral markings were seen on the electrode surface at the end of the experiment recording these oscillations.

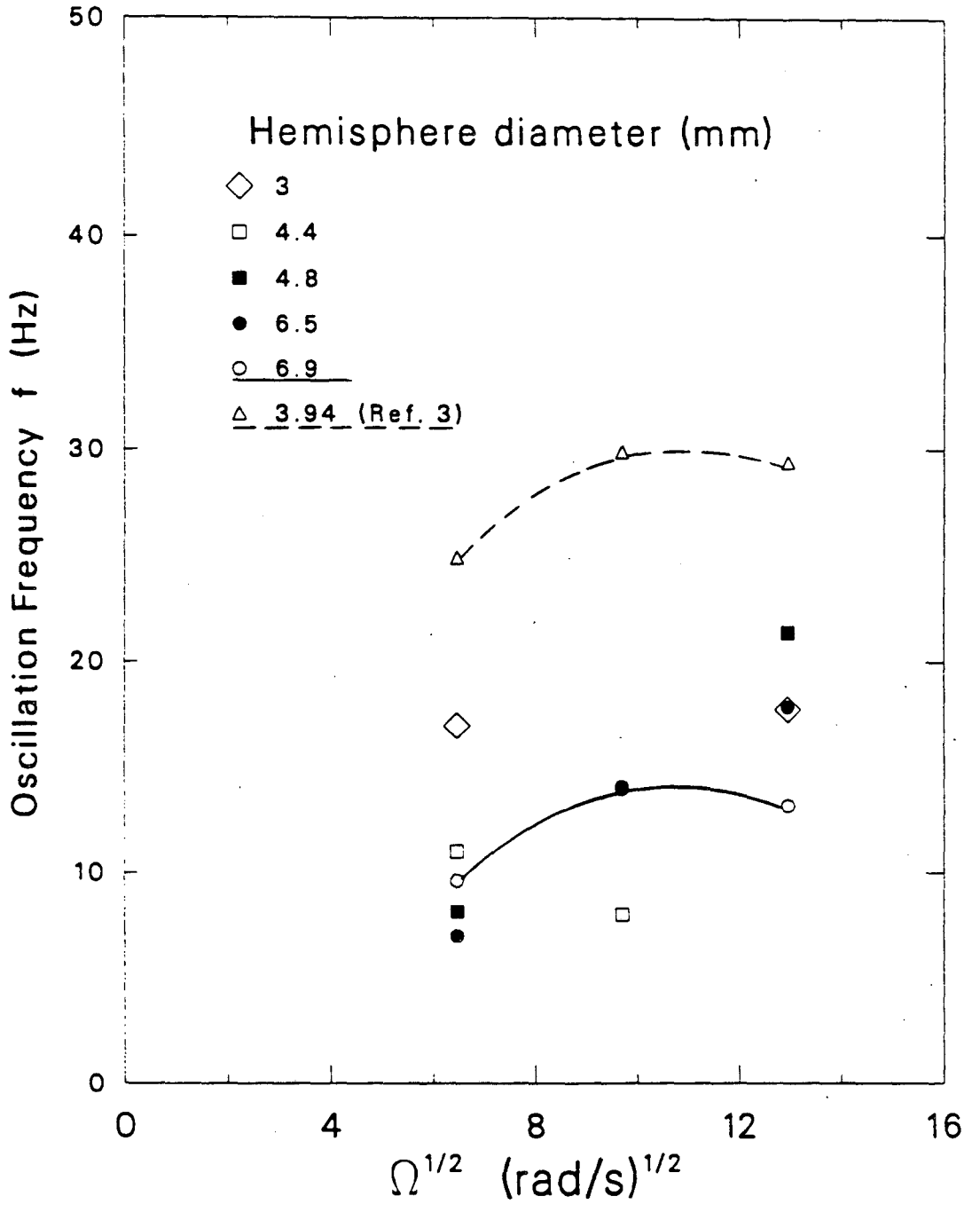

XBL 877-3136

Figure 2-17. Frequency of oscillations for several rotating hemispherical electrodes as a function of the electrode rotation speed.

The frequency of oscillations for rotating hemispherical electrodes is plotted *vs.* the square root of the electrode rotation speed, in figure 2-17. For a hemispherical electrode of a given diameter, the oscillation frequency is a relatively weak function of the rotation speed; generally, the frequency increases with increasing rotation speed. The frequency of oscillations for rotating disk electrodes was found to be a linear function of the rotation speed (11, 3), and it is not clear why the frequency for hemispherical electrodes is a weaker function of the rotation speed. For a given rotation speed, the oscillation frequency appears to vary significantly with the hemisphere diameter, but a systematic relationship between oscillation frequency and hemispherical electrode size is not evident in figure 2-17. For rotating disk electrodes, the oscillation frequency was found to be nearly independent of electrode size (3).

2.7. Conclusions

Overall the anodic polarization curves for rotating hemispherical iron electrodes are similar to those for disk electrodes. For both electrode geometries, the polarization curves obtained using a normal potentiostat exhibit discontinuous active-passive transitions and a hysteresis, whereas the polarization curves obtained using a polarization control device with a positive-slope load line are Z-shaped displaying a limiting current plateau and a continuous and reversible passivation curve. Both electrodes also display current oscillations at constant potential within certain potential ranges on the limiting current pla-

teau.

Some observed differences between hemispherical and disk electrodes are:

(i) The slope of the passivation curve for disk electrodes was found to increase with decreasing electrode diameter (2), but no monotonic relationship between the slope of the passivation curve and the hemisphere diameter is evident.

(ii) The frequency of current oscillations for hemispherical electrodes is a weak function of the rotation speed compared with that for disk electrodes.

(iii) The frequency of current oscillations at a given electrode rotation speed appears to vary more widely with the hemisphere electrode diameter than with the disk diameter.

(iv) Some more subtle differences are observed in the waveform shape and sustenance of current oscillations between hemispherical and disk electrodes as well as between hemispheres of different diameters.

Qualitatively the differences between hemispherical and disk electrodes may be attributed to differences between the current, potential, and concentration distributions of the two electrode geometries. The primary current distribution seems to play an important role in the system. However several other factors are also present, and a detailed quantitative analysis would be required to elucidate the system behavior conclusively.

References for Chapter 2

1. I. Epelboin, C. Gabrielli, M. Keddam, J.-C. Lestrade, and H. Takenouti, "Passivation of Iron in Sulfuric Acid Medium," *Journal of the Electrochemical Society*, **119**, 1632-1637 (1972).

2. Philip P. Russell and John Newman, "Experimental Determination of the Passive-Active Transition for Iron in 1M Sulfuric Acid," *Journal of the Electrochemical Society*, **130**, 547-553 (1983).

3. Philip P. Russell and John Newman, "Current Oscillations Observed within the Limiting Current Plateau for Iron in Sulfuric Acid," *Journal of the Electrochemical Society*, **133**, 2093-2097 (1986).

4. Philip P. Russell, *Corrosion of Iron: The Active - Passive Transition and Sustained Electrochemical Oscillations*, Ph. D. Dissertation, University of California, Berkeley, CA (1984).

5. I. Epelboin and M. Keddam, "Kinetics of Formation of Primary and Secondary Passivity in Sulfuric Aqueous Media," *Electrochimica Acta*, **17**, 177-186 (1972).

6. Theodore R. Beck, "Formation of Salt Films during Passivation of Iron," *Journal of the Electrochemical Society*, **129**, 2412-2418 (1982).

7. I. Epelboin, C. Gabrielli, M. Keddam, and H. Takenouti, "The Study of the Passivation Process by the Electrode Impedance Analysis," *Comprehensive Treatise of Electrochemistry*, Vol. 4, chapter 3, J. O'M. Bockris, B. E. Conway, E. Yeager, and R. E. White, Editors,

Plenum Press, New York (1981).

8. Kemal Nişancioğlu and John Newman, "Current Distribution on a Rotating Sphere below the Limiting Current," *Journal of the Electrochemical Society*, **121**, 241-246 (1974).

9. John Newman, "Mass Transfer to a Rotating Sphere at High Schmidt Numbers," *Journal of the Electrochemical Society*, **119**, 69-71 (1972).

10. Philip Russell and John Newman, "Anodic Dissolution of Iron in Acidic Sulfate Electrolytes, II. Mathematical model of Current Oscillations Observed under Potentiostatic Conditions," *Journal of the Electrochemical Society*, **134**, submitted (1987).

11. J. J. Podestá, R. C. V. Piatti, and A. J. Arvia, "The Potentiostatic Current Oscillations at Iron/Sulfuric Acid Solution Interfaces," *Journal of the Electrochemical Society*, **126**, 1363-1367 (1979).

CHAPTER 3

AC Impedance: Experimental Results

3.1. Introduction

Chapter 2 has shown the steady-state behavior of the iron-sulfuric acid system. The transient behavior of the system is next considered. This chapter gives the results of alternating current impedance measurements. The experimental apparatus and procedure are described, and the results are presented.

The impedance was measured at several points along the polarization curve as illustrated in figure 3-1. Several rotating hemispherical as well as disk electrodes were used in these experiments. The results for the hemispheres are compared with the results for the disks in order to elucidate the effect of a nonuniform current distribution on impedance measurements. The results obtained here are also qualitatively compared with those obtained by other investigators.

The data are presented first as complex-plane plots of the impedance. We chose this form of presentation mainly for esthetic reasons. Bode plots are also given for selected experiments.

Four experiments, labeled A, B, C, and D, are analyzed using the Kramers-Kronig relations, in chapter 4.

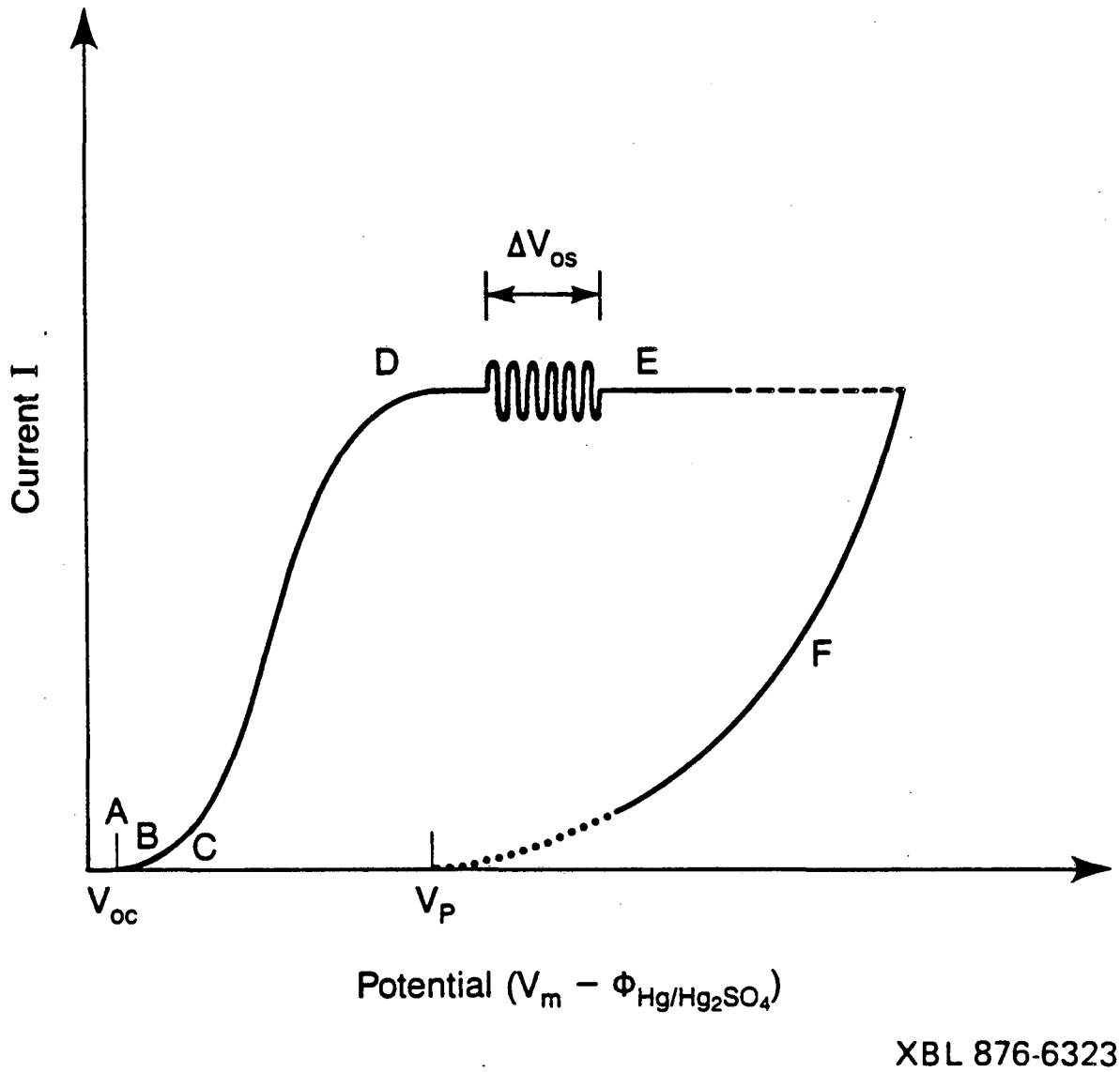

Figure 3-1. Diagram of the anodic polarization curve. A, B, C, D, E, and F indicate the points where the impedance was measured.

3.2. Experimental Apparatus and Procedure

Three hemispherical electrodes with different diameters were used in the impedance experiments. The configuration and surface preparation of the hemispherical electrodes were described in section 2.3. In addition, three rotating disk electrodes, each with a different diameter, were used. These disk electrodes were fabricated by Russell (1) in this laboratory. The surface preparation procedure for the disks was the same as for the hemispheres, except for the use of a polishing wheel (Ecomet III, Buehler, Ltd.) for the disks. The polishing wheel has a flat surface and therefore cannot be used for hemispherical electrodes.

The experimental cell arrangement was the same as for the steady-state experiments (figure 2-2). The potentiostat, the sweep generator, and the oscilloscope were also used in the same way. The impedance experiments at the open-circuit potential were carried out under galvanostatic control and at all other potentials under potentiostatic control, which is generally preferable for metal-dissolution reactions. The measuring resistor of the potentiostat was set at a value close to that of the system under study (10 or 100 Ω). This choice for the measuring resistor value allows a more accurate measurement (2). The pump of the constant temperature bath was turned off during the impedance measurement to avoid noise and distortions of the signals. The temperature still remained at 25 ± 0.15° C.

The main instrument performing the impedance measurement was a Solartron 1254 frequency response analyser (FRA). The principle of measurement is described in section 1.6.2. The small-amplitude

sinusoidal signal generated by the FRA was superimposed on the steady-state potentiostat input to control the polarization of the electrochemical cell. The resulting voltage between the working and reference electrodes and the current were measured simultaneously by the FRA.

The DC (steady-state) component of the voltage and current signals was approximately subtracted from each of the signals before they reached the FRA to increase the sensitivity of the measurement. A device fabricated by the LBL Electronics Shop was used for the subtraction, and triaxial cables were used to transmit the voltage and current signals from the potentiostat to the input channels of the FRA. The input channels were set at the direct (DC) coupling configuration, which minimizes phase shift, particularly at low frequencies. In some experiments, the DC component of the signals was not subtracted, and the FRA input channels were set at the AC coupling configuration to block the DC component.

Figure 3-2 gives a schematic diagram of the experimental apparatus. The measured impedance data were temporarily stored in the memory file of the FRA and then stored on data cartridges using a Hewlett Packard 9825 desktop computer. The data were subsequently transferred to a large-scale computer for further treatment.

Some important aspects of the experimental impedance measurement, introduced in section 1.6.2, are now discussed more specifically.

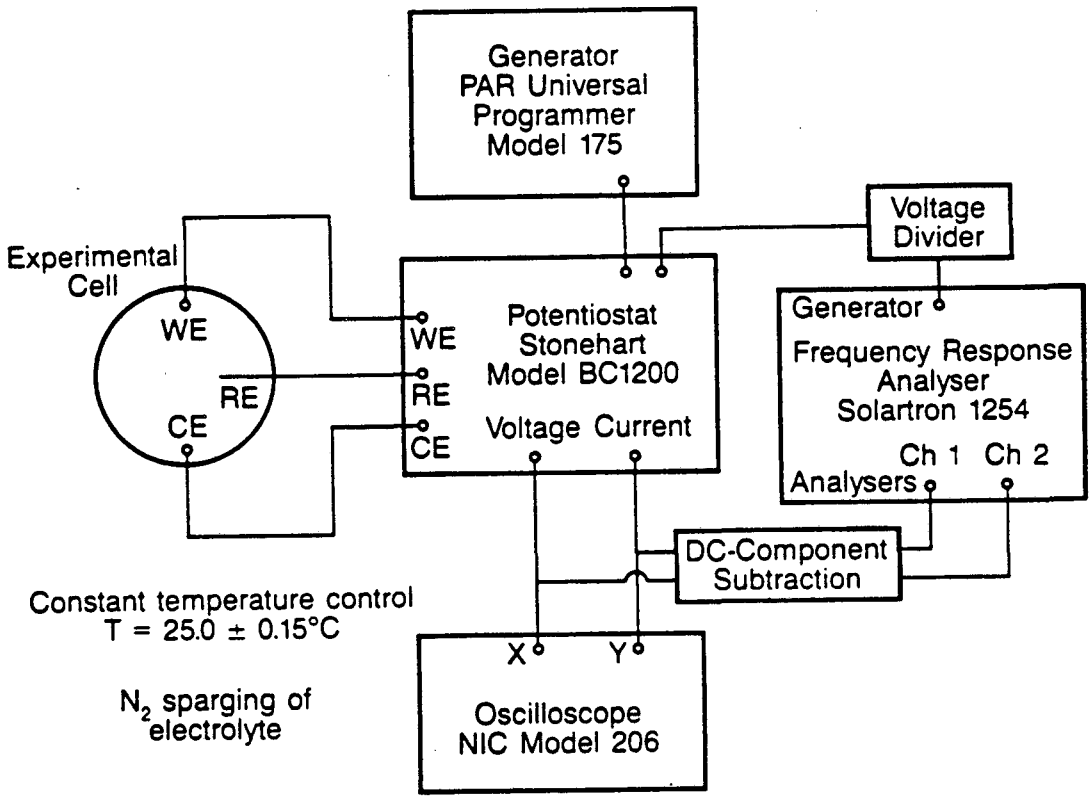

XBL 876-6326

Figure 3-2. Schematic diagram of the experimental apparatus.

Linearity.

Perturbing signals of small amplitude are required to satisfy the linearity condition. The Solartron FRA can generate a sinusoidal signal of amplitude between 10 mV and 10.23 V. Since digital generators have a low signal-to-noise ratio for small amplitude signals, it is better to use a bigger amplitude signal from the generator and reduce the signal by another device, *e.g.*, it is better to use a 10 V signal reduced by a factor of 1000 rather than a 10 mV signal directly (3). In this work, we used a voltage-dividing device consisting of a parallel combination of high-precision resistors, which reduced the generator signal by a factor of 1000.

In order to determine the appropriate perturbation amplitude for the iron-sulfuric acid system, we first did some preliminary experiments measuring the impedance at a particular frequency using several different amplitudes for some polarization points. In these experiments, the measured impedance did not vary with the amplitude for amplitudes of 1 to 5 mV rms. A strict linearity check would require a very large number of preliminary experiments at several frequencies for each polarization point and for each electrode. We carried out a small number of preliminary experiments for a linearity check and finally decided to use perturbing signals of 2 to 5 mV rms amplitude. Using smaller signals would probably result in more significant noise problems.

Frequency Range.

The Solartron FRA can provide a sinusoidal signal in the frequency range 10 μHz to 65.5 kHz and can automatically perform impedance measurements sweeping the frequency from a chosen minimum to a chosen maximum value, or *vice versa*, in a number of frequency steps. In these experiments, five frequency steps per decade were typically used. Increasing as well as decreasing frequency sweeps were carried out for some experiments, and this provided a good check for the accuracy and reproducibility of the data.

The maximum frequency was usually set at 65 kHz, and the minimum frequency was set at 0.01 to 0.05 Hz for low-current experiments and at 0.10 to 0.50 Hz for high-current experiments, where the electrode surface changed dramatically with time. The maximum available experimental frequency was often not sufficiently high to give the infinite-frequency limit of the electrochemical impedance, and the minimum experimental frequency used was often not sufficiently low to give the zero-frequency limit of the impedance.

The measurement time was 2 to 5 minutes for the frequency range 0.100 Hz to 65 kHz and 15 to 20 minutes for the range 0.010 Hz to 65 kHz. However additional time was required for setting up the experiment and reaching a steady-state. Moreover, two or more successive frequency sweeps were carried out for some experiments. Thus the time for an experiment, from the moment the electrode was immersed in the electrolyte until the end of the impedance measurement, varied from 10 minutes to 2 hours.

Noise. The experimental arrangement was carefully designed to reduce noise as far as possible. The "auto-integration" feature of the Solartron FRA was used in order to obtain accurate measurements, even in the presence of noise, within a reasonable time. With auto-integration, the analyser continues the measurement of the voltage and current signals at each frequency until the measured results become self-consistent, or until a specified maximum measurement time is reached. The criterion for consistent measurements can be set to either < 1% error or < 10% error, with 90% confidence, and if the criterion is not met, the instrument reports an error message indicating noisy data.

In this manner, it was possible to obtain impedance data with a precision generally within 1% at low currents and within 10% at high currents. In some cases, particularly at very high current densities, noise could not be eliminated, and the data had poor precision. A precision within 1% for electrochemical impedance measurements, with currently available instrumentation and techniques, is considered good. For instance, the typical precision of several run averages using a multiple-frequency perturbation and a fast Fourier transform analysis was found to be 0.5 to 1% for copper corrosion (4).

3.3. Corrosion at $\bar{I} = 0$ (Open-Circuit Potential)

3.3.1. Experimental

The impedance measurements at the open-circuit corrosion potential were carried out under galvanostatic control. The open-circuit potential for the iron-sulfuric acid system is not very stable and can change

by a few mV during an experiment. Galvanostatic control was therefore chosen to ensure that the steady-state current was always zero, corresponding to open-circuit conditions. The applied current perturbation had an amplitude of 20 μA (unless otherwise noted), and the DC component of the potential was subtracted from the potential signal as described in section 3.2 (unless otherwise noted).

Three or four successive frequency sweeps were performed for each of the open-circuit experiments. The impedance measurement time was 10 to 15 minutes for a sweep with a minimum frequency of 20 mHz and ~20 minutes for a sweep with a minimum frequency of 10 mHz. The impedance measurement started ~10 minutes after the electrode was immersed in the electrolyte, and additional time was required for adjusting settings on the instrumentation before each frequency sweep. Thus the duration of an experiment was 1 to 2 hours.

During the open-circuit experiments for the hemispherical electrodes at 900 rpm, a small ring-shaped gas bubble (evolved H_2) was sometimes observed around the equator of the electrode. This bubble was removed by momentarily increasing the rotation speed between frequency sweeps.

The impedance data changed significantly during the first 30 to 50 minutes of measurement and then became reasonably constant. However the data obtained from two consecutive frequency sweeps in an experiment were never identical. At the end of the experiment, the electrode surface appeared a little different from the beginning of the experiment. The electrode surface still appeared smooth, but somewhat cloudy, and a

very mild dissolution texture could be seen. Thus we decided that it was not meaningful for a fundamental analysis to carry the measurements any further.

Keddam *et al.* (5) performed impedance measurements for iron disks in 1 M H_2SO_4 near the open-circuit potential. They observed that, at a potential 60 mV cathodic to the open-circuit potential, a steady-state current was reached only after a 20-hour polarization, and they indicate that this slow approach to a steady state is due to hydrogen adsorption, which is still significant at the open-circuit potential. This process may explain why the iron-sulfuric acid system reaches a steady state slowly at the open-circuit potential.

Mansfeld *et al.* (2, figure 15) report impedance data for iron in weakly acidic sulfate solution, taken over a 24-hour period. They show that the impedance measured after 0.3 hr of polarization was much larger than the impedance after 2 hr and the impedance after 5 hr of polarization was approximately the same as that after 2 hr; the impedance data after 22 hr were much different. Those data illustrate how corrosion systems can change with time. In contrast, Smyrl and Stephenson (6) measured the impedance of copper in 0.1 N HCl (a system with a relatively small corrosion rate), and they report that the measurements after 10 and 30 minutes were identical to the 2-minute measurements.

Practical determinations of corrosion rates from AC impedance data would probably require impedance measurements over longer periods of time than those used here. However determining the corrosion rate was not the focus of this work.

3.3.2. Results

The impedance data from several experiments for a hemisphere with diameter d = 4.0 mm at a rotation speed Ω = 900 rpm are shown in figures 3-3 through 3-5.

Figure 3-3 is a complex-plane plot of four sets of impedance data from an experiment which lasted 75 minutes. Notice how the measured impedance changes with time. Bode plots of the same data are shown in figures 3-4. The Bode plots give a clearer picture of how the impedance at each frequency varies.

Figure 3-5 shows the impedance measured in four different experiments under similar conditions. Each set of data was obtained about one hour after the immersion of the electrode, and thus this figure illustrates the reproducibility of the data. The hemisphere diameter was slightly different for each experiment, and expressing the impedance in units of ohm$\cdot$cm^2 allows a direct comparison of the data from each experiment. Notice that the data from these experiments agree fairly well. The data from the fourth experiment seem to deviate more than the other data. This deviation may be due to poor reproducibility of the data, or due to the larger perturbation amplitude for the fourth experiment, which may have violated the linearity condition.

Figure 3-6 shows the impedance of a bigger hemisphere (d = 8.2 mm) at two different rotation speeds, and thus indicates the significance of mass transfer effects. The impedance appears to be smaller at 1600 rpm than at 900 rpm, especially at low perturbation frequencies, indicating an enhancement of the current due to increased mass transfer rate. At

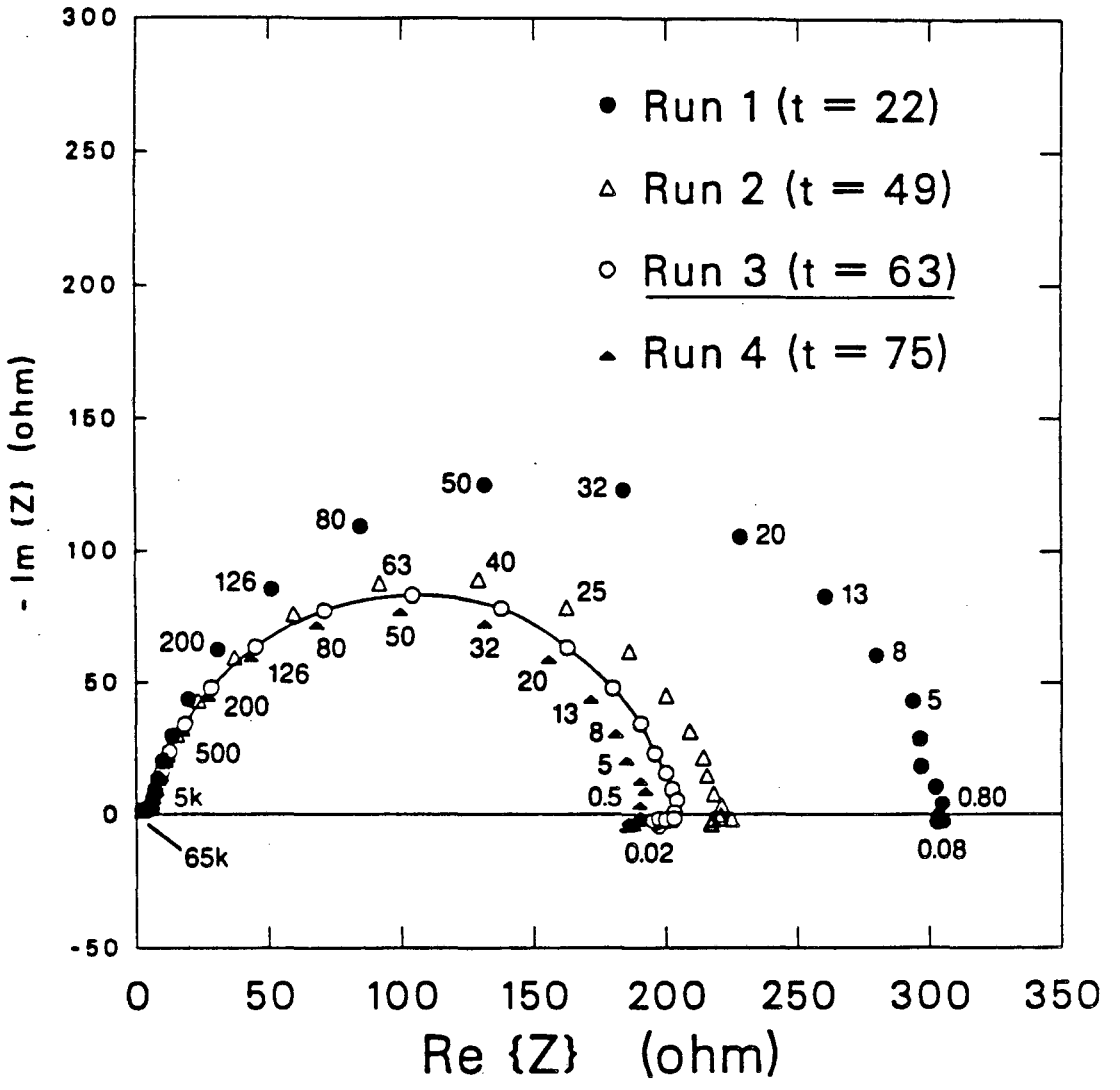

XBL 877-3138

Figure 3-3. Complex-plane plot of the impedance of a rotating hemispherical electrode (d = 3.97 mm, Ω = 900 rpm) at the open-circuit (corrosion) potential. Increasing frequency sweeps. The parameter is frequency in Hz. t is the time at the end of the impedance measurement in minutes after the moment the electrode was immersed in the electrolyte. (Run 3 is labeled experiment A.)

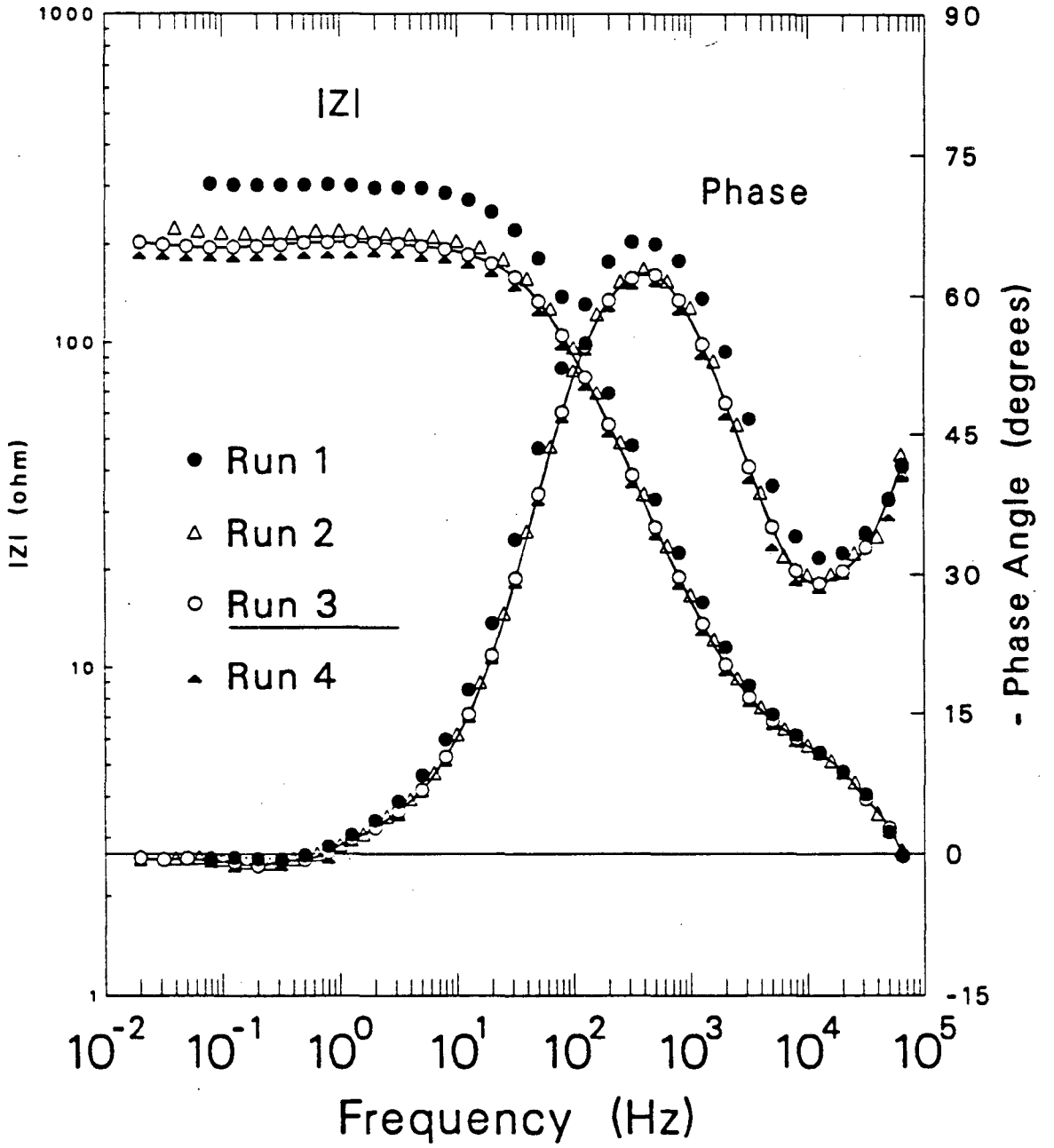

XBL 877-3132

Figure 3-4. Bode plot of the data shown in the complex plane in figure 3-3.

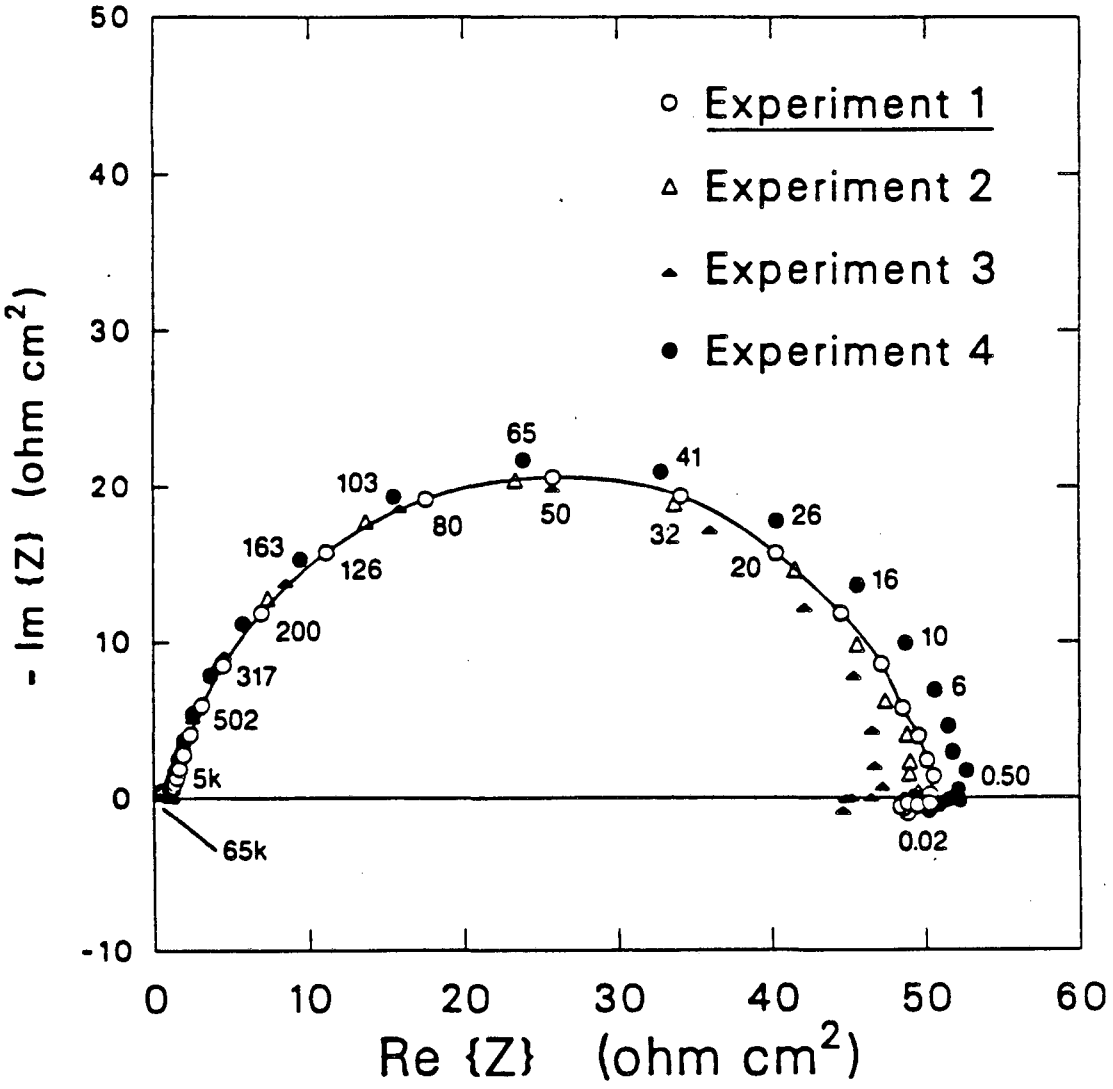

XBL 877-3158

Figure 3-5. The impedance of a rotating hemisphere (d = 4.0 mm, Ω = 900 rpm) measured in four different experiments under similar conditions.
Experiment 1: run 3 in figure 3-3 (increasing frequency sweep).
Experiment 2: increasing frequency sweep.
Experiment 3: decreasing frequency sweep; the DC component of the potential signal was not subtracted during the measurement.
Experiment 4: decreasing frequency sweep; $|\Delta I|$ = 25 μA rms.

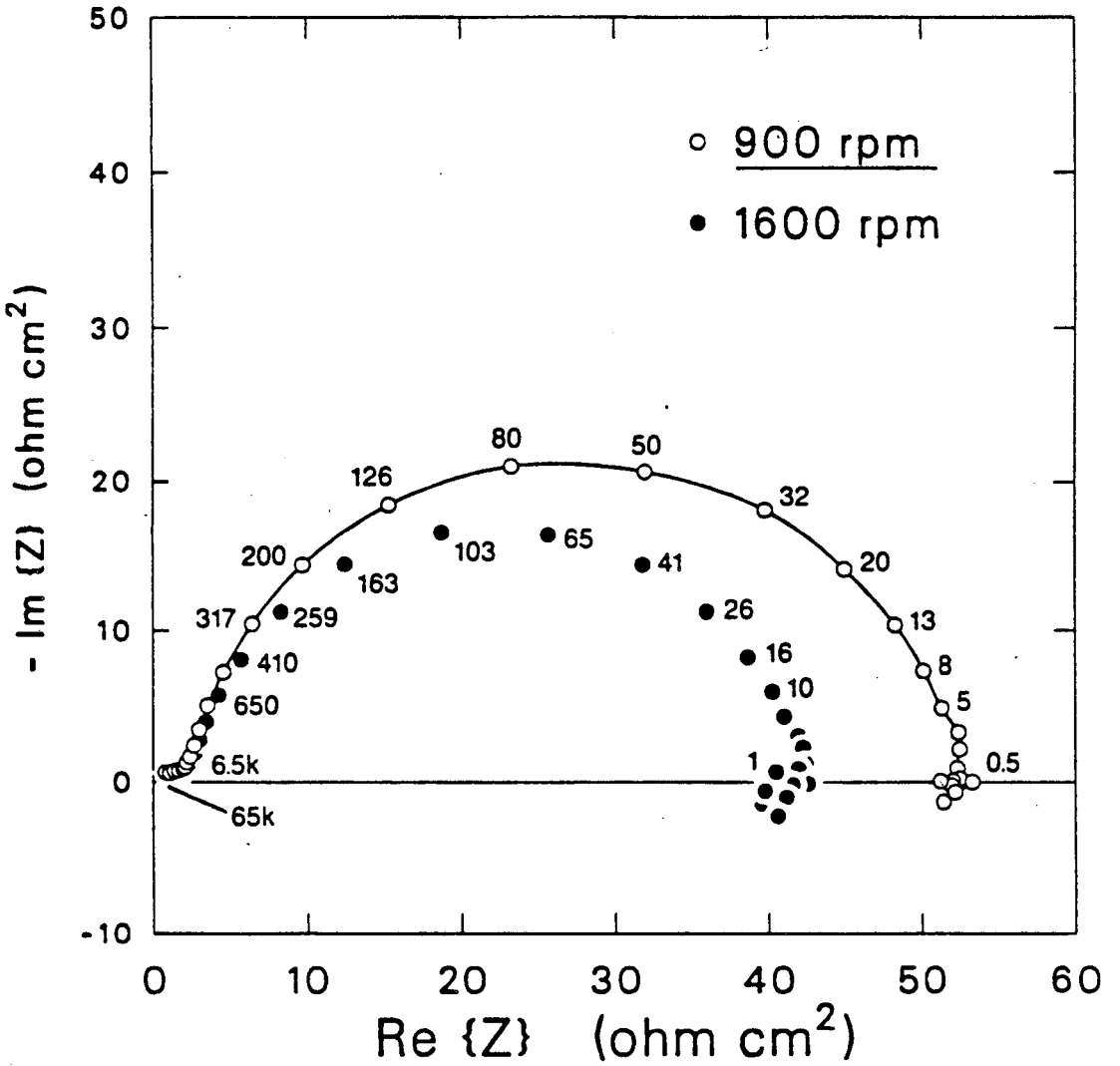

XBL 877-3157

Figure 3-6. The impedance of a rotating hemisphere (d = 8.2 mm) at two different rotation speeds (two separate experiments).
1600 rpm — Decreasing frequency sweep.
900 rpm — Increasing frequency sweep.

high perturbation frequencies the curves for the two rotation speeds coincide. However one cannot draw any definitive conclusion about the significance of mass transfer effects for iron at the open-circuit potential from these data, since a completely steady state was not reached in these experiments. The polarization curves presented in chapter 2 show no increase in the current with increasing rotation speed, until potentials more than ~0.5 Volt anodic to the open-circuit potential are reached. Also, Keddam *et al.* (5) state that the iron dissolution current is free of mass transfer effects at low current densities.

Two interesting features of these impedance diagrams for the hemispherical electrodes are the low-frequency data having negative imaginary parts and the small capacitive loop at high frequencies (above 10 kHz), in addition to the big capacitive loop which is generally assumed to be due to the double-layer capacity. The low-frequency data were noisy, and a well-defined inductive loop was never obtained in these experiments. Thus one cannot determine from these data alone whether a low-frequency inductive loop exists for the iron hemispheres at the open-circuit potential, or the obtained data contain random errors.[†] Similarly, considering the possibility of experimental artifacts and the presence of noise in the data at high frequencies, one cannot determine with certainty from these data whether the high-frequency capacitive loop is a real characteristic of the electrochemical system.

[†] See the Kramers-Kronig test for a set of these data, in chapter 4.

Figure 3-7 illustrates the uncertainty at high frequencies. This figure is a Bode plot of the phase angle measured in two experiments. The main difference in the conditions for these two experiments was that the DC component of the voltage signal was not subtracted before reaching the FRA in experiment 3 and was subtracted in experiment 4. The direction of the frequency sweep was downward in both experiments. The two experiments disagree significantly at high frequencies: the data from experiment 4 exhibit two capacitive time constants, whereas the data from experiment 3 exhibit only one capacitive time constant.

The data from all the other experiments with hemispherical electrodes presented in this section show two capacitive time constants. The data from a few other experiments, not presented here, where the DC component was not subtracted show only one capacitive time constant.

Consider now some results obtained for a rotating disk electrode ($d = 3.2$ mm, $\Omega = 1600$ rpm). Figure 3-8 shows the data from two experiments in the complex plane, and figure 3-9 shows Bode plots of the data. Notice again how the measured impedance changes with time. Notice also that the phase angle of the highest-frequency points is still away from zero, which means that the ohmic limit of the impedance was not reached in these experiments.

The shape of the complex impedance diagram as well as the values of the capacitive and inductive time constants agree with the results of Keddam *et al.* (5, Fig. 2) for a rotating disk ($d = 3$ mm, $\Omega = 1600$ rpm) at the open-circuit potential. However the magnitude of the impedance measured in this work is about half of that measured by Keddam *et al.*

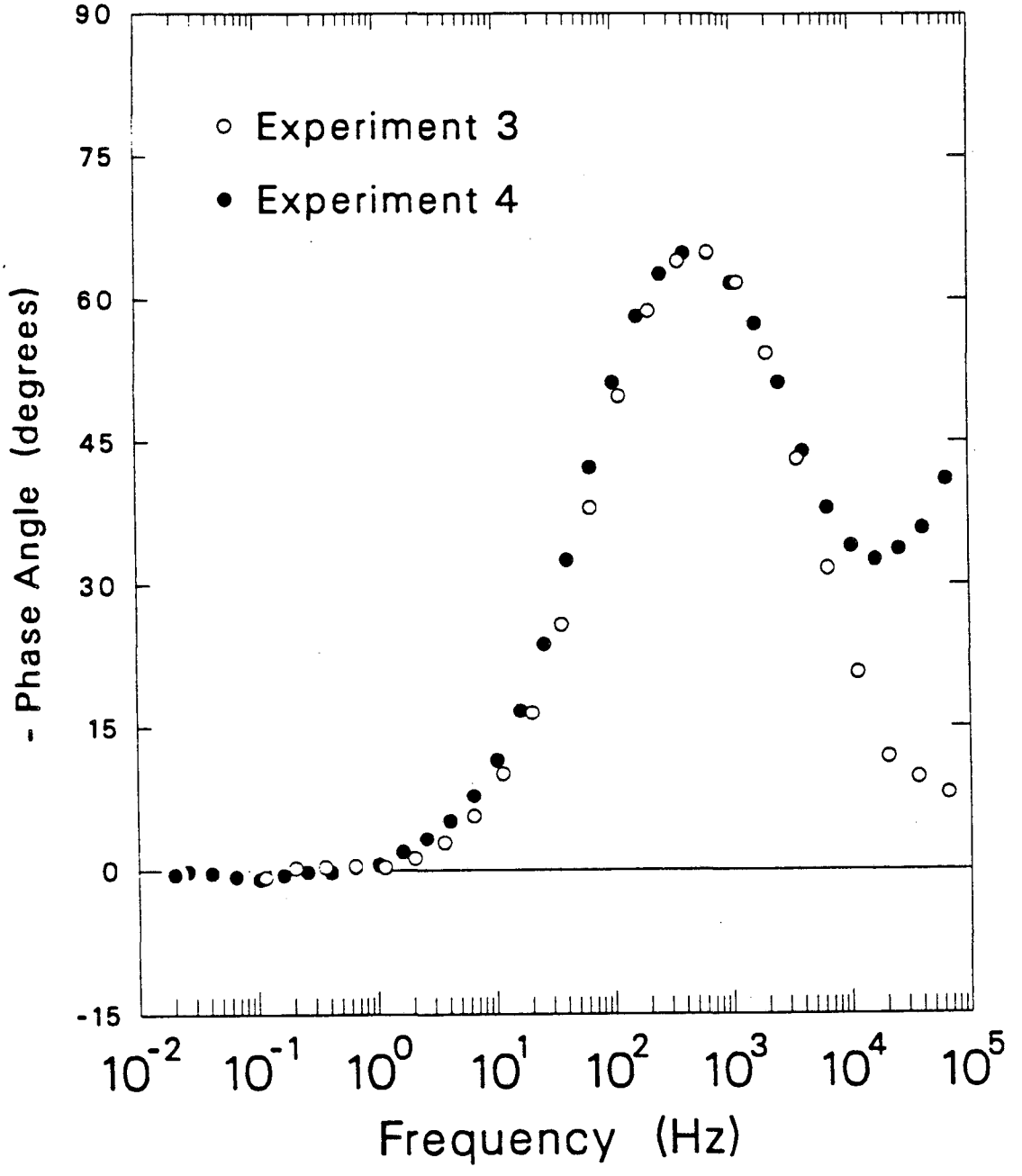

XBL 877-3133

Figure 3-7. Bode plot (phase angle) for a rotating hemispherical electrode (d = 4.0 mm, Ω = 900 rpm), illustrating the uncertainty at high frequencies. These data are also plotted in the complex impedance plane in figure 3-5, experiments 3 and 4.

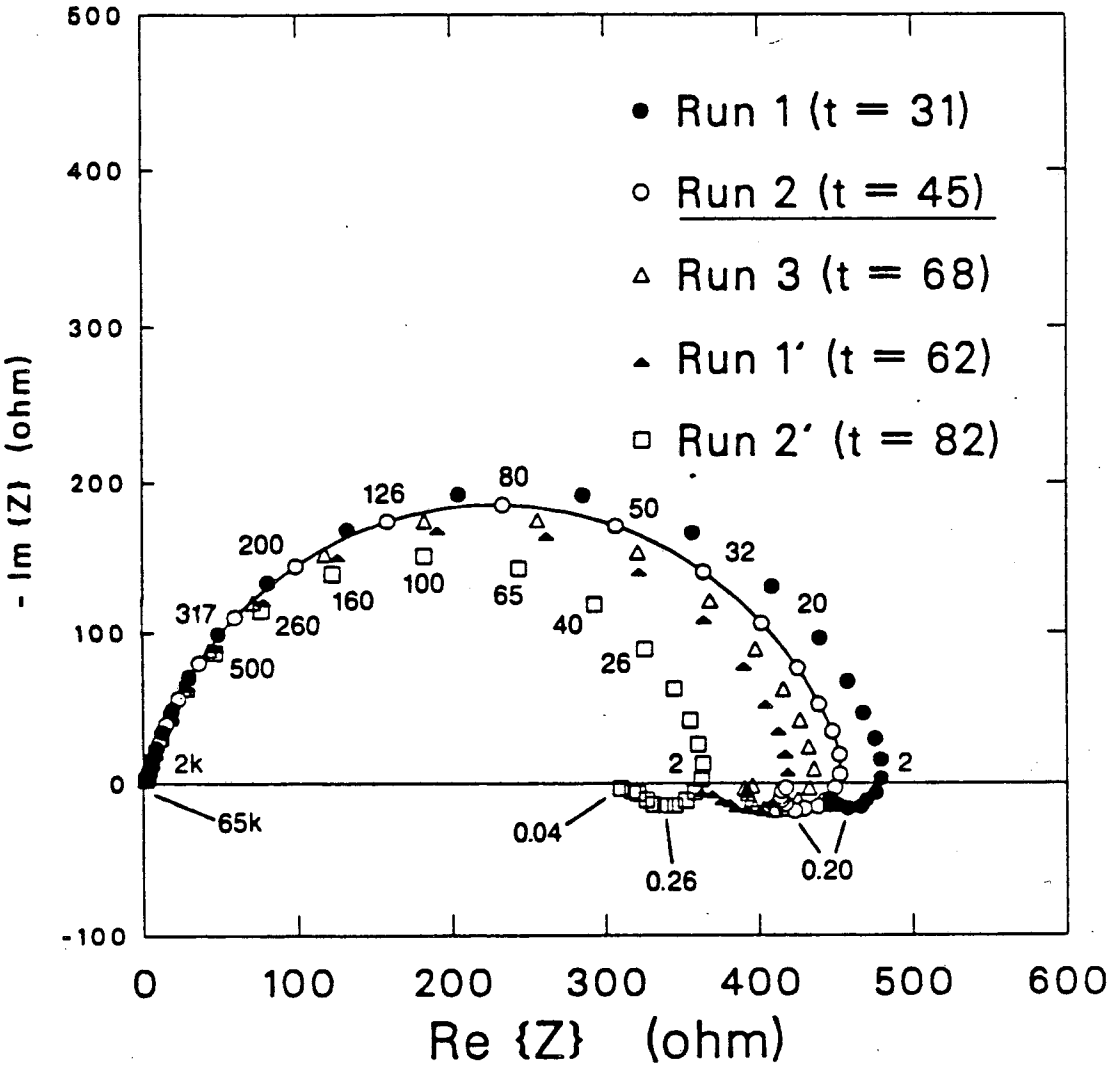

XBL 877-3156

Figure 3-8. Complex-plane plot of the impedance of a rotating disk electrode (d = 3.2 mm, Ω = 1600 rpm) at the open-circuit potential.
Run 1, run 2, and run 3: increasing frequency sweeps.
Run 1' and run 2': decreasing frequency sweeps.
The parameter is frequency in Hz. t is the time at the end of the impedance measurement in minutes (after the moment the electrode was immersed in the electrolyte).
(Run 2 is labeled experiment B.)

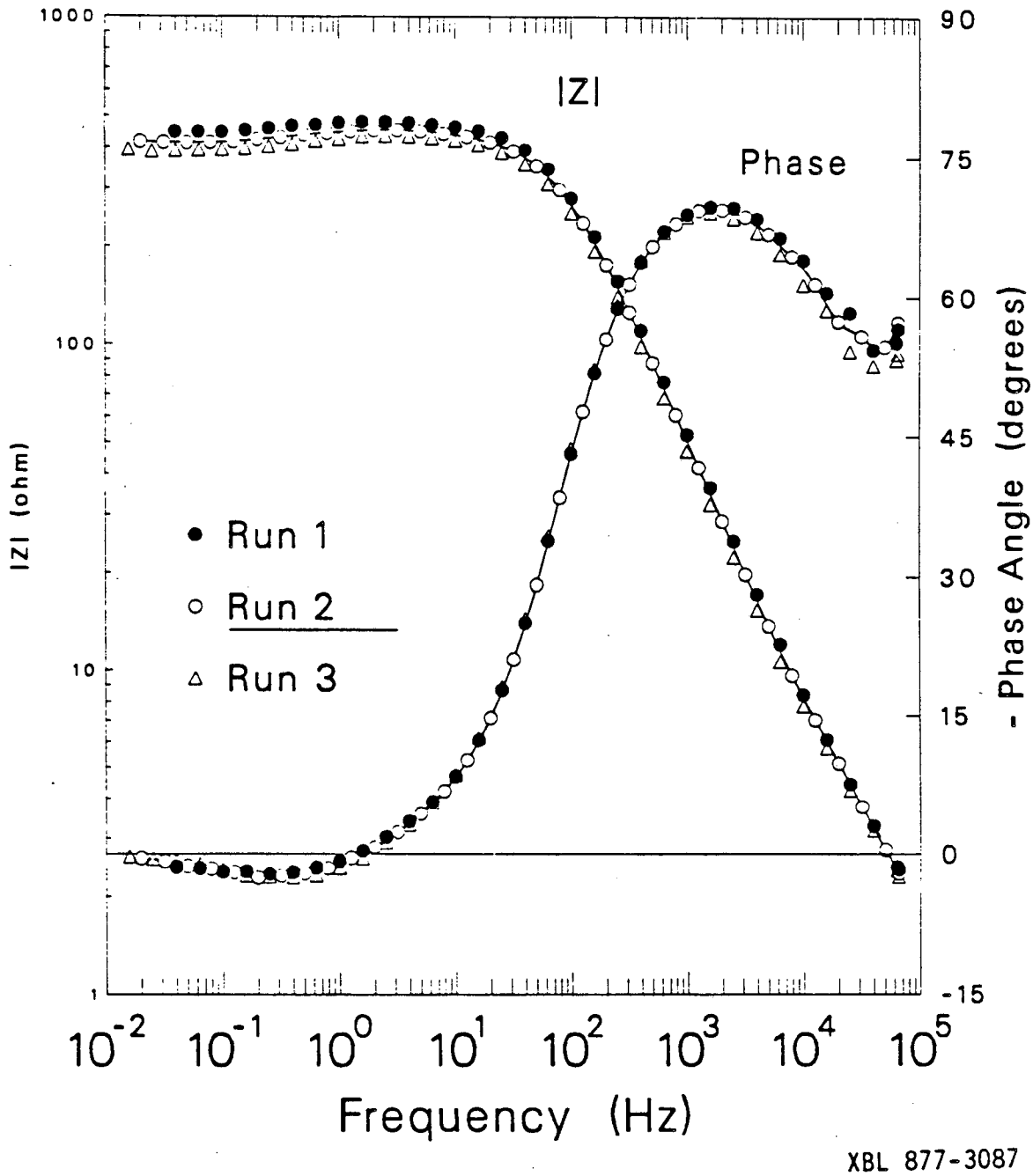

Figure 3-9. Bode plot of the data shown in the complex plane in figure 3-8.

This difference may be due to longer measurement times in the work of Keddam *et al.* (5). Lorenz and Mansfeld (7, Fig. 6) also give a complex impedance diagram with the same shape for iron in 0.5 M H_2SO_4 aerated solution at Ω = 3600 rpm.

There are two main differences between the impedance results for the disk electrode and the results for the hemispherical electrodes shown in this section. The impedance for the disk has a low-frequency inductive loop, which is apparently absent in the impedance for the hemispheres, and a second high-frequency capacitive loop is not observed for the disks (compare *e.g.*, figures 3-4 and 3-9).

The reason for the observed different behavior at low frequencies is not evident. The different behavior at high frequencies can be either due to artifacts in the measuring instrumentation, or due to the different primary current distributions for the hemispherical and the disk electrodes, since the electrode approaches the primary current distribution at high frequencies (8). Considering that the hemisphere has a uniform primary current distribution (9) and the disk has a highly nonuniform primary distribution (10), one may expect that the experimental results obtained with hemispheres are closer to the true behavior of the electrochemical system.

3.4. Anodic Dissolution at Low Currents

3.4.1. Experimental

The impedance was measured at two different anodic potentials in the low-current range: $\bar{V} = -0.850$ V, which corresponds to current densities of 20 to 40 mA/cm^2 (depending on the electrode used) and $\bar{V} = -0.800$ V, which corresponds to current densities of 40 to 200 mA/cm^2. All the steady-state electrode potential values $\bar{V}$ given in this chapter are measured relative to the Hg/Hg_2SO_4 reference electrode located in the bulk solution, essentially at infinity. A few experiments were done at $\bar{V} = -0.900$ V, but the data from those experiments are not shown here. The potential was stepped from the open-circuit potential value to the desired value, and a small potential perturbation was superimposed. The DC component of the current and potential signals was subtracted during the impedance measurements (unless otherwise noted).

The minimum frequency was usually set at 0.01 Hz for the experiments at $\bar{V} = -0.850$ and at 0.03 to 0.05 Hz at $\bar{V} = -0.800$ V. The impedance measurement started ~10 minutes after the electrode was immersed in the electrolyte. Thus the duration of an experiment was 15 to 30 minutes, and the electrode surface changed significantly during this time due to dissolution of the metal. The diameter of the hemispherical electrodes decreased by a few hundredths of a millimeter. The surface of the hemisphere was still nearly smooth, but did not appear completely homogeneous; in particular some parts of the surface were shiny and some parts were not. For the disk electrodes, a slight step was formed between the metal disk and the insulator as the disk dissolved, and granular corrosion of the metal was evident.

In the experiments at low (as well as high) anodic currents, the solution ohmic resistance (which corresponds to the infinite-frequency limit of the impedance) was a significant part of the measured impedance, in contrast to the experiments at the open-circuit potential. A relatively high ohmic resistance impairs the accuracy of the measurement of the electrochemical interface impedance, and various techniques can be used to compensate for the ohmic resistance in impedance measurements (3). However ohmic compensation can yield stability problems (3). Moreover the solution ohmic resistance is not known exactly *a priori* and does not have a unique value for electrodes with a nonuniform current distribution. Thus we decided not to attempt to compensate for the solution resistance in any of the impedance measurement experiments. It is perhaps better to try to account for the solution resistance rigorously in a theoretical model rather than compensating for the solution resistance incorrectly in the experimental measurement.

3.4.2. Results

Figures 3-10 and 3-11 show the impedance of a hemisphere (d = 4 mm) at $\bar{V} = -0.850$ V. Figure 3-11 illustrates that mass transfer effects are not important at low anodic potentials. The impedance of a bigger hemisphere at the same potential is given in figure 3-12, and the impedance of a disk is given in figures 3-13 and 3-14.

Figure 3-14 shows a discrepancy between the two experiments for the disk. The discrepancy is probably due to a difference in the time when the impedance was measured rather than nonreproducibility of the data.

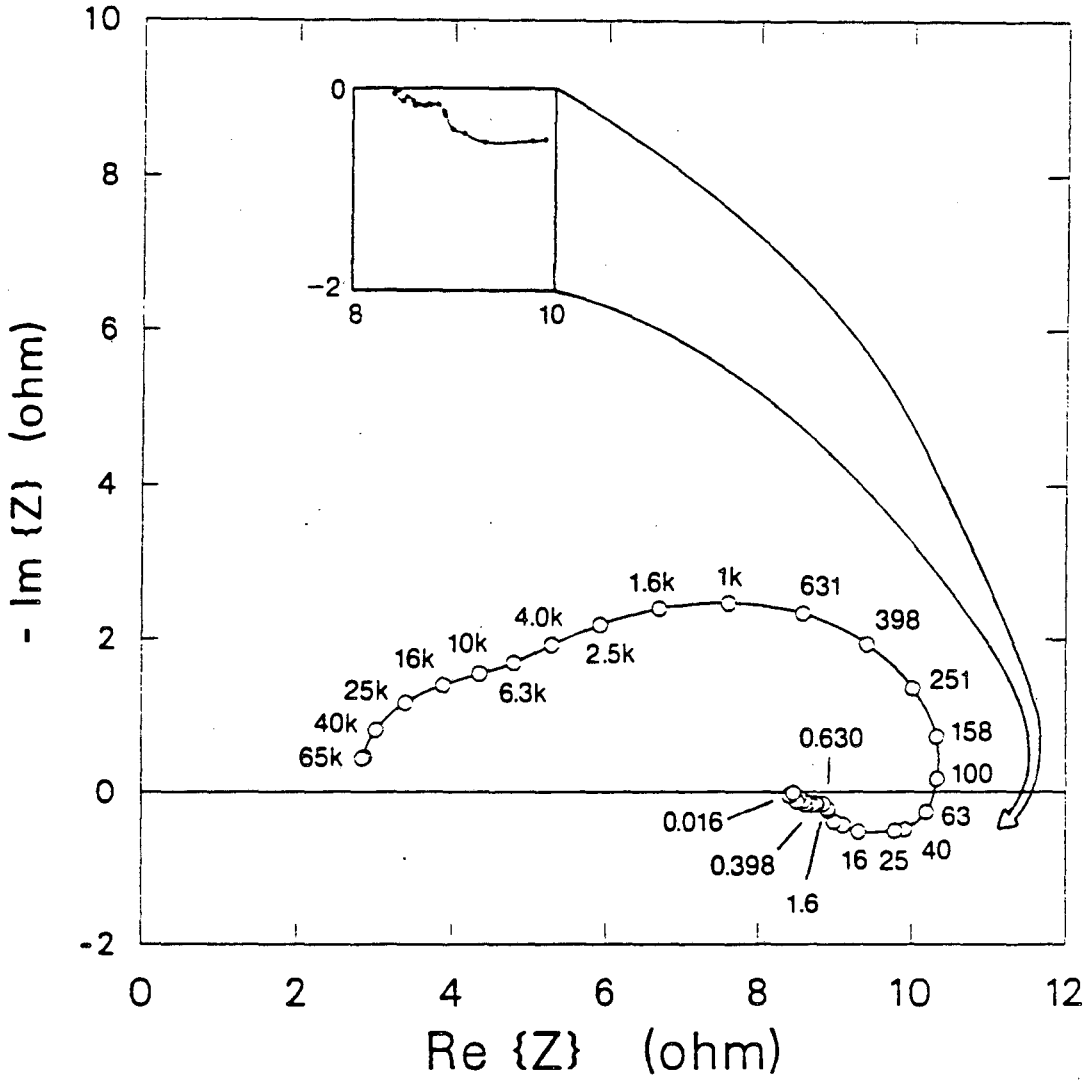

XBL 877-3155

Figure 3-10. Complex-plane plot of the impedance of a rotating hemispherical electrode (d = 3.93 mm at the beginning of the experiment ⟶ 3.91 mm at the end of the experiment, Ω = 1600 rpm) at low current.
$\bar{V}$ = -0.850 V, $\bar{I}$ = 6 mA (25mA/cm^2), $|\Delta V|$ = 2 mV rms. Increasing frequency sweep. The parameter is frequency in Hz. (Labeled experiment C)

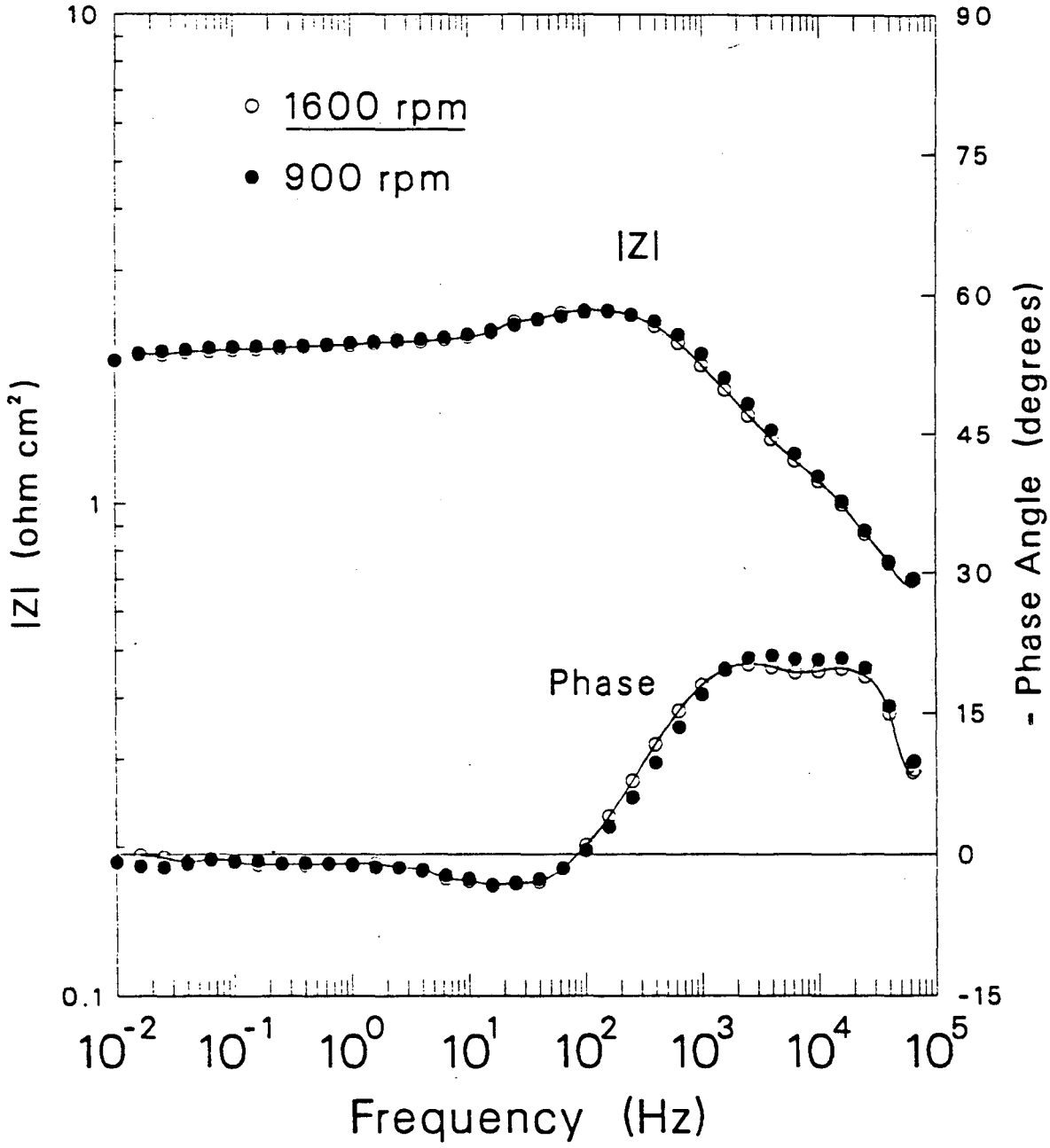

XBL 877-3085

Figure 3-11. The impedance of a rotating hemisphere (d = 3.9 mm) at two different rotation speeds (two separate experiments; the data from the experiment at 1600 rpm are also given in figure 3-10).
$\bar{V}$ = -0.850 V, $\bar{I}$ = 6 mA (25mA/cm^2), $|\Delta V|$ = 2 mV rms. Increasing frequency sweeps.

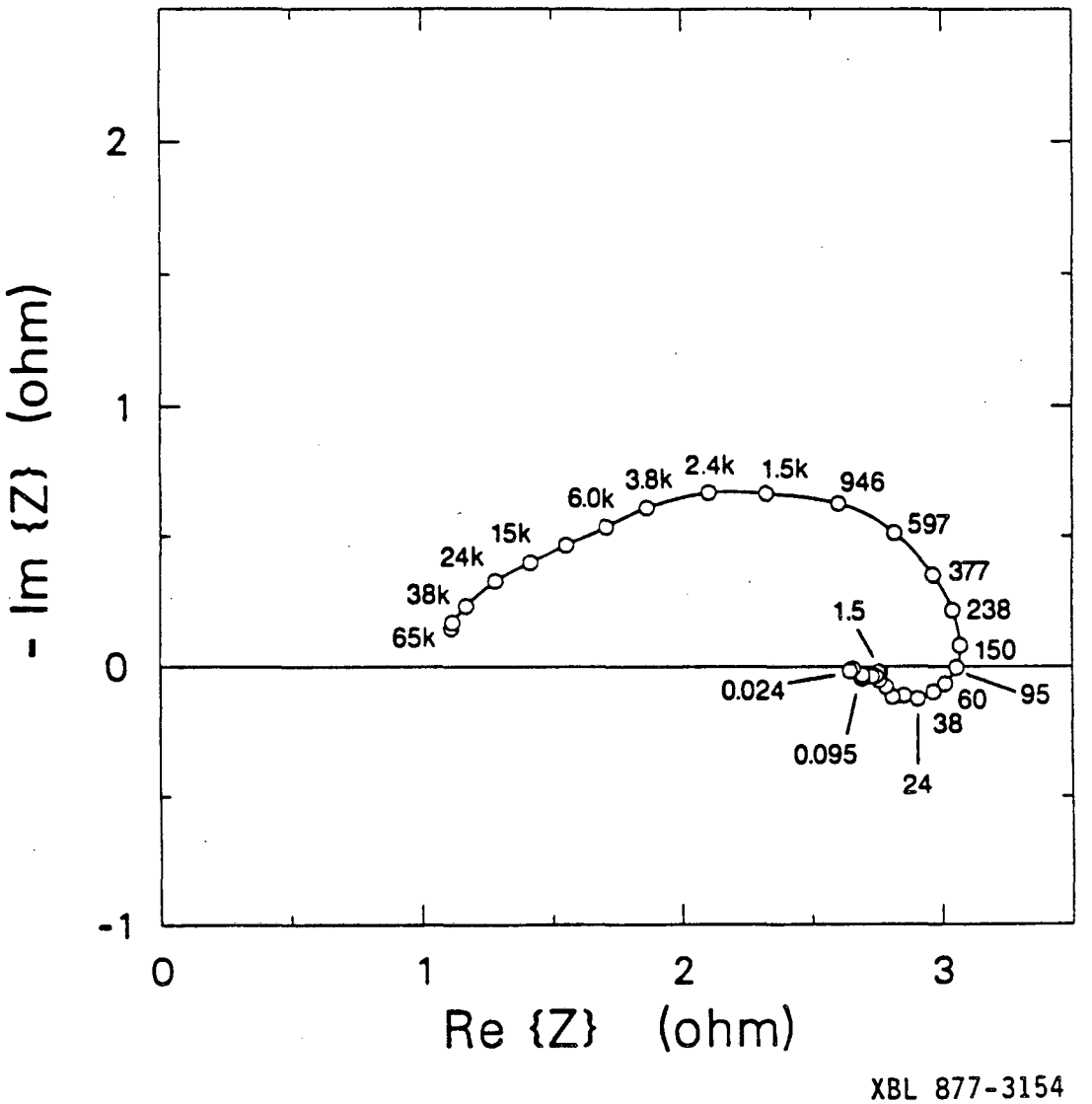

Figure 3-12. Complex-plane plot of the impedance of a rotating hemispherical electrode (d = 8.19 mm, Ω = 1600 rpm). $\bar{V}$ = −0.850 V, $\bar{I}$ = 23 mA (22mA/cm^2), |ΔV| = 2 mV rms. Increasing frequency sweep.

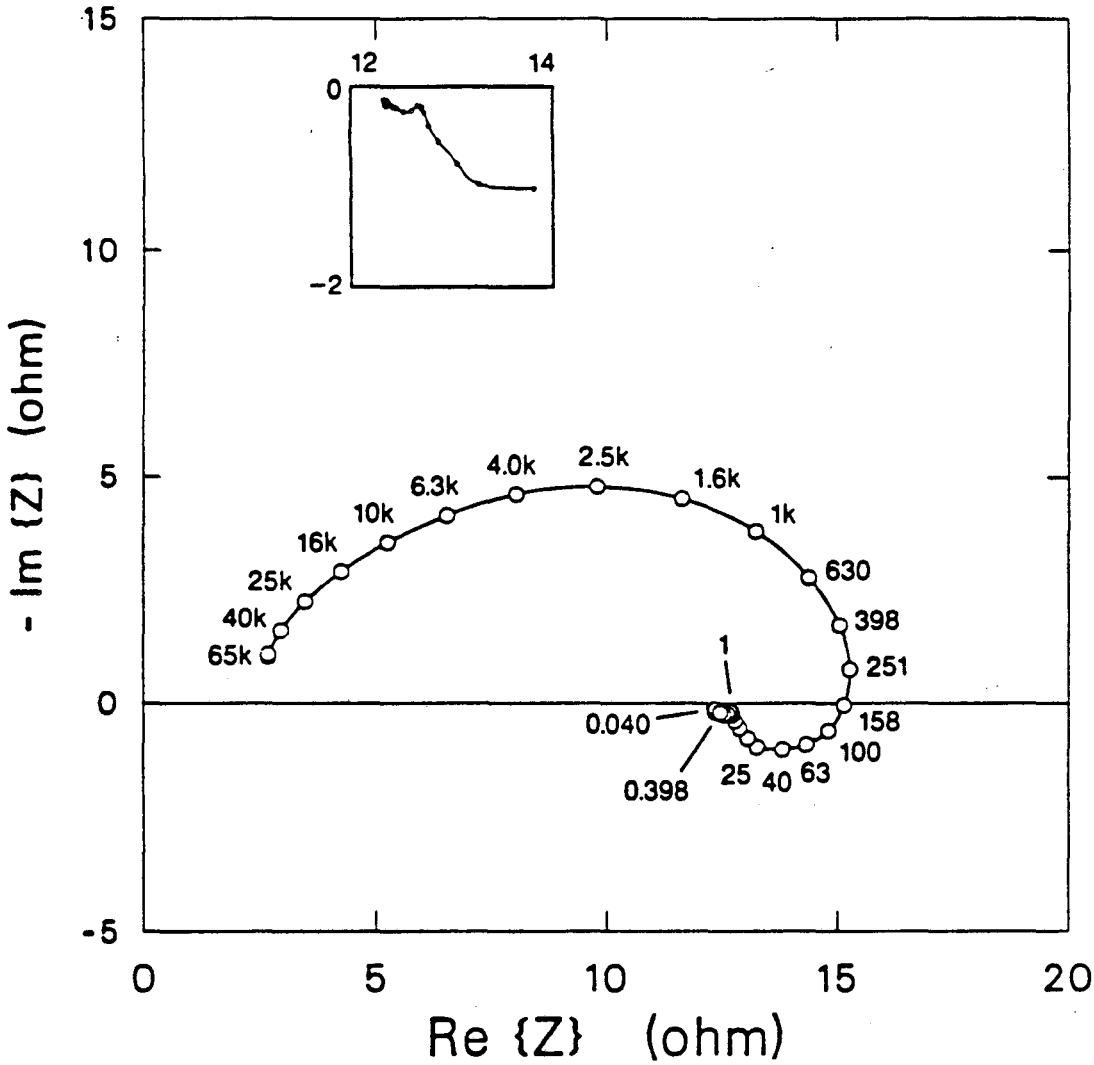

XBL 877-3153

Figure 3-13(a). Complex-plane plot of the impedance of a rotating disk electrode (d = 3.2 mm, Ω = 1600 rpm) at low current. $\bar{V}$ = −0.850 V, $\bar{I}$ = 3 mA (37 mA/cm^2), |ΔV| = 2 mV rms. Increasing frequency sweep. (Labeled experiment D)

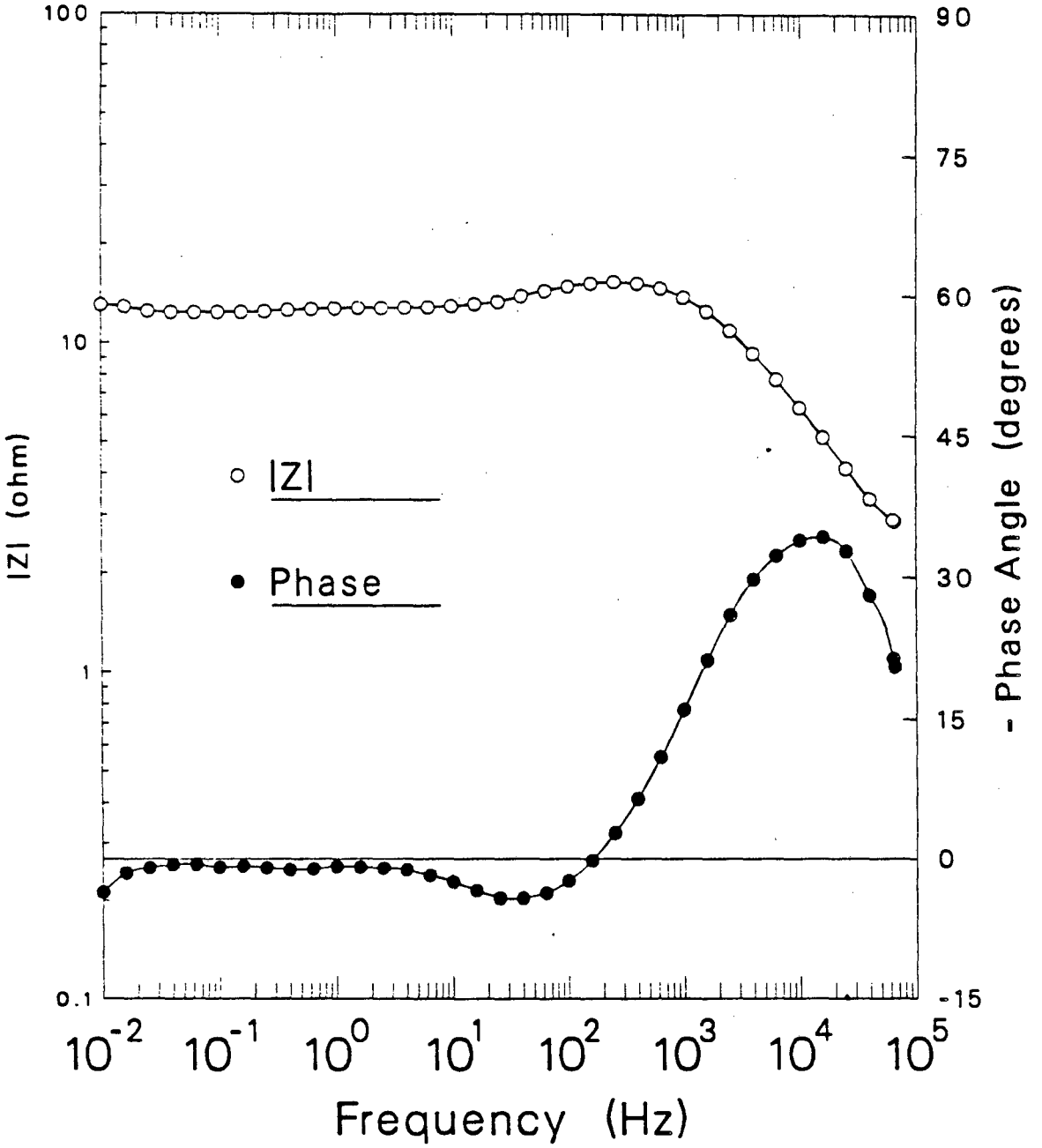

XBL 877-3084

Figure 3-13(b). Bode plot for the same experiment.

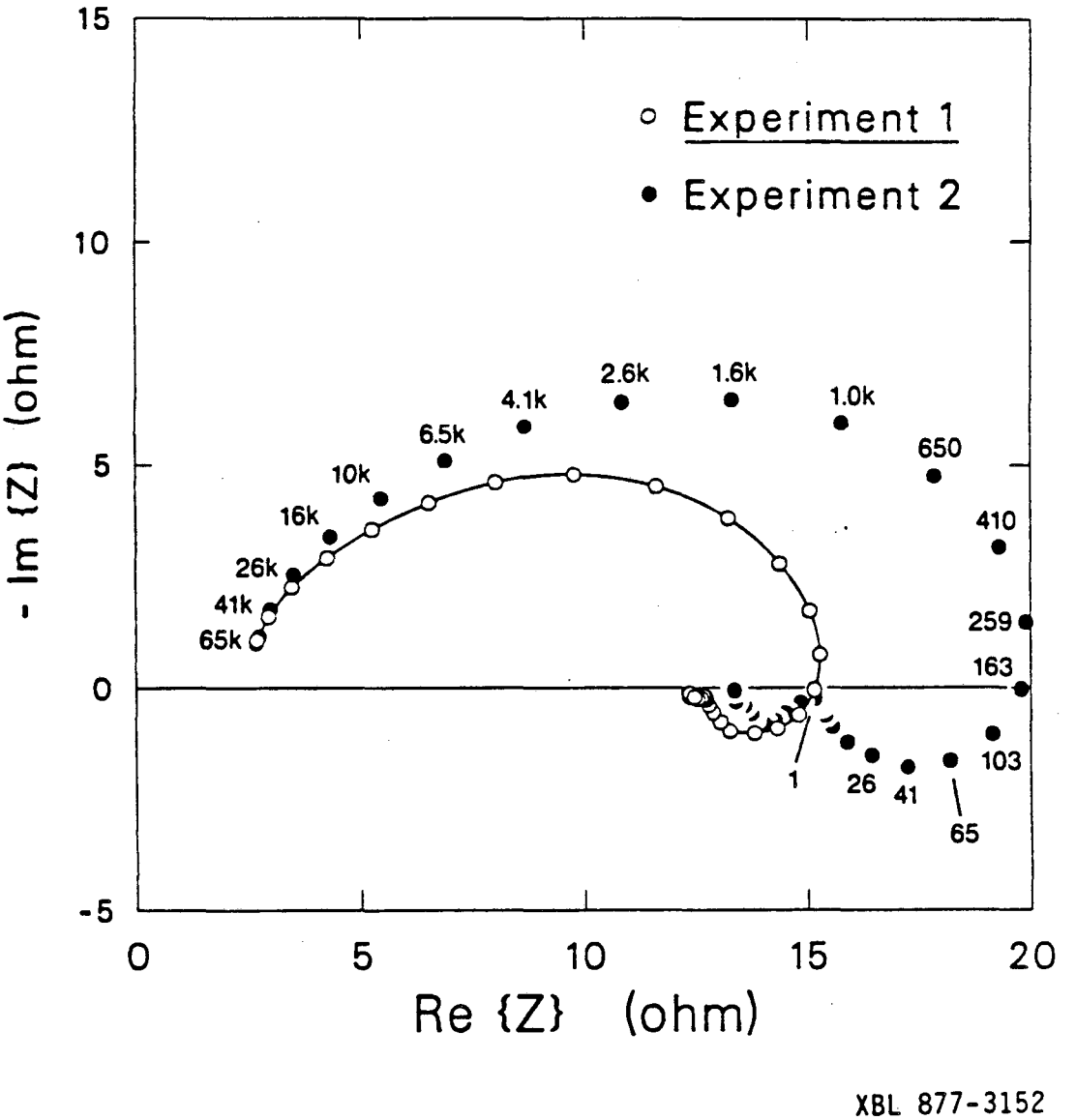

Figure 3-14. Complex-plane plot of the impedance measured in two experiments for a rotating disk electrode (d = 3.2 mm, Ω = 1600 rpm).
$\bar{V}$ = −0.850 V, $\bar{I}$ = 3 mA (37mA/cm^2), |ΔV| = 2 mV rms.
Experiment 1: increasing frequency sweep (also shown in figure 3-13).
Experiment 2: decreasing frequency sweep.

Specifically the impedance at frequencies between 65 kHz and ~1 Hz was measured after ~20 minutes of polarization at $\bar{V}$ in experiment 1 and after only ~5 minutes of polarization in experiment 2. Keddam *et al.* (5) have observed that at low anodic currents the current reaches a steady state within 10 minutes for the Fe/H_2SO_4 system. Thus it seems that the system had not yet reached a steady state in experiment 2 at frequencies above 1 Hz.

Each of the figures 3-10 through 3-14 shows two inductive loops. The first inductive loop occurs in the frequency range 100 Hz to 1 Hz approximately, and the second inductive loop occurs at frequencies below 1 Hz, for all of these experiments. The bottom of the first inductive loop occurs at 20 to 50 Hz. Bechet *et al.* (11, Fig.1) and Keddam *et al.* (5, Fig.2, also shown here in figure 1-2) also observed two inductive loops in the same frequency ranges in their impedance measurements for iron rotating disks. Note especially diagram D_o in Fig. 2 of Reference (5), which corresponds to figure 3-13. These authors (5, 11) attribute the two inductive loops to adsorbed intermediate species in the iron dissolution mechanism.

Again we observe a difference between the impedance for the hemispherical and the disk electrodes at very high frequencies. The impedance for the hemispheres shows a second capacitive time constant which is absent in the impedance for the disks. However the second high-frequency capacitive loop for the hemispheres is now nearly indistinguishable from the bigger capacitive loop.

Some experiments at $\bar{V} = -0.900$ V (lower anodic current density) using hemispherical as well as disk electrodes also showed two inductive time constants, but the two time constants were almost indistinguishable from each other. Bechet *et al.* (11) and Keddam *et al.* (5) made the same observation in their experiments. Then as the current density increased (up to 200 mA/cm^2), they observed two inductive loops that were more readily separate. They attribute the lowest-frequency inductive loop observed at very low currents (near the corrosion potential) to the adsorption-desorption of hydrogen, which no longer occurs at current densities above ~15 mA/cm^2.

Let us now look at the results for $\bar{V} = -0.800$ V. Figures 3-15 and 3-16 show the impedance of two hemispheres of different diameters. The impedance exhibits an inductive loop at frequencies between about 200 Hz and 2 Hz, which is nearly the same frequency range as the first inductive loop observed at $\bar{V} = -0.850$ V.

However a second inductive loop at frequencies below 1 Hz is no longer observed for the bigger hemisphere, and the impedance rather appears to have a capacitive character at those frequencies. This behavior is similar to that observed by Keddam *et al.* (5, Figures 4 and 5) for a disk electrode in Na_2SO_4/H_2SO_4 electrolyte solution of pH greater than 2, where the lower-frequency inductive loop was transformed into a capacitive loop as the anodic potential increased. We repeated the experiments with the hemispheres several times, but could not obtain reliable data free of noise at frequencies below 0.5 Hz, and the lower-frequency behavior was not clearly discerned as either an inductive or a

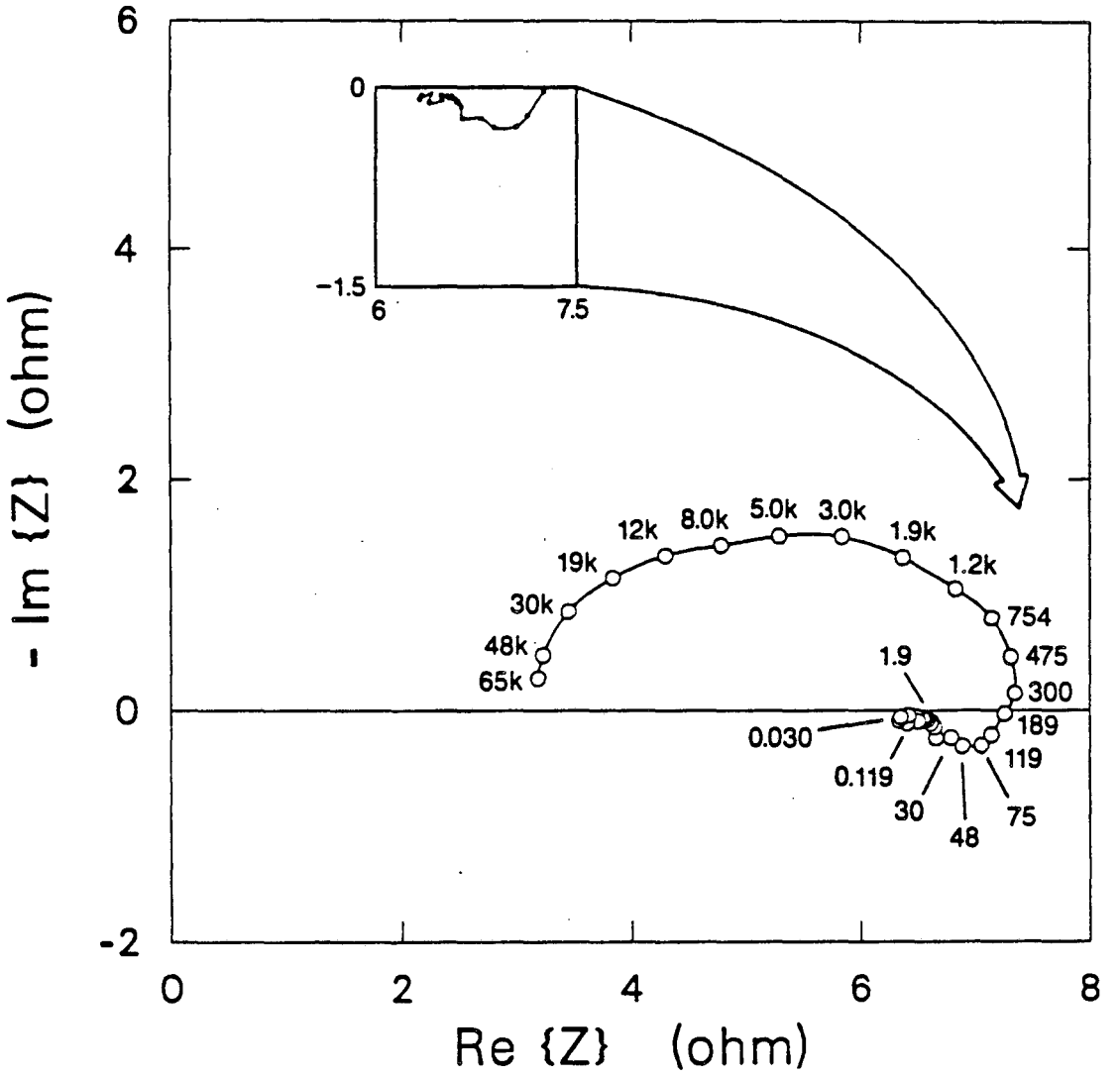

XBL 877-3151

Figure 3-15. Complex-plane plot of the impedance of a rotating hemispherical electrode (d = 3.86 → 3.84 mm, Ω = 1600 rpm).
$\bar{V}$ = −0.800 V, $\bar{I}$ = 13.5 mA (58mA/cm^2), |ΔV| = 2 mV rms.
Increasing frequency sweep.

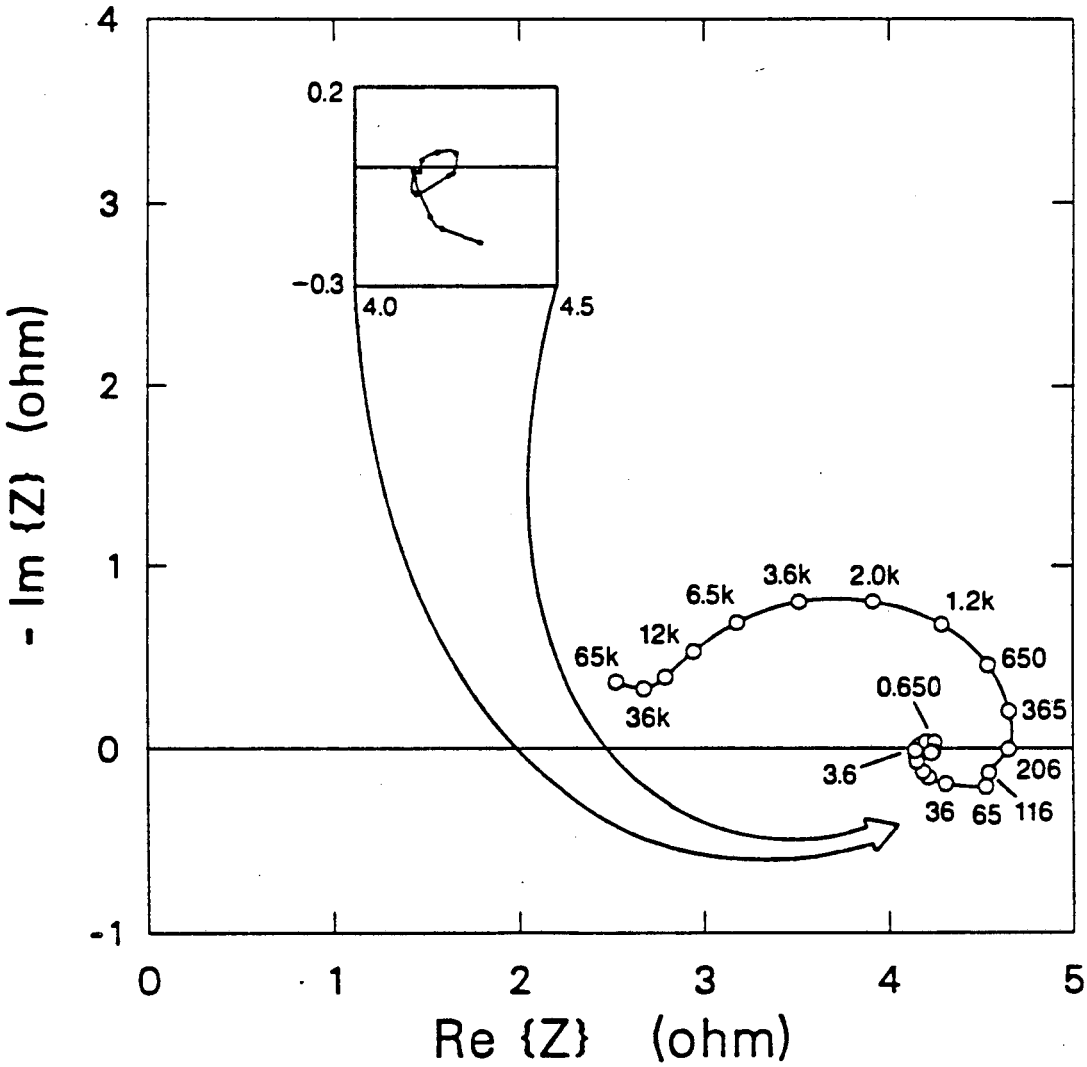

XBL 877-3150

Figure 3-16. Complex-plane plot of the impedance of a rotating hemisphere ($d_{\bar{h}}$ = 6.03 → 5.96 mm, Ω = 900 rpm). $\bar{V}$ = −0.800 V, $\bar{I}$ = 22 mA (39mA/cm^2), |ΔV| = 2 mV rms. Decreasing frequency sweep. The DC component of the current and potential signals was not subtracted during the impedance measurement.

capacitive loop.

Consider now the results for the disk electrodes. Figures 3-17 and 3-18 give the impedance measured in two experiments for disk electrodes (d = 3 mm). Two inductive loops are clearly seen. The bottom of the first inductive loop occurs at a frequency of about 100 Hz, which is higher than that at $\bar{V} = -0.850$ V. These data agree with the data of Keddam *et al.* (5, Fig.2, diagrams E_o and F_o) for the same system.

An interesting feature of the impedance for the disks at this potential is the intersecting loop (loopy-loop) between the two inductive loops, illustrated in the expanded view in figure 3-18. A loopy-loop was observed at this potential for disk electrodes with different diameters in some experiments, and in other experiments a loopy-loop was not clearly observed.

Figures 3-19 and 3-20 show the impedance measured in two consecutive frequency sweeps in an experiment with a smaller diameter disk electrode. At the end of the impedance measurement the open-circuit potential had shifted by ~30 mV in the cathodic direction relative to the open-circuit potential at the beginning of the experiment. The impedance measured in the first frequency sweep (figure 3-19) shows two inductive loops and is similar to the impedance of the bigger disk (figures 3-17 and 3-18). However the impedance measured in the second frequency sweep (figure 3-20) shows only one inductive loop. (Note that all the data points in figures 3-19 and 3-20 have a precision within 1% according to the FRA.)

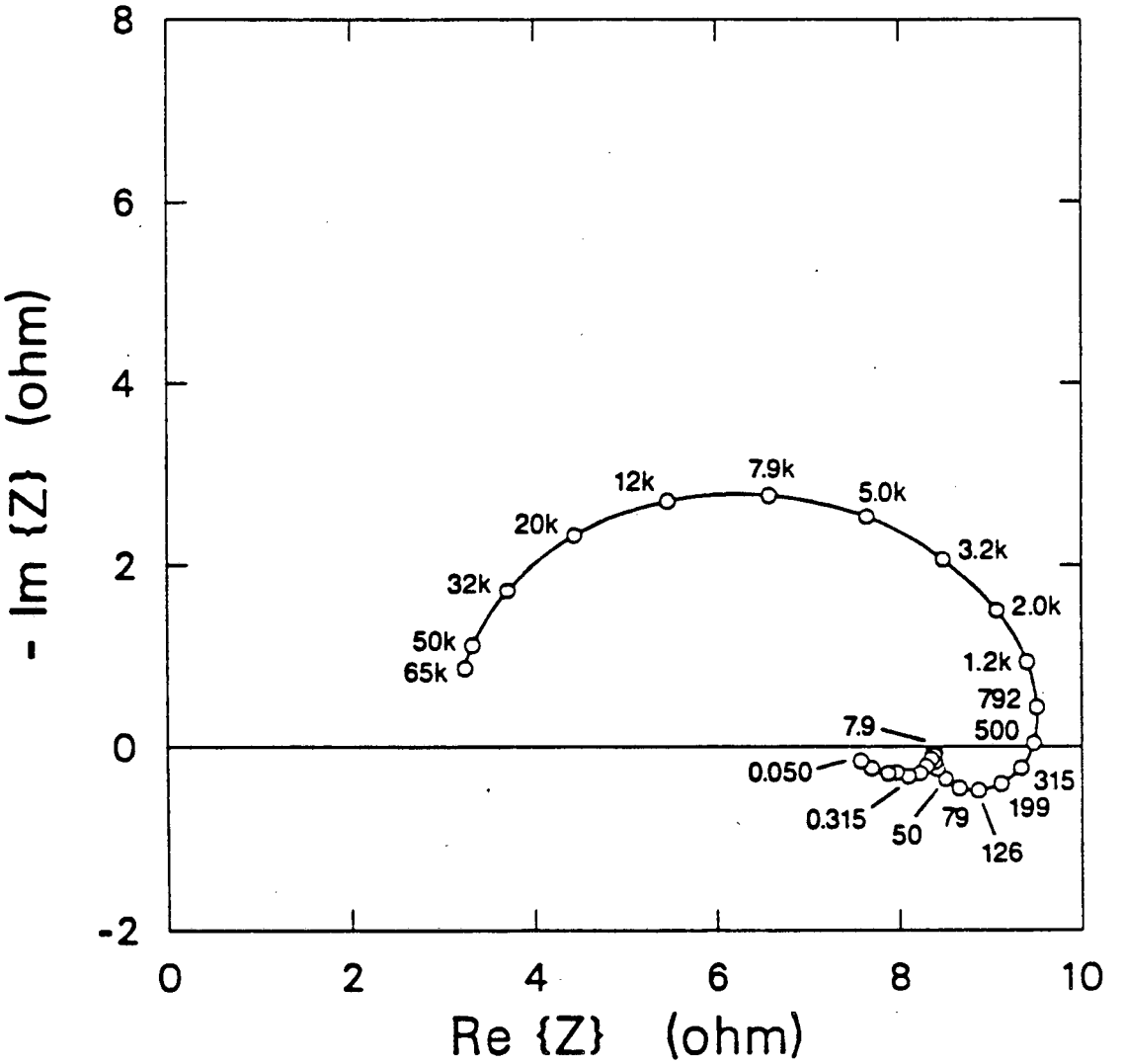

XBL 877-3149

Figure 3-17. Complex-plane plot of the impedance of a rotating disk (d = 3.0 mm, Ω = 1600 rpm).
$\bar{V}$ = -0.800 V, $\bar{I}$ = 8.8 mA (120mA/cm^2), |ΔV| = 2 mV rms.
Increasing frequency sweep.

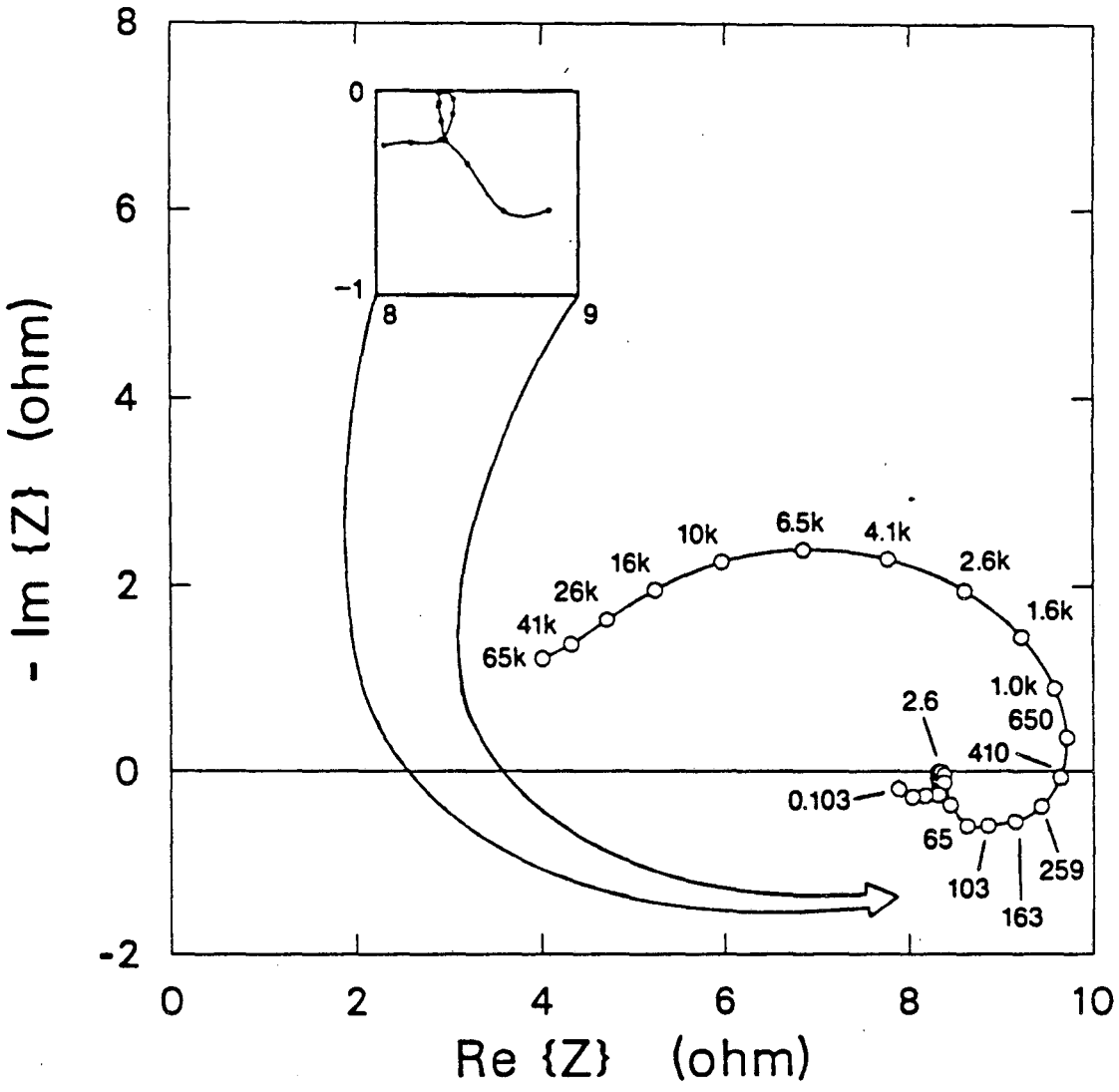

XBL 877-3148

Figure 3-18. Complex-plane plot of the impedance of a rotating disk (d = 3.2 mm, Ω = 1600 rpm).
$\bar{V}$ = -0.800 V, $\bar{I}$ = 8 mA (100 mA/cm^2), $|\Delta V|$ = 5 mV rms. Decreasing frequency sweep. The DC component of the current and potential signals was not subtracted during the measurement.

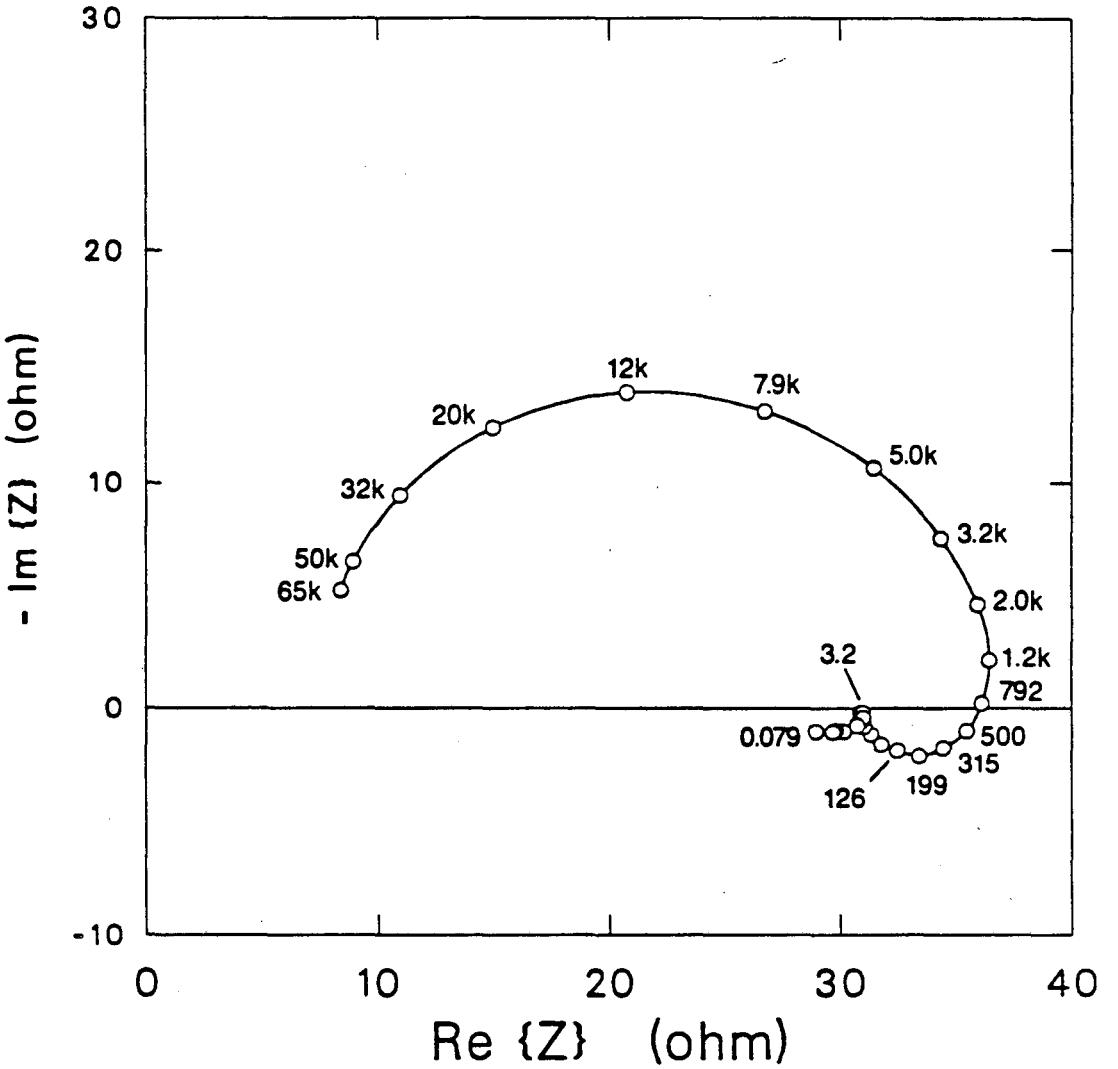

XBL 877-3147

Figure 3-19. Complex-plane plot of the impedance of a rotating disk electrode ($d = 1$ mm, $\Omega = 1600$ rpm), $\bar{V} = -0.800$ V, $\bar{I} = 1.8$ mA (230mA/cm^2), $|\Delta V| = 2$ mV rms. Increasing frequency sweep.

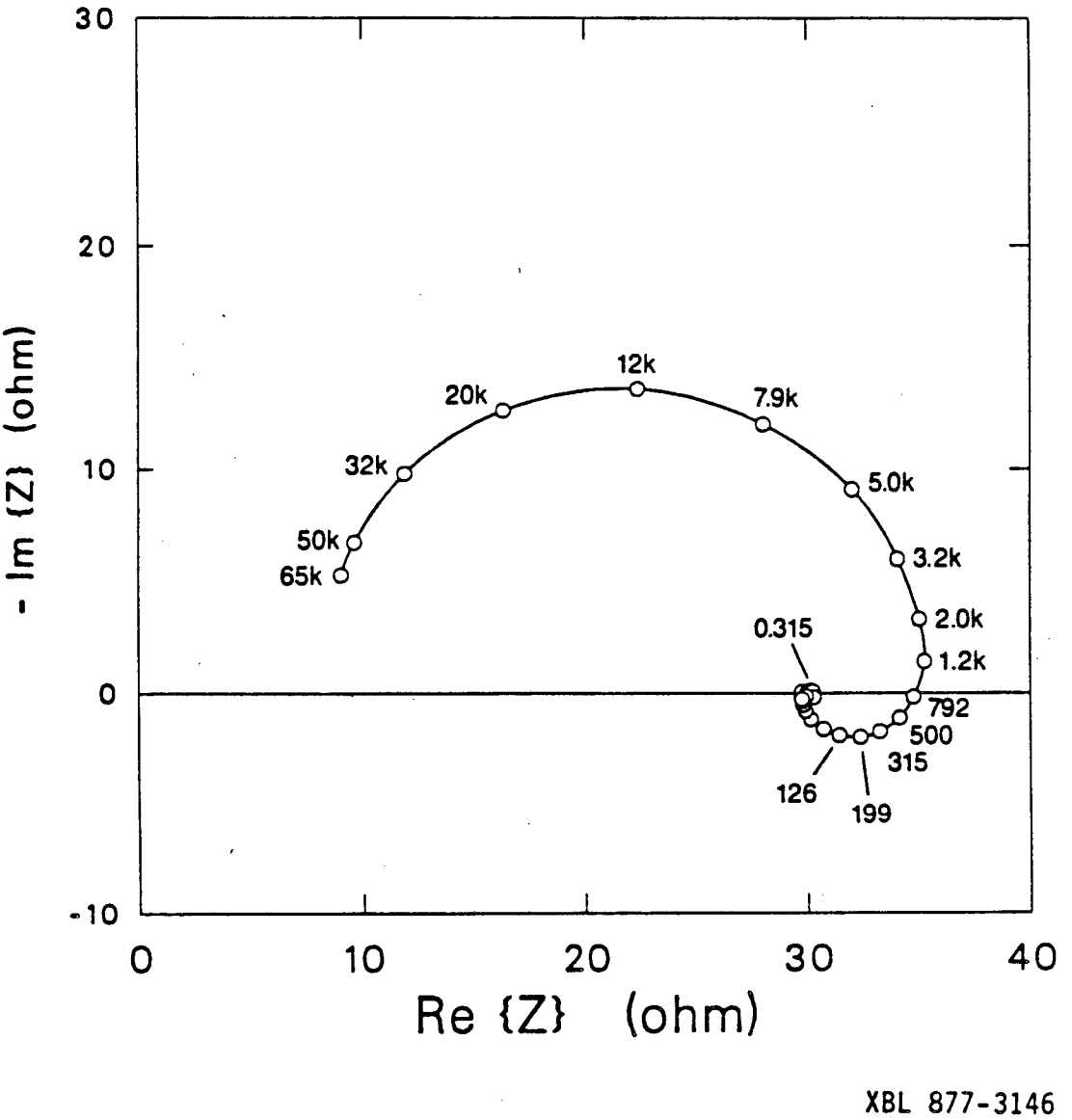

Figure 3-20. Impedance data obtained immediately after the data in figure 3-24. The measurement started 15 minutes after the immersion of the electrode and lasted for 6 minutes. Increasing frequency sweep.

If the inductive loops in the impedance arise from intermediate species in the reaction mechanism, one does not normally expect these loops to disappear with time. It is not evident whether the difference between these two sets of impedance data was due to the shift in the open-circuit potential, or due to the change in the electrode geometry and morphology, or perhaps due to not having reached a steady state before the first measurement, or due to some other experimental artifact.

3.5. Anodic Dissolution at High Currents — Limiting Current Plateau

3.5.1. Experimental

Accurate impedance measurements at high current densities were hard to perform with the available experimental setup. More accurate measurements at these currents could be possible if a mercury chamber instead of a silver-carbon brush were used for the electrical connection of the rotator to reduce noise problems (see section 2.3) and if the DC component of the current and voltage signals were accurately subtracted.

During these experiments, the electrode surface changed much more than during the lower-current experiments. The hemispherical electrode appeared to dissolve more near the pole than near the equator, as expected under mass-transfer limitations (9). At these conditions the hemispherical electrode no longer has the advantage of a more uniform current distribution than the disk electrode. The disk electrodes receded into the insulator as they dissolved, and two different dissolution morphologies were observed. Near or at the lower-potential end of

the limiting current plateau, granular dissolution was observed. At the higher-potential end of the plateau, beyond the oscillatory region, the disk appeared to dissolve more uniformly, and the disk surface looked smooth after the experiment. These observations are consistent with the observations of Miller (12), who used optical and electron microscopy for iron disks subjected to an impinging jet of sulfuric acid.

The data obtained at the lower-potential end of the limiting current plateau generally had a precision within 10% at frequencies above 1 Hz, but at lower frequencies the signals became very noisy. The data obtained at the higher-potential end of the plateau had poorer precision. The data from several experiments at the same conditions gave similar impedance diagrams.

To obtain good impedance results under these conditions of rapid dissolution, alternative measurement methods much faster than the one used here are perhaps needed. For example, fast Fourier transform (FFT) techniques could be used. The presence of a porous salt film at the limiting current plateau for the Fe/H_2SO_4 system probably makes accurate impedance measurements inherently more difficult.

3.5.2. Results

We do not consider the results obtained here reliable, but we present some results in figures 3-21 through 3-23 to illustrate the complex behavior of the system.

Very few experimental impedance data are available in the literature for the Fe/H_2SO_4 system near or at the limiting current. We have

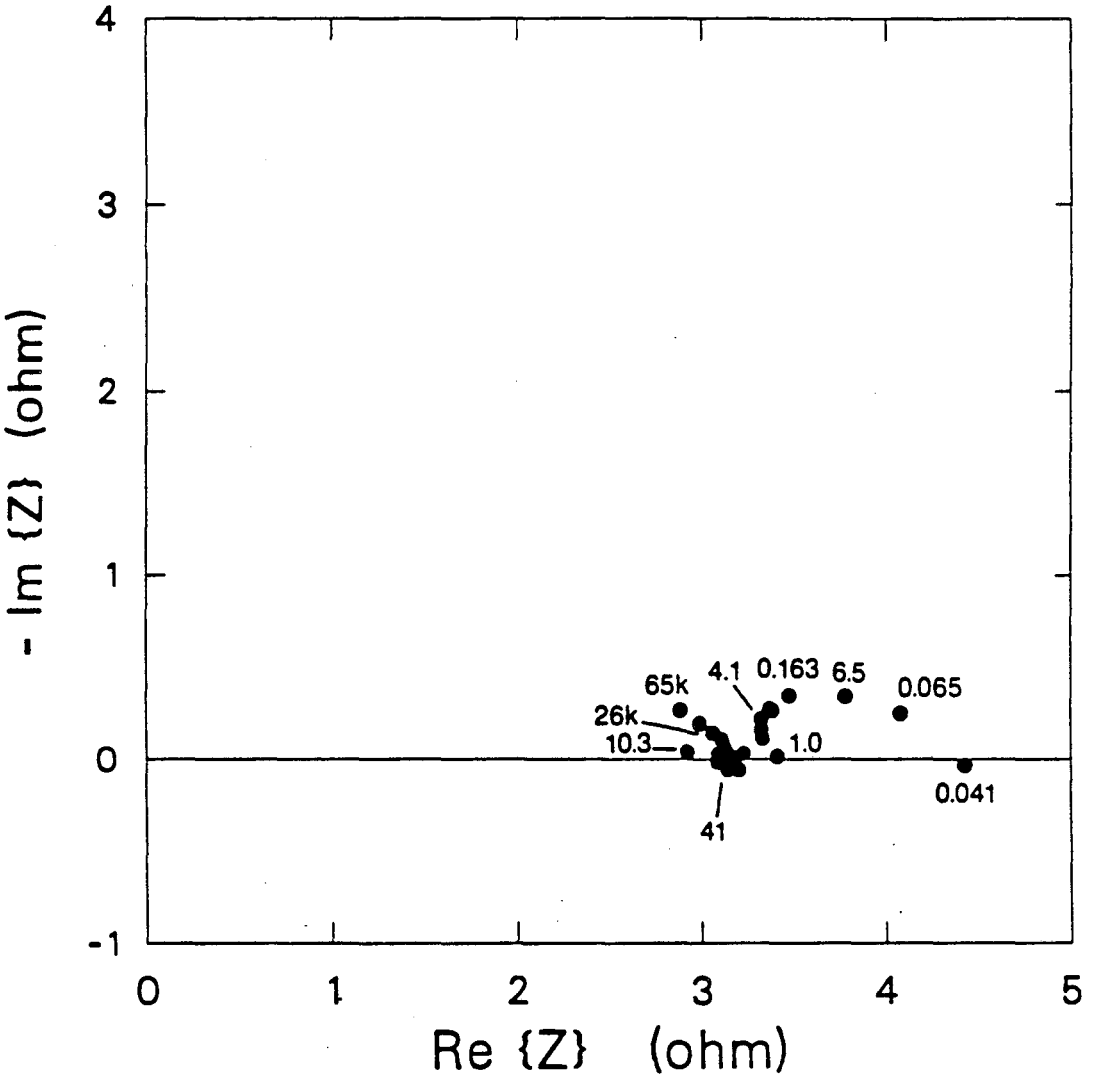

XBL 877-3145

Figure 3-21. Complex-plane plot of the impedance of a rotating hemispherical electrode ($d = 6.37 \rightarrow 6.22$ mm, $\Omega = 400$ rpm) near the limiting current plateau.
$\bar{V} = 0.103$ V, $\bar{I} = 0.3$ A, $|\Delta V| = 3.5$ mV rms.
Decreasing frequency sweep. The DC component of the current and potential signals was not subtracted during the impedance measurement. The parameter is frequency in Hz.

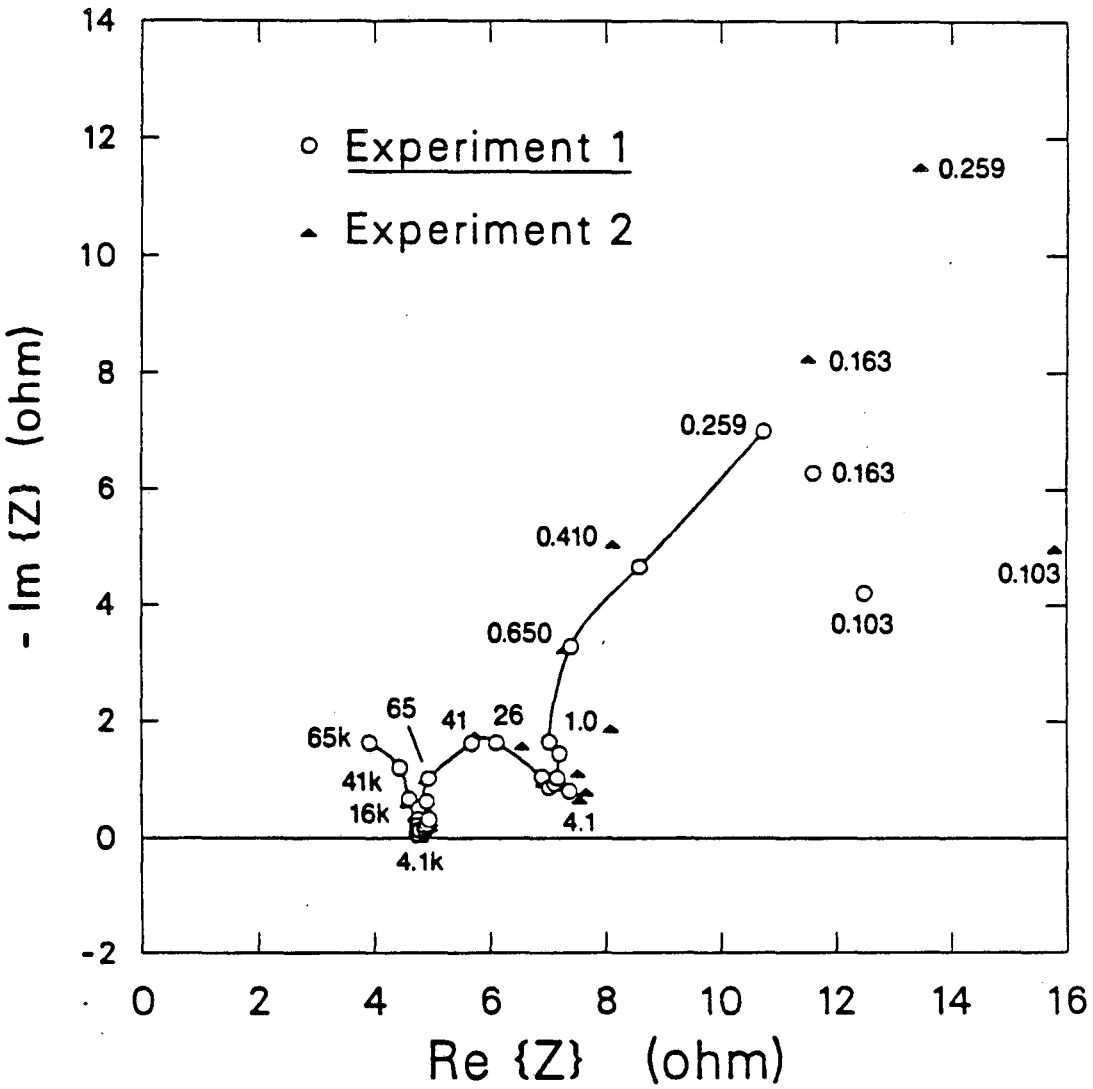

XBL 877-3144

Figure 3-22. Complex-plane plot of the impedance of a rotating disk electrode (d = 3.2 mm, Ω = 1600 rpm) at the limiting current plateau before the oscillatory region. The data obtained in two separate experiments under the same conditions are given.
$\bar{V}$ = −0.255 V, $\bar{I}$ = 0.10 A (1.25A/cm^2), |ΔV| = 5 mV rms. Decreasing frequency sweeps. The DC component of the current and potential signals was not subtracted during the measurements.

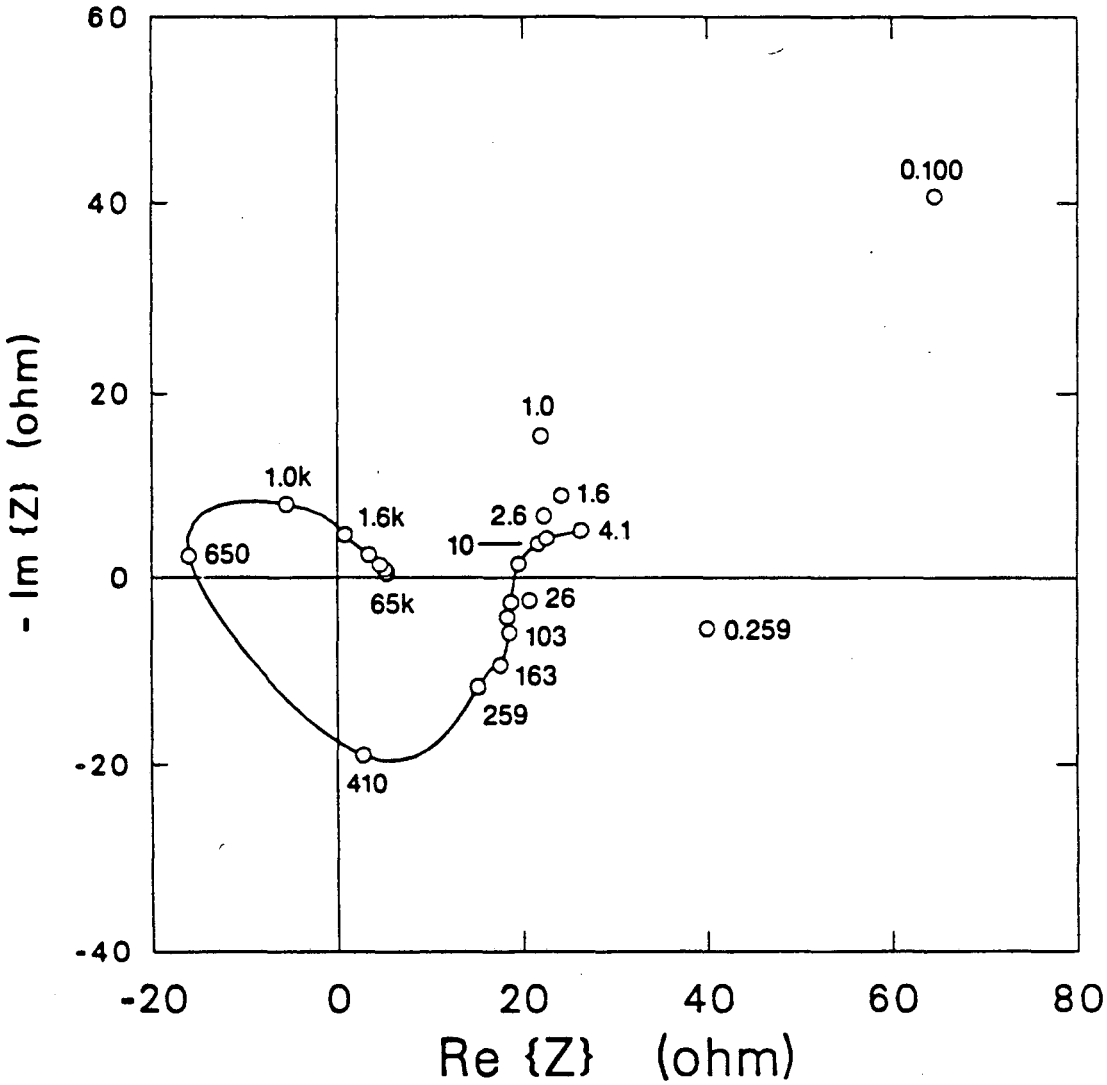

XBL 877-3143

Figure 3-23. Complex-plane plot of the impedance of a rotating disk (d = 3.2 mm, Ω = 1600 rpm) at the limiting current plateau after the oscillatory region. (However the current was oscillating at the end of the impedance measurement) $\bar{V}$ = 0.087 V, $\bar{I}$ = 0.10 A (1.25 A/cm^2), $|\Delta V|$ = 5 mV rms. Decreasing frequency sweep. The DC component of the current and potential signals was not subtracted during the measurement.

found only one experimental impedance diagram for an iron rotating disk in 1 M H_2SO_4 at the limiting current (13, Fig. 33), exhibiting a particularly complicated behavior and two other impedance diagrams for Fe in H_2SO_4/Na_2SO_4 electrolyte near the limiting current (13, Fig. 31 and 33; also 14, Fig. 1(c)).

At the limiting current, the impedance becomes infinite as $\omega \longrightarrow 0$, since the zero-frequency limit of the impedance is equal to the slope of the steady-state polarization curve. We could not clearly observe the low-frequency behavior in these experimental results because of noise and rapid dissolution of the electrode.

Consider the data in figure 3-22. The impedance diagram has three capacitive loops: a loop at frequencies above ~5 kHz, another loop with a time constant corresponding to ~40 Hz, and another loop at frequencies below ~1 Hz. The lowest-frequency loop is usually considered to show the influence of convective diffusion and is absent in the impedance at lower currents where mass-transfer limitations are negligible (see also 14, Fig.1). Notice also that the frequency range of the highest-frequency loop is the same as that of the highest-frequency capacitive loop observed for hemispherical electrodes at low currents as well as at the open-circuit potential; this indicates that the highest-frequency loop propably arises from the reaction mechanism for iron dissolution and is more readily evident in experiments with hemispherical electrodes.

The impedance diagram in figure 3-22 is similar to the one given in References (13, 14). The latter diagram however does not clearly show

three capacitive loops. A theoretical impedance diagram with three capacitive loops has also been obtained from the model of Epelboin *et al.* (14, 15), which is discussed in detail in section 1.3.2. The model includes a multiple-step dissolution mechanism with an adsorbed intermediate species and Nernst-diffusion of an artificial reacting species. Other experimental data with three capacitive time constants at high current densities are presented by Keddam *et al.* (16) for Fe-Cr alloys in sulfuric acid.

3.6. Passivation

3.6.1. Experimental

The impedance was measured along the passivation curve for several hemispherical as well as disk electrodes. The electrode was polarized at a point usually near the middle of the Z-shaped passivation curve using the positive-slope load line provided by the potentiostat, as described in section 2.3, and a voltage perturbation was superimposed. The DC component of the current and potential signals was not subtracted during the impedance measurement.

The obtained data generally had a precision within 10% at frequencies above 50 Hz and were noisy at lower frequencies. Often the steady-state polarization point appeared to shift during the impedance measurement as illustrated in figure 3-24, perhaps because the perturbation was not small enough, or because the system regulation along the passivation curve was not completely stable.

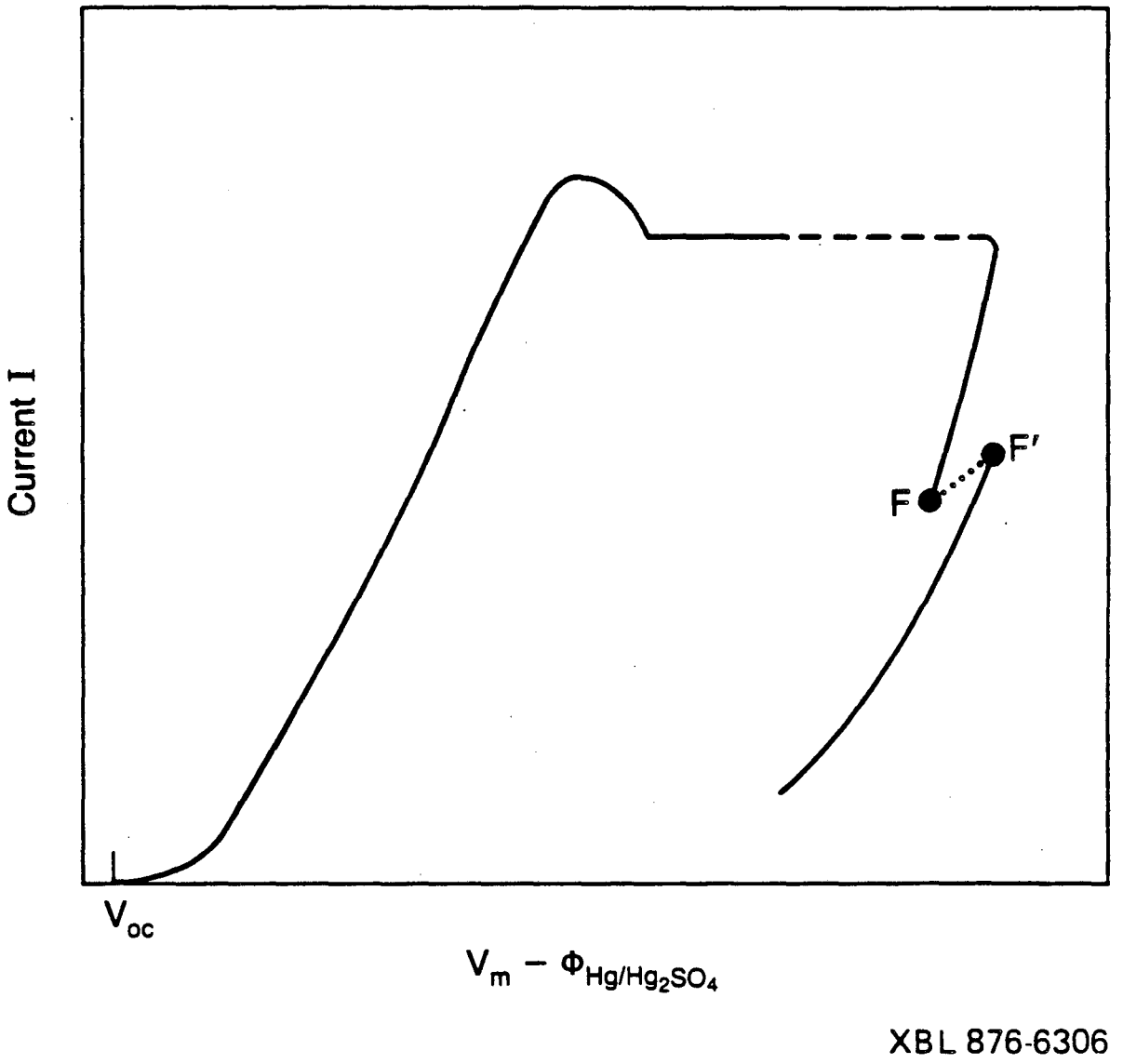

Figure 3-24. Shift of the steady-state polarization point from F to F' during the impedance measurement.

3.6.2. Electrode Dissolution Profiles

An interesting part of these experiments was observing the electrode dissolution profile, which can give insight into the passivation process. A part of the electrode dissolved rapidly, *i.e.*, was active, while the remaining part appeared unattacked, *i.e.*, was passive. The active part of the electrode appeared to dissolve uniformly, and its surface looked smooth and shiny after the experiment. The difference between the parts of the electode was so sharp, and the experiment lasted long enough that the overall shape of the dissolution profile could be seen after the experiment even without a microscope. Schematic diagrams of the observed dissolution profiles for the rotating hemispherical and disk electrodes are given in figure 3-25.

Under the experimental conditions used, the hemispherical electrodes dissolved much more near the equator than near the pole forming a sharp step. At higher currents (closer to the limiting current plateau) the same shape of the dissolution profile was observed with a larger area of the hemisphere dissolving, indicating that the hemisphere passivates first near the pole and as the system moves along the active-to-passive-transition curve, the passivated area increases toward the equator. The dissolution profiles of a passivating rotating hemisphere are not well understood. Some tentative qualitative explanations for the observed profiles are given in section 2.5.2.

Under the conditions used, the rotating disk electrodes dissolved rapidly in the outer ring part, while the center disk appeared passive. The area of the dissolved outer ring decreased as the electrode was

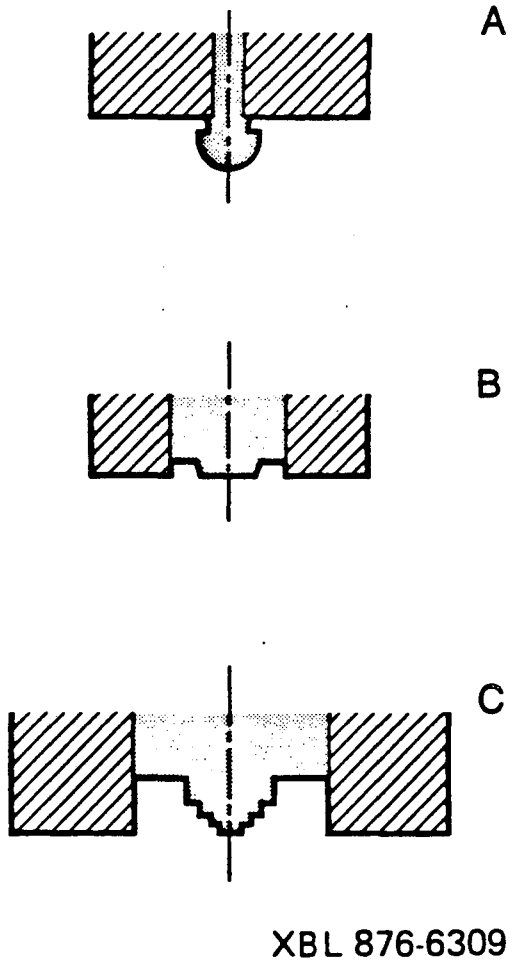

Figure 3-25. Schematic diagrams of the experimentally observed electrode dissolution profiles at the passivation curve. The shaded area represents the insulator and the dotted area represents the metal.
A - rotating hemisphere
B - rotating disk
C - rotating disk polarized successively at four points along the active-to-passive transition curve.

polarized at lower currents along the passivation curve. A particularly interesting profile was obtained for a disk electrode that was polarized successively at four points along the passivation curve (active to passive transition), spending 2-3 minutes at each point. Using a conventional optical microscope, four steps were seen on the electrode surface with the outer ring always dissolving more than the center disk (diagram C in figure 3-25). Dissolution profiles of a rotating disk electrode with a dissolved outer ring and a passive center disk were also observed by Epelboin and Gabrielli *et al.* (13, 17) at rotation speeds in the same range as those used here.

3.6.3. Results

The experimental impedance results are given in figures 3-26 through 3-29 for hemispherical and disk electrodes. All these impedance diagrams exhibit similar behavior. One may notice that the low-frequency capacitive loop occurs at roughly the same frequency range as one of the capacitive loops observed at the limiting current (figure 3-27).

These impedance diagrams are similar to those obtained by Gabrielli (13, Fig. 46) and Epelboin *et al.* (18, Fig. 14) for a rotating disk electrode. Some experimental impedance results for a rotating ring electrode along the passivation curve are given in (13, 14, 18). These authors (13, 14, 18) emphasize that having a zero-frequency-limit impedance (polarization resistance) greater than the infinite-frequency-limit impedance (solution ohmic resistance) corresponds to a

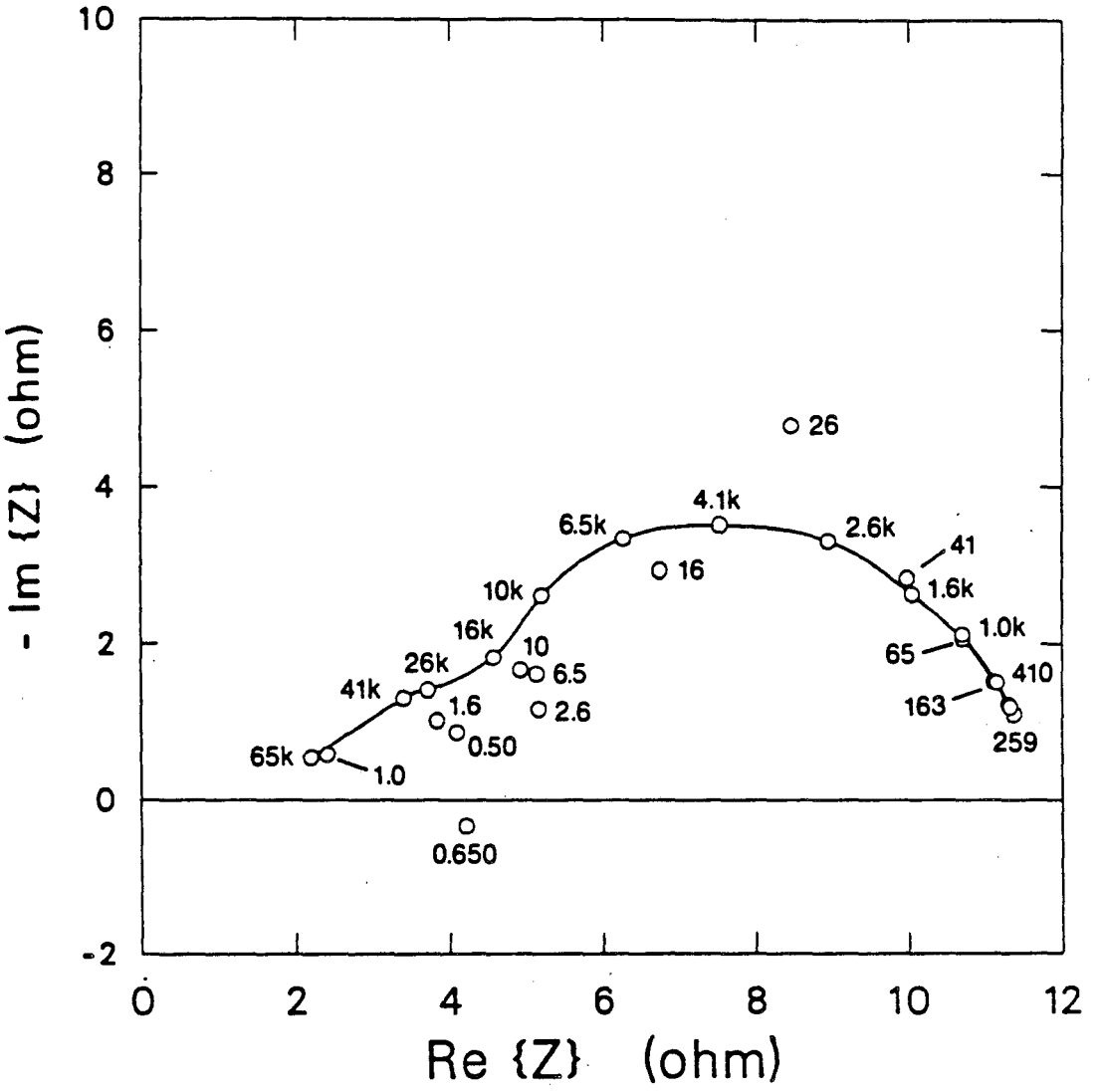

XBL 877-3142

Figure 3-26. Complex-plane plot of the impedance of a rotating hemisphere (d = 4 mm, Ω = 900 rpm) at the passivation curve. $\bar{V}$ = 0.65 V, $\bar{I}$ ≈ 125 mA, |ΔV| = 2.5 mV rms. Decreasing frequency sweep. The parameter is frequency in Hz.

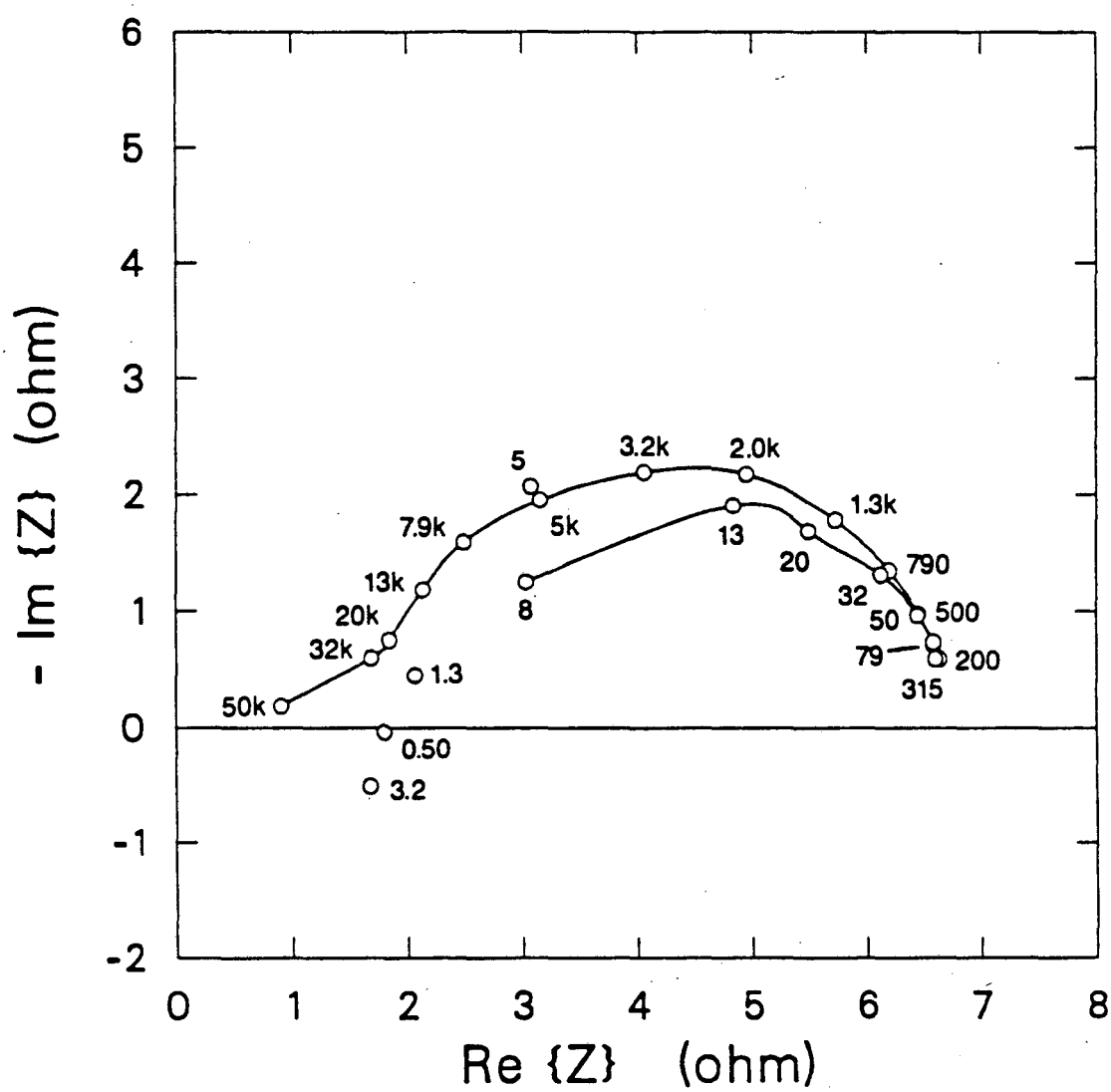

XBL 877-3141

Figure 3-27. Complex-plane plot of the impedance of a rotating hemisphere (d = 6.9 mm, Ω = 400 rpm) at the passivation curve. $\bar{V}$ = 0.7 V, $\bar{I}$ ≈ 180 mA, |ΔV| = 5 mV rms. Decreasing frequency sweep.

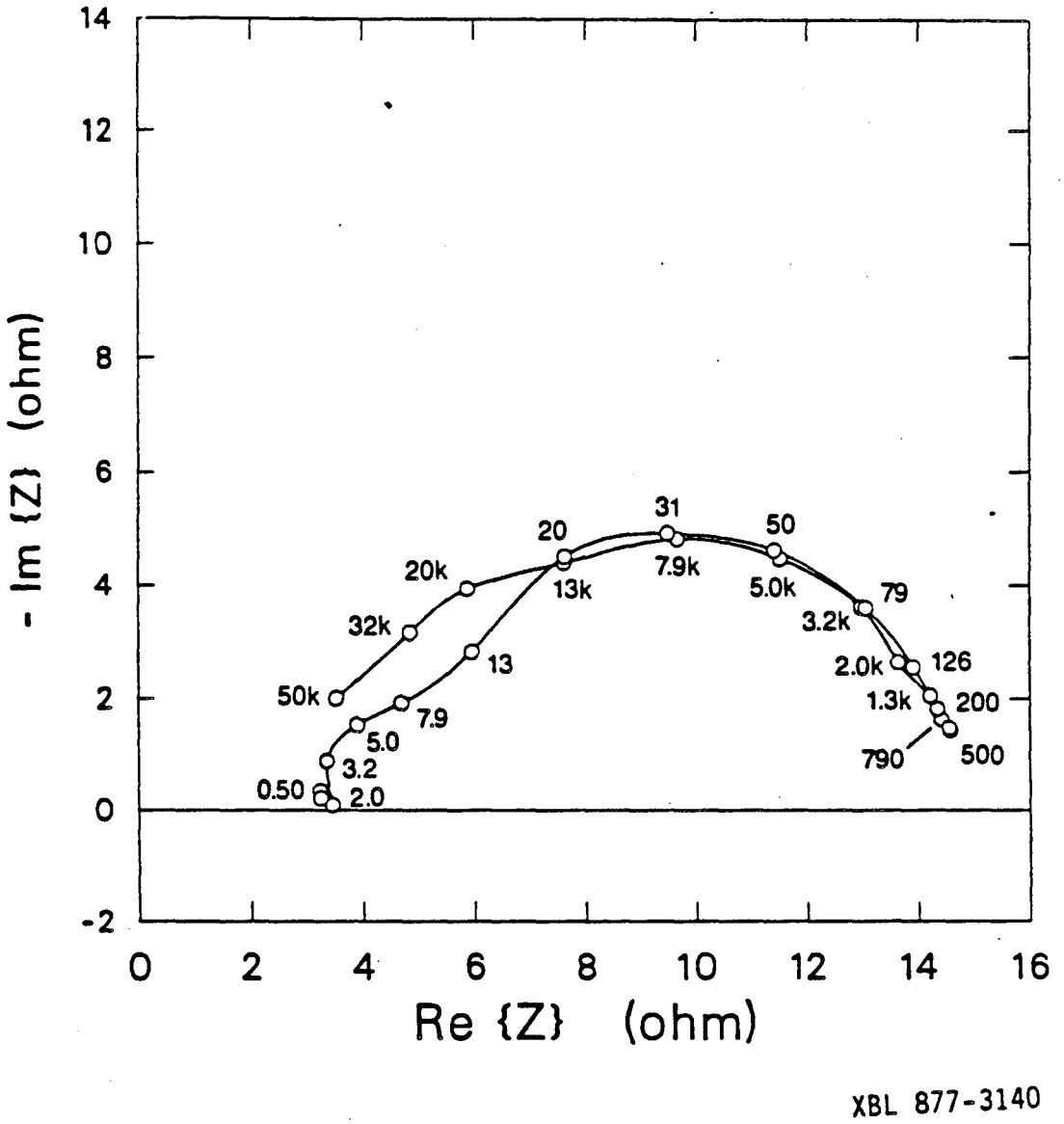

Figure 3-28. Complex-plane plot of the impedance of a rotating disk electrode (d = 3.2 mm, Ω = 1600 rpm) at the passivation curve. $\bar{V}$ = 0.35 V, $\bar{I}$ ≈ 60 mA, |ΔV| = 5 mV rms. Decreasing frequency sweep.

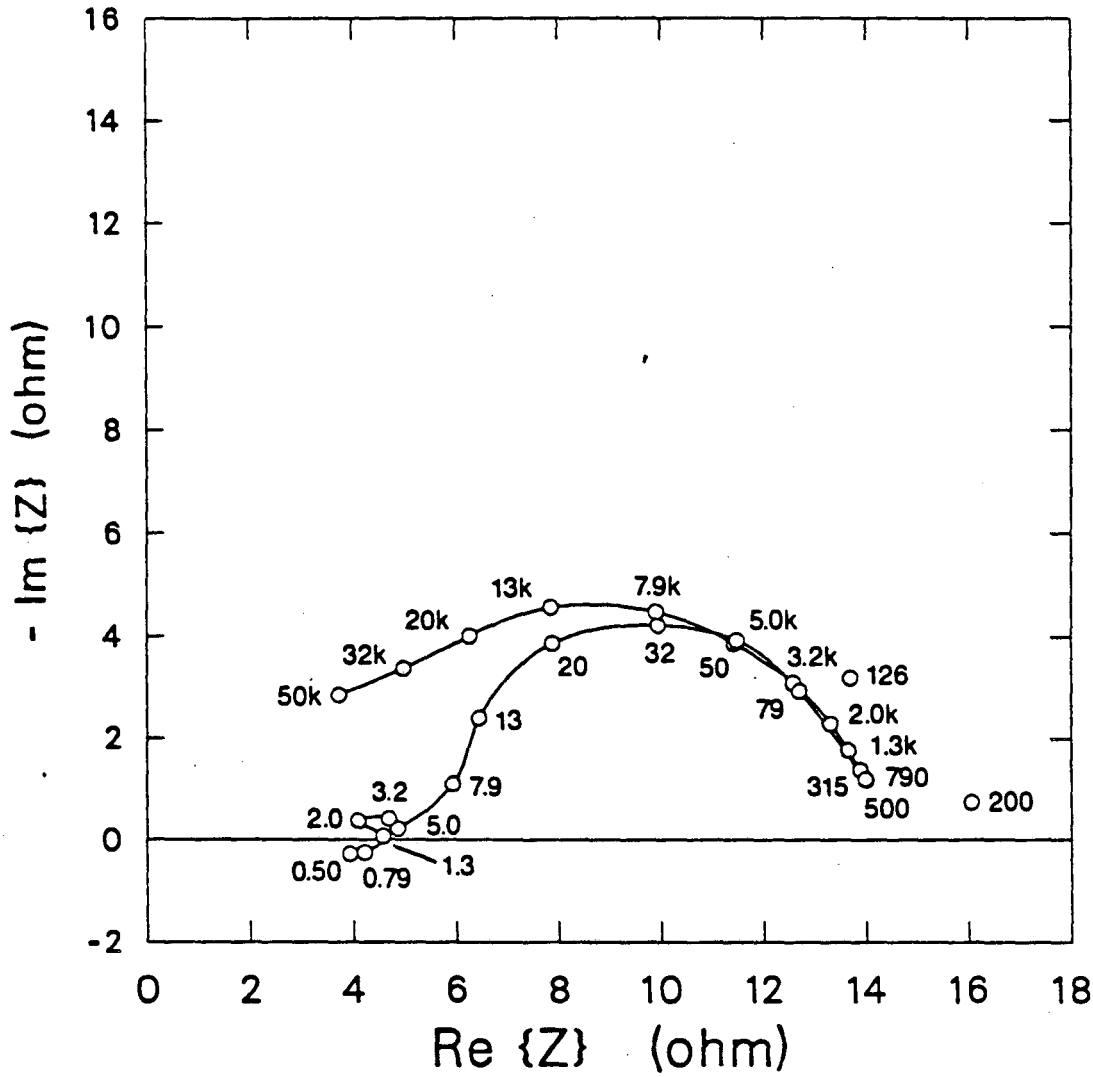

XBL 877-3139

Figure 3-29. Complex-plane plot of the impedance of a rotating disk electrode ($d = 4.9$ mm, $\Omega = 1600$ rpm) at the passivation curve. $\bar{V} = 0.4$ V, $\bar{I} \approx 70$ mA, $|\Delta V| = 5$ mV rms. Decreasing frequency sweep.

positive slope of the passivation curve and indicates multiple steady states of the electrochemical system even after correcting for the ohmic drop. However since the electrode is partly active and partly passive, such a straightforward interpretation of the impedance diagrams without rigorously taking into account all the occurring phenomena may not be valid.

3.7. Summary

The results of these experiments are summarized in figures 3-30 through 3-33, which show how the impedance varies with perturbation frequency and potential (or current).

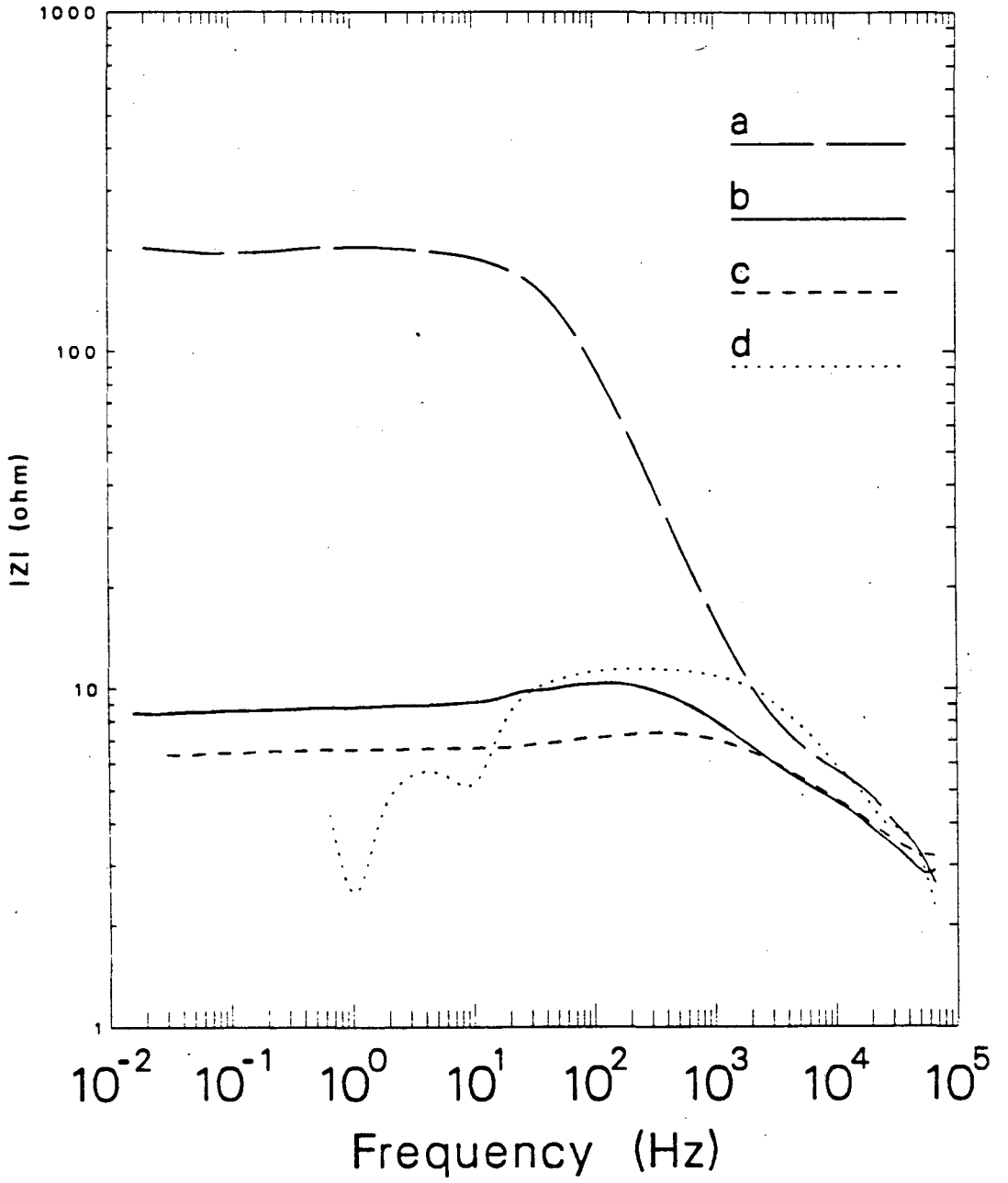

XBL 877-3082

Figure 3-30. The impedance of a rotating hemispherical electrode (d = 4 mm) at different potentials. a: $\bar{I}$ = 0 (experiment A); b: $\bar{V}$ = −0.850 V (experiment C); c: $\bar{V}$ = −0.800 V (see figure 3-15); d: $\bar{V}$ = 0.65 V, passivation (see figure 3-26). Bode plots — impedance magnitude.

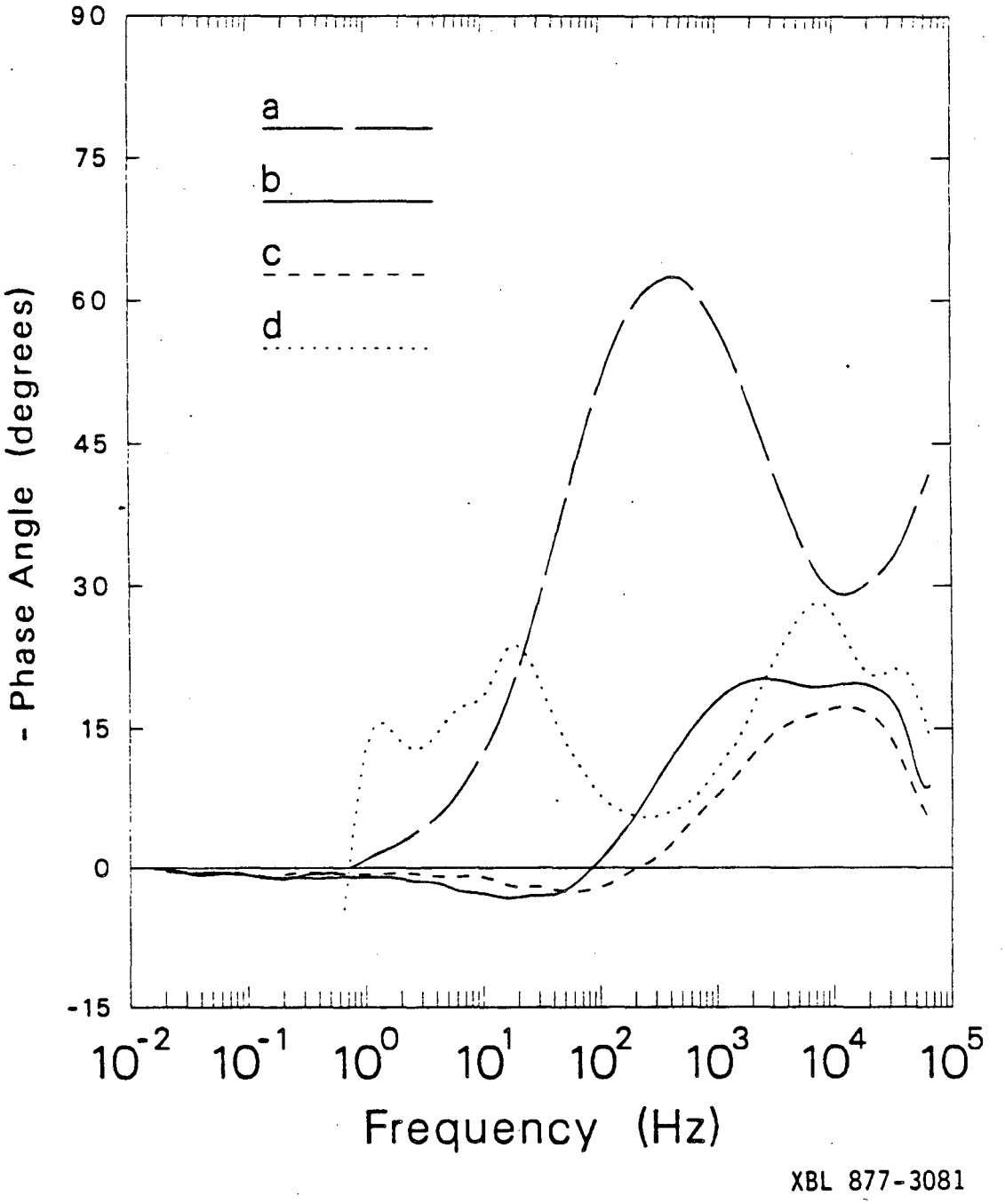

Figure 3-31. Bode plots — phase angle for the same experiments as in figure 3-30.

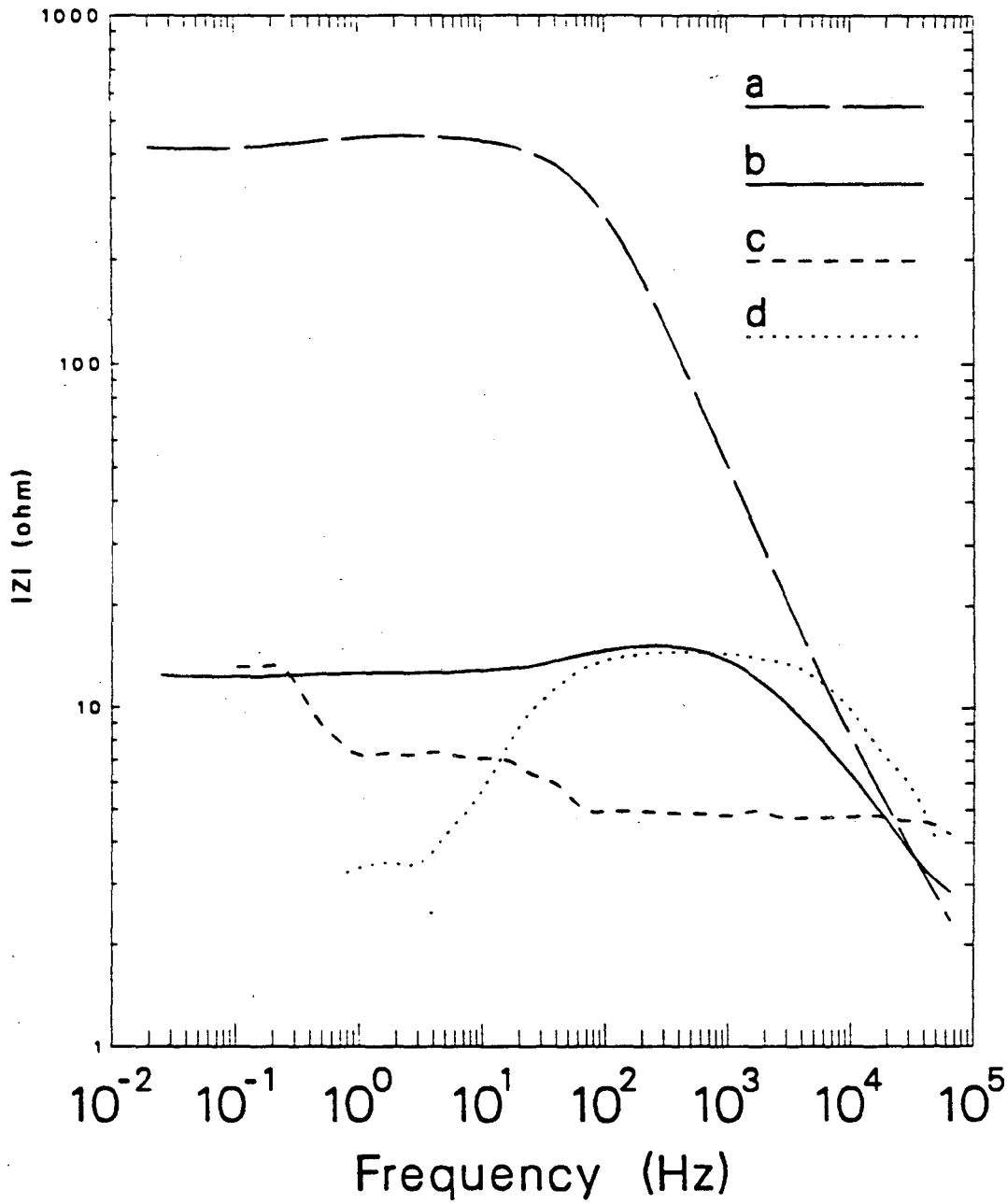

XBL 877-3134

Figure 3-32. The impedance of a rotating disk electrode (d = 3.2 mm, Ω = 1600 rpm) at different potentials. a: $\bar{I}$ = 0 (experiment B); b: $\bar{V}$ = −0.850 V (experiment D); c: $\bar{V}$ = −0.255 V, limiting current (see figure 3-22); d: $\bar{V}$ = 0.35 V, passivation (see figure 3-28). Bode plots — impedance magnitude.

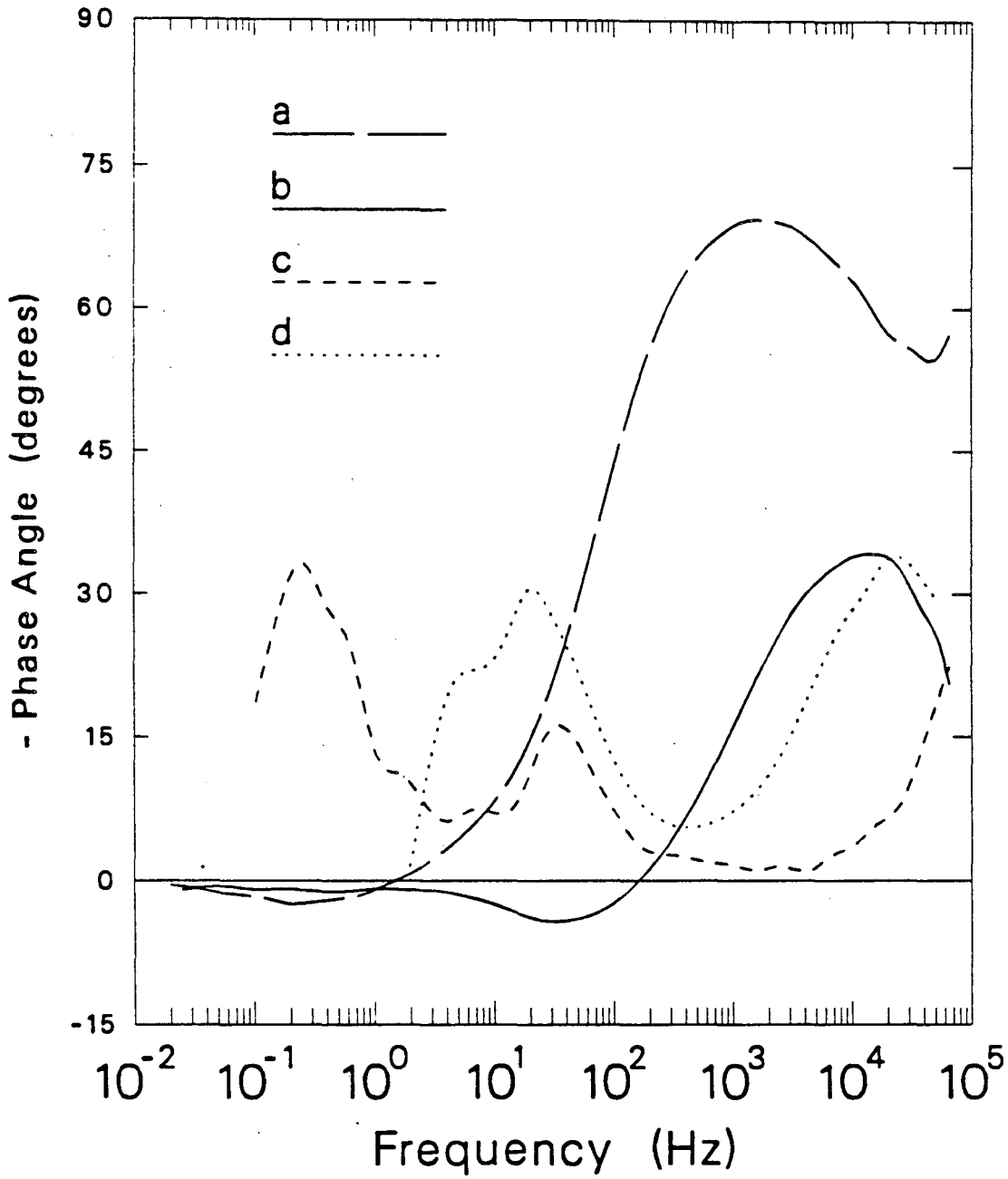

XBL 877-3135

Figure 3-33. Bode plots — phase angle for the same experiments as in figure 3-32.

References for Chapter 3

1. Philip P. Russell, *Corrosion of Iron: The Active - Passive Transition and Sustained Electrochemical Oscillations*, Ph. D. Dissertation, University of California, Berkeley, CA (1984).

2. F. Mansfeld, M. W. Kendig, and S. Tsai, "Recording and Analysis of AC Impedance Data for Corrosion Studies, II. Experimental Approach and Results," *Corrosion*, **38**, 570-580 (1982).

3. Claude Gabrielli, *Identification of Electrochemical Processes by Frequency Response Analysis*, Solartron Instrumentation Group monograph, The Solartron Electronic Group Ltd., Farnborough, England (1980).

4. William H. Smyrl, "Digital Impedance for Faradaic Analysis, I. Introduction to Digital Signal Analysis and Impedance Measurements for Electrochemical and Corrosion Systems," *Journal of the Electrochemical Society*, **132**, 1551-1555 (1985).

5. M. Keddam, O. R. Mattos, and H. Takenouti, "Reaction Model for Iron Dissolution Studied by Electrode Impedance, I. Experimental Results and Reaction Model," *Journal of the Electrochemical Society*, **128**, 257-266 (1981).

6. William H. Smyrl and Larry L. Stephenson, "Digital Impedance for Faradaic Analysis, III. Copper Corrosion in Oxygenated 0.1N HCl," *Journal of the Electrochemical Society*, **132**, 1563-1567 (1985).

7. W. J. Lorenz and F. Mansfeld, "Determination of Corrosion Rates by Electrochemical DC and AC Methods," *Corrosion Science*, 21, 647-672 (1981).

8. John Newman, "Frequency Dispersion in Capacity Measurements at a Disk Electrode," *Journal of the Electrochemical Society*, 117, 198-203 (1970).

9. Kemal Nişancioğlu and John Newman, "Current Distribution on a Rotating Sphere below the Limiting Current," *Journal of the Electrochemical Society*, 121, 241-246 (1974).

10. John Newman, *Electrochemical Systems*, Prentice-Hall, Inc., Englewood Cliffs, N.J. (1973).

11. B. Bechet, I. Epelboin and M. Keddam, "New Data from Impedance Measurements Concerning the Anodic Dissolution of Iron in Acidic Sulphuric Media," *Journal of Electroanalytical Chemistry and Interfacial Electrochemistry*, 76, 129-134 (1977).

12. Michael G. Miller, *The Influence of Fluid Velocity on the Corrosion of Iron in 1M Sulfuric Acid*, M. S. Thesis, University of Virginia, May 1985.

13. Claude Gabrielli, *Régulation et Analyse des Systèmes à Etats Stationnaires Multiples. Application à l'Identification des Processus de Passivation Electrochimique du Fer*, Thèse de Doctorat, Université de Paris, No. C.N.R.S. A.O. 8060 (1973), Editions *Métaux, Corrosion, Industrie*, No. 573, 574, 577, 578 (1973).

14. I. Epelboin, C. Gabrielli, M. Keddam and H. Takenouti, "A Model of the Anodic Behaviour of Iron in Sulphuric Acid Medium," *Electrochimica Acta*, **20**, 913-916 (1975).

15. I. Epelboin, C. Gabrielli, and M. Keddam, "Rôle de la Diffusion dans les Phénomènes de Passivation et de Corrosion Localisée du Fer en Milieu Acide," *Corrosion Science*, **15**, 155-171 (1975).

16. M. Keddam, O.R. Mattos and H. Takenouti, "Mechanism of Anodic Dissolution of Iron-Chromium Alloys Investigated by Electrode Impedances—I. Experimental Results and Reaction Model," *Electrochimica Acta*, **31**, 1147-1158 (1986).

17. I. Epelboin, C. Gabrielli, M. Keddam, J.-C. Lestrade, and H. Takenouti, "Passivation of Iron in Sulfuric Acid Medium," *Journal of the Electrochemical Society*, **119**, 1632-1637 (1972).

18. I. Epelboin, C. Gabrielli, M. Keddam, and H. Takenouti, "The Study of the Passivation Process by the Electrode Impedance Analysis," *Comprehensive Treatise of Electrochemistry*, Vol. 4, chapter 3, J. O'M. Bockris, B. E. Conway, E. Yeager, and R. E. White, Editors, Plenum Press, New York (1981).

CHAPTER 4

Application of the Kramers-Kronig Relations to Test the Consistency of Electrochemical Impedance Data

4.1. Introduction

Chapter 3 has presented a variety of experimental impedance results, exhibiting positive and negative imaginary parts or multiple loops in a complex plot. Such results are not well understood, and one may question the validity or accuracy of impedance data, especially considering the difficulty of obtaining reproducible experimental data at very high or very low frequencies.

The Kramers-Kronig (K-K) relations provide a means of testing the consistency of electrochemical impedance data. The use of the K-K relations is analogous to the use of the Gibbs-Duhem equation in thermodynamics for testing the consistency of multicomponent equilibrium data. The K-K relations arise on a mathematical basis and give the interrelationship between the real and imaginary parts of complex functions that satisfy certain conditions.

In this chapter, we first outline the equations and underlying assumptions for the Kramers-Kronig relations, and briefly review the literature on the use of these relations in electrochemistry. We then discuss the significance of the K-K relations for electrochemical impedance studies and introduce the questions that arise in their appli-

cation. We then present, in detail, a method for calculating the real part of the impedance from the imaginary part, and *vice versa*, by means of the K-K relations.

More specifically, we apply the method to test the consistency of data from four different experiments (A through D in chapter 3) with the K-K relations. These experimental data are chosen because they show some interesting behavior and they are fairly reproducible, so that one may expect that the data will satisfy the K-K relations. The method given here is general and can be applied to experimental data as well as theoretical results.

4.1.1. The Kramers-Kronig Relations for the Impedance

The impedance Z of a system is expressed as a complex function of the frequency ω :

$$Z(\omega) = Z_R(\omega) + jZ_I(\omega) \quad . \qquad [4\text{-}1]$$

The Kramers-Kronig relations (1,2) for the impedance are:

$$Z_R(\omega_c) - Z_\infty = -\frac{1}{\pi} \fint_{-\infty}^{\infty} \frac{Z_I(\omega)}{\omega - \omega_c} d\omega \qquad [4\text{-}2]$$

and

$$Z_I(\omega_c) = \frac{1}{\pi} \fint_{-\infty}^{\infty} \frac{Z_R(\omega) - Z_\infty}{\omega - \omega_c} d\omega \ , \qquad [4\text{-}3]$$

where $\fint$ denotes the Cauchy principal value of the integral and $Z_\infty = \lim_{\omega \to \infty} Z(\omega)$.

Since $Z_R(\omega)$ is even and $Z_I(\omega)$ is odd w.r.t. ω , the Kramers-Kronig relations become

$$Z_R(\omega_c) - Z_\infty = -\frac{2}{\pi} \fint_0^\infty \frac{\omega Z_I(\omega)}{\omega^2 - \omega_c^2}\, d\omega \qquad [4\text{-}4]$$

and

$$Z_I(\omega_c) = \frac{2\omega_c}{\pi} \fint_0^\infty \frac{Z_R(\omega) - Z_\infty}{\omega^2 - \omega_c^2}\, d\omega \ . \qquad [4\text{-}5]$$

A complete mathematical derivation of these equations is given by several authors (1-5). Thus the Kramers-Kronig relations give the real part of the impedance at a particular frequency (ω_c) as an integral of the imaginary part over all frequencies from zero to infinity, and *vice versa*.

Several alternative forms of the K-K relations are given by Bode (3). Equations 4-6 through 4-8 are forms that have been used in the electrochemical literature, but will not be used here.

$$Z_R(\omega_c) - Z_R(0) = -\frac{2\omega_c^2}{\pi} \fint_0^\infty \frac{Z_I(\omega)/\omega}{\omega^2 - \omega_c^2}\, d\omega \qquad [4\text{-}6]$$

$$\phi(\omega_c) = \frac{1}{\pi} \int_{-\infty}^{\infty} \frac{d \ln|Z(\omega)|}{du} \ln\left(\coth \frac{|u|}{2}\right) du \qquad [4\text{-}7]$$

$$\ln \frac{|Z(\omega_c)|}{|Z_\infty|} = -\frac{1}{\pi\omega_c} \int_{-\infty}^{\infty} \frac{d(\omega\phi)}{du} \ln\left(\coth \frac{|u|}{2}\right) du \ , \qquad [4\text{-}8]$$

where $u = \ln(\omega/\omega_c)$ and ϕ is the phase angle. The last two equations (6) allow one to calculate the phase angle from the amplitude of the

impedance, and *vice versa*. However, they involve differentiation of numerical data in addition to integration, and calculations based on these equations would be less accurate.

The main feature that the impedance function $Z(\omega)$ must have in order to satisfy the Kramers-Kronig relations is being analytic in the lower half of the complex frequency plane. This feature is a consequence of the causality principle in physics, which requires the time variable to be positive in a Laplace transform formulation of the impedance (4,5). Physically, the conditions that an electrochemical system must fulfill in order to have an analytic impedance function, which would therefore obey the K-K relations, may be stated as:

Linearity. The system must have a linear relationship between current and voltage. This condition is usually fulfilled by using small amplitude perturbations.

Finite values. The impedance function $Z(\omega)$ must be well behaved near $\omega = 0$ and finite for all $\omega > 0$, including $\omega \longrightarrow \infty$. The impedance of an electrochemical system normally has these properties.

Stability. The system must be stable so that there are no poles, other than the simple poles $\omega = \omega_c$ and $\omega = 0$, in the lower half-plane. Physically, the effect of the perturbation should die out when the perturbation ceases so that the system returns to its original steady state. This could be a controversial condition, particularly for a corroding system, which inherently changes with time.

4.1.2. Literature Review

The Kramers-Kronig relations are used in physics (4) and in the analysis of electrical circuits (3). They have been used in electrochemistry, only recently, by some investigators.

In the early 1970's, Tyagi and Kolbasov (7) used the K-K relations to calculate the phase angle at some frequencies from measurements of the amplitude of the impedance for two redox systems. Van Meirhaeghe *et al.* (8) have advocated the importance of the K-K relations in the analysis of electrochemical impedance. Tuck (9) has carried out some calculations using the K-K relations to examine the validity of experimental impedance data for aluminum in acetate solution.

Kendig and Mansfeld (10) have proposed a method for determining the polarization resistance and hence the corrosion rate, using a simplified expression based on the K-K relations (equations 4-4, 4-6). They only integrate the imaginary part of the impedance over a limited range, from the highest experimental frequency to the frequency corresponding to the maximum value of $-Z_I$, assuming that Z_I is symmetric w.r.t. $\ln \omega$. This assumption severely limits the applicability and accuracy of the proposed method.

D. Macdonald *et al.* (11) also use equations 4-4 and 4-6 to calculate the polarization resistance from experimental impedance data for corrosion systems. They then compare the calculated value for the polarization resistance with that obtained by subtracting the infinite-frequency intercept from the zero-frequency intercept of the experimental complex plot, and claim that this method is a simple, accurate, and

convenient tool for assesing the validity of corrosion impedance data. This is rather a limited and approximate test, as it relies on the calculation of a single value, it ignores the integrals at $\omega \longrightarrow 0$ and $\omega \longrightarrow \infty$, and it includes significant uncertainty in determining the polarization resistance directly from experimental impedance plots. Note also that these authors give the opposite sign in equation 4-4 and in equation 4-6.

Cahan *et al.* (6) use another form of the K-K relations (equation 4-7) to calculate the phase angle from the magnitude of the impedance and thus test the consistency of experimental data. A disadvantage of this method is that it involves differentiation of experimental data, which magnifies errors. Cahan *et al.* include extrapolation of the experimental data to zero and infinite frequency in their calculations, contrary to the previous workers, who assume that the integrals at the low and high frequency ends are negligible.

More recently, M. Urquidi-Macdonald *et al.* (12) present an algorithm for calculating the real part of the impedance from the imaginary part, and *vice versa*, using the K-K relations for experimental data. This algorithm includes polynomial fitting of the data, numerical integration, and some not adequately specified extrapolation. Notice that Macdonald *et al.* (12) treat the singularities in the integrals incorrectly.

Jakšić and Newman (5) give a more rigorous method for evaluating the real part from the imaginary part of the theoretical impedance for a disk electrode, and *vice versa*, from the K-K relations (equations 4-4,

4-5). They show that the theory for the impedance of a rotating disk electrode, developed earlier by Newman (13), is consistent with the K-K relations.

4.1.3. Significance of the Kramers-Kronig Relations for the Electrochemical Impedance

The Kramers-Kronig relations allow the calculation of either the real or imaginary part of a complex function, such as the impedance or the dielectric constant, from the corresponding part. Thus they can be valuable in physics for calculating certain unknown quantities from available empirical data (4). The K-K relations are also important for the analysis of electrical circuits (3).

In electrochemical impedance studies, one is very unlikely to use the K-K relations to calculate a quantity that is not already known. Experimental measurements give both the real and imaginary parts of the impedance with roughly the same accuracy, and theoretical models naturally give expressions for both parts. The significance of the Kramers-Kronig relations then is that they provide a test for the accuracy and consistency of experimental data, or for the validity of theoretical results. The test consists of calculation of the real or imaginary part of the impedance through the K-K relations and comparison of the calculated results with the experimental or theoretical values.

Such a test is particularly valuable because it is difficult to obtain reliable impedance data, as we have emphasized earlier, and one needs to subject impedance data to rigorous checks before one can draw

any definitive conclusions about the system behavior from the available data.

4.1.4. Some Questions

How can we interpret the results of a Kramers-Kronig consistency test for a set of data? The conditions for the application of the K-K relations are quite general, with the possible exception of the stability condition for certain systems, and so we expect good data to obey the K-K relations. If a set of data is found to be consistent with the K-K relations, the data may still contain other errors or artifacts. For instance, extraneous resistances, capacitances, or inductances, in the measuring instrumentation, will produce data which satisfy the K-K relations.

If a set of data is found to be inconsistent with the K-K relations and if we assume that the basic applicability conditions are not violated, we need to consider whether the data contain serious errors, or the evaluation of the integrals over an infinite frequency range is not accurate enough. Comparing the values calculated through the K-K relations with the data values can give insight into the source and magnitude of the discrepancy. In particular, a significant deviation over some frequency range suggests a systematic error in the data, and deviations of single points suggest random errors, such as reproducibility of experimental data or noise.

How do we carry out calculations with the Kramers-Kronig relations? There are several questions we need to consider. First, how should we

treat experimental data? It is common practice to fit experimental data by a smooth or piecewise smooth analytic function to reduce the effect of noise or random errors and subsequently compare the smoothed experimental values with calculated values or predicted trends. The results may then depend on the accuracy of the fit; furthermore, useful information (insight into any deviations) may be lost through the process of forcing the data to be smooth. Alternatively, we can use the experimental data directly, perhaps assuming an interpolating function between successive experimental points. However, this procedure may overemphasize individual data points, which may be bad.

Another critical question is how to extrapolate data in frequency ranges where there are no data. According to the K-K relations, the integrals are to be evaluated over the entire frequency range from zero to infinity, but data are available over only a finite range. One may assume that the integrals at the low and high frequency ends are negligible, but this can be a bad assumption. Therefore one needs to investigate the asymptotic behavior of the system as $\omega \longrightarrow 0$ and $\omega \longrightarrow \infty$.

This is not a straightforward task, since good experimental data are most difficult to obtain at very low or very high frequencies, where several experimental artifacts may be present. The theoretical analysis of the electrochemical impedance is also most uncertain or controversial at those frequencies. Therefore we need to make *a priori* assumptions about the least well known behavior of the system in order to calculate any results from the K-K relations, and then change our assumptions, if necessary, to obtain a consistent behavior.

Finally, when can we say that the data are consistent with the Kramers-Kronig relations? With currently available impedance measurement equipment, good experimental data have a precision within 1% (chapter 3). Considering also the uncertainty in the calculations, what is the maximum acceptable difference between the data and the results calculated by the K-K relations?

These questions will be explored as we discuss in detail the method of using the Kramers-Kronig relations and as we apply the method to four different experiments (chapter 3, figures 3-3, 3-8, 3-10, and 3-13):

Experiment A: hemisphere, $d = 4.0$ mm, $\Omega = 900$ rpm, $\bar{I} = 0$.

Experiment B: disk, $d = 3.2$ mm, $\Omega = 1600$ rpm, $\bar{I} = 0$.

Experiment C: hemisphere, $d = 3.9$ mm, $\Omega = 1600$ rpm, $\bar{V} = -0.850$ V.

Experiment D: disk, $d = 3.2$ mm, $\Omega = 1600$ rpm, $\bar{V} = -0.850$ V.

The computer programs used to implement the method are given in appendix A.

4.2. Integration Scheme

4.2.1. Integrals

We need to evaluate the integrals in the Kramers-Kronig equations 4-4 and 4-5, to calculate the real part of the impedance from the imaginary part, and *vice versa*. These integrals have a singularity at $\omega = \omega_c$ and therefore cannot be evaluated directly. The behavior of the integrals is illustrated in figures 4-1 and 4-2, which give the integrand calculated for each data point, for experiment A. Notice that

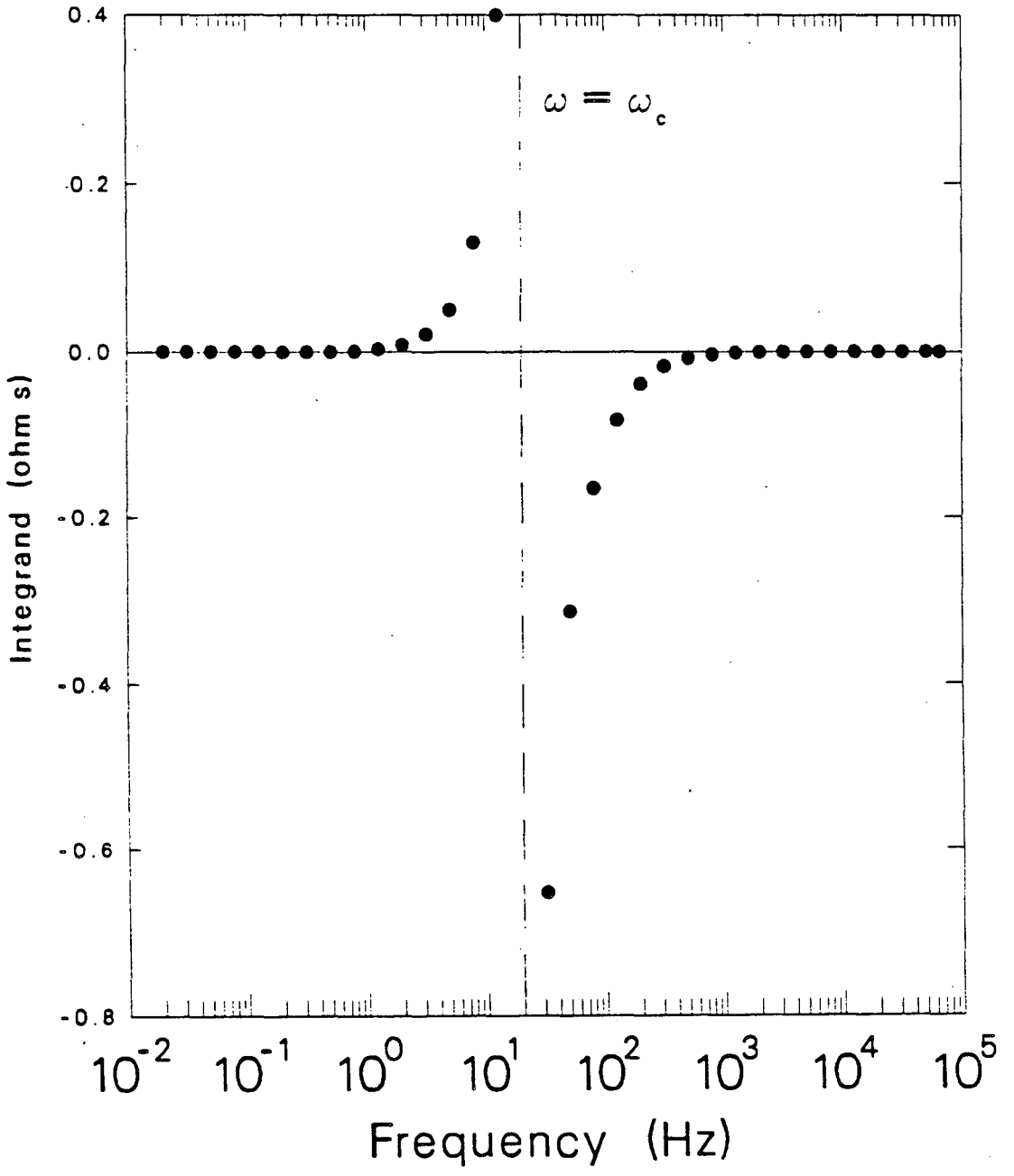

XBL 877-3116

Figure 4-1. Integrand in equation 4-4 for the calculation of $Z_R(\omega_c)$:

• $\dfrac{\omega Z_I(\omega)}{\omega^2 - \omega_c^2}$ values from experiment A, $\omega_c = 2\pi \cdot 20\ s^{-1}$.

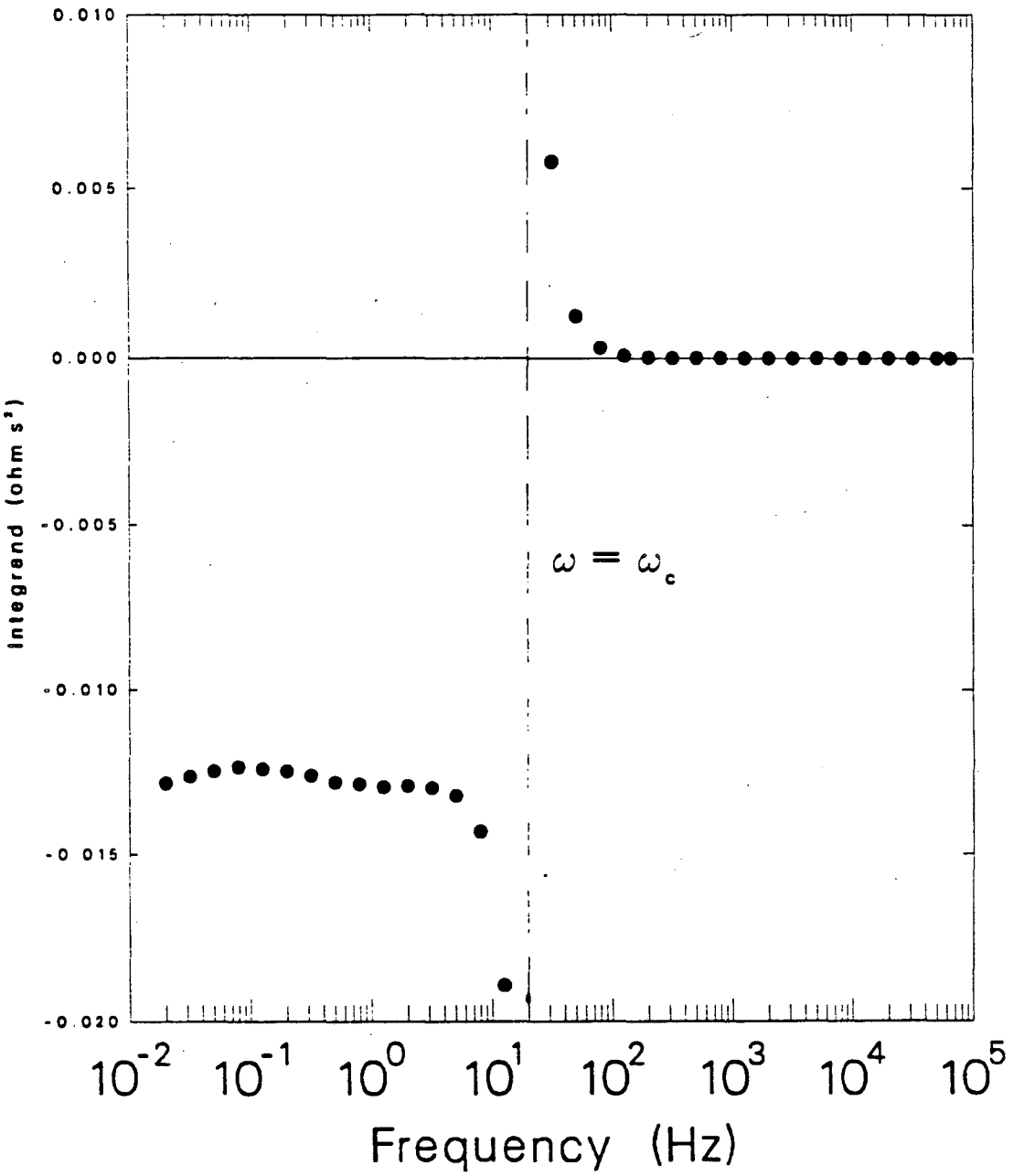

XBL 877-3117

Figure 4-2. Integrand in equation 4-5 for the calculation of $Z_I(\omega_c)$:

• $\dfrac{Z_R(\omega)}{\omega^2 - \omega_c^2}$ values from experiment A, $\omega_c = 2\pi \cdot 20\ s^{-1}$.

the integrand for both the real and the imaginary part approaches $-\infty$ as $\omega \longrightarrow \omega_c$ from the negative (left) side and $+\infty$ as $\omega \longrightarrow \omega_c$ from the positive (right) side.

To avoid this singularity, we use the relation

$$\oint_0^\infty \frac{d\omega}{\omega^2 - \omega_c^2} = 0 \ , \qquad [4\text{-}9]$$

and write the integrals in a different form:

$$Z_R(\omega_c) - Z_\infty = -\frac{2}{\pi} \int_0^\infty \frac{\omega Z_I(\omega) - \omega_c Z_I(\omega_c)}{\omega^2 - \omega_c^2} \, d\omega \qquad [4\text{-}10]$$

$$Z_I(\omega_c) = \frac{2\omega_c}{\pi} \int_0^\infty \frac{Z_R(\omega) - Z_R(\omega_c)}{\omega^2 - \omega_c^2} \, d\omega \qquad [4\text{-}11]$$

Equations 4-10 and 4-11 represent a form of the Kramers-Kronig relations that contains no singularities. Since the singularities have been effectively eliminated from the integrals, there is no longer a need to refer to the Cauchy principal value. Now the integrals are well behaved and should present no numerical difficulties in their evaluation.

The integrands in equations 4-10 and 4-11 are shown in figures 4-3 and 4-4 respectively, for experiment A. The magnitude of the integrand changes drastically within roughly two frequency decades, near $\omega = \omega_c$, and varies much less away from $\omega = \omega_c$. The integrands approach zero as $\omega \longrightarrow \infty$ and some constant non-zero value as $\omega \longrightarrow 0$. This is the general behavior expected due to the factor $(\omega^2 - \omega_c^2)$ in the denominator.

Alternatively, we can write the integrals in equations 4-10 and 4-11 as

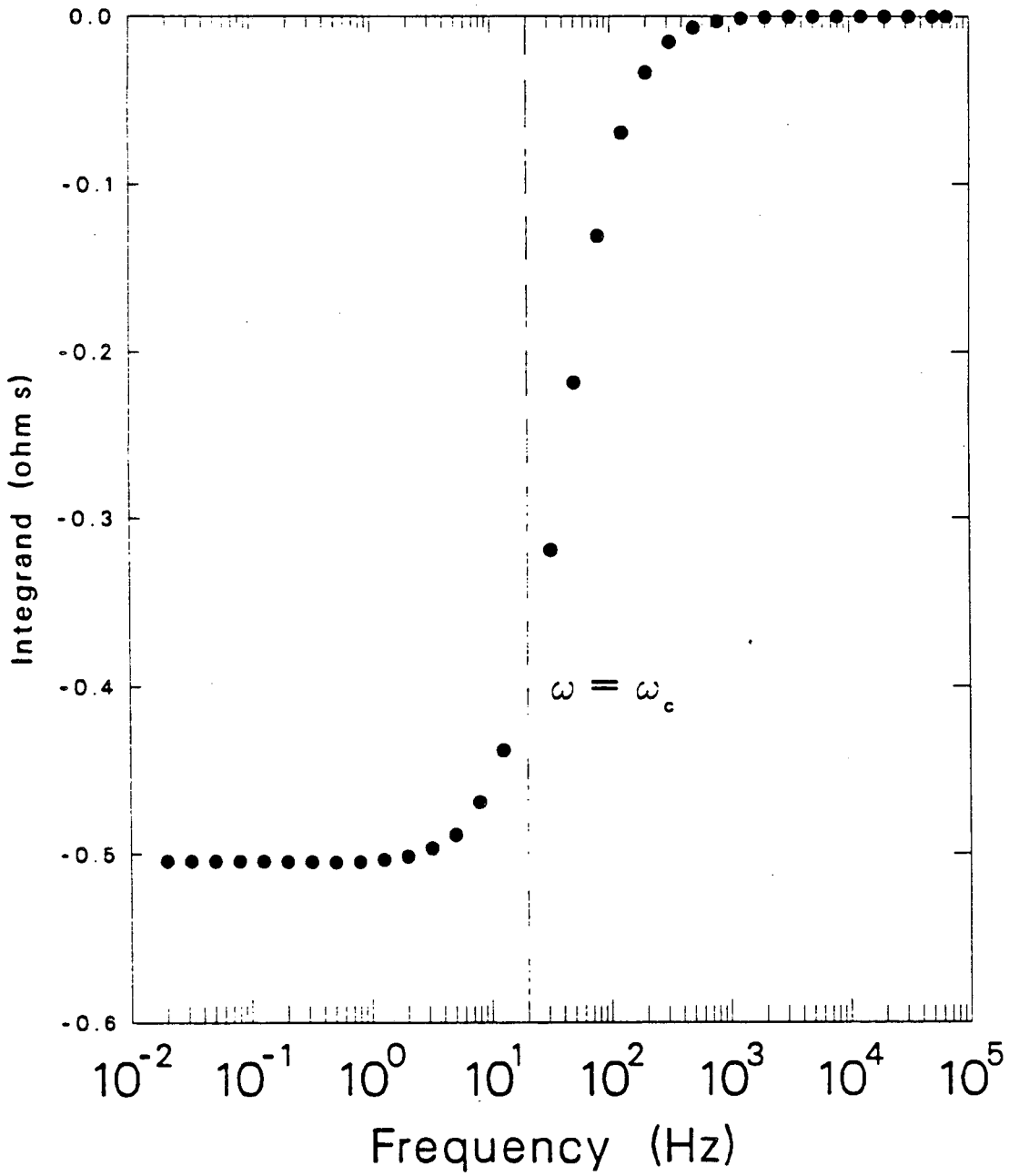

XBL 877-3119

Figure 4-3. Integrand in equation 4-10 for the calculation of $Z_R(\omega_c)$:

• $\dfrac{\omega Z_I(\omega) - \omega_c Z_I(\omega_c)}{\omega^2 - \omega_c^2}$ values from experiment A, $\omega_c = 2\pi \cdot 20\ s^{-1}$.

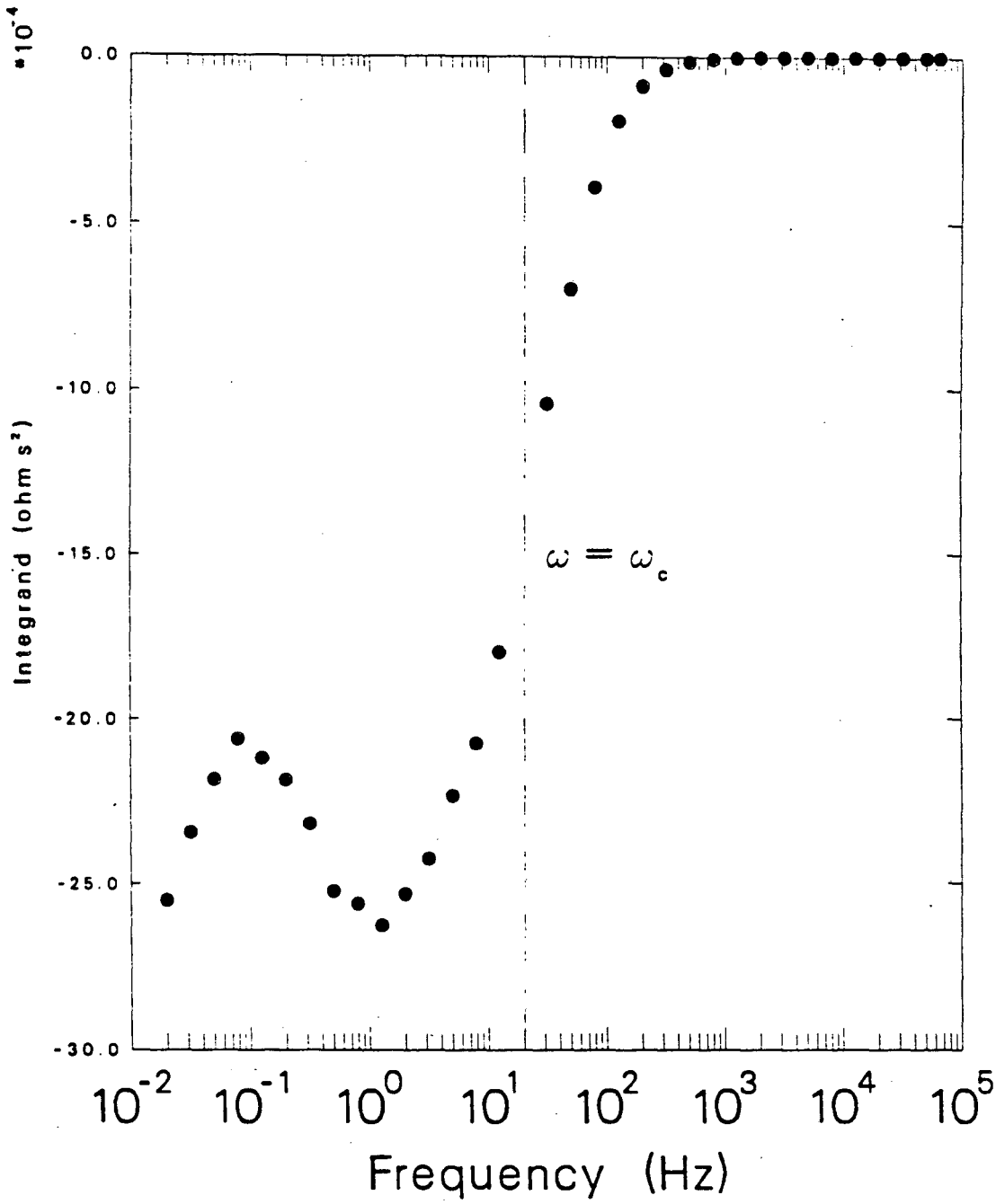

XBL 877-3118

Figure 4-4. Integrand in equation 4-11 for the calculation of $Z_I(\omega_c)$:

• $\dfrac{Z_R(\omega) - Z_R(\omega_c)}{\omega^2 - \omega_c^2}$ values from experiment A, $\omega_c = 2\pi \cdot 20\ s^{-1}$.

$$Z_R(\omega_c) - Z_\infty = -\frac{2}{\pi}\int_0^\infty \frac{\omega Z_I(\omega) - \omega_c Z_I(\omega_c)}{\omega^2 - \omega_c^2}\,\omega\, d(\ln\omega) \qquad [4\text{-}12]$$

and

$$Z_I(\omega_c) = \frac{2\omega_c}{\pi}\int_0^\infty \frac{Z_R(\omega) - Z_R(\omega_c)}{\omega^2 - \omega_c^2}\,\omega\, d(\ln\omega)\ , \qquad [4\text{-}13]$$

where the integration variable is $\ln\omega$ instead of ω . Figures 4-5 and 4-6 show the integrands above, for experiment A.

Evaluating the integrals according to equations 4-12 and 4-13 may be advantageous if the integrand is a simpler function of $\ln\omega$ rather than ω . Evaluating the integrals both linearly, according to equations 4-10 and 4-11, and logarithmically, according to equations 4-12 and 4-13, provides a check on the accuracy of the calculations.

In the following discussion, we will focus on equations 4-10 and 4-11 for the calculation of the real and imaginary part of the impedance. The integrals are evaluated as the sum of three terms:

$$\int_0^\infty = \int_0^{\omega_{min}} + \int_{\omega_{min}}^{\omega_{max}} + \int_{\omega_{max}}^\infty \qquad [4\text{-}14]$$

where $\omega_{min} \le \omega \le \omega_{max}$ is the experimental data frequency range.

4.2.2. Fitting / Interpolation Functions

In this section, we consider integration over the experimental frequency range only. We will consider integration over the low and high frequency ends in section 4.3.

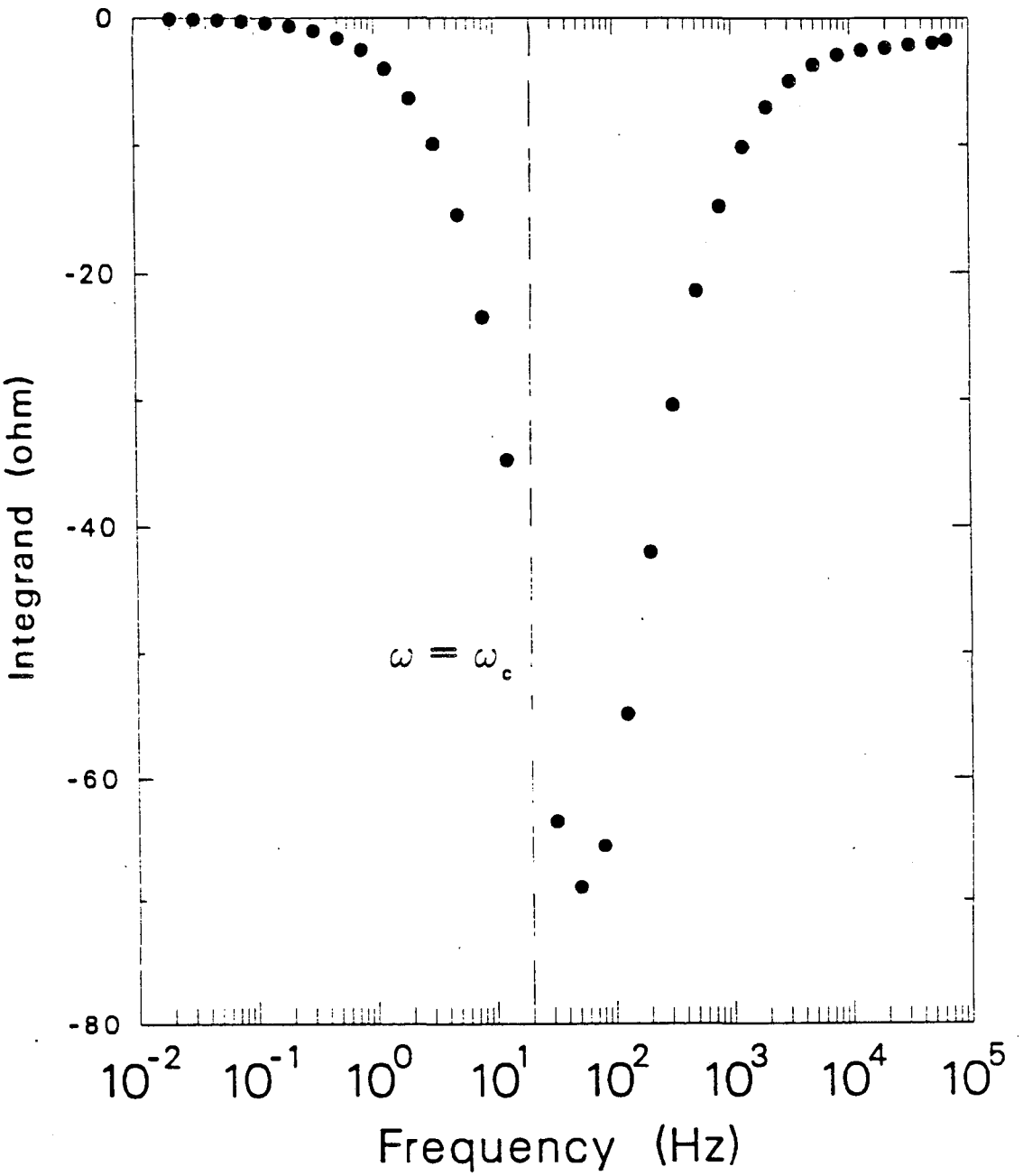

XBL 877-3120

Figure 4-5. Integrand in equation 4-12 for the calculation of $Z_R(\omega_c)$:

• $\dfrac{\omega Z_I(\omega) - \omega_c Z_I(\omega_c)}{\omega^2 - \omega_c^2}\,\omega$ values from experiment A, $\omega_c = 2\pi \cdot 20\ s^{-1}$.

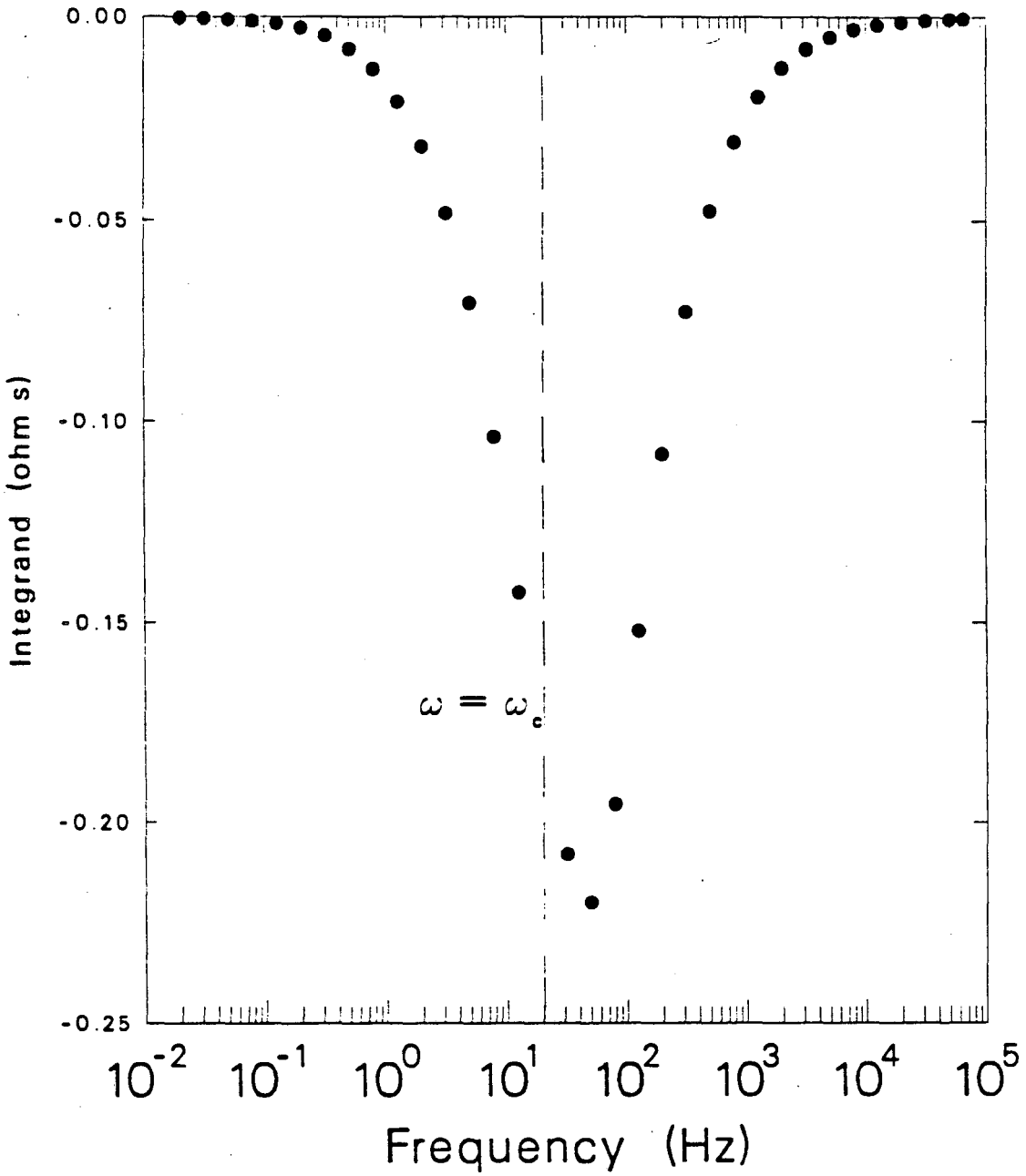

XBL 877-3121

Figure 4-6. Integrand in equation 4-13 for the calculation of $Z_I(\omega_c)$:

• $\dfrac{Z_R(\omega) - Z_R(\omega_c)}{\omega^2 - \omega_c^2}\,\omega$ values from experiment A, $\omega_c = 2\pi \cdot 20\ s^{-1}$.

We need to integrate experimental data according to the Kramers-Kronig relations (equations 4-10, 4-11). For good data, we can perform a direct numerical integration. However, typical data consists of a few points per frequency decade (five points in the examples treated here), and numerical integration using only these points would be inaccurate. We therefore need functions to fit the data over an extensive frequency range, or functions to interpolate between adjacent data points, so that we can integrate accurately.

Ideally, we would like to have accurate analytic functions for the real and the imaginary parts of the impedance, valid over the entire frequency range. Practically, in the absence of a complete theoretical model that describes the data, or for data that exhibit complicated behavior, we do not have such an ideal function, and we have to proceed through approximate methods. We begin by seeking functions that correlate the data. Specifically we need a function for $\omega Z_I(\omega)$ and a function for $Z_R(\omega)$.

Figure 4-7 shows $\omega Z_I(\omega)$ *vs*. the logarithm of frequency, for experiment A. ωZ_I is roughly linear with $\ln \omega$ over small frequency intervals. Such a linear relationship has been found empirically for several electrochemical systems, within a limited frequency range (8). Newman's (13) solution to the rotating-disk impedance problem also gives a linear asymptote at high frequencies:

$$(-\omega Z_I)^* \longrightarrow 0.563 + \frac{1}{4} \ln \omega^* \quad \text{as} \quad \omega^* \longrightarrow \infty \ , \qquad [4\text{-}15]$$

where the asterisk indicates dimensionless quantities. Figure 4-8 shows Z_R *vs*. frequency on a log-log graph, for experiment A. Plotting the

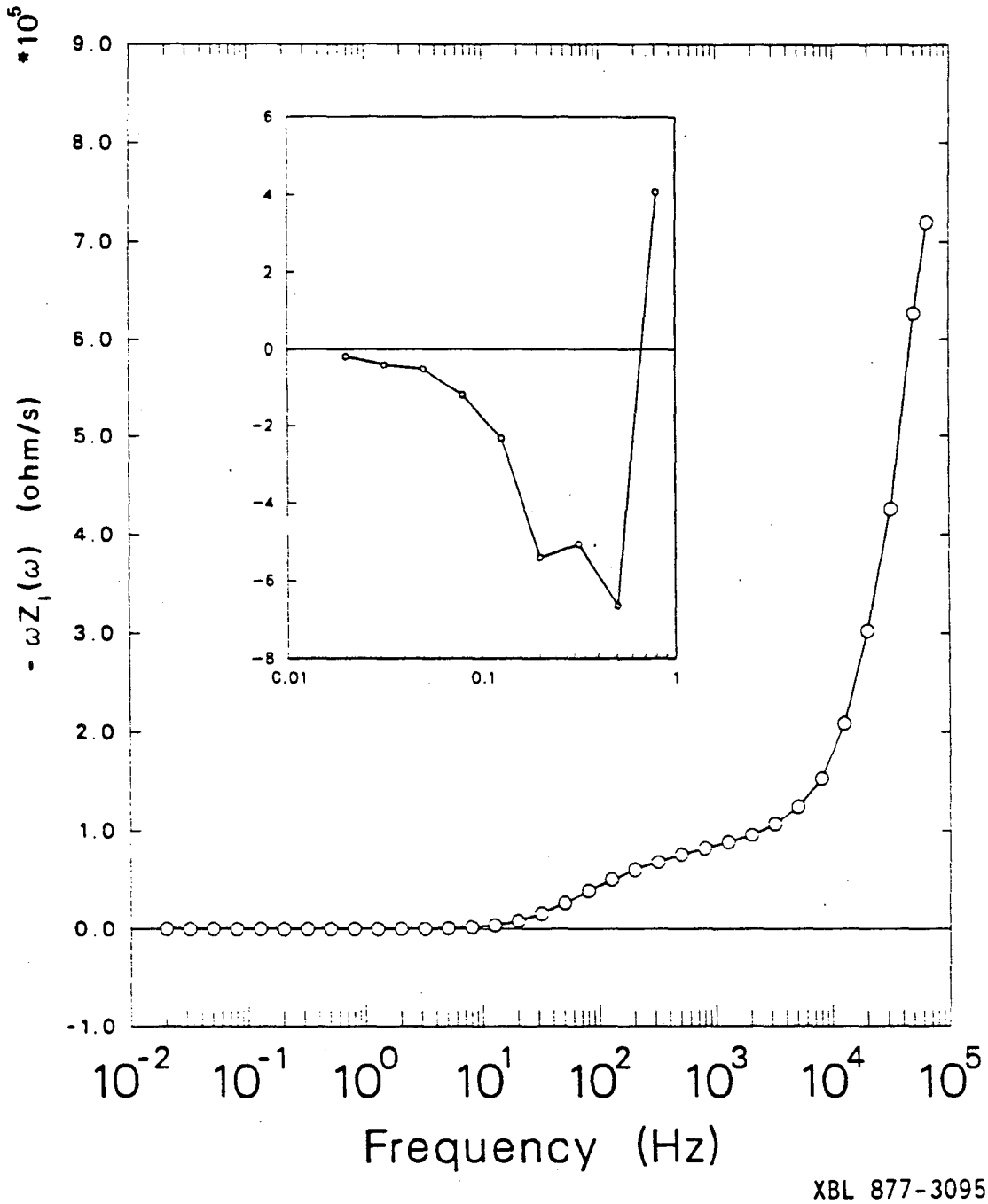

Figure 4-7. Frequency dependence of the imaginary part of the impedance for experiment A.
o data values.
— interpolating function defined by equation 4-16.

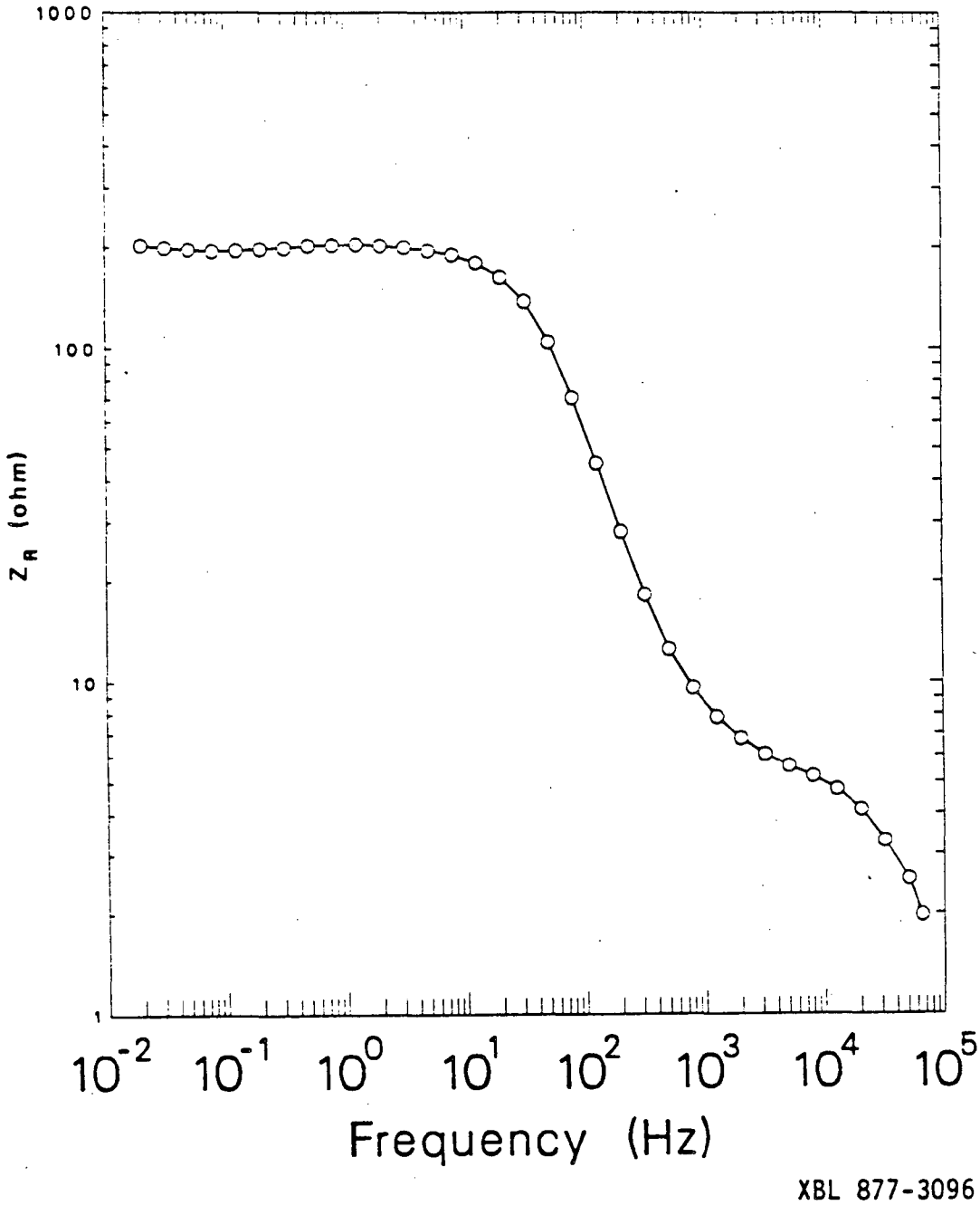

Figure 4-8. Frequency dependence of the real part of the impedance for experiment A.
O data values.
— interpolating function defined by equation 4-17.

data in this way is similar to a Bode plot, with Z_R instead of $|Z|$. Figures 4-9 through 4-14 show the same functions, for experiments B, C, and D.

All these graphs are roughly linear over small frequency intervals. We conclude that a set of convenient, general, and accurate fitting or interpolating functions is:

$$-\omega Z_I(\omega) = A_I \ln \omega + B_I \qquad [4\text{-}16]$$

for the imaginary part and

$$Z_R(\omega) = B_R \omega^{A_R} \qquad [4\text{-}17]$$

for the real part, where the coefficients A_I , B_I , A_R , and B_R are determined for each interval between adjacent data points. These are the functions plotted in figures 4-7 through 4-14.

Using equations 4-16 and 4-17, we can numerically evaluate the integrals in the K-K relations, equations 4-10 and 4-11 (or 4-12 and 4-13). Trapezoidal rule integration with an appropriate number of points should be sufficient.

Note that the limits of the integrands as $\omega \longrightarrow \omega_c$, determined by L' Hospital's rule, are now given by

$$\lim_{\omega \longrightarrow \omega_c} -\frac{\omega Z_I(\omega) - \omega_c Z_I(\omega_c)}{\omega^2 - \omega_c^2} = \frac{A_I}{2\omega_c^2} \qquad [4\text{-}18]$$

and

$$\lim_{\omega \longrightarrow \omega_c} \frac{Z_R(\omega) - Z_R(\omega_c)}{\omega^2 - \omega_c^2} = \frac{A_R}{2\omega_c^2} B_R \omega_c^{A_R} , \qquad [4\text{-}19]$$

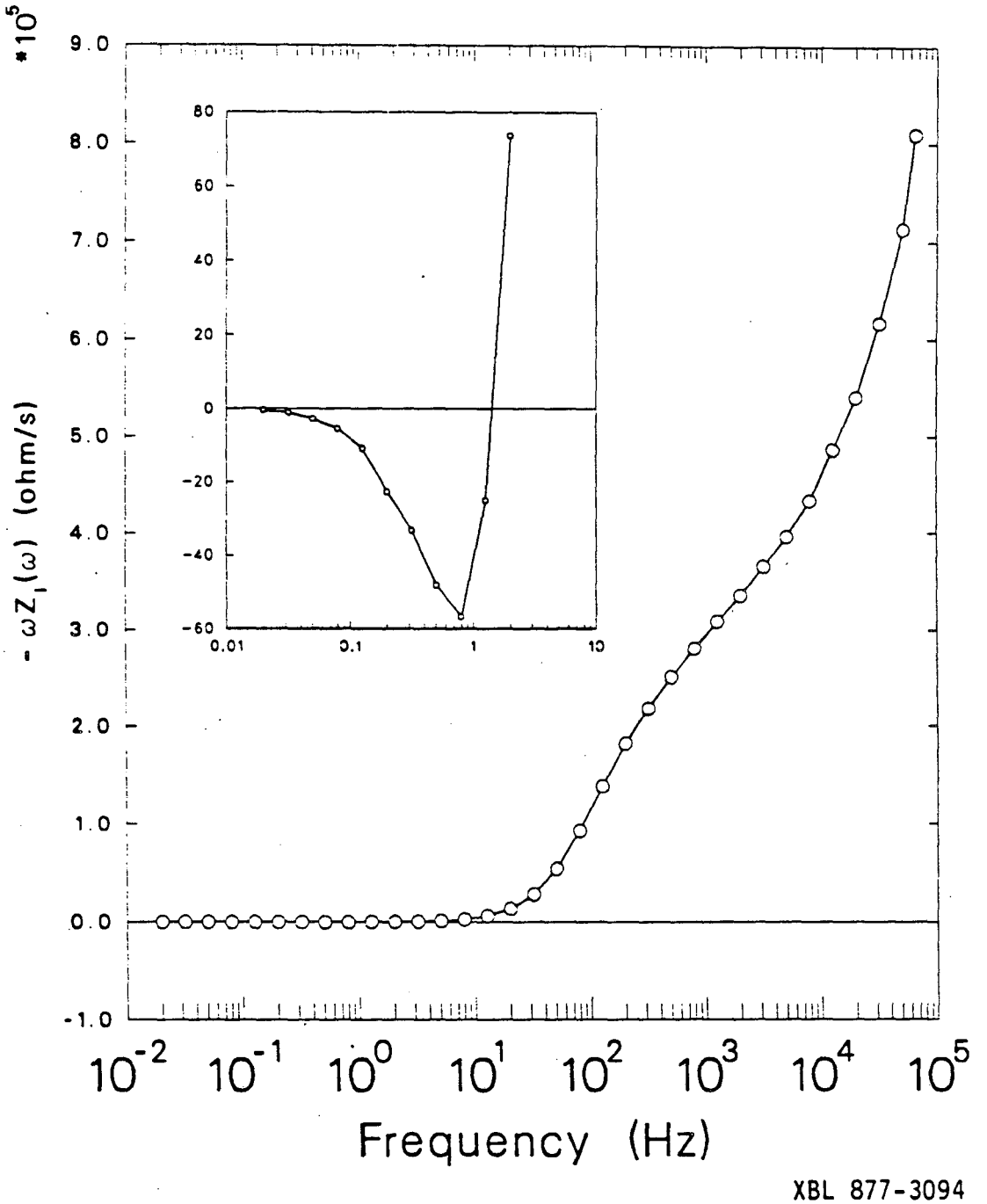

Figure 4-9. Frequency dependence of the imaginary part of the impedance for experiment B.
O data values.
— interpolating function defined by equation 4-16.

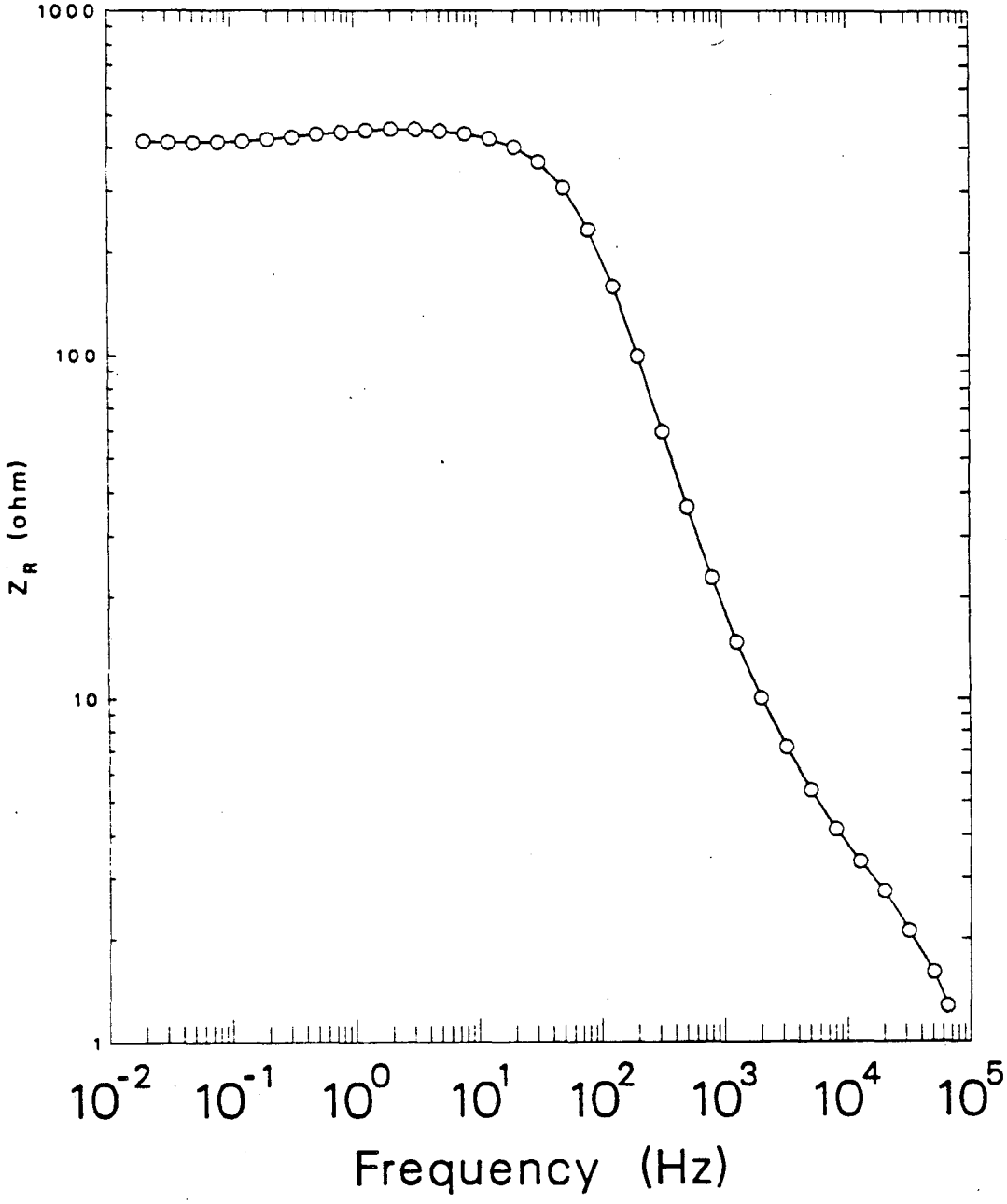

XBL 877-3122

Figure 4-10. Frequency dependence of the real part of the impedance for experiment B.
O data values.
— interpolating function defined by equation 4-17.

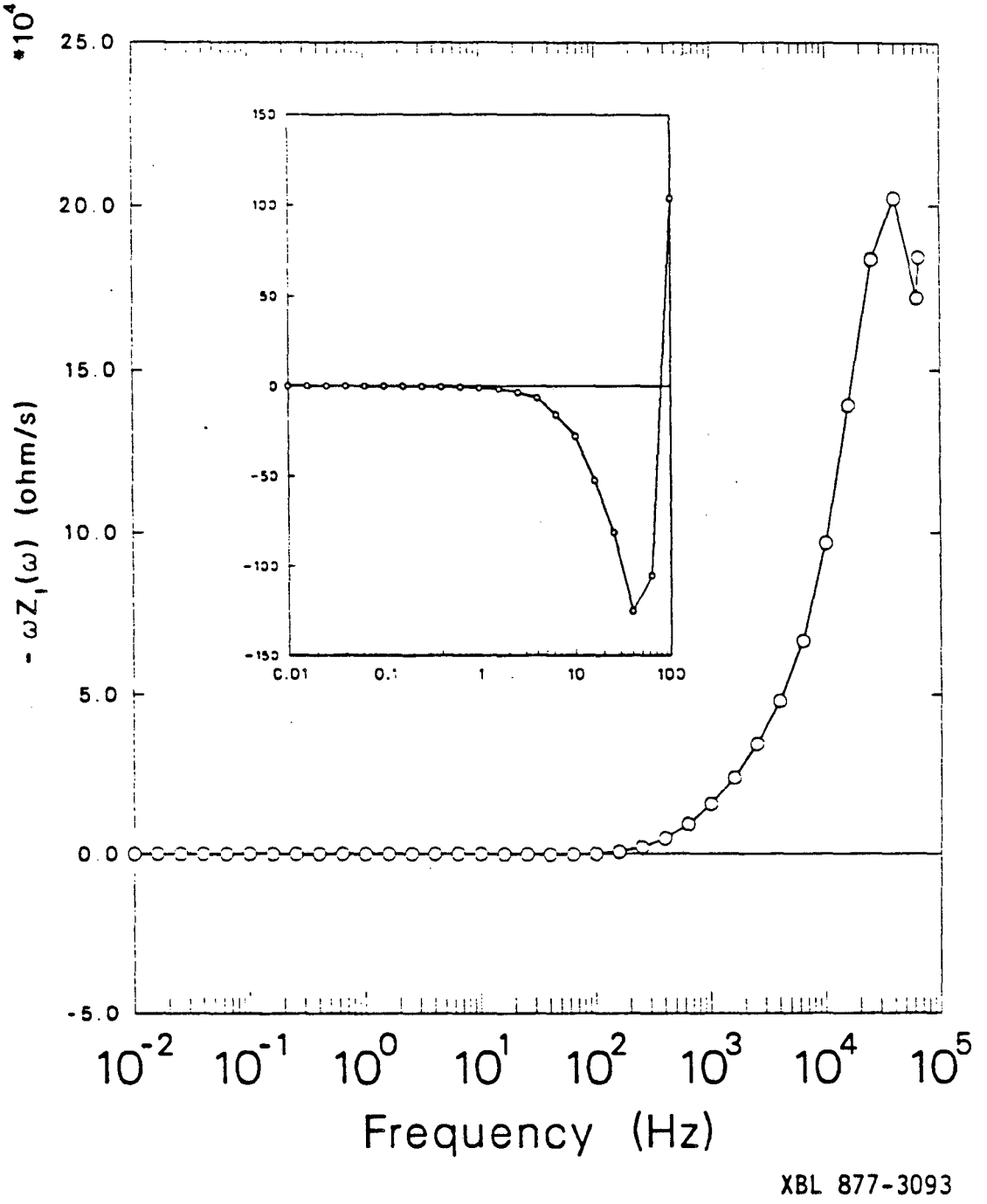

Figure 4-11. Frequency dependence of the imaginary part of the impedance for experiment C.
O data values.
— interpolating function defined by equation 4-16.

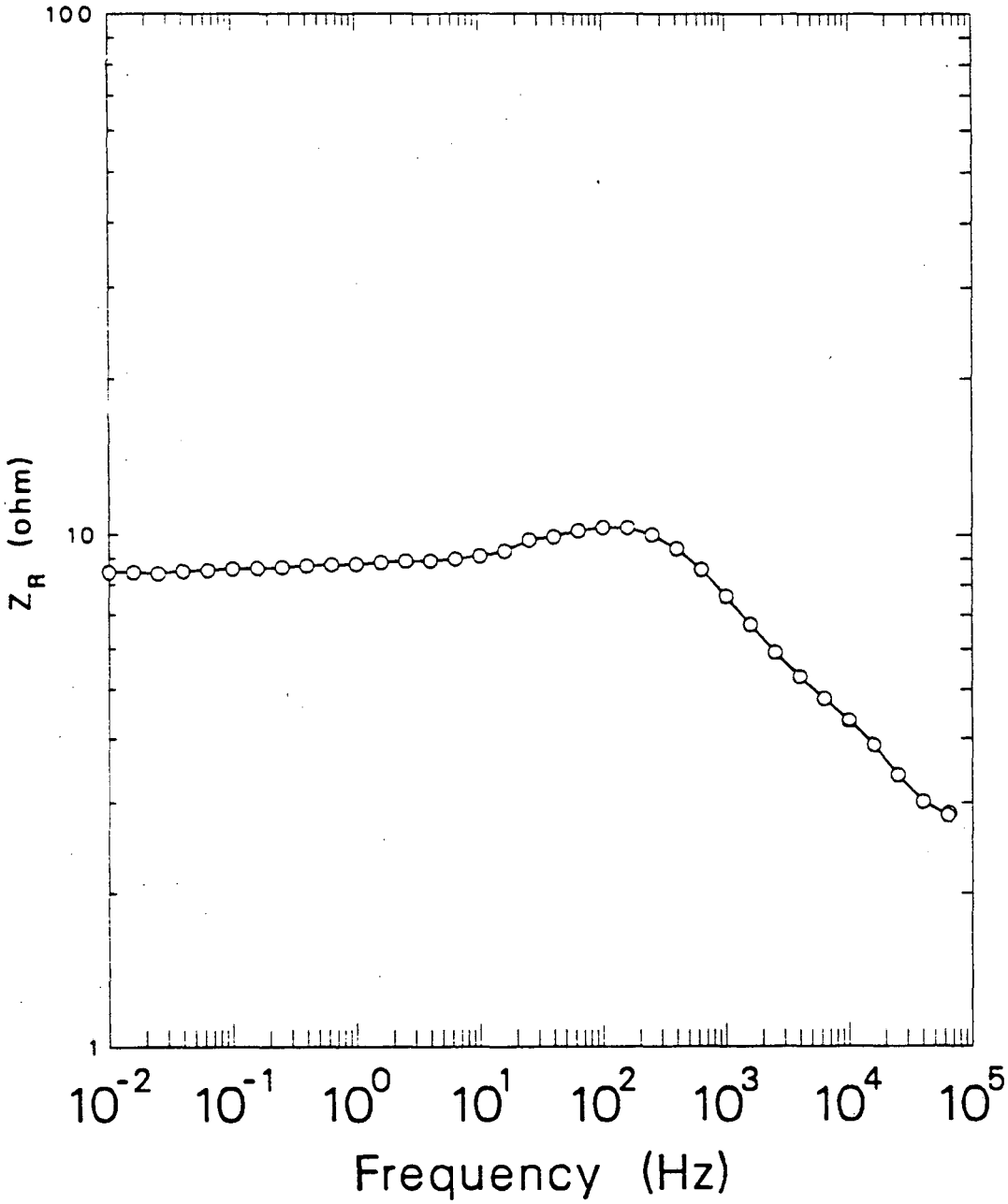

XBL 877-3123

Figure 4-12. Frequency dependence of the real part of the impedance for experiment C.
O data values.
— interpolating function defined by equation 4-17.

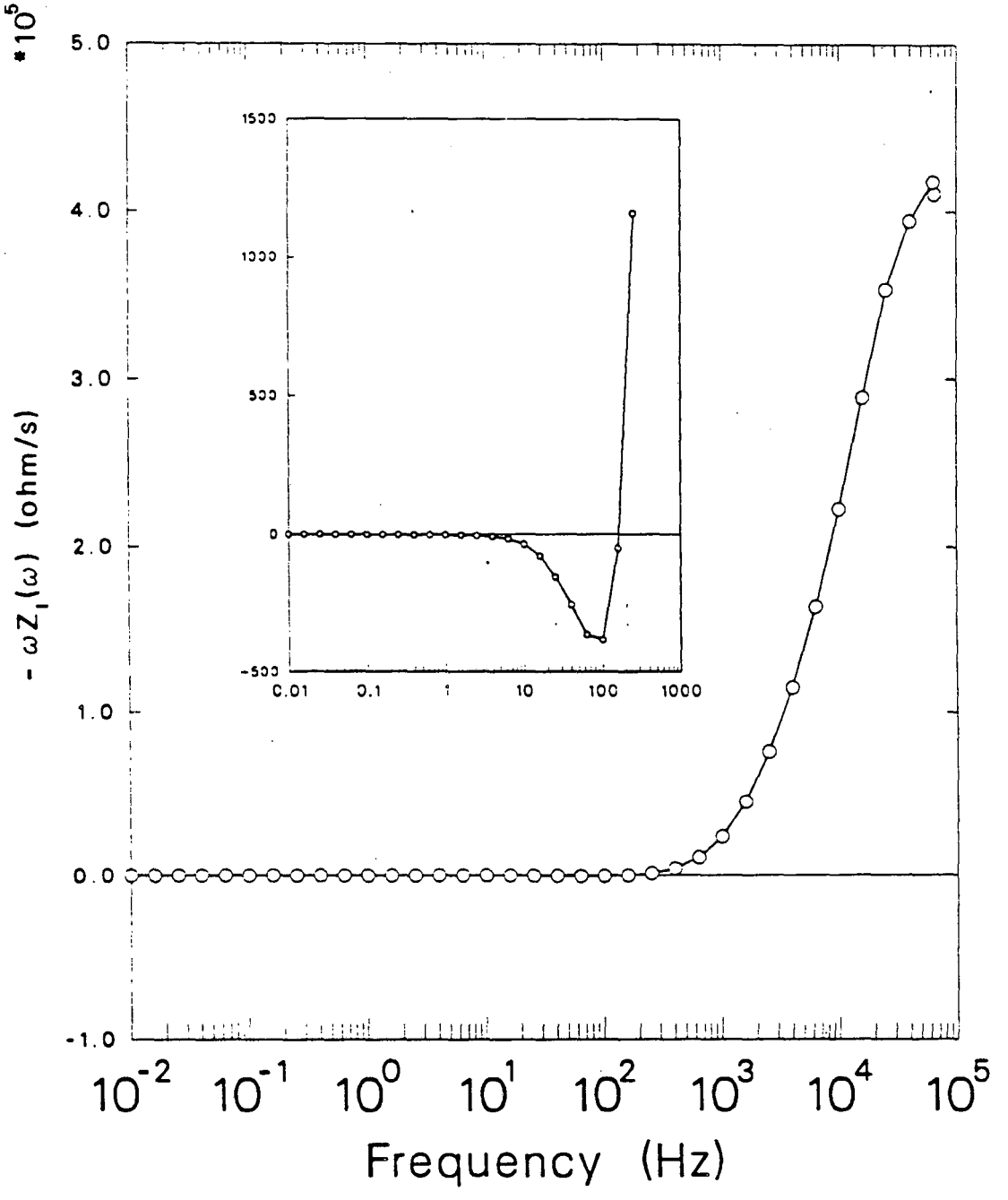

XBL 877-3092

Figure 4-13. Frequency dependence of the imaginary part of the impedance for experiment D.
O data values.
— interpolating function defined by equation 4-16.

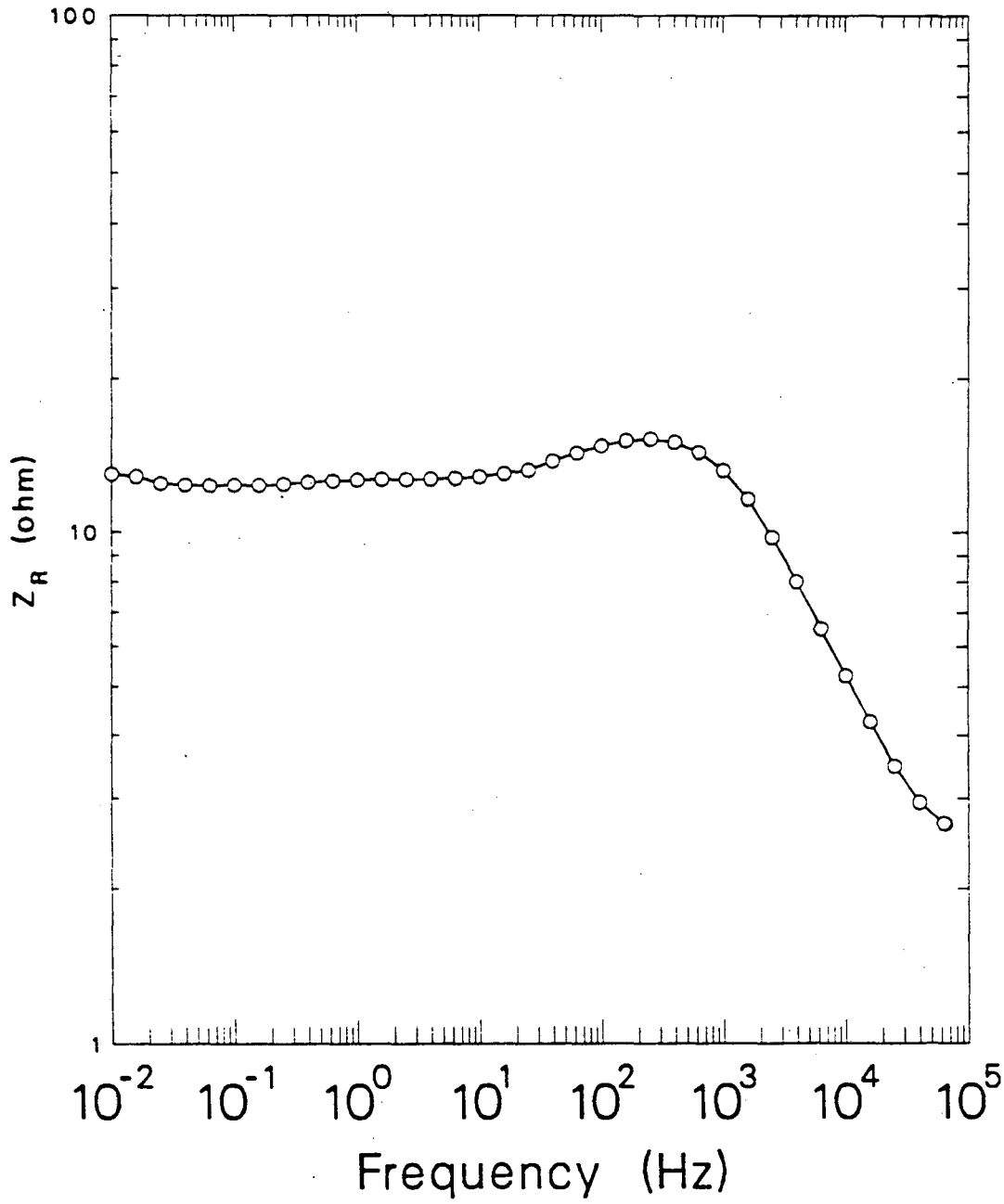

XBL 877-3124

Figure 4-14. Frequency dependence of the real part of the impedance for experiment D.
O data values.
— interpolating function defined by equation 4-17.

where A_I , A_R , and B_R are the coefficients for the interval containing ω_c . These expressions illustrate that the singularities in the original form of the K-K relations have been removed.

A feature of this method for interpolation and integration is that it follows exactly each experimental data point, which may not be desirable in some cases. Consider, for example, the low-frequency data for experiment A in figure 4-7 (also see the complex-plane impedance plot, figure 3-3). These data obviously contain a lot of noise, and one might say *a priori* that these particular points are bad and therefore decide not to use them at all, or try to use a smoother fitting function in that region. However we decided to carry on the calculation for all the data points in this experiment in order to see how the apparently bad points can affect the calculated results and what conclusions one can draw from them.

An alternative method is to use fitting functions that allow analytic integration. A convenient choice is to use third order polynomials:

$$-\omega Z_I(\omega) = a_{I1} + a_{I2}\omega + a_{I3}\omega^2 + a_{I4}\omega^3 \qquad [4\text{-}20]$$

$$Z_R(\omega) = a_{R1} + a_{R2}\omega + a_{R3}\omega^2 + a_{R4}\omega^3 , \qquad [4\text{-}21]$$

where the a-coefficients are fitted for chosen intervals, containing at least four data points. The coefficients are determined by a least squares technique (14). Different order polynomials can also be used in the same manner. Notice that these polynomial fitting functions are smoother than the fitting functions represented by equations 4-16 and

4-17, but they follow the data less closely, i.e. they are less accurate. This polynomial fitting procedure is similar to the one used by Mcdonald *et al.* (11).

Substituting equations 4-20 and 4-21 into equations 4-10 and 4-11 results in an approximate form of the K-K relations, involving analytic integrals in the experimental range. The integrals needed are listed below:

$$\int \frac{d\omega}{\omega^2 - \omega_c^2} = \frac{1}{2\omega_c} \ln \frac{|\omega - \omega_c|}{\omega + \omega_c} \qquad [4\text{-}22]$$

$$\int \frac{\omega d\omega}{\omega^2 - \omega_c^2} = \frac{1}{2} \ln |\omega^2 - \omega_c^2| \qquad [4\text{-}23]$$

$$\int \frac{\omega^2 d\omega}{\omega^2 - \omega_c^2} = \frac{1}{2} \omega_c \ln \frac{|\omega - \omega_c|}{\omega + \omega_c} + \omega \qquad [4\text{-}24]$$

$$\int \frac{\omega^3 d\omega}{\omega^2 - \omega_c^2} = \frac{1}{2} \omega_c^2 \ln |\omega^2 - \omega_c^2| + \frac{1}{2} \omega^2 \qquad [4\text{-}25]$$

For simplicity, the integration constants have been omitted from these expressions. The integrals above are evaluated at the endpoints of each frequency interval where a polynomial is fitted.

We applied both methods to experiments A through D and obtained similar results. The results presented in section 4.4 have been calculated according to the first method (equations 4-16, 4-17).

4.3. Extrapolation to Zero and Infinite Frequency

So far, we have evaluated the integrals over the frequency range where data are available (ω_{min} to ω_{max}) . Now we need to estimate the value of the integrals in the range where data are not available, specifically in the low-frequency range, $0 \leq \omega < \omega_{min}$, and the high-frequency range, $\omega_{max} < \omega < \infty$.

Having little knowledge of the system behavior in these ranges, it is not meaningful to use any complicated mathematical expressions to describe the system behavior. One may simply use linear extrapolation of the data, consistent with the expected asymptotic behavior. Inevitably, there is some arbitrariness in extrapolating data, and one can try to reduce the arbitrariness by changing the parameters involved and observing the results. This is the approach used here.

4.3.1. Extrapolation to $\omega = 0$

Consider first the low-frequency end. Extrapolation of the imaginary part, $\omega Z_I(\omega)$, is relatively easy. Since $Z_I(\omega) \longrightarrow 0$ (finite) as $\omega \longrightarrow 0$, for any electrochemical system, $\omega Z_I(0) = 0$. Consider then how $Z_I(\omega)$ approaches zero as $\omega \longrightarrow 0$. If the electrochemical interface behaved simply like a capacitance connected in parallel with a resistance, then $Z_I(\omega)$ would be proportional to ω for $\omega \longrightarrow 0$. The imaginary part of the convective Warburg impedance is also roughly proportional to ω for $\omega \longrightarrow 0$ (see *e.g.* figure 5-1). When the electrochemical impedance displays an inductive character, the low-frequency behavior is not readily predicted, but we may still expect $Z_I(\omega)$ to be roughly

proportional to ω.

An extrapolation consistent with the expected asymptotic behavior is then given by

$$\omega Z_I(\omega) = A_{I0}\,\omega^2 \quad \text{for} \quad 0 \le \omega \le \omega_{min} \qquad [4\text{-}26]$$

with

$$A_{I0} = \frac{Z_I(\omega_{min})}{\omega_{min}} .$$

Figure 4-15 illustrates several possibilities for extrapolation of the real part of the impedance. In this case, $Z_R \longrightarrow R_0$ as $\omega \longrightarrow 0$, where R_0 is a constant corresponding to the polarization resistance. An extrapolation is defined by

$$Z_R(\omega) = A_{R0}\,\omega^2 + R_0 \quad \text{for} \quad 0 \le \omega \le \omega_{min} \qquad [4\text{-}27]$$

with

$$A_{R0} = \frac{Z_R(\omega_{min}) - R_0}{\omega_{min}^2} . \qquad [4\text{-}28]$$

The extrapolation of Z_R thus involves one unknown or adjustable parameter, R_0 . The value of R_0 will be close to the value of $Z_R(\omega_{min})$ if ω_{min} is small enough. We can get an estimate for R_0 from the experimental data, but there is considerable uncertainty in such an estimate, especially for data that exhibit inductive behavior at low frequencies. One may also want to treat $Z_R(\omega_{min})$ as an adjustable parameter, if one thinks that particular data value is bad, but doing so would contradict including the same point in the experimental range integration.

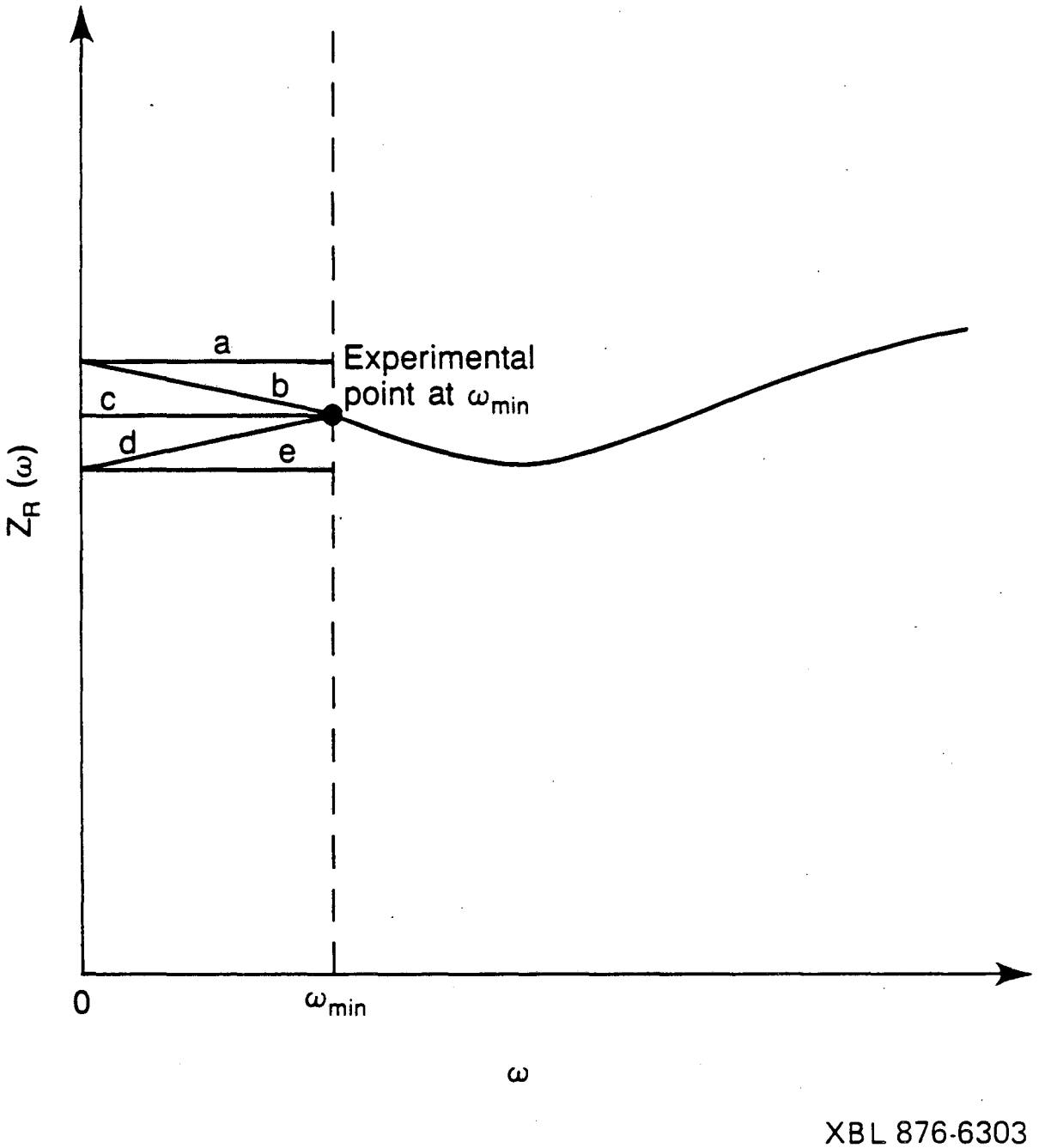

Figure 4-15. Extrapolation of the real part of the impedance to $\omega = 0$ (equations 4-27, 4-28). Lines a through e illustrate several possible configurations corresponding to different parameter values.

Using equations 4-26 through 4-28 for extrapolation leads to analytic approximations for the integrals in the low-frequency end. Let us consider the effect of this extrapolation on the calculated real and imaginary part of the impedance.

Calculations including the low-frequency extrapolation of the imaginary part, for experiments A through D, show that the extrapolation has a small effect on the calculated real part at small ω_c . Specifically, for ω_c within the three lower frequency decades of the experimental data range, the contribution of the integral in the low frequency end is about three orders of magnitude smaller than the contribution of the integral in the experimental range; then, as the frequency ω_c increases, the contribution of the extrapolation becomes negligible.

Calculations including the low-frequency extrapolation of the real part, for several different parameter values, show the following general trends: The extrapolation has an effect on the calculated imaginary part of the impedance at small ω_c values and no effect at higher ω_c . Specifically, for ω_c within the two lower frequency decades of the experimental range, the contribution of the integral in the low-frequency end is one or usually two orders of magnitude smaller than the contribution of the integral in the experimental range. For ω_c in the next higher frequency decade, the contribution of the extrapolation is three orders of magnitude smaller than the experimental contribution, and for higher ω_c , the extrapolation contribution becomes negligible. Varying the parameters, within some reasonable limits, gives varying results, but does not change the order of magnitude of the extrapolation

effect. Using obviously unreasonable parameter values gives calculated results that disagree significantly with the experimental data.

4.3.2. Extrapolation to $\omega \longrightarrow \infty$

Consider now the high-frequency end. Extrapolation in this range is more uncertain than the extrapolation in the low frequency range.

Let us look at the behavior of the imaginary part. As shown in figures 4-7, 4-9, 4-11, and 4-13, $-\omega Z_I(\omega)$ is increasing rapidly at high frequencies. Initially, one may think that $-\omega Z_I(\omega)$ increases without limit as $\omega \longrightarrow \infty$, but this may not be the case. We usually expect an electrochemical interface to have a capacitive behavior due to the double-layer capacity, as $\omega \longrightarrow \infty$. $Z_I(\omega)$ would then be inversely proportional to ω as $\omega \longrightarrow \infty$, and therefore $\lim_{\omega \longrightarrow \infty} \omega Z_I(\omega)$ should be a finite constant (C). †

Thus we expect $-\omega Z_I(\omega)$ to increase at a decreasing rate, at high frequencies, and finally approach asymptotically a constant value. An approximation of this behavior, using straight line segments, is illustrated in figure 4-16 and is represented by

$$-\omega Z_I(\omega) = A_{I\infty}\omega + B_{I\infty} \quad \text{for} \quad \omega_{max} \leq \omega \leq \omega_\infty \qquad [4\text{-}29]$$

---

† This expected behavior is not always valid. For a rotating disk electrode, Newman's theoretical model (13) yields the high-frequency asumptote given by equation 4-15, and there is no infinite-frequency limit. The disk behavior results from an infinite primary current density at the edge. Experimentally, the disk electrode may not be exactly on the same level as the insulator, and this geometric effect would yield a finite limit as $\omega \longrightarrow \infty$.

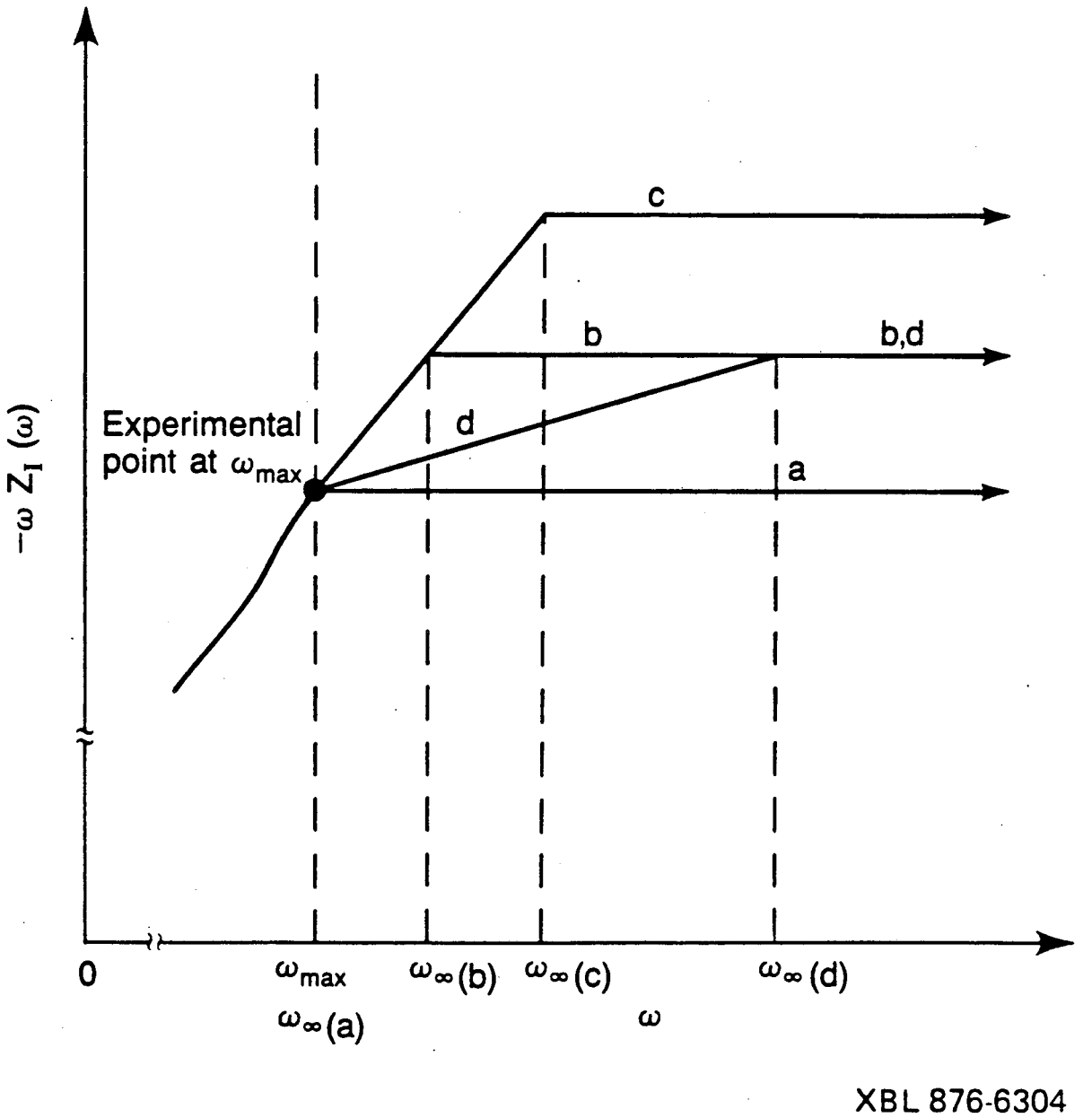

Figure 4-16. Extrapolation of the imaginary part of the impedance to $\omega \longrightarrow \infty$ (equations 4-29, 4-30). Lines a through d illustrate several possible configurations.

$$= C \qquad \text{for} \quad \omega \geq \omega_\infty ,$$

where

$$C = A_{I\infty}\omega_\infty + B_{I\infty} . \qquad [4\text{-}30]$$

The extrapolation of the imaginary part, defined by the equations above, includes three adjustable parameters, the straight-line coefficients, $A_{I\infty}$ and $B_{I\infty}$, and the frequency ω_∞ where ωZ_I stops changing.

Similarly, we can extrapolate the real part of the impedance according to

$$Z_R(\omega) = A_{R\infty}\omega + B_{R\infty} \qquad \text{for} \quad \omega_{max} \leq \omega \leq \omega_\infty \qquad [4\text{-}31]$$

$$= R_\infty \qquad \text{for} \quad \omega \geq \omega_\infty ,$$

where

$$A_{R\infty} = \frac{R_\infty - Z_R(\omega_{max})}{\omega_\infty - \omega_{max}} \quad \text{and} \quad B_{R\infty} = Z_R(\omega_{max}) - A_{R\infty}\omega_{max} . \qquad [4\text{-}32]$$

Here Z_R is allowed to vary linearly with ω until it reaches the value R_∞ at $\omega = \omega_\infty$. Beyond ω_∞ , Z_R is assumed to remain constant. R_∞ is an important parameter, corresponding to the infinite frequency or ohmic limit of the electrochemical impedance ($Z_\infty = R_\Omega$). We have already discused the uncertainties involved in determining this limiting value from experimental data.

This extrapolation scheme for $Z_R(\omega)$ is illustrated in figure 4-17. The extrapolation includes two adjustable parameters, R_∞ and ω_∞ . As in the low-frequency extrapolation of Z_R , one may also treat $Z_R(\omega_{max})$ as an adjustable parameter, rather than using the data value directly. Then the extrapolation would include three adjustable parameters.

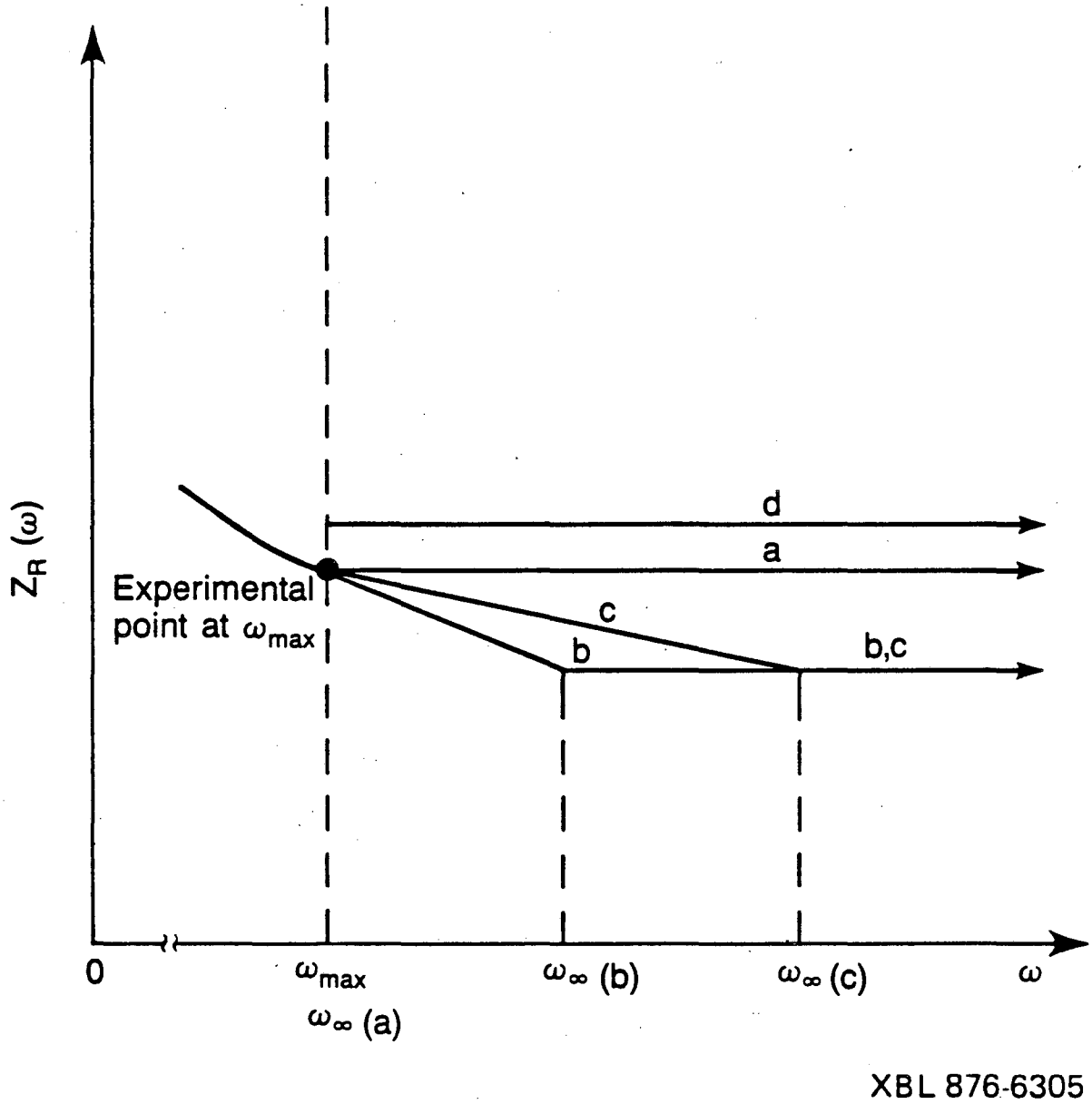

Figure 4-17. Extrapolation of the real part of the impedance to $\omega \longrightarrow \infty$ (equations 4-31, 4-32). Lines a through d illustrate several possible configurations.

Equations 4-29 through 4-32 lead to analytic approximations for the integrals in the high-frequency end. Let us consider now the effect of the high-frequency extrapolation on the calculated real and imaginary part of the impedance.

Calculations using several different parameter values show that the high-frequency extrapolation of the imaginary part adds a roughly constant value to the calculated real part. The value of the integral in the high-frequency end is usually one or two orders of magnitude smaller than the value of the integral in the experimental range, for ω_c throughout the experimental frequency range. The calculated values depend significantly on the parameters ω_∞ and $A_{I\infty}$ (slope of the extended line), and so one needs to be careful in the choice of values for these parameters.

Calculations including the high-frequency extrapolation of the real part show general trends similar to those for the low-frequency extrapolation of the real part (section 4.3.1). The extrapolation has a significant effect on the calculated imaginary part at high ω_c and a less significant, and finally negligible effect at smaller ω_c .

4.3.3. Concluding Remarks

We conclude that it is important to include extrapolation of the data to both zero and infinite frequency in the calculations for the K-K relations. As expected, extrapolation in the low (high) frequency end generally has a small but significant effect on the calculated impedance, within the two or three lower (higher) frequency decades of

the data range. For higher (lower) frequencies, the extrapolation has a decreasing and finally negligible effect.

The infinite-frequency extrapolation of the imaginary part to calculate the real part has the greatest effect and does not follow the general trend described above. This extrapolation affects the calculated real part of the impedance significantly, throughout the data frequency range, because the imaginary part varies greatly at high frequencies.

The experimental data examples treated here cover a wide frequency range, from very low to very high frequencies. Extrapolation to zero and infinite frequency would probably be more critical for data that cover a more limited frequency range.

4.4. Results

Finally, let us look at the calculated results for experiments A, B, C, and D. The results are presented as graphs of the real and imaginary part of the impedance *vs*. the logarithm of frequency. The experimental data are given together with two sets of calculated results. The first set has been calculated by integrating over the experimental frequency range only, and the second set has been calculated by including extrapolation to zero and infinite frequency as well. The parameters used for extrapolation are also given.

In order to choose values for the extrapolation parameters, we first carried out calculations including extrapolation in the low-frequency end only, for several different parameter values, and compared

the results. We chose the parameters that seemed physically meaningful and gave relatively good agreement with the experimental data. We repeated the same procedure, including extrapolation in the high-frequency end only, and finally calculated the results including extrapolation in both the low and high frequency ends, using the chosen parameter values.

Figures 4-18 and 4-19 show the results for the real and imaginary parts of the impedance, for experiment A. Overall, the calculated results are in agreement with the experimental results, and extrapolation does not seem to have an important effect. Notice the low-frequency values (frequency < 1 Hz) in figure 4-19 for the imaginary part. Here there is a significant difference between experimental and calculated values, and this difference could not be eliminated, even though we have tried several different parameter values for the low-frequency extrapolation. As noted in section 4.2.2, these particular experimental points are noisy, having a precision between 1 and 10% or worse. The precision given by the measurement instrument, for higher frequencies in experiment A, as well as for most of the other experimental data in this section, is within 1%. For higher frequencies in experiment A, there is no discrepancy between calculated and experimental values. Thus we may conclude that noisy data, which are likely to be bad data, will probably not satisfy the K-K relations.

Figures 4-20 and 4-21 show the results for experiment B. The calculated values agree well with the experimental values everywhere in the data range. Figure 4-21 illustrates the effect of extrapolation to zero

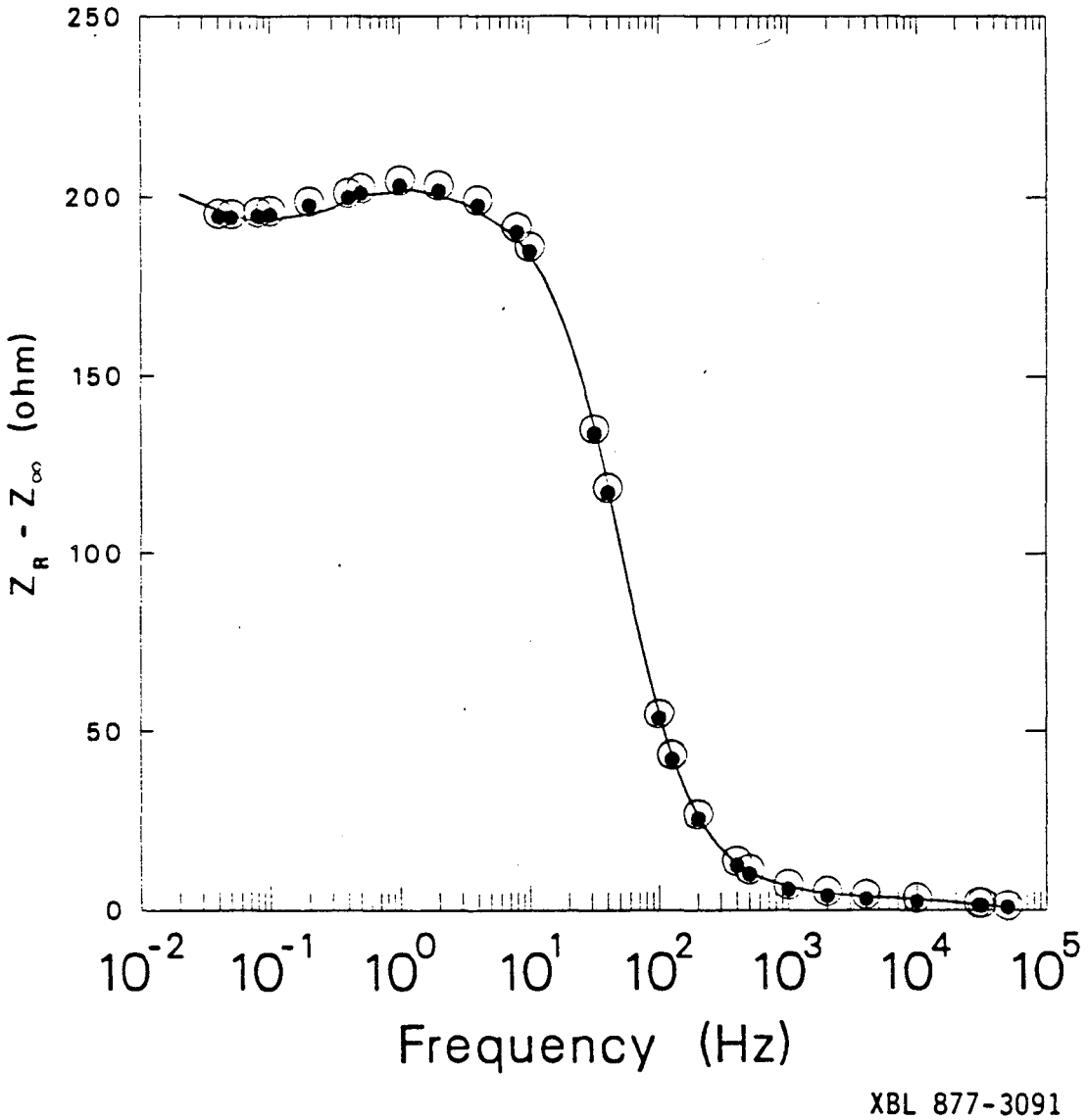

Figure 4-18. Real part of the impedance for experiment A.
— experimental data, assuming $Z_\infty = R_\infty = 2.00\ \Omega$.
• values calculated from the K-K relation (equation 4-10) without extrapolation.
O values calculated from the K-K relation including extrapolation to $\omega = 0$ and $\omega \longrightarrow \infty$, with:

$\omega_\infty = 2\pi\times10^5\ s^{-1}$; $A_{I\infty} = 6.309$, $B_{I\infty} = 3.097\times10^5$ (coefficients of the straight line connecting the two higher-frequency experimental points).

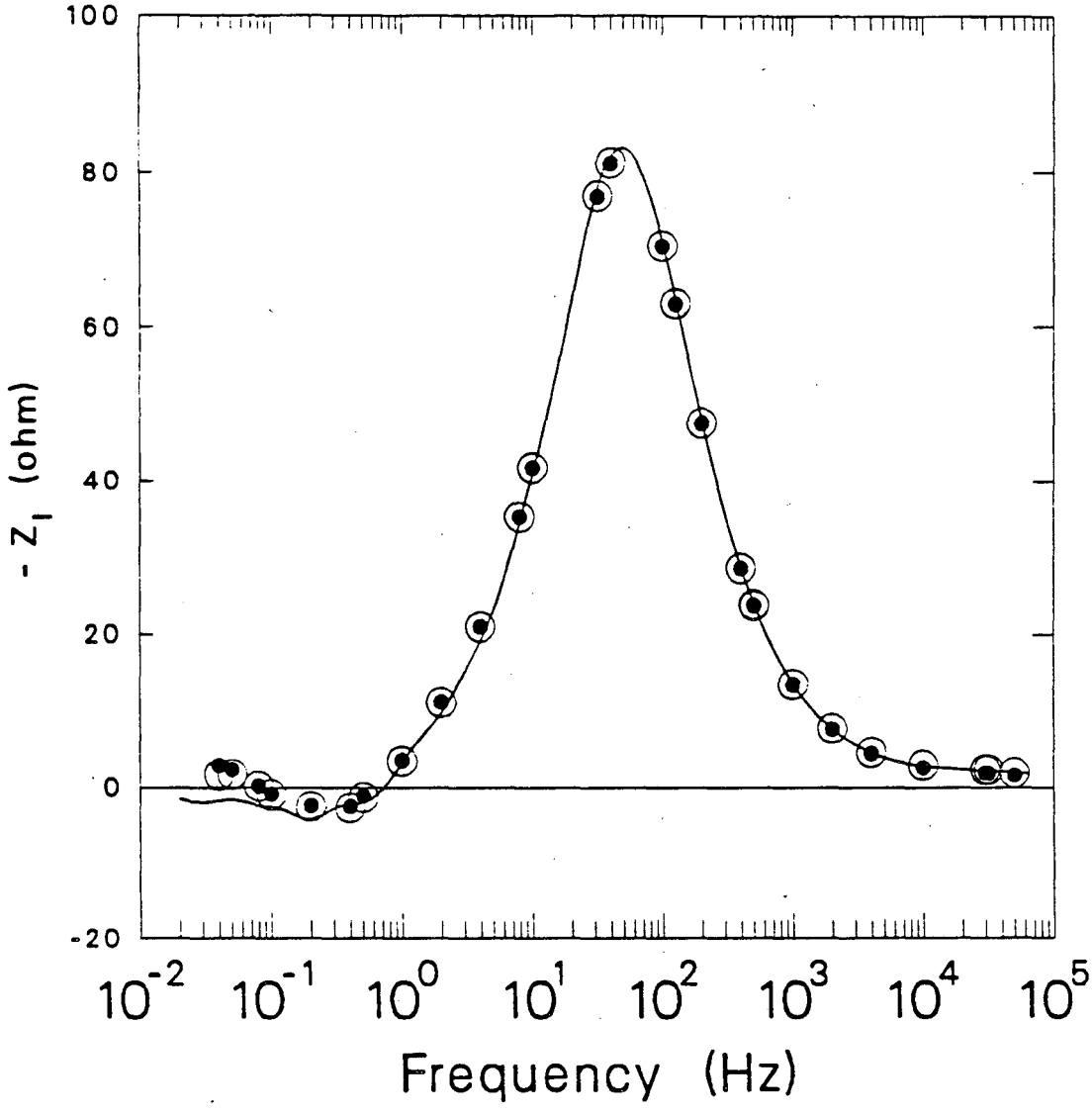

XBL 877-3125

Figure 4-19. Imaginary part of the impedance for experiment A.
— experimental data.
• values calculated from the K-K relation (equation 4-11) without extrapolation.
O values calculated from the K-K relation including extrapolation to $\omega = 0$ and $\omega \longrightarrow \infty$, with:
$R_0 = 195\ \Omega$ (estimated zero-frequency intercept of the experimental complex-plane plot), $Z_R(\omega_{min}) = 195\ \Omega$ (experimental value = 203), and
$R_\infty = 2.00\ \Omega$ (= theoretical R_{ohm} value), $Z_R(\omega_{max}) = 2.00\ \Omega$ (experimental value = 1.98).

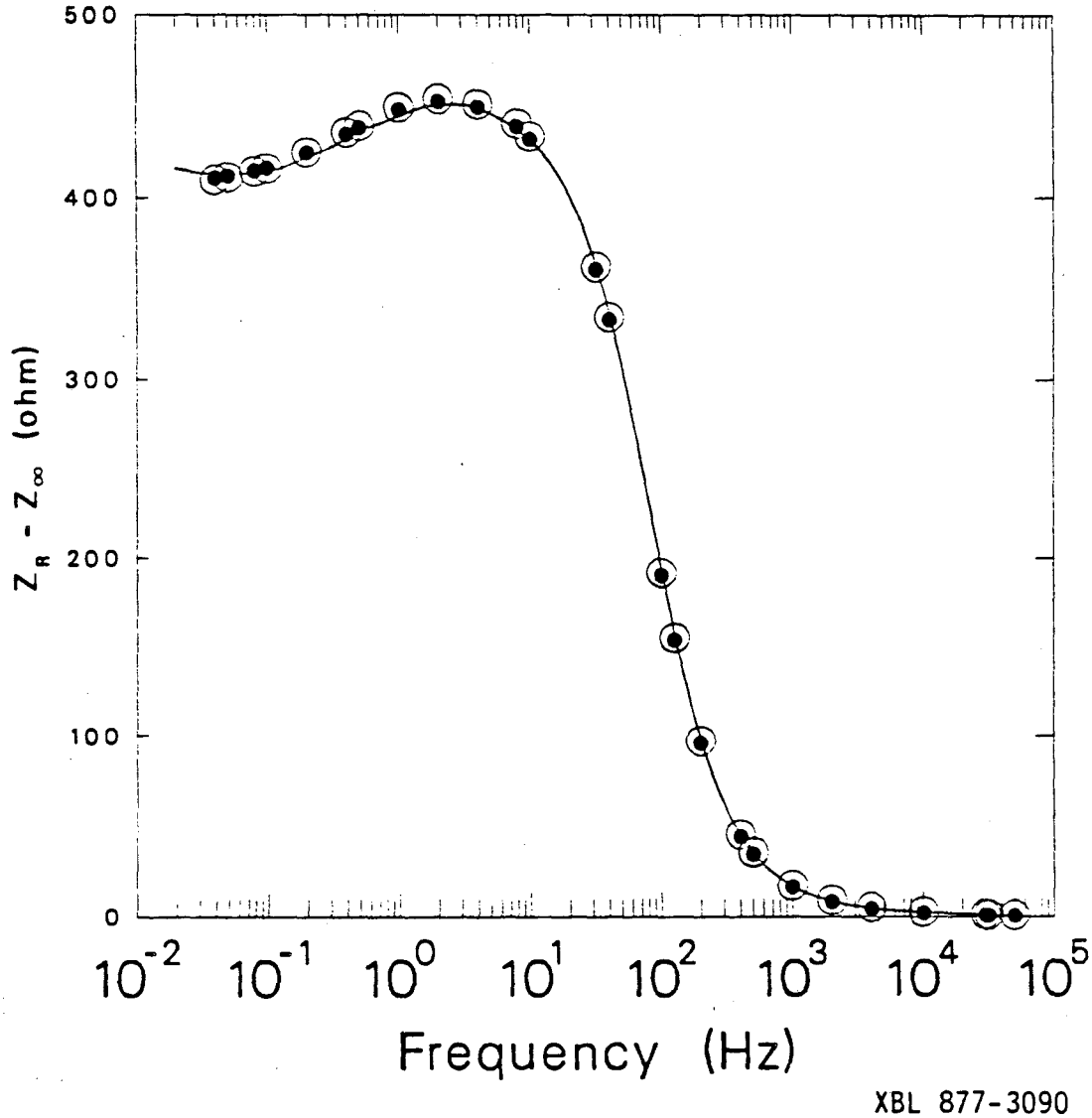

Figure 4-20. Real part of the impedance for experiment B.
— experimental data, assuming $Z_\infty = R_\infty = 1.27\ \Omega$.
• values calculated from the K-K relation (equation 4-10) without extrapolation.
O values calculated from the K-K relation including extrapolation to $\omega = 0$ and $\omega \longrightarrow \infty$, with:

$\omega_\infty = 2\pi\times10^5\ s^{-1}$; $A_{I\infty} = 5.76$, $B_{I\infty} = 4.312\times10^5$ (coefficients determined by linear regression including the three higher-frequency experimental points).

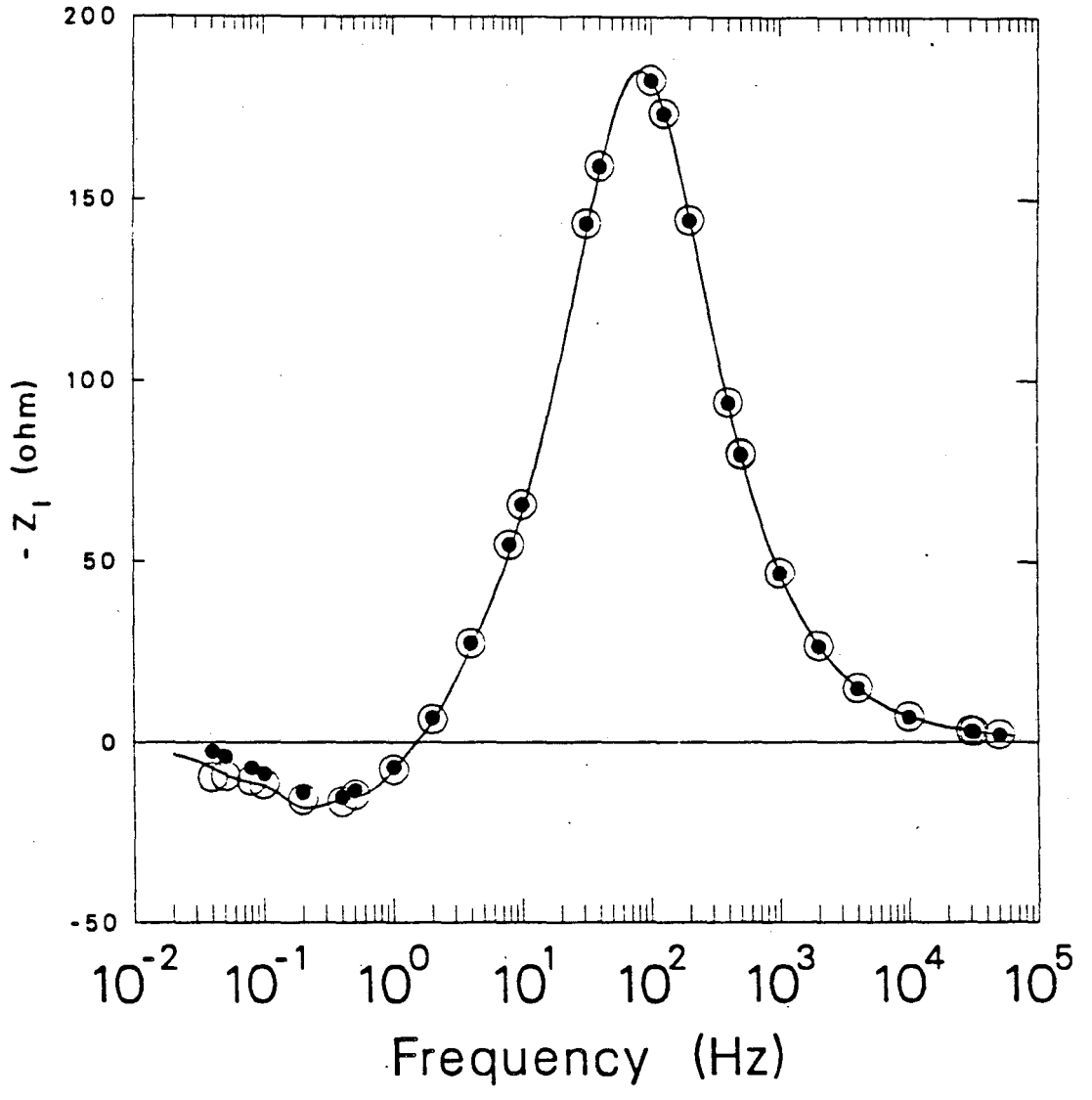

XBL 877-3126

Figure 4-21. Imaginary part of the impedance for experiment B.
— experimental data.
• values calculated from the K-K relation (equation 4-11) without extrapolation.
O values calculated from the K-K relation including extrapolation to $\omega = 0$ and $\omega \longrightarrow \infty$, with:
$R_0 = 394\ \Omega$ (estimated zero-frequency intercept of the experimental complex-plane plot), $Z_R(\omega_{min}) = 394\ \Omega$ (experimental value = 418), and
$R_\infty = 1.27\ \Omega$, $Z_R(\omega_{max}) = 1.27\ \Omega$ (experimental value).

frequency — the values calculated at low frequency, without extrapolation, deviate from the experimental values; including extrapolation brings the calculated values very close to the experimental ones. We may conclude that this data set is consistent with the K-K relations.

Figures 4-22 through 4-24 give the results for experiment C. Now we can observe clearly the difference between the experimental Z_R data and the ($Z_R - Z_\infty$) values calculated according to the K-K relations, as well as the effect of extrapolation on the calculated values. These features are not apparent in figures 4-18 and 4-20, showing the real part of the impedance for experiments A and B, perhaps because the impedance scale there is not sensitive enough.

Figure 4-22 compares the experimental $Z_R(\omega)$ data with the $(Z_R(\omega) - Z_\infty)$ values, calculated from the K-K relations without any extrapolation. The distance between the experimental and calculated curves (marked by the vertical lines in the figure) corresponds to the value of Z_∞ and should therefore be a constant for consistent data. In addition, the high-frequency limit of the calculated values should be zero. Figure 4-22 shows that the distance between the curves is approximately constant and the calculated results are approaching zero, at high frequencies. Thus these data initially appear consistent with the K-K relations.

Since we don't know with certainty the value of Z_∞ , we have to assume $Z_\infty \approx R_\infty$ and use the assumed R_∞ value, for a more direct comparison between the experimental and calculated real part, as well as for the high-frequency extrapolation of the real part in order to

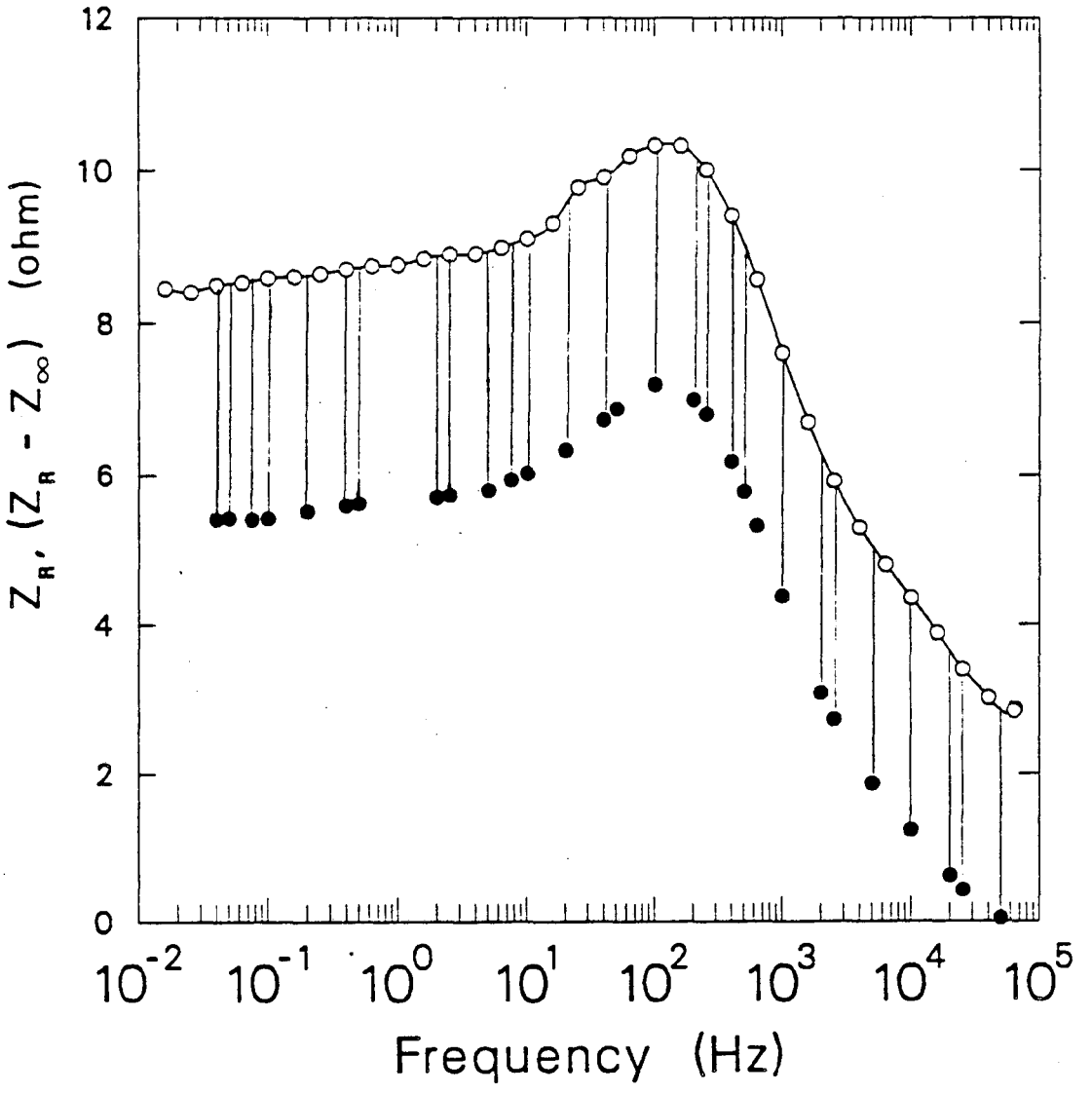

XBL 877-3115

Figure 4-22. Real part of the impedance for experiment C.
-O- experimental data for Z_R.
• values of $(Z_R - Z_\infty)$ calculated from the K-K relation (equation 4-10) without extrapolation.
The vertical lines marking the difference between experimental and calculated values should have a constant length corresponding to the value of Z_∞.

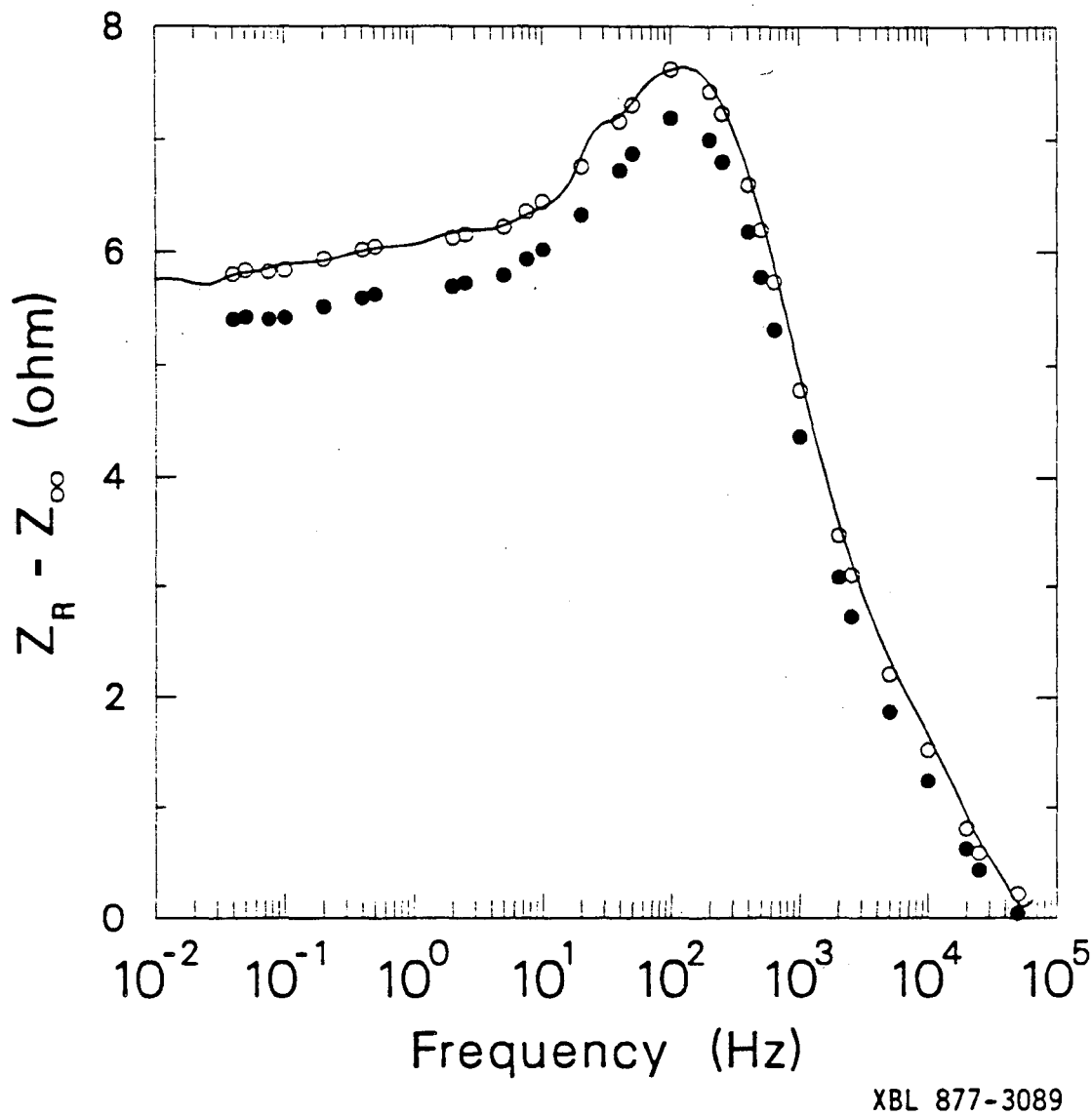

Figure 4-23. Real part of the impedance for experiment C.
— experimental data, assuming $Z_\infty = R_\infty = 2.70\ \Omega$.
• values calculated from the K-K relation (equation 4-10) without extrapolation.
○ values calculated from the K-K relation including extrapolation to $\omega = 0$ and $\omega \longrightarrow \infty$, with:

$\omega_\infty = 2\pi(1.1\times10^5)\ s^{-1}$; $A_{I\infty} = 1.262$, $B_{I\infty} = 1.521\times10^5$ (coefficients of the straight line connecting two high-frequency experimental points).

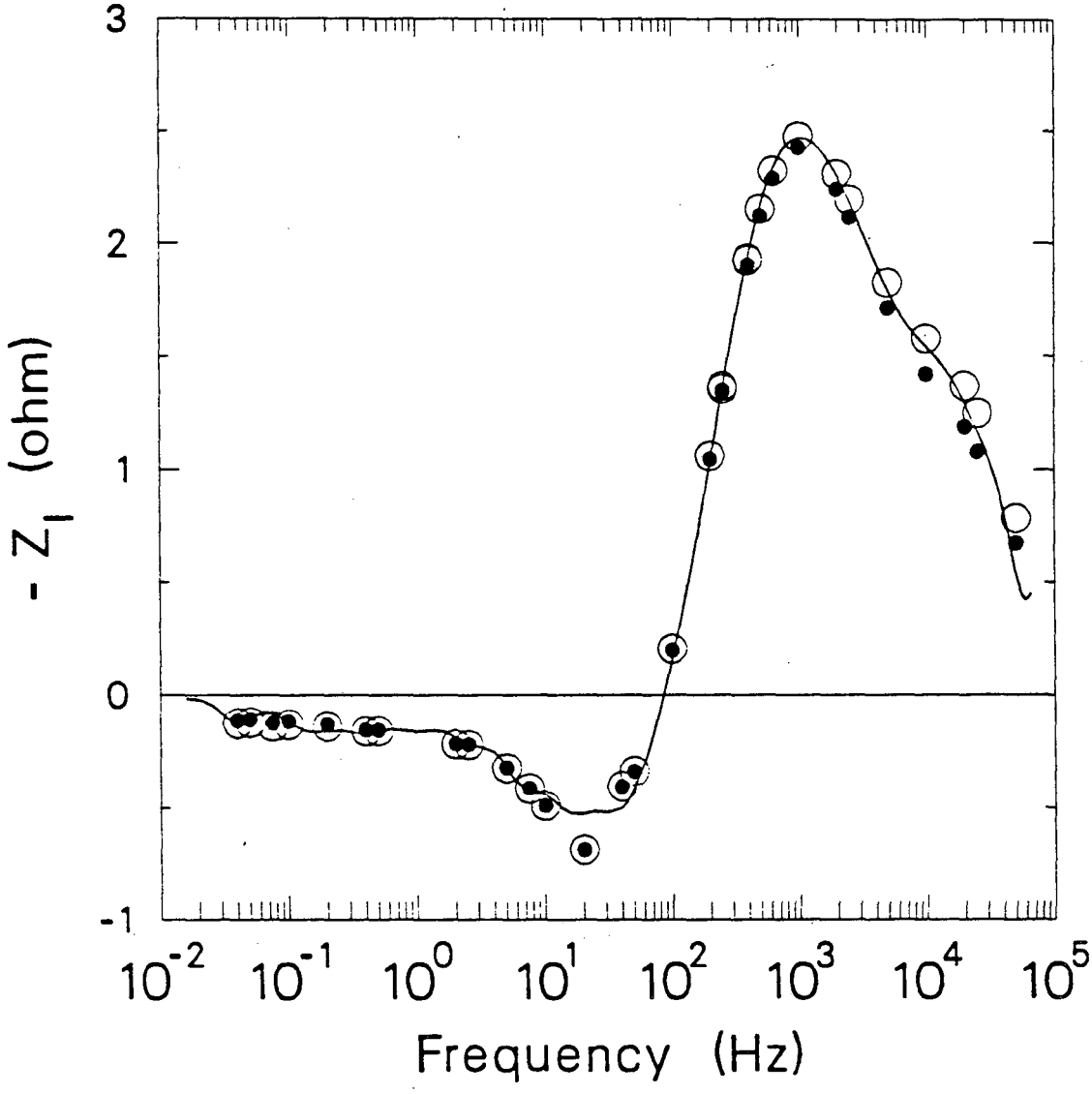

XBL 877-3127

Figure 4-24. Imaginary part of the impedance for experiment C.
— experimental data.
• values calculated from the K-K relation (equation 4-11) without extrapolation.
O values calculated from the K-K relation including extrapolation to $\omega = 0$ and $\omega \longrightarrow \infty$, with:
$R_0 = 8.453\ \Omega$, $Z_R(\omega_{min}) = 8.453\ \Omega$ (experimental value), and $\omega_\infty = 2\pi(1.1\times10^5)\ s^{-1}$, $R_\infty = 2.70\ \Omega$ (estimated infinite-frequency intercept of the experimental complex-plane plot), $Z_R(\omega_{max}) = 2.867\ \Omega$ (experimental value).

calculate the imaginary part. Figure 4-23 then compares the experimental and calculated values for $(Z_R(\omega) - R_\infty)$. The values calculated without any extrapolation are about 0.5 ohm below the experimental values, whereas the values calculated including extrapolation are very close to the experimental values. The difference between the two sets of calculated results is essentially the effect of extrapolating the imaginary part to infinite frequency, as discussed in section 4.3. The trends illustrated in figures 4-22 and 4-23 indicate that the data are consistent with the K-K relations.

The imaginary part of the impedance for experiment C is shown in figure 4-24. Notice the point at a frequency of 20 Hz — a single point deviating from the experimental curve. The most likely explanation for such a random deviation is that the experimental data values near that frequency are bad. In fact, the experimental measurement near that frequency indicated that the data did not satisfy the 1% precision criterion, contrary to the rest of the data. Note also that a curve through the calculated points, including the point in question, would be smoother than the experimental curve around that frequency.

Consider now the effect of extrapolation illustrated in figure 4-24. At high frequencies (> 1 kHZ), the values calculated without extrapolation deviate from the experimental values. Including extrapolation, particularly to infinite frequency, brings the calculated values closer to the experimental ones. At low frequencies, the calculated values are in agreement with the experimental data, and extrapolation has no significant effect. We can rationalize why the low-frequency

extrapolation has no significant effect, whereas the high-frequency extrapolation has a significant effect for the data in figure 4-24, by considering that the minimum experimental frequency is very close to zero, and there is no more significant change in the real part of the impedance, whereas the maximum experimental frequency is still away from the limiting frequency where the impedance stops changing. We conclude that this data set is consistent with the K-K relations.

Figures 4-25 through 4-27 show the results for experiment D. The results for both the real and the imaginary parts of the impedance are similar to those for experiment C. Two differences are that there is no deviating single point for experiment D and the low-frequency extrapolation has an effect, bringing the calculated values closer to the experimental curve. Again we conclude that this experiment satisfies the K-K relations.

In conclusion, the data for experiments A through D have been shown to be consistent with the Kramers-Kronig relations. The values calculated for the real and imaginary part of the impedance, through the K-K relations, are in good agreement with the experimentally measured values, with the exception of a few points where random deviations occur. Generally, the difference between calculated and experimental values is a few percent, which may be considered satisfactory, as the measurement precision was generally about 1%. Moreover the calculations have shown that the results follow the trends one generally expects from the K-K relations. However one should always keep in mind the questions and uncertainties in the application of the K-K relations.

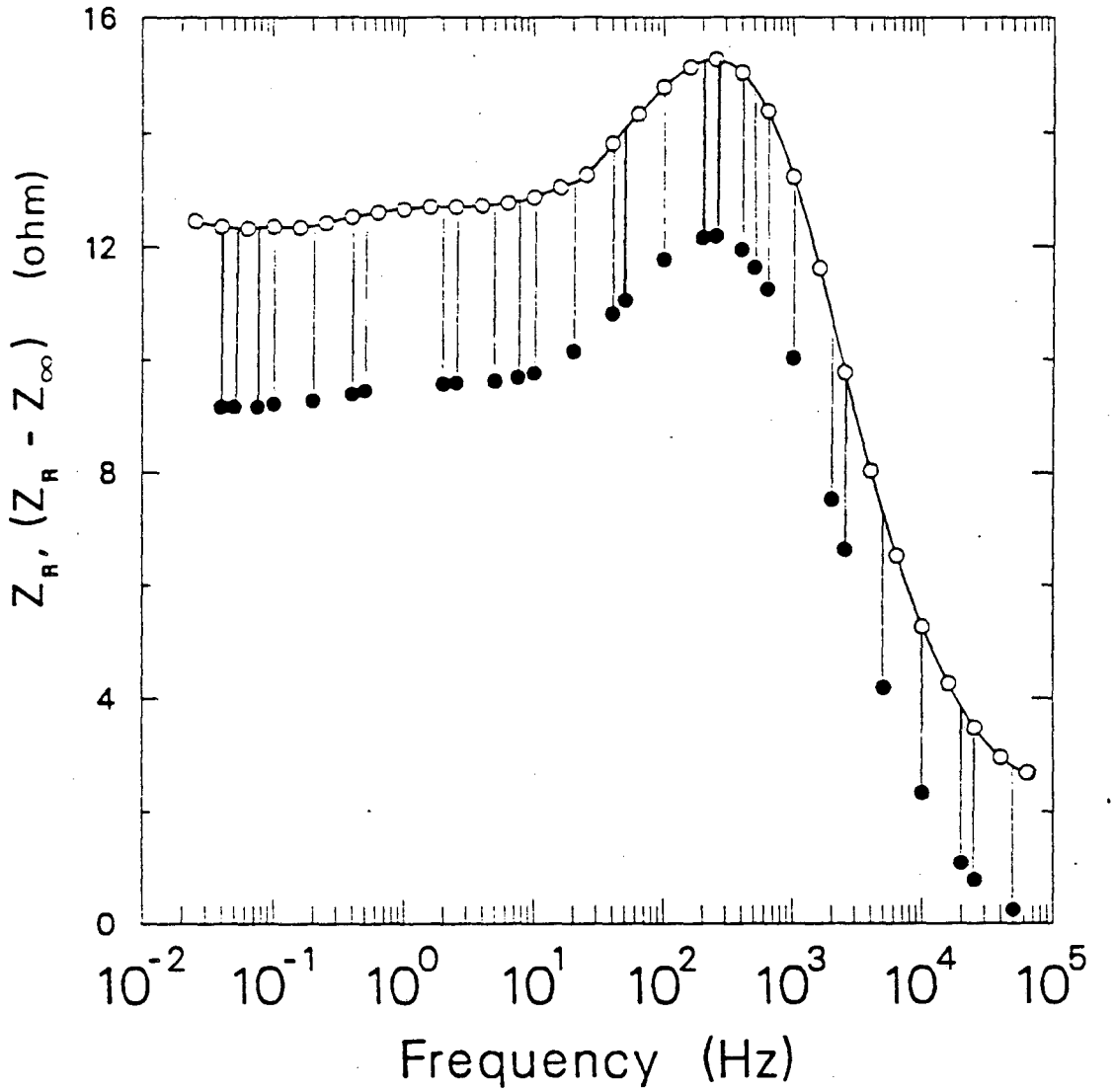

XBL 877-3114

Figure 4-25. Real part of the impedance for experiment D.
-O- experimental data for Z_R.
• values of $(Z_R - Z_\infty)$ calculated from the K-K relation (equation 4-10) without extrapolation.
The vertical lines marking the difference between experimental and calculated values should have a constant length corresponding to the value of Z_∞.

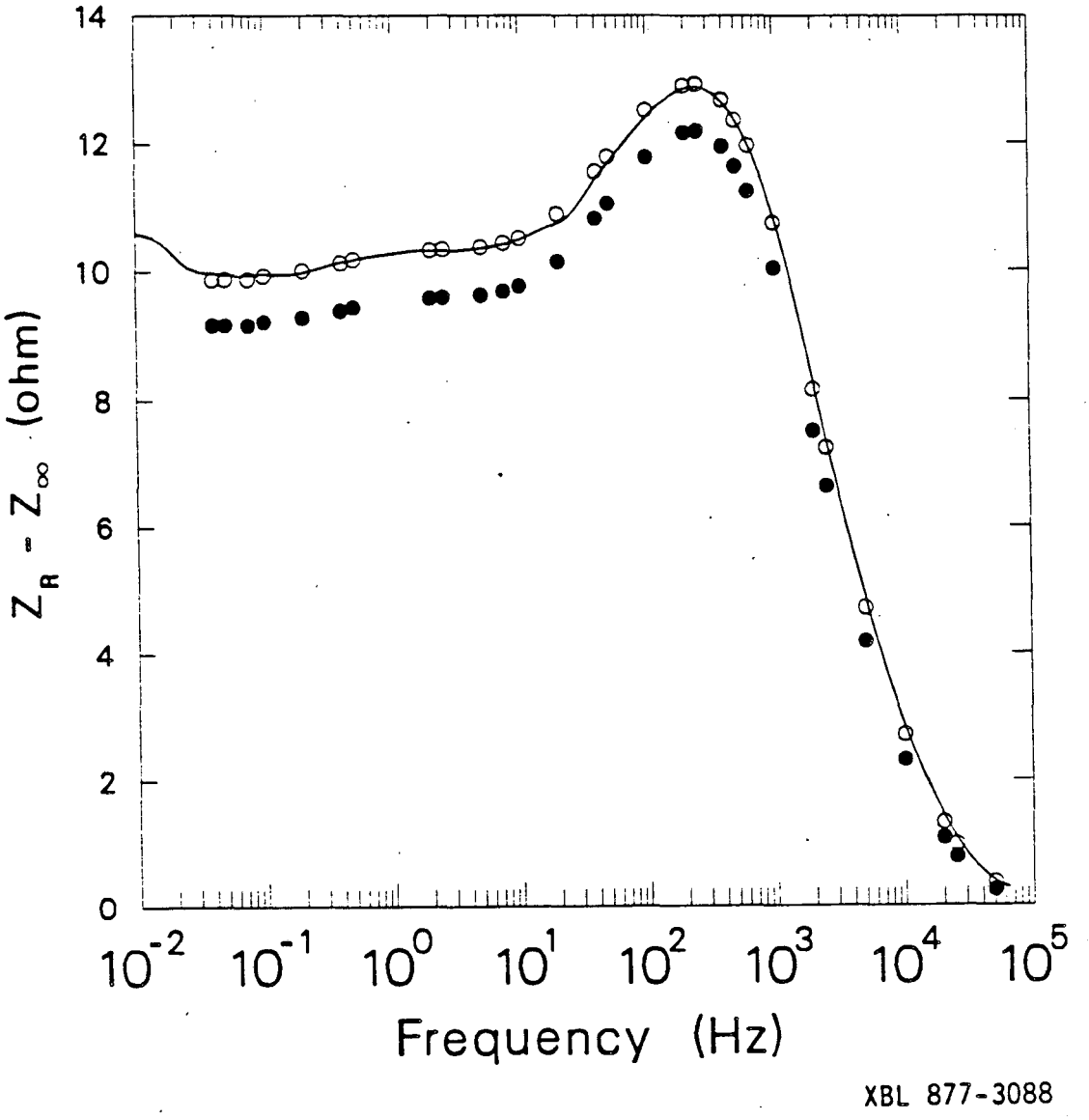

Figure 4-26. Real part of the impedance for experiment D.
— experimental data, assuming $Z_\infty = R_\infty = 2.40\ \Omega$.
• values calculated from the K-K relation (equation 4-10) without extrapolation.
O values calculated from the K-K relation including extrapolation to $\omega = 0$ and $\omega \longrightarrow \infty$, with:

$\omega_\infty = 2\pi(1.5\times10^5)\ s^{-1}$; $A_{I\infty} = 1.006$, $B_{I\infty} = 3.545\times10^5$ (coefficients of the straight line connecting two high-frequency experimental points).

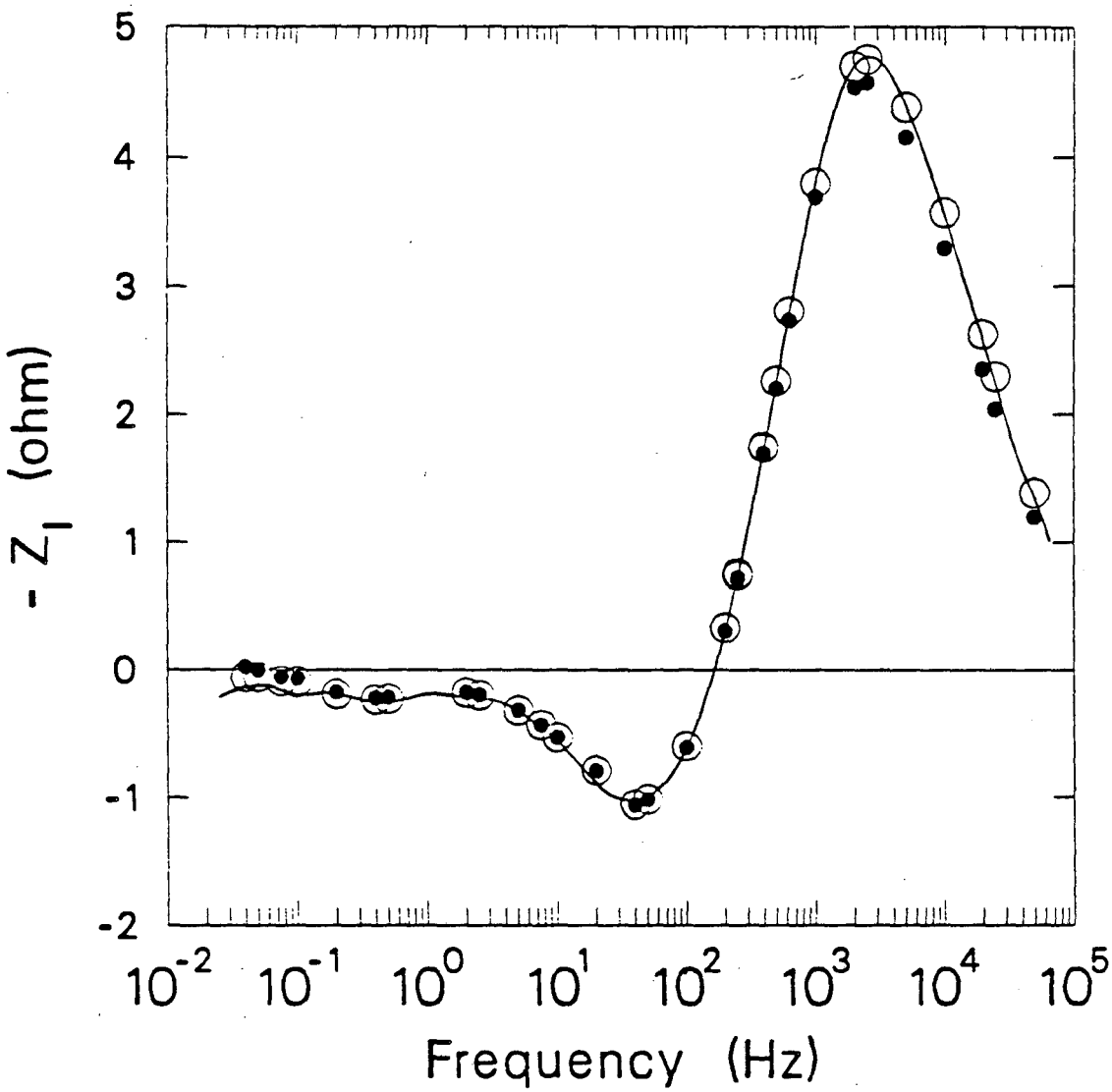

Figure 4-27. Imaginary part of the impedance for experiment D.
— experimental data. XBL 877-3128
• values calculated from the K-K relation (equation 4-11) without extrapolation.
O values calculated from the K-K relation including extrapolation to $\omega = 0$ and $\omega \longrightarrow \infty$, with:
$R_0 = 12.20\ \Omega$ (estimated zero-frequency intercept of the experimental complex-plane plot), $Z_R(\omega_{min}) = 12.20\ \Omega$ (experimental value = 12.46), and

$\omega_\infty = 2\pi(1.5\times10^5)\ s^{-1}$, $R_\infty = 2.40\ \Omega$ (estimated infinite-frequency intercept of the experimental complex-plane plot), $Z_R(\omega_{max}) = 2.682\ \Omega$ (experimental value).

It is also interesting to note that experiments A and C are for a rotating hemispherical electrode, while experiments B and D are the corresponding experiments for a rotating disk electrode. The results of the K-K analysis for these experiments have shown no systematic difference between the hemisphere and the disk electrodes, and therefore the consistency with the K-K relations appears to be unaffected by the uniformity or non-uniformity of the primary current distribution.

As noted in chapter 3, the experimental results for the disk electrode, B and D, are very similar to the experimental results of Keddam *et al.* (15). However Cahan and Chen (16) state, without any evidence, that the latter results are an example of experimental data, "which will produce semicircles and other curves in a complex plane plot, but which do not satisfy the Kramers-Kronig relations!" They also write that, "Such curves cannot, then, be interpreted as impedance." Contrary to these apparently arbitrary statements, the results obtained here show that one can rather expect data such as experiments A through D or the experiments of Keddam *et al.* (15) to be consistent with the Kramers-Kronig relations.

An important implication of the work presented here is that electrochemical impedance data having inductive loops (negative imaginary parts) — a characteristic which has been controversial in electrochemical research and literature — can be consistent with the Kramers-Kronig relations, and this consistency is an indication that such behavior is a valid characteristic of the electrochemical interface.

References for Chapter 4

1. H. A. Kramers, "Die Dispersion und Absorption von Röntgenstrahlen," *Physikalische Zeitschrift*, **30**, 522-523 (1929). Also *Collected Scientific Papers*, p. 347, North-Holland Publishing Company, Amsterdam (1956).

2. R. de L. Kronig, "On the Theory of Dispersion of X-Rays," *Journal of the Optical Society of America and Review of Scientific Instruments*, **12**, 547-557 (1926).

3. H. W. Bode, *Network Analysis and Feedback Amplifier Design*, chapter 14, Nostrand, New York (1945).

4. L. D. Landau and E. M. Lifshitz, *Electrodynamics of Continuous Media*, Vol.8, Course of Theoretical Physics, pp. 256-284, Pergamon Press, New York (1960).

5. Milan M. Jakšić and John Newman, "The Kramers-Kronig Relations and Evaluation of Impedance for a Disk Electrode," *Journal of the Electrochemical Society*, **133**, 1097-1101 (1986).

6. B. D. Cahan, C. T. Chen, D. Radman, and D. A. Scherson, "On the Questions of Presentation and Analysis of Impedance Measurements in Electrochemical Systems," unpublished manuscript.

7. V. A. Tyagi and G. Ya. Kolbasov, *Elektrokhimia*, **8**, 59 (1972).

8. R. L. Van Meirhaeghe, E. C. Dudoit, F. Cardon, and W. P. Gomez, "On the Application of the Kramers-Kronig Relations to Problems Concerning the Frequency Dependence of Electrode Impedance," *Electro-*

chimica Acta, **21**, 39-43 (1976).

9. C. D. S. Tuck, "The Use of Computers in the Verification and Analysis of Data from Electrochemical Impedance Measurements," Abstract 191, pp. 276-277, The Electrochemical Society Extended Abstracts, Vol. 84-2. New Orleans, LA, Oct. 7-12, 1984.

10. M. Kendig and F. Mansfeld, "Corrosion Rates from Impedance Measurements: An Improved Approach for Rapid Automatic Analysis," *Corrosion*, **39**, 466-467 (1983).

11. Digby D. Macdonald and Mirna Urquidi-Macdonald, "Application of Kramers-Kronig Transforms in the Analysis of Electrochemical Systems, I. Polarization Resistance," *Journal of the Electrochemical Society*, **132**, 2316-2319 (1985).

12. M. Urquidi-Macdonald, S. Real, and D. D. Macdonald, "Application of Kramers-Kronig Transforms in the Analysis of Electrochemical Impedance Data, II. Transformations in the Complex Plane," *Journal of the Electrochemical Society*, **133**, 2018-2024 (1986).

13. John Newman, "Frequency Dispersion in Capacity Measurements at a Disk Electrode," *Journal of the Electrochemical Society*, **117**, 198-203 (1970).

14. R. Hornbeck, *Numerical Methods*, pp. 122-125, Quantum Publishers, Inc., New York (1975).

15. M. Keddam, O. R. Mattos, and H. Takenouti, "Reaction Model for Iron Dissolution Studied by Electrode Impedance, I. Experimental Results and Reaction Model," *Journal of the Electrochemical Society*, **128**,

257-266 (1981).

16. Boris D. Cahan and Chia-Tien Chen, "The Nature of the Passive Film on Iron, II. A-C Impedance Studies," *Journal of the Electrochemical Society*, **129**, 474-480 (1982).

CHAPTER 5

Theoretical Models of the Electrochemical Impedance: Application to the Fe/H_2SO_4 System

5.1. Introduction

This chapter presents some calculated impedance results for the iron - sulfuric acid system, using the theoretical formulation described in section 1.6.1.

The characteristics of the Fe/H_2SO_4 system include multiple electron-transfer and adsorption/desorption reactions, mass transfer of species in the electrolytic solution, formation of porous salt and passivating oxide films on the electrode, and double-layer charging under alternating current conditions. A mathematical impedance model accounting for all these phenomena is not currently available, and the results presented here are only preliminary. The purpose of this analysis is to investigate some aspects of the system and to indicate directions for further research.

In particular, the analysis in this chapter focuses on the effect of mass transfer of the Fe^{++} ion produced by the dissolution reaction on the impedance of the Fe/H_2SO_4 system. We have discussed the controversy about the role of OH^- ion (or an analogous reactant species) in the reaction mechanism and the limiting current and passivation behavior of the Fe/H_2SO_4 system, in section 1.3. An objective of the analysis is to help resolve this controversy, using the electrochemical impedance tech-

nique.

The experimental results in chapter 3 indicate that the mass-transfer impedance is negligible at low currents but significant at high currents in the limiting-current region. Calculations are carried out at two regions of the anodic polarization curve, at low currents corresponding to the experiments in section 3.4 (specifically experiments C and D) and around the limiting current plateau corresponding to the experiments in section 3.5, in order to find out whether the employed models can predict the observed mass-transfer effects on the impedance of the system. All calculations are for a rotation speed Ω = 1600 rpm = 167.6 rad/s. The high-current calculations are performed at a steady-state current density of 1.3 A/cm^2, which is the limiting current density observed experimentally by Russell (5, 4) for rotating disk electrodes.

The faradaic impedance is first estimated using analytical expressions from infinitely-dilute-solution theory. At low current densities where the electrolytic solution remains fairly dilute, calculations based on infinitely-dilute-solution theory may be adequate, but at high current densities where the electrolytic solution near the electrode is nearly saturated with $FeSO_4$, application of concentrated-solution theory may be necessary. The faradaic impedance is then calculated numerically at low as well as high current densities with a concentrated solution model (1), which uses the Stefan-Maxwell equation for multicomponent diffusion. In addition, the effect of a porous $FeSO_4$ film on the electrochemical impedance of the system is roughly estimated.

5.2. Reaction Kinetics — Charge-Transfer Resistance

The reaction mechanism for iron dissolution involves multiple reactions including adsorbed intermediates (see section 1.3.1). However in these preliminary calculations, the iron dissolution reaction is treated as a simple (elementary) reaction

$$Fe \rightleftarrows Fe^{++} + 2e^{-} , \qquad [5\text{-}1]$$

and the reaction kinetics are expressed by a Butler-Volmer relationship (equation 1-34)

$$i_1 = nFk_a \exp\left(\frac{(1-\beta)nF}{RT} V_o\right) - nFk_c\, c_{2,0} \exp\left(\frac{-\beta nF}{RT} V_o\right) \qquad [5\text{-}2]$$

where $$V_o = V_m - \Phi_o ,$$

i_1 is the current density due to reaction 5-1, and the subscript 2 refers to the Fe^{++} ion. This kinetic equation has the same form as that used by Law and Newman (2) and was also used by Russell and Newman (3-5), assuming $\beta = 1/2$. The potential values in the kinetic equation are relative to a normal hydrogen reference electrode (NHE).

Values of k_a and k_c were obtained by Russell and Newman (3) by fitting the kinetic equation to steady-state polarization data for a rotating hemispherical electrode. The same values are used in these calculations and are listed in table 5-1 with other input parameters.

Note that the partial current density due to the cathodic (second) term in equation 5-2 is several orders of magnitude smaller than the partial current density due to the anodic term in the range of interest here. One can then obtain a value of the potential driving force $\bar{V}_o$ at

a specified value of the steady-state current density $\bar{i}_1$.

$$\bar{V}_o \approx \frac{RT}{(1 - \beta)nF} \ln \left(\frac{\bar{i}_1}{nFk_a} \right) . \qquad [5\text{-}3]$$

Near the open-circuit potential, hydrogen evolution should also be considered.

$$2H^+ + 2e^- \rightleftarrows H_2 . \qquad [5\text{-}4]$$

Hydrogen evolution on iron also occurs in a multi-step mechanism (6, 7). Kinetic data for the cathodic hydrogen reaction near the open-circuit potential for iron corrosion are given, for example, in References (7-9). A kinetic equation for the cathodic hydrogen reaction, determined by Bockris *et al.* (8) and Kelly (7), is

$$i_{c,H} = - Fk_{c,H}\, a_H \exp \left(\frac{-F}{2RT} V_o \right) \qquad [5\text{-}5]$$

where a_H is the activity of the hydrogen ion. The partial current density due to hydrogen evolution is negligible in the range considered here, and it is not included in the calculations.

In addition, hydrogen ions participate in the homogeneous chemical reaction

$$HSO_4^- \rightleftarrows H^+ + SO_4^{-2} , \qquad [5\text{-}6]$$

which is assumed to be near equilibrium conditions, described by (10)

$$K_{eq} = \frac{c_H\, c_{SO_4}}{c_{HSO_4}} . \qquad [5\text{-}7]$$

With the simple description of the reaction kinetics given by equation 5-2, the charge-transfer resistance is obtained.

$$R_t^{-1} = \left(\frac{\partial i_1}{\partial V_o}\right)_{ss} = \qquad [5\text{-}8]$$

$$= \frac{(nF)^2}{RT} \left\{ k_a \ (1 - \beta) \ \exp \left(\frac{(1 - \beta)nF}{RT} \bar{V}_o\right) \right.$$

$$\left. + \ k_c \ \beta \ \bar{c}_{2,0} \ \exp \left(\frac{- \beta nF}{RT} \bar{V}_o\right) \right\} .$$

5.3. Infinitely-Dilute-Solution Calculations

In an infinitely dilute solution, the current is given by (equations 1-35 and 1-39)

$$i_1 = \frac{nF}{s_2} D_2 \left(\frac{\partial c_2}{\partial y}\right)_{y=0} . \qquad [5\text{-}9]$$

The faradaic impedance from dilute-solution theory is given by equation 1-60, using the kinetic equation 5-2.

$$Z_F = R_t + R_t \ k_c \ \exp \left(\frac{- \beta nF}{RT} \bar{V}_o\right) \frac{\delta_2}{D_2} \frac{1}{\Gamma(4/3)} \left\{\frac{-1}{\Theta_2'(0)}\right\} . \qquad [5\text{-}10]$$

The second term in the above equation is the convective diffusion impedance Z_D, according to the dilute-solution theory; and the dimensionless convective Warburg impedance function $\frac{-1}{\Theta_i'(0)}$ is discussed in section 1.6.1.4.

For a more convenient notation we write

$$R_D = Z_D\ \Gamma(4/3) \left\{\frac{-1}{\theta_2'(0)}\right\}^{-1}$$

$$= R_t\ k_c\ \exp\left(\frac{-\beta nF}{RT}\ \bar{V}_o\right) \frac{\delta_2}{D_2}\ . \qquad [5\text{-}11]$$

R_D is approximately equal to the zero-frequency limit of Z_D.

To calculate the impedance, particularly R_t and R_D, we first need values of the steady-state variables $\bar{i}_1$, $\bar{V}_o$, and $\bar{c}_{2,0}$. The Nernst diffusion-layer approximation is used to get a relationship between the steady-state current and the Fe^{++} concentration at the interface. Equation 5-9 then gives

$$\bar{i}_1 = \frac{nF}{s_2}\ D_2\ \frac{\bar{c}_{2,\infty} - \bar{c}_{2,0}}{\delta_2}\ . \qquad [5\text{-}12]$$

Since $\bar{c}_{2,\infty} = 0$ and $s_2 = -1$,

$$\bar{i}_1 = nF\ \frac{D_2}{\delta_2}\ \bar{c}_{2,0}\ . \qquad [5\text{-}13]$$

Equations 5-2 and 5-13 allow calculation of $\bar{V}_o$ and $\bar{c}_{2,0}$ at a specified $\bar{i}_1$. R_t and R_D are then calculated from equations 5-8 and 5-11.

5.4. Concentrated Solution Model

An impedance model using concentrated-solution theory has been presented by Tribollet and Newman (1).

Brief Description of the Model

The central equation in the model is the Stefan-Maxwell equation for multicomponent diffusion, written in the form (see equations 1-40 and 1-41)

$$\nabla x_i + \frac{z_i F}{RT} x_i \nabla\Phi = \sum_{k \neq i} \frac{x_i \underline{J}_k - x_k \underline{J}_i}{c D_{ik}} , \qquad [5\text{-}14]$$

where the activity coefficients are assumed to be equal to one. This equation describes the motion of species i relative to the surrounding fluid, accounting for composition gradients, electrostatic potential (Φ) gradients (migration), and interactions with other species. $\underline{J}_i$ is the molar flux of species i relative to the mass-average velocity, and D_{ik} is a diffusion coefficient describing the interaction of species i and k ($D_{ik} = D_{ki}$). The composition is expressed in terms of the mole fraction x_i of every species including the 'solvent' H_2O, and c is the total concentration.

The set of equations 5-14 for each species is used in conjuction with material balance relations (equation 1-36), which also account for any number of homogeneous chemical reactions. These equations together with the electroneutrality equation provide a sufficient number of equations to solve for all the unknowns, which are the mole fractions of each species and the potential Φ.

The relationship between the molar fluxes and partial current densities at the interface (equation 1-35) is a boundary condition for this set of equations. The model has provision for multiple electron-

transfer reactions at the interface, but it has no provision for adsorption/desorption reactions or adsorbed species. Another boundary condition is that far from the electrode surface, the mole fractions approach their values in the bulk solution.

The mathematical model is one-dimensional, considering variations only in the direction y normal to the surface of a rotating disk electrode. It uses rotating disk hydrodynamics described by

$$v_y = (\Omega\nu)^{1/2} \left(- a\zeta^2 + \frac{1}{3}\zeta^3 - \frac{0.616}{6}\zeta^4\right) \qquad [5\text{-}15]$$

where

$$\zeta = y \left(\frac{\Omega}{\nu}\right)^{1/2} .$$

It is also possible to deal more exactly with the governing hydrodynamic relations to handle a nonzero interfacial velocity and composition-dependent viscosity and density (11).

The equations are solved numerically with a finite difference technique. The mathematical model first treats the steady-state problem and then solves the alternating problem at specified perturbation frequencies. Finally it calculates the faradaic impedance, according to equation 1-33, as a function of frequency, without considering double-layer effects.

Application to the Fe/H_2SO_4 System

In this application of the concentrated-solution model, the simplified description of electrochemical kinetics given in section 5.2 (equations 5-1, 5-2, and 5-8) is used. The homogeneous reaction of partial dissociation of HSO_4^- (equation 5-6) is included only in the boundary

condition specifying the bulk solution composition. Specifically, the bulk concentrations of H^+, SO_4^{-2}, and HSO_4^- are calculated from the equilibrium condition (equation 5-7) and the bulk concentration of sulfuric acid (*i.e.*, 1 M H_2SO_4). The bulk concentrations are given in table 5-2.

An important question that arises in the application of concentrated-solution theory is whether there are sufficient data for the diffusion coefficients D_{ik}, which describe the interactions between the species in the system. Sufficient data are not available for the Fe/H_2SO_4-H_2O system, and the interactions between ionic species are not adequately accounted for in the present application.

The coefficients D_{i1} where 1 denotes the H_2O species and i is an ionic species are expected to be reasonably constant, independent of composition (10). The available values of the diffusion coefficients D_i for each ion at infinite dilution in H_2O should therefore be a reasonable approximation for D_{i1}.

However the coefficients D_{ik} when both i and k are ionic species are functions of composition, and we do not have enough data for their values in this system. A rough order-of-magnitude estimate is used in the application of the model. In effect, the contributions of ion–ion interactions, embodied in D_{ik}, to the concentration and potential distributions are made negligible relative to the ion–H_2O interactions (D_{i1}). With the diffusion coefficients set in this manner, the concentrated-solution model comes close to a dilute-solution model including the effect of migration.

We visualize using a concentrated-solution impedance model with a more realistic description of the reaction mechanism and more accurate transport properties, in the future.

5.5. Parameter Values Used in Calculations

Physical property data, kinetic parameters, and other parameters are given in table 5-1.

The product of D_i and viscosity is approximately constant, at constant temperature (10). D_2, the diffusion coefficient of Fe^{++}, as well as D_3, D_4, and D_5, have been therefore reduced from their values at infinite dilution in H_2O (given in Ref. 10), by a factor approximately equal to the ratio of the viscosities of 1 M H_2SO_4 aqueous solution and H_2O (given in Ref. 12). For the concentrated-solution calculations, the diffusion coefficients $\mathcal{D}_{21}$, $\mathcal{D}_{31}$, $\mathcal{D}_{41}$, and $\mathcal{D}_{51}$ are then set equal to D_2, D_3, D_4, and D_5 respectively.

For the high-current calculations, different values of D_i (i = 2, 3, 4, 5) and kinematic viscosity ν (sets a, b) are used in order to test the effect of these parameters. In set a, the kinematic viscosity of 1 M H_2SO_4 at 20° C (12) and values of D_i as discussed in the paragraph above are used. In set b, the values of D_i used by Russell and Newman (3, 4) (which are reduced by a factor of 4 from their infinite dilution values) and the ν value used in (3, 4) are used. In set c, the values of D_i and ν used by Russell and Newman (3, 4) are used.

Table 5-1. Parameter values used in the calculations

Kinetic Parameters For Reaction 5-1 (Ref. 3)	
k_a	2.0052×10^{-3} mol·cm^{-2}·s^{-1}
k_c	2.6701×10^{-15} cm·s^{-1}
n	2
β	½

Diffusion Coefficients			
i	species	$D_i \times 10^5$ (cm^2·s^{-1})	
		(a)	(b) (from Ref. 3)
2	Fe^{++}	0.50	0.1658
3	SO_4^{-2}	0.7987	0.2663
4	H^+	6.984	2.328
5	HSO_4^-	0.997	0.3323

Other Parameters	
ν	0.01142 (a) 0.0398 (b) cm^2/s
K_{eq}	5×10^{-5} mol/cm^3, Equilibrium constant for reaction 5-6, (3)
T	298.15 K
κ	0.40 Ω^{-1}·cm^{-1} (18)

Table 5-2. Bulk solution composition

i	Species	$c_i \times 10^3$ (mol/cm^3)
1	H_2O	55.5
2	Fe^{++}	0
3	SO_4^{-2}	0.0456
4	H^+	1.0456
5	HSO_4^-	0.9544
	Total concentration c	57.5

5.6. Results and Discussion

Table 5-3 shows the calculated results for three cases using the dilute-solution expressions. The values of $\bar{i}_1$, $\bar{V}_o$, and R_t from the concentrated-solution model are the same as those shown in table 5-3, while the $\bar{c}_{2,0}$ values are smaller; the concentration $\bar{c}_{2,0}$ is 0.02565, 0.03762, 0.8479, and 1.697 M for cases I, II, III(a), and III(b), respectively.

Figures 5-1 and 5-2 show a comparison of the mass-transfer inpedance Z_D according to the infinitely-dilute-solution and concentrated-solution calculations for cases II and III(b), respectively. For the low-current case (II), figure 5-1 shows good agreement between the infinite-dilution and concentrated-solution values, while for the high-current case (III), significant differences are displayed in figure 5-2. The difference between the dilute-solution and concentrated-solution results, is mainly due to the effect of migration, which is not accounted for in the analytic infinitely-dilute-solution calculations. Figure 5-3 shows the concentrated-solution-model results for case III(a) and III(b).

Notice that the calculated mass-transfer impedance is 8 to 10 orders of magnitude smaller than the charge-transfer resistance. Different D_i or ν values affect the calculated $\bar{c}_{2,0}$ and Z_D, for case III, but still Z_D remains negligible relative to the charge-transfer resistance. For cases I and II, the calculated charge transfer resistance corresponds approximately to the low-frequency intercept of the capacitive loop on the real impedance axis.

Table 5-3. Results of infinitely-dilute-solution calculations

Case number	$\bar{i}_i$ (A/cm^2)	$\bar{V}_o$ (V *vs.* NHE)	$\bar{c}_2 \times 10^3$ (mol/cm^3)	R_t eq. 5-8 ($\Omega \cdot cm^2$)	R_D eq. 5-11 ($\Omega \cdot cm^2$)
I(a)	0.0250	-0.2478	0.0262	1.0276	8.577×10^{-9}
II(a)	0.0370	-0.2378	0.0387	0.6944	3.916×10^{-9}
III(a)	1.300	-0.1463	1.361	0.01976	3.173×10^{-12}
III(b)	1.300	-0.1463	3.498	0.01976	8.156×10^{-12}

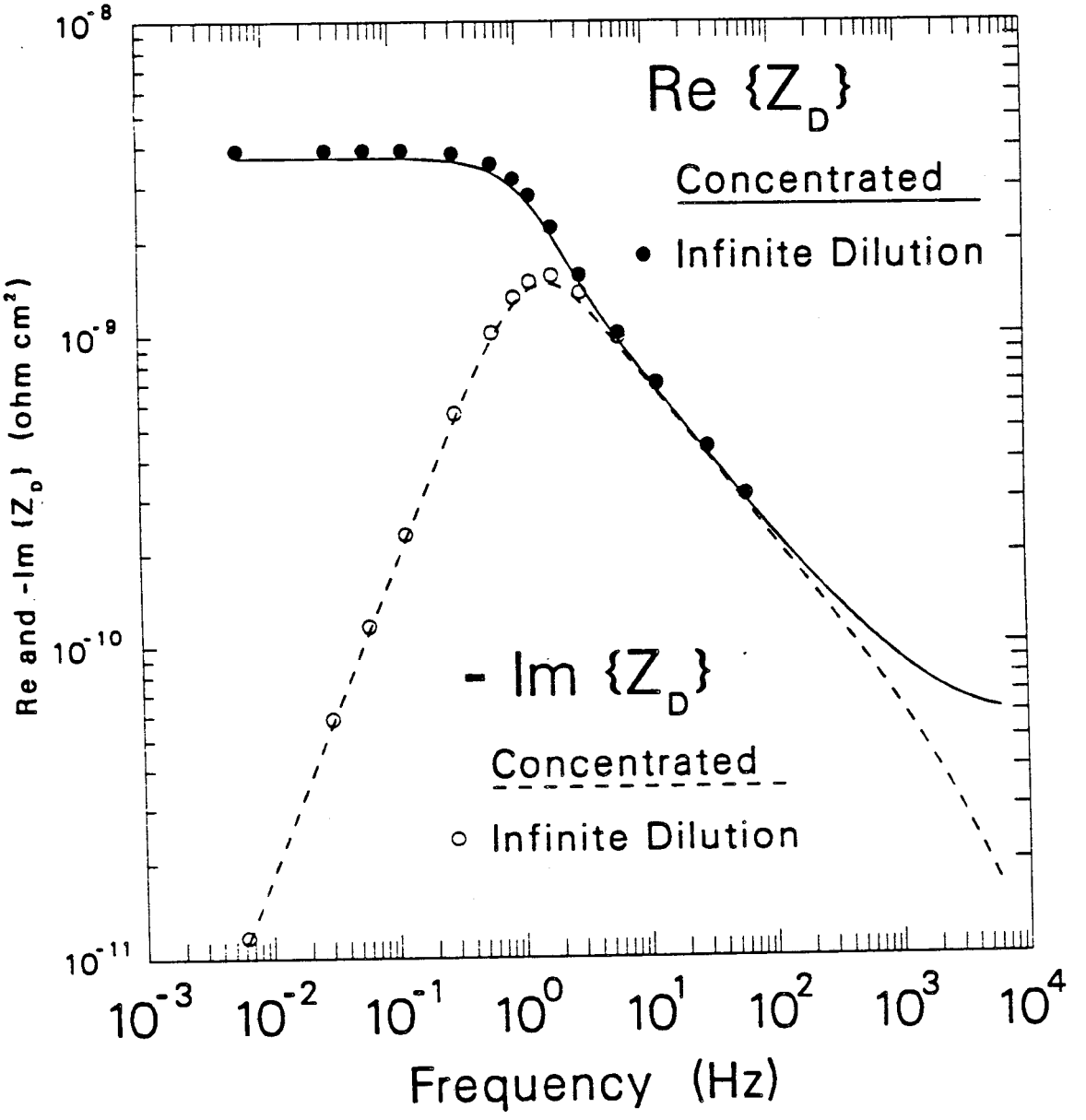

XBL 877-3129

Figure 5-1. Convective Warburg impedance calculated according to infinitely-dilute-solution theory and a concentrated-solution model for case II ($\bar{i}_1$ = 37 mA/cm^2). The infinite-dilution values are calculated from equation 5-10 with the exact solution for $(-1/\Theta_2'(0))$ given in Reference (13).

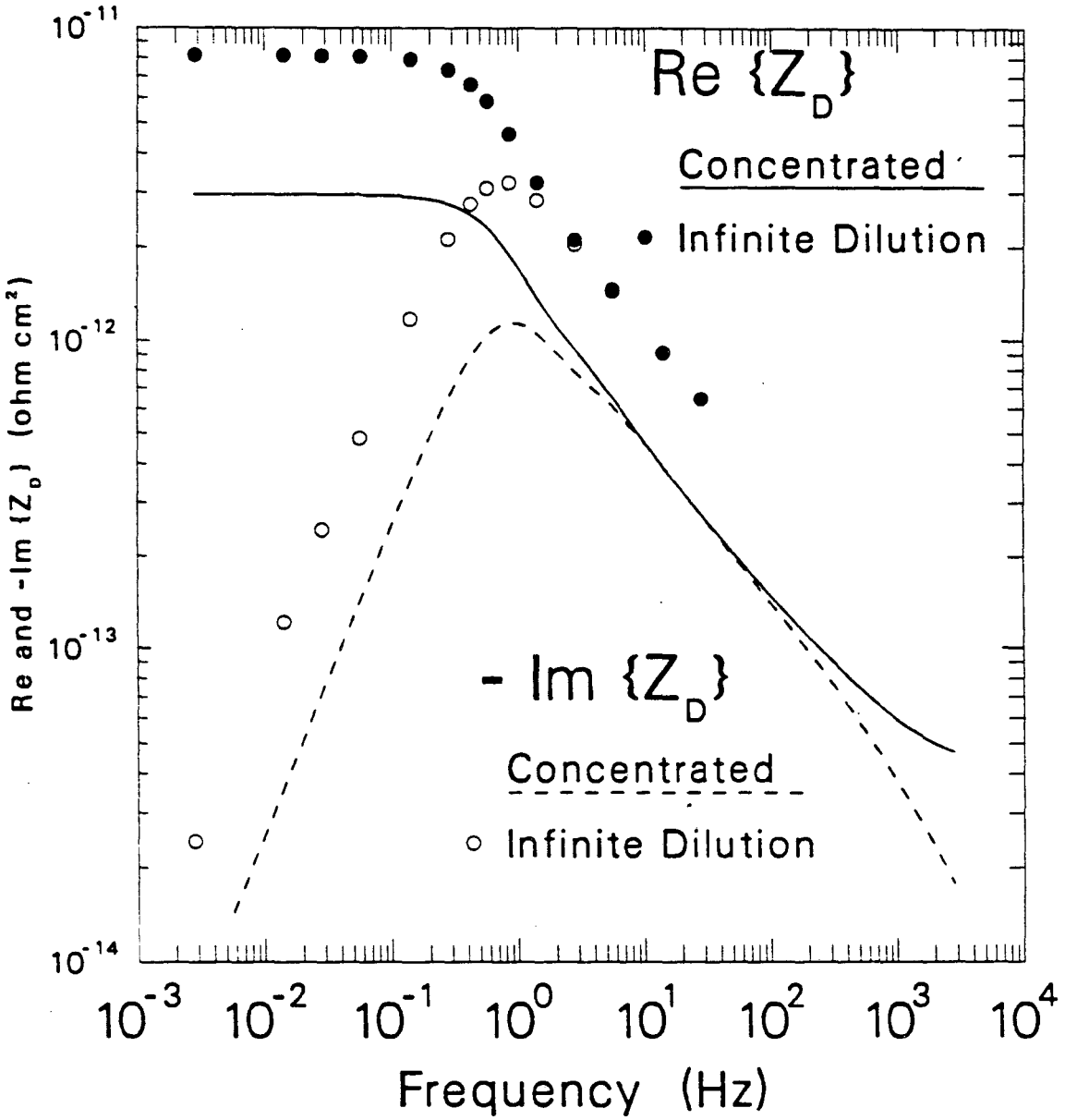

XBL 877-3130

Figure 5-2. Convective Warburg impedance calculated according to infinitely-dilute-solution theory and a concentrated-solution model for case III(b) ($\bar{i}_1$ = 1.3 A/cm^2). The infinite-dilution values are calculated from equation 5-10 with the exact solution for $\{-1/\theta_2'(0)\}$ given in Reference (13).

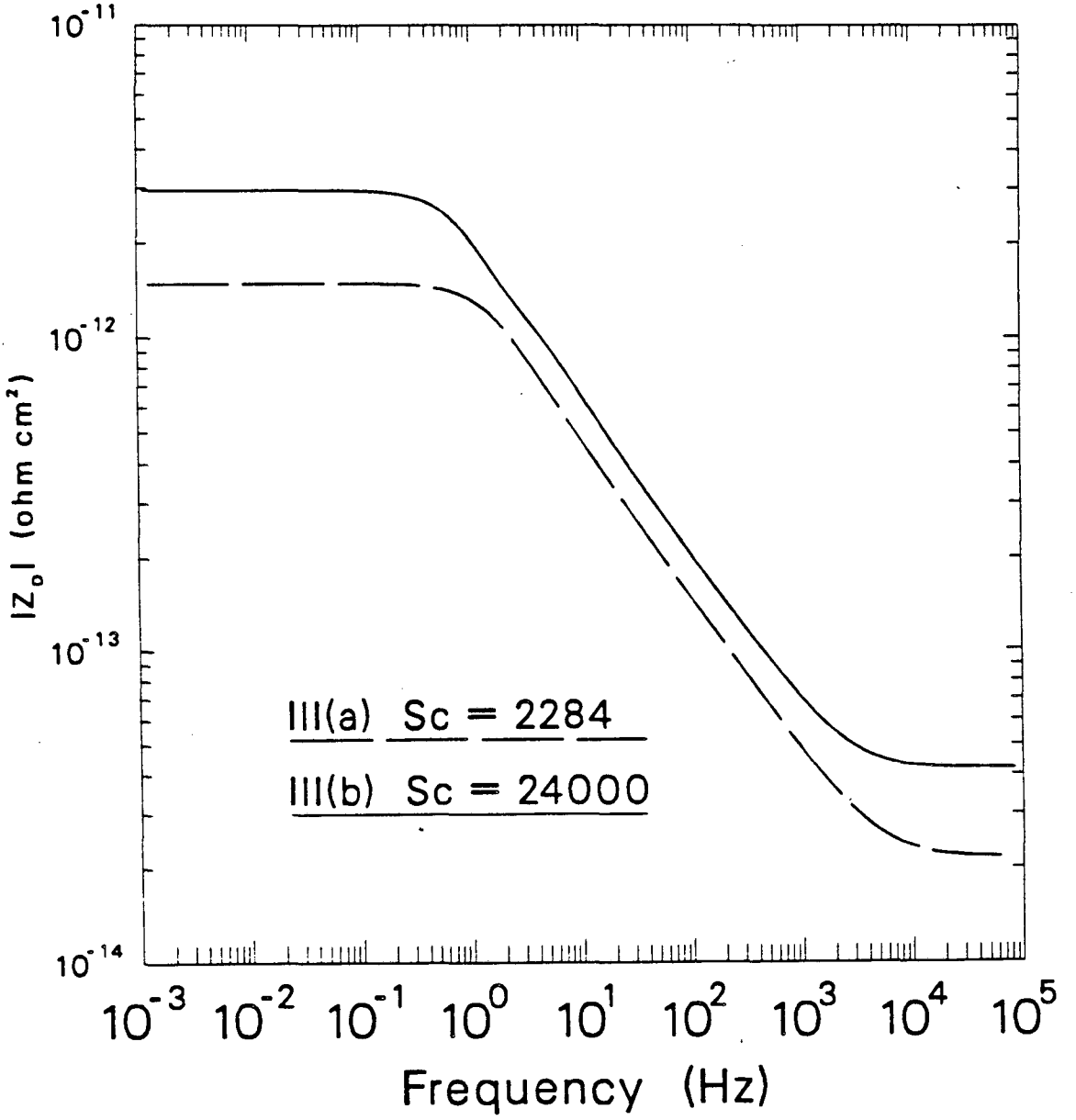

XBL 877-3131

Figure 5-3. Magnitude of the mass-transfer impedance calculated using a concentrated-solution model for case III ($\bar{i}_1$ = 1.3 A/cm^2) with two different sets of D_i and ν values.

The most significant result of these calculations is that the mass-transfer impedance Z_D is negligible for all the cases considered. A negligible mass-transfer impedance for cases I and II is in agreement with the experimental results. However in both steady-state and impedance experiments at high currents, corresponding to case III, significant mass-transfer effects appear.

Remember the model of Epelboin *et al.* (14, 15, see discussion in section 1.3) which considerered diffusion of a OH^- reactant species and required concentration values about ten orders of magnitude greater than the bulk OH^- concentration or a diffusion coefficient ~10 orders of magnitude greater than the expected value for OH^- to yield the experimentally observed limiting current value.

We may conclude that mass transfer of Fe^{++} in itself has negligible effect on the observed impedance behavior of the system, mainly because Fe^{++} is involved in the cathodic iron reaction which is a slow reaction and produces a negligible partial current density at the high anodic potentials corresponding to high currents. However Fe^{++} mass-transfer can affect the electrochemical system in other indirect ways, which have not been included in the calculations above.

A major way in which limitations in the transfer of Fe^{++} are manifested in the Fe/H_2SO_4 system is formation of a porous $FeSO_4$ film (see sections 1.3.2 and 1.3.3). Mass-transfer limitations in electrochemical systems usually appear in steady-state experiments as a current plateau. Russell and Newman (4) give an analysis of the steady-state limiting current showing that the steady-state current can remain constant while

the applied potential changes, if certain conditions are satisfied; these conditions are relationships between the salt film thickness, the film porosity, the fraction of the electrode covered by $FeSO_4$, and the potential.

Let us then consider probable effects of the salt film on the electrochemical impedance.

Effect of Porous Salt Film on the Electrochemical Impedance

Here we are interested in order-of-magnitude estimations of the effect of the salt film to see whether it can be significant. A rigorous treatment of the impedance of the Fe/H_2SO_4 system would then require a model that includes the salt film as an integral part, in a way similar to the model of Russell and Newman (3) transformed for alternating current conditions, in addition to the electrode and double-layer processes and the electrolytic solution.

At first, the salt film is expected to result in an additional diffusion impedance. The mathematical formulation for this diffusion impedance would be very similar to that described in section 1.6.1.4.

If negligible convection in the pores of the film is assumed and migration is ignored, a simplified material balance for the ferrous ion in the porous film may be written (16).

$$\frac{\partial c_2}{\partial t} = D_{2e} \frac{\partial^2 c_2}{\partial y^2} , \qquad [5\text{-}16]$$

where D_{2e} is an effective diffusion coefficient in the porous film and may be approximated by

$$D_{2e} = D_2 \, (\epsilon_f)^{1.5} \qquad [5\text{-}17]$$

where ϵ_f is the porosity of the salt film, which, as a first approximation, is assumed to be a constant.

As a first approximation, assume a (constant) steady-state film thickness $\bar{\delta}_f$; the solution for the dimensionless mass-transfer impedance is then given by equation 1-64 (Nernst model), substituting $\bar{\delta}_f$ for δ_i and D_{2e} for D_i.

Note that according to previous studies of salt films in similar systems (see section 1.3.2), the film thickness is about 1 to 20 μm, which is of the same order of magnitude as the diffusion-layer thickness in the electrolytic solution for this application, and the porosity may be ~ 1 %, corresponding to a slightly porous film.

Equation 1-56 relating the current to the flux at the electrode is modified to account for the porosity of the film; the faradaic current density is divided by ϵ_f in the modified equation.

The resulting expression for the impedance due to diffusion of Fe^{++} in the solution in the pores of the salt film, using the approximations discussed above, is

$$Z_{D,f} = R_t \left(\frac{\partial i_{1avg}}{\partial c_{2,0}}\right)_{ss} \frac{s_2}{nF} \; \frac{\bar{\delta}_f}{D_{2e}\,\epsilon_f} \; \frac{1}{\Gamma(4/3)} \left\{\frac{-1}{\Theta_{N2}'(0)}\right\} . \qquad [5\text{-}18]$$

$\{-1/\Theta_{N2}'(0)\}$ varies with frequency (equation 1-64); it is of the order of 1 for finite frequencies and approaches zero as $\omega \longrightarrow \infty$.

The average (superficial) current density i_{1avg} is included in the impedance expression because a fraction of the electrode surface may be

blocked by the salt film (see footnote after equation 1-19). The charge-transfer resistance is also modified.

$$R_t^{-1} = \left(\frac{\partial i_{1avg}}{\partial V_o}\right)_{ss} . \qquad [5\text{-}19]$$

If the free fraction of the electrode surface is denoted by ϵ_s, then

$$i_{1avg} = \epsilon_s \, i_1 \qquad [5\text{-}20]$$

with i_1 given by the kinetic equation 5-2. For simplicity we assume ϵ_s is constant. Then the zero-frequency limit of $Z_{D,f}$ in equation 5-18 is

$$R_{D,f} = R_t \, \epsilon_s \, k_c \exp\left(\frac{-\beta nF}{RT} \bar{V}_o\right) \frac{\bar{\delta}_f}{D_{2e} \, \epsilon_f} . \qquad [5\text{-}21]$$

Besides acting as a diffusion barrier, the salt film results in an additional potential gradient. The total potential may be written as (see equation 1-22)

$$V = V_o + \Delta\Phi_{c,f} + \Delta\Phi_{\Omega,f} + \Delta\Phi_{c,s} + \Delta\Phi_{\Omega} . \qquad [5\text{-}22]$$

The ohmic potential drop through the salt film is given approximately by

$$\Delta\Phi_{\Omega,f} = \frac{i_{avg}}{\kappa_f} \frac{\delta_f}{\epsilon_f} . \qquad [5\text{-}23]$$

$\Delta\Phi_{c,f}$ and $\Delta\Phi_{c,s}$ are the potentials associated with concentration gradients in the solution within the pores of the film and in the solution outside the film, respectively. $\Delta\Phi_{\Omega}$ is the ohmic potential drop in the solution assuming a conductivity equal to its bulk value, and it is equal to $i_{avg}AR_{\Omega}$, where R_{Ω} is given by equation 1-15 for a disk electrode and A is the electrode area.

Consider the potential $\Delta\Phi_{\Omega,f}$, which is expected to be much larger than $\Delta\Phi_{c,f}$. At a first glance, $\Delta\Phi_{\Omega,f}$ may be expected to influence the electrochemical impedance in a way analogous to the ohmic resistance in the bulk solution (R_Ω). However $\Delta\Phi_{\Omega,f}$ is a function of the $FeSO_4$ film thickness and porosity, which are determined by the flux of Fe^{++}. Since species concentrations and fluxes are oscillating under alternating current conditions, $\Delta\Phi_{\Omega,f}$ results in an impedance term varying with frequency, perhaps in a manner similar to the diffusion impedance. The magnitude of the impedance arising from the potential drop $\Delta\Phi_{\Omega,f}$ may be roughly $\frac{1}{\kappa_f}\frac{\bar{\delta}_f}{\epsilon_f}$. κ_f, the conductivity of the solution in the pores of the film, is estimated by Russell and Newman (4) to be 0.132 $\Omega^{-1}\cdot cm^{-1}$ for the Fe/H_2SO_4 system.

We can now make some rough calculations to estimate the order of magnitude of the salt film effects on the electrochemical impedance, for the case of a rotating disk electrode at the limiting current 1.3 A/cm^2 (Ω = 1600 rpm). We may use some of the data from the steady-state analysis of Russell and Newman (4), for the same case.

For example, assume $\epsilon_s = 10^{-2}$. This ϵ_s value requires $\bar{V}_o = -0.028$ V, calculated from equation 5-3 with i_1 according to equation 5-20. We may also assume $\bar{c}_{2,0}$ is at the $FeSO_4$ saturation value, which is about 2 M (17). The value of $\bar{\delta}_f/\epsilon_f$ estimated by Russell and Newman (4) for cell potentials near the beginning of the limiting current plateau is ~ 100 μm; if ϵ_f is taken as ~ 10^{-2} this value corresponds to $\bar{\delta}_f$ ~ 1 μm. The impedance due to the ohmic resistance

through the film is ~ 0.08 $\Omega \cdot cm^2$, for this value of $\bar{\delta}_f/\epsilon_f$. For comparison, the bulk solution ohmic resistance for a 3 mm disk is 0.3 $\Omega \cdot cm^2$.

R_t and $R_{D,f}$ are calculated from equations 5-19 and 5-21. For this case, R_t is 0.0197 $\Omega \cdot cm^2$, which is about the same as without the film, and $R_{D,f}$ is 1×10^{-11}, which is a little larger but of the same order of magnitude as the mass-transfer impedance without considering the film.

As another example, assume $\epsilon_s = 10^{-1}$. Then $\bar{V}_o = -0.087$ V, and $R_t = 0.0198\ \Omega \cdot cm^2$. From the analysis of Russell and Newman (4), $\bar{\delta}_f/\epsilon_f \sim$ 200 μm, for this case. If we take $\epsilon_f = 0.05$ (corresponding to $\bar{\delta}_f = 10\ \mu m$), then $R_{D,f}$ is 2×10^{-10}, which is ~ 25 times greater than the mass-transfer impedance without the film.

From these estimates, we may conclude that even though the diffusion impedance due to the $FeSO_4$ film may be 10 or 100 times greater than the mass transfer impedance without considering the film, the mass-transfer impedance is still found to be negligible. But the impedance due to the potential drop $\Delta\Omega_{\Omega,f}$ may be important; it may be greater than the charge-transfer resistance and of the same order of magnitude as the bulk ohmic resistance. Thus a salt film can account for the mass-transfer influences apparent in experimental results.

As indicated in section 3.5, very limited and not so reliable experimental impedance data exist for the Fe/H_2SO_4 system in the limiting current region. More experimental as well theoretical work is therefore needed to elucidate the effect of porous salt films.

References for Chapter 5

1. Bernard Tribollet and John Newman, "Impedance Model for a Concentrated Solution, Application to the Electrodissolution of Copper in Chloride Solutions," *Journal of the Electrochemical Society*, **131**, 2780-2785 (1984).

2. Clarence G. Law, Jr., and John Newman, "A Model for the Anodic Dissolution of Iron in Sulfuric Acid," *Journal of the Electrochemical Society*, **126**, 2150-2155 (1979).

3. Philip Russell and John Newman, "Anodic Dissolution of Iron in Acidic Sulfate Electrolytes, I. Formation and Growth of a Porous Salt Film," *Journal of the Electrochemical Society*, **133**, 59-69 (1986).

4. Philip Russell and John Newman, "Anodic Dissolution of Iron in Acidic Sulfate Electrolytes, II. Mathematical Model of Current Oscillations Observed under Potentiostatic Conditions," *Journal of the Electrochemical Society*, **134**, 1051-1059 (1987).

5. Philip P. Russell, *Corrosion of Iron: The Active - Passive Transition and Sustained Electrochemical Oscillations*, Ph. D. Dissertation, University of California, Berkeley, CA (1984).

6. J. O'M. Bockris and D. F. A. Koch, "Comparative Rates of the Electrolytic Evolution of Hydrogen and Deuterium on Iron, Tungsten and Platinum," *The Journal of Physical Chemistry*, **65**, 1941-1948 (1961).

7. Eugene J. Kelly, "The Active Iron Electrode, I. Iron Dissolution and Hydrogen Evolution Reactions in Acidic Sulfate Solutions," *Journal of the Electrochemical Society*, **112**, 124-131 (1965).

8. J. O'M. Bockris, D. Dražić, and A. R. Despić, "The Electrode Kinetics of the Deposition and Dissolution of Iron," *Electrochimica Acta*, **4**, 325-361 (1961).

9. H. Bala, "The Corrosion of Iron in Sulphate Solutions at pH = 0-2," *Electrochimica Acta*, **29**, 119-129 (1984).

10. John Newman, *Electrochemical Systems*, Prentice-Hall, Inc., Englewood Cliffs, New Jersey (1973).

11. Richard Pollard and John Newman, "Silicon Deposition on a Rotating Disk," *Journal of the Electrochemical Society*, **127**, 744-752 (1980).

12. *CRC Handbook of Chemistry and Physics*, 63rd Edition, 1982—1983, Robert C. Weast, Editor, CRC Press, Inc., Boca Raton, Florida.

13. Bernard Tribollet and John Newman, "Analytic Expression of the Warburg Impedance for a Rotating Disk Electrode," *Journal of the Electrochemical Society*, **130**, 822-824 (1983).

14. I. Epelboin, C. Gabrielli, M. Keddam, and H. Takenouti, "A Model of the Anodic Behaviour of Iron in Sulphuric Acid Medium," *Electrochimica Acta*, **20**, 913-916 (1975).

15. I. Epelboin, C. Gabrielli, and M. Keddam, "Rôle de la Diffusion dans les Phénomènes de Passivation et de Corrosion Localisée du Fer en Milieu Acide," *Corrosion Science*, **15**, 155-171 (1975).

16. William Tiedemann and John Newman, "Growing Porous Layers," *Journal of the Electrochemical Society*, **119**, 186-188 (1972).

17. W. F. Linke, *Solubilities*, 1, Fourth Edition, American Chemical Society, New York (1958).

18. T. W. Chapman and J. Newman, *A Compilation of Selected Thermodynamic and Transport Properties of Binary Electrolytes in Aqueous Solution*, University of California Radiation Laboratory Report # 17767, Berkeley, California (1968).

```
c ******************************************************************
c     KRAMERS-KRONIG  PROGRAM          KK1
c ******************************************************************
c  -- Numerical integration over the experimental frequency range
c       Trapezium Rule  Integration  w.r.t.  (F)  or  LN(F)
c       Straight Line Segments  interpolating between
c       each  2  successive  experimental data points
c  -- Extrapolation of experimental data
c       to   F = 0   and  F = infinity
c       Analytic or numerical integration in the extrapolated regions
c ******************************************************************
c   N = # experimental data points
c   F = frequency (Hz)
c   ZR = real component of impedance
c   ZI = - imaginary component of impedance
c   ZIF = (ZI)*Frequency(Hz)*(2*3.14)
c   Zohm = theoretical value for the ohmic resistance
c   FC = the frequency at which ZR and ZI will be calculated
c        according to the Kramers-Kronig relations
c   ZRFC = ZR at FC
c   ZIMFC = ZI at FC
c   ZIFC = ZIF at FC
c   ZRC = calculated value for (ZR - ZRINF)
c   ZRINF = value of  ZR  at  F = infinity
c   ZIC = calculated value for  ZI
c ************************************
c   NFC = # frequencies  FC
c   NLOG = 0 -- Numerical integration w.r.t. (F) -- linear scale
c   NLOG = 1 -- Numerical integration w.r.t. LN(F) -- logarithmic scale
c   NP = # points on each line segment
c   (K,NP) = experimental point index
c   KFC = index # for FC = K-index of lowest frequency
c         experimental point with F > FC
c   FLOG = LN (F)
c   HFLOG = (FLOG) logarithmic interval size -- generally constant
c   HF =  (F) linear interval size -- not constant
c   HM = frequency interval variable for trapezium rule integration
c   NEXTR = parameters to choose what extrapolation will be used
c     NEXTR0 = 0 -- no extrapolation to F = 0
c     NEXTR0 = 1 -- extrapolation to  F = 0
c     NEXTRH = 0 -- no extrapolation to F = INFINITY
c     NEXTRH = 1 -- extrapolation to F = INFINITY
c              using subroutine EXTRA1
c     NEXTRH = 2 -- extrapolation to F = INFINITY
c              using subroutine EXTRA2
c   ZR0 and ZR1 = parameters for extrapolation to F = 0
c   ZRE1, ZRE2, FE2, AIE, BIE, NE = parameters for extrapolation
c                                   to F = INFINITY
c   NPRI = parameters used to print information if  NPRI = 1
c     NPRI1 -- Print experimental data
c     NPRI2 -- Print calculated integrand values at each
```

```
c               experimental point for each FC
c     NPRII -- Print calculated integral values in the
c               experimental and extrapolated ranges
c     NPRIAB -- Print calculated straight line coefficients (A,B)
c     NPRIFC -- Print FC, ZRFC, and ZIMFC
c ******************************************************************
c
      implicit double precision (a-h,o-z)
      dimension zi(40),zrc(40),zic(40),zrinf(40),dzr(40),dzi(40),
     1            zir(40,150),zii(40,150),sumzr(40),sumzi(40)
      common /all/f(40,150),zif(40,150),np,nfc,fc(40),
     1            zrfc(40),zifc(40),fc2(40)
      common /linear/n,nlog,npriab,nprifc,flog(40,150),
     1            ar(40),br(40),expbr(40),ai(40),bi(40),
     1            zr(40,150),zrlog(40),f2(40,150),kfc(40),
     1            zimfc(40),hm(40,150)
      common /extr0/zire0(40),ziie0(40),zr0,zrl
      common /extrh/zireh(40),ziieh(40),fel,ne,zrel,
     1            are,bre,aie,bie
      common /extrc/zirec(40),ziiec(40),zre2,zife2,fe2
c ******************************************************************
c
c Read program parameters
      read(5,*)nac,n,nfc,zohm,nlog,np,nextr0,nextrh
      read(5,*)zr0,zrl,zrel,zre2
      read(5,*)fe2,ne,aie,bie
      read(5,*)npril,npri2,nprii,npriab,nprifc
      write(6,82)nac,zohm
      write(6,83)np,nlog,nextr0,nextrh
      write(6,84)zr0,zrl,zrel,zre2
c
c Read and print experimental data
      if(npril.eq.1)write(6,10)
      do 2 k=1,n
      read(5,*)f(k,np),zr(k,np),zi(k)
c Calculate variables for lines
      flog(k,np)=dlog(f(k,np))
      f2(k,np)=f(k,np)**2
      zrlog(k)=dlog(zr(k,np))
      zif(k,np)=zi(k)*f(k,np)*6.2831853d00
      if(npril.eq.0)go to 2
      write(6,20)k,f(k,np),zr(k,np),zi(k),zif(k,np)
  2   continue
c
c Read frequencies  FC(I).    FC can be at an experimental point
c or between experimental points
      do 3 i=1,nfc
      read(5,*)kfc(i),fc(i)
  3   fc2(i)=fc(i)**2
c *************************
c Calculate straight lines
```

```
      call LINES
c
c ***************************
c Set all extrapolated integral values to zero
c for the case of no extrapolation
      nextra=nextr0*nextrh
      if(nextra.eq.0) then
       do i=1,nfc
       zire0(i)=0.0d00
       ziie0(i)=0.0d00
       zireh(i)=0.0d00
       ziieh(i)=0.0d00
       end do
      end if
c ******************************************************
c
c   Extrapolation to   F = 0
c
      if(nextr0.eq.1) call EXTRA0
c
c ******************************************************
c
c   Extrapolation to  F = INFINITY
c
c The high frequency range is divided into  2  regions:
c  1 st region: FE1 to FE2  -- ZR and  ZIF changing with Frequency
c       choose method  EXTRA1  or  EXTRA2
c  2 nd region: FE2 to INFINITY  -- ZR and ZIF assumed constant
c       subroutine  EXTRAC
c
      if(nextrh.eq.0)go to 4
      fe1=f(n,np)
      write(6,86)fe1,fe2,ne
c
      if(nextrh.eq.1) then
        call EXTRA1
      else
        call EXTRA2
      end if
c
      write(6,87)are,bre,aie,bie,zife2
      call EXTRAC
c calculated integral values
      do 4 i=1,nfc
      zireh(i)=zireh(i)+zirec(i)
      ziieh(i)=ziieh(i)+ziiec(i)
  4   continue
c ***************************************************
c
c   Integration in experimental frequency range
c
```

```
c Calculate integrands  ZIR and ZII  for each FC value
c
      do 6 i=1,nfc
c
      if(npri2.eq.1)write(6,30)fc(i)
c We need to calculate zir,zii for 1st experimental point separately
      denom=f2(1,np)-fc2(i)
      if(nlog.eq.1) denom=denom/f(1,np)
      zir(1,np)=(zif(1,np)-zifc(i))/denom
      zii(1,np)=(zr(1,np)-zrfc(i))/denom
      sumr=zir(1,np)*hm(1,np)
      sumi=zii(1,np)*hm(1,np)
      k=1
      if(npri2.eq.1)write(6,40)k,f(1,np),zir(1,np),zii(1,np)
c
      do 55 k=2,n
      do 5 m=1,np
c
c Check if   FC = F(K,M)
      if(fc(i).eq.f(k,m)) then
c     write(6,70)
c limits of integrands when  F = FC
      denom=fc2(i)
      if(nlog.eq.1) denom=fc(i)
      zir(k,m)=0.5d00*ai(kfc(i))/denom
      zii(k,m)=0.5d00*ar(kfc(i))*expbr(kfc(i))
      zii(k,m)=zii(k,m)*fc(i)**ar(kfc(i))/denom
c
      else
      denom=f2(k,m)-fc2(i)
      if(nlog.eq.1) denom=denom/f(k,m)
      zir(k,m)=(zif(k,m)-zifc(i))/denom
      zii(k,m)=(zr(k,m)-zrfc(i))/denom
      end if
c
c Calculate sum for trapezium rule
      sumr=sumr+zir(k,m)*hm(k,m)
  5   sumi=sumi+zii(k,m)*hm(k,m)
c ********************************
c Print calculated  ZIR and ZII at experimental points only
      if(npri2.eq.0)go to 55
      write(6,40)k,f(k,np),zir(k,np),zii(k,np)
  55  continue
c ********************************
c
      sumzr(i)=sumr*0.5d00
      sumzi(i)=sumi*0.5d00
c
c Add integral values in extrapolated regions
      sumr=sumzr(i)+zire0(i)+zireh(i)
      sumi=sumzi(i)+ziie0(i)+ziieh(i)
```

```
c Finally calculate  ZR and ZI from K-K relations
c
      zrc(i)=sumr/9.8696044d00
      zic(i)=sumi*fc(i)*0.636619772d00
c
c Calculate fractional difference between calculated and
c experimental / interpolated  Z values
c ZR-difference assuming  ZRINF = Zohm
      dzr(i)=(zrc(i)+zohm-zrfc(i))/zrfc(i)
      dzi(i)=-(zic(i)+zimfc(i))/zimfc(i)
c calculated value for  ZRINF .  This should be a constant
      zrinf(i)=zrfc(i)-zrc(i)
  6   zic(i)=-zic(i)
c
c ***********************************************************
c Print calculated integral values
      if(nprii.eq.0)go to 11
      write(6,80)
      do 7 i=1,nfc
  7   write(6,85)fc(i),sumzr(i),zire0(i),zireh(i)
      write(6,81)
      do 8 i=1,nfc
  8   write(6,85)fc(i),sumzi(i),ziie0(i),ziieh(i)
c
c Print results
  11  write(6,50)
      write(7,52)
      do 12 i=1,nfc
      write(7,61)fc(i),zrc(i)
  12  write(6,60)fc(i),zrc(i),zrinf(i),dzr(i)
      write(6,51)
      write(8,52)
      do 13 i=1,nfc
      write(8,61)fc(i),zic(i)
  13  write(6,60)fc(i),zimfc(i),zic(i),dzi(i)
c ****************************************************************
  10  format(//7x,'EXPERIMENTAL  DATA'/7x,'K',5x,'F(K)  Hz',12x,
     1      'ZR(K)     (ohm)',3x,'-ZI(K)',9x,'ZIF(K)'/)
  20  format(5x,i3,4x,e12.5,7x,e12.5,4x,e12.5,3x,e15.7)
  30  format(//9x,'FC =    ',e12.5,
     1        /7x,'K',7x,'F(K)',16x,'ZIR(K)',12x,'ZII(K)'/)
  40  format(5x,i3,5x,e12.5,5x,e15.7,4x,e15.7)
  50  format(//10x,'CALCULATED  VALUES'//8x,'FC  (Hz)',9x,
     1        'ZRC - ZRINF  (ohm)'2x,'ZRINF',13x,'DZR'/)
  51  format(//8x,'FC  (Hz)',12x,'-ZI     (ohm)',5x,'-ZIC',13x,'-DZI'/)
  52  format('"K-K CALCULATION"')
  60  format(5x,e12.5,6x,e13.6,5x,e13.6,6x,e13.6,5x,e13.6,5x,e13.6)
  61  format(e12.5,' ,',e13.6)
  70  format(10x,'FC = F(K,M)')
  80  format(//6x,'FC  (Hz)',10x,'SUMZR',14x,'ZIRE0',13x,'ZIREH'/)
  81  format(//6x,'FC  (Hz)',10x,'SUMZI',14x,'ZIIE0',13x,'ZIIEH'/)
```

```
 82  format(//10x,'AC  EXPERIMENT  ##   'i4,10x,'Zohm = ',f8.5/)
 83  format(6x,'STRAIGHT LINES NP = ',i3,'  NLOG =',i2,
    1          '   NEXTRO =',i2,'  NEXTRH =',i2)
 84  format(/6x,'ZRO =',f10.4,3x,'ZR1 =',f10.4/
    1        6x,'ZRE1 =',f8.4,4x,'ZRE2 =',f8.4)
 85  format(5x,e12.6,3x,e15.7,3x,e15.7,3x,e15.7)
 86  format(/10x,'EXTRAPOLATION   TO   F = INFINITY'/
    1       5x,'FE1 = ',e12.5,5x,'FE2 = ',e12.5,5x,'NE = ',i3)
 87  format(/5x,'ARE =',e15.7,3x,'BRE =',e15.7/
    1        5x,'AIE =',e15.7,3x,'BIE =',e15.7,2x,'ZIFE2 =',e15.7)
c ******************************************************************
      stop
      end
c
c ******************************************************************
      SUBROUTINE  LINES
c ******************************************************************
c  Straight line segments between each 2 successive experimental points
c   Equation used for ZR :   ZRLOG = AR*FLOG + BR
c   Equation used for ZI :    ZIF  = AI*FLOG + BI
c   Calculate line equation coefficients
c   Generate new points on line segments
c   Set frequency interval size variable  HM (K,M)
c   for trapezium rule integration (linear or logarithmic)
c   N = # experimental points
c   NP = # points on each line segment including
c        one experimental point with index (NP)
c   NPRIAB -- print line coefficients (A,B) if  npriab = 1
c   Each line segment with index (K) contains 1 experimental point with
c   index (K,NP)  and  (NP - 1) other points, (K,M)
c   to the left of the experimental point
*******************************************************
c
      implicit double precision (a-h,o-z)
      dimension dflog(40),hflog(40),hf(40,150)
      common /all/f(40,150),zif(40,150),np,nfc,fc(40),
     1            zrfc(40),zifc(40),fc2(40)
      common /linear/n,nlog,npriab,nprifc,flog(40,150),
     1            ar(40),br(40),expbr(40),ai(40),bi(40),
     1            zr(40,150),zrlog(40),f2(40,150),kfc(40),
     1            zimfc(40),hm(40,150)
c ****************************************************
c
c Calculate line coefficients
c
      if(npriab.eq.1)write(6,100)
      do 21 k=2,n
      dflog(k)=flog(k,np)-flog(k-1,np)
      ar(k)=(zrlog(k)-zrlog(k-1))/dflog(k)
      ai(k)=(zif(k,np)-zif(k-1,np))/dflog(k)
      br(k)=zrlog(k)-ar(k)*flog(k,np)
```

```
      bi(k)=zif(k,np)-ai(k)*flog(k,np)
      expbr(k)=dexp(br(k))
      if(npriab.eq.1)write(6,200)k,ar(k),br(k),ai(k),bi(k)
   21 continue
c ********************************
c
c Calculate new points on each line
c
c first calculate  Z  at FC
      if(nprifc.eq.1) write(6,300)
c      write(7,500)
c      write(8,500)
      do 22 i=1,nfc
      fclog=dlog(fc(i))
      zrfc(i)=dexp(ar(kfc(i))*fclog+br(kfc(i)))
      zifc(i)=ai(kfc(i))*fclog+bi(kfc(i))
      zimfc(i)=zifc(i)/(fc(i)*6.2831853d00)
c      write(7,600)fc(i),zrfc(i)
c      write(8,600)fc(i),zimfc(i)
      if(nprifc.eq.1) write(6,400)kfc(i),fc(i),zrfc(i),zimfc(i)
   22 continue
c
      nf=np-1
      do 25 k=2,n
c Use equal size intervals on logarithmic frequency scale
      hflog(k)=dflog(k)/np
c for  1st new point on each line
      flog(k,1)=flog(k-1,np)+hflog(k)
      do 24 m=2,nf
   24 flog(k,m)=flog(k,m-1)+hflog(k)
c
c Calculate F, ZR, and ZIF for new points
      do 25 m=1,nf
      f(k,m)=dexp(flog(k,m))
      f2(k,m)=f(k,m)**2
      zr(k,m)=dexp(ar(k)*flog(k,m)+br(k))
   25 zif(k,m)=ai(k)*flog(k,m)+bi(k)
c ******************************************
      if(nlog.eq.0) then
c
c Calculate corresponding linear frequency interval size (HF)
c  generally:    HF(K,M) = F(K,M) - F(K,M-1)
c
      do 26 k=2,n
c for  1st point of each line
      hf(k,1)=f(k,1)-f(k-1,np)
      do 26 m=2,np
   26 hf(k,m)=f(k,m)-f(k,m-1)
c
c for last point of each line, except the last line
      nl=n-1
```

```
      do 27 k=2,n1
  27  hf(k,np+1)=hf(k+1,1)
c for last (final) experimental point
      hf(n,np+1)=0.0d00
c **********************
c Set frequency interval variable (HM) for linear integration
      do 28 k=2,n
      do 28 m=1,np
  28  hm(k,m)=hf(k,m)+hf(k,m+1)
c for 1st experimental point
      hm(1,np)=hf(2,1)
c ***************************************************
      else
c
c Set frequency interval variable (HM) for logarithmic integration
c
c for last experimental point
      hflog(n+1)=0.0d00
c
      do 31 k=2,n
c for each experimental point
      hm(k,np)=hflog(k)+hflog(k+1)
c for non-experimental points
      do 31 m=1,nf
  31  hm(k,m)=hflog(k)*2.0d00
c for 1st experimental point
      hm(1,np)=hflog(2)
c
      end if
c ************************************************************
  100 format(//7x,'STRAIGHT  LINE  EQUATION  COEFFICIENTS'/7x,
     1     'K',7x,'AR(K)',13x,'BR(K)',13x,'AI(K)',13x,'BI(K)'/)
  200 format(5x,i3,3x,d15.7,3x,d15.7,3x,d15.7,3x,d15.7)
  300 format(//6x,'KFC',4x,'FC  (Hz)',15x,'ZRFC',13x,'ZIMFC'/)
  400 format(5x,i3,3x,e12.5,8x,e15.6,3x,e15.6)
  500 format('"EXPERIMENTAL"')
  600 format(e12.5,' ,',e13.6)
c ******************
      return
      end
c
c ***********************************************************************
c    SUBROUTINE    EXTRA0      **   From   FMIN  to  F = 0
c ***********************************************************************
c Extrapolate experimental data from the minimum experimental frequency
c   Calculate integrals   ZIRE0 and ZIIE0  in extrapolated region
c   First approximation :
c   Straight line quadratic extrapolation for  ZR(F)  and  ZIF(F)
c     ZR = ZR0  at  F = 0    and   ZR  = ZR1        at  F = FMIN
c     ZIF = 0  at   F = 0    and   ZIF = ZIF(FMIN)  at  F = FMIN
c     ZR (F) = AR0*F**2 + ZR0     from  FMIN  to  F = 0
```

```
c     ZIF(F) = AI0*F**2           from  FMIN  to  F = 0
c   Then we can integrate analytically
c ***********************************************************
      subroutine extra0
      implicit double precision (a-h,o-z)
      common /all/f(40,150),zif(40,150),np,nfc,fc(40),
     1            zrfc(40),zifc(40),fc2(40)
      common /extr0/zire0(40),ziie0(40),zr0,zrl
c ***********************************************************
c
      fmin=f(1,np)
c Calculate straight line equation coefficients
      ar0=(zrl-zr0)/fmin**2
      ai0=zif(1,np)/fmin**2
c
c Calculate integrals  ZIIE0 and ZIRE0  for each  FC
      do 2 i=1,nfc
      clogl=0.5d00*dlog((fc(i)-fmin)/(fc(i)+fmin))
      ziie0(i)=ar0*(fc(i)*clogl+fmin)
      ziie0(i)=ziie0(i)+(zr0-zrfc(i))*clogl/fc(i)
  2   zire0(i)=ai0*(fc(i)*clogl+fmin)-zifc(i)*clogl/fc(i)
c **************
      return
      end
c
c ********************************************************************
c    SUBROUTINE   EXTRA1      **   From   FE1  to  FE2
c ********************************************************************
c Extrapolate experimental data from the maximum experimental frequency
c   FE1 to a chosen higher frequency  FE2
c   Calculate integrals in extrapolated region : ZIREH and ZIIEH
c   First approximation :
c   Straight line extrapolation for  ZR (F)  and  ZIF (F)
c     ZR = ZRE1   at  F = FE1
c     ZR = ZRE2   at  F = FE2
c     ZR (F)  = ARE*F + BRE
c     ZIF (F) = AIE*F + BIE
c   For  ZR  specify both ZRE1 and ZRE2 and calculate line coefficients
c   For  ZIF specify line coefficients
c   Then integrate analytically
c ***********************************************
c
      subroutine extral
      implicit double precision (a-h,o-z)
      common /all/f(40,150),zif(40,150),np,nfc,fc(40),
     1            zrfc(40),zifc(40),fc2(40)
      common /extrh/zireh(40),ziieh(40),fel,ne,zrel,
     1            are,bre,aie,bie
      common /extrc/zirec(40),ziiec(40),zre2,zife2,fe2
c ***********************************************
c
```

```
      fe12=fe1**2
      fe22=fe2**2
c Calculate straight line coefficients for  ZR (F)
      are=(zre2-zre1)/(fe2-fe1)
      bre=zre1-are*fe1
c
c Calculate integrals (ZIREH and ZIIEH) for each  FC
      do 2 i=1,nfc
      fl1=(fe2-fc(i))*(fe1+fc(i))/((fe2+fc(i))*(fe1-fc(i)))
      cl1=0.5d00*dlog(fl1)/fc(i)
      cl2=0.5d00*dlog((fe22-fc2(i))/(fe12-fc2(i)))
      ziieh(i)=cl1*(bre-zrfc(i))+cl2*are
  2   zireh(i)=cl1*(bie-zifc(i))+cl2*aie
c
c Calculate  ZIFE2  for subroutine  EXTRAC
      zife2=aie*fe2+bie
c *********************
      return
      end
c
c ***********************************************************************
c    SUBROUTINE   EXTRA2      **   From   FE1  to  FE2
c ***********************************************************************
c   Extrapolate experimental data
c   Calculate integrals in extrapolated region :  ZIREH and ZIIEH
c   -- Second approximation :
c   Straight line equations in extrapolated region (E)
c      LN(ZRE) = ARE*LN(FE) + BRE
c   i.e.  ZRE(FE) = (FE**ARE)*exp(BRE)
c      ZIFE(FE) = AIE*LN(FE) + BIE
c ********************************
c   Then use Trapezium Rule to integrate numerically
c   Integration  w.r.t.  LN(FE) -- Logarithmic frequency scale
c   FE1 = lower frequency end of extrapolated region
c   FE2 = higher frequency end of extrapolated region
c   NE = # points used in extrapolated region
c        not including the endpoints  FE1 and FE2
c   M = extrapolated point index #
c   HLOG = logarithmic frequency interval size  (constant)
c ************************************************************
      subroutine extra2
      implicit double precision (a-h,o-z)
      dimension fe(150),felog(150),f2e(150),
     1          zre(150),zife(150),zire(40),ziie(40)
      common /all/f(40,150),zif(40,150),np,nfc,fc(40),
     1              zrfc(40),zifc(40),fc2(40)
      common /extrh/zireh(40),ziieh(40),fe1,ne,zre1,
     1              are,bre,aie,bie
      common /extrc/zirec(40),ziiec(40),zre2,zife2,fe2
c ************************************************************
c
```

```
c Endpoints
      fellog=dlog(fe1)
      fe2log=dlog(fe2)
      f2e1=fe1**2
      f2e2=fe2**2
      hlog=(fe2log-fellog)/ne
c Calculate line coefficients for ZRE (F) from specified ZRE1 and ZRE2
      are=dlog(zre2/zre1)/(fe2log-fellog)
      bre=dlog(zre1)-are*fellog
c ******************************
c
c Points at equal logarithmic frequency intervals
c
c first point
      felog(1)=fellog+hlog
      fe(1)=dexp(felog(1))
      f2e(1)=fe(1)**2
c
c other points
      do 2 m=2,ne
      felog(m)=felog(m-1)+hlog
      fe(m)=dexp(felog(m))
  2   f2e(m)=fe(m)**2
c
c Calculate  ZRE and ZIFE  for  extrapolated points
      zife1=aie*fellog+bie
      zife2=aie*fe2log+bie
      do 3 m=1,ne
      zre(m)=dexp(are*felog(m)+bre)
  3   zife(m)=aie*felog(m)+bie
c ************************************************
c
c Calculate integrals for each  FC
c
      do 6 i=1,nfc
c endpoints separately
      denom=(f2e1-fc2(i))/fe1
      sumre=(zife1-zifc(i))/denom
      sumie=(zre1-zrfc(i))/denom
      denom=(f2e2-fc2(i))/fe2
      sumre=(sumre+(zife2-zifc(i))/denom)*0.5d00
      sumie=(sumie+(zre2-zrfc(i))/denom)*0.5d00
c
c other points
      do 5 m=1,ne
c Calculate integrands
      denom=(f2e(m)-fc2(i))/fe(m)
      zire(m)=(zife(m)-zifc(i))/denom
      ziie(m)=(zre(m)-zrfc(i))/denom
c Trapezium rule sum
      sumre=sumre+zire(m)
```

```
  5   sumie=sumie+ziie(m)
c ****************************
c Finally the integral values
c
      zireh(i)=sumre*hlog
  6   ziieh(i)=sumie*hlog
c
c ****************************
      return
      end
c
c ***********************************************************************
c    SUBROUTINE   EXTRAC      **   From   FE2  to  F = INFINITY
c ***********************************************************************
c   Extrapolate data from the chosen frequency  FE2  to infinity
c   Calculate integrals in extrapolated region : ZIREC  and  ZIIEC
c   In this region, assume :
c     ZR (F)  = ZRE2  = CONSTANT
c     ZIF (F) = ZIFE2 = CONSTANT
c   Then integrate analytically
c ***********************************************
      subroutine extrac
      implicit double precision (a-h,o-z)
      common /all/f(40,150),zif(40,150),np,nfc,fc(40),
     1            zrfc(40),zifc(40),fc2(40)
      common /extrc/zirec(40),ziiec(40),zre2,zife2,fe2
c ***********************************************
c
      do 2 i=1,nfc
      clog=0.5d00*dlog((fe2-fc(i))/(fe2+fc(i)))/fc(i)
      ziiec(i)=clog*(zrfc(i)-zre2)
  2   zirec(i)=clog*(zifc(i)-zife2)
c
      return
      end
```

```
c ***********************************************************************
c KRAMERS-KRONIG  PROGRAM           KKPOLY
c ***********************************************************************
c  -- Polynomial  Fitting of experimental data
c     over chosen frequency intervals (segments)
c     Use  3 rd  order polynomials for
c        ZR (F)
c        ZIF (F)
c     The experimental data are divided into segments
c     A different polynomial is used for each segment
c     to obtain the best possible fit
c  -- Analytic  Integration of resulting functions
c  -- Linear extrapolation of experimental data to
c        F = 0  and  F = infinity
c     Analytic integration in extrapolated regions
c ***************************************************************
c   N = # experimental data points
c   F = frequency (Hz)
c   ZR = real component of impedance
c   ZI = - imaginary component of impedance
c   ZIF = (ZI)*Frequency(Hz)*(2*3.14)
c   Zohm = theoretical value for the ohmic resistance
c   FC = the frequency at which ZR and ZI will be calculated
c        according to the Kramers-Kronig relations
c   ZRFC = ZR at FC
c   ZIMFC = ZI at FC
c   ZIFC = ZIF at FC
c   ZRC = calculated value for (ZR - ZRINF)
c   ZRINF = value of  ZR  at  F = infinity
c   ZIC = calculated value for  ZI
c ***********************************
c   NFC = # frequencies  FC
c   NORDER = the order of the polynomials.  NORDER =  3
c   NPOLY = # segments
c   K = experimental point index #
c   KFC = K-index of FC
c   KFIRST = K-index of first experimental point in each segment
c   KLAST = K-index of last experimental point in each segment
c   NEXTR = parameters to choose what extrapolation will be used
c   NPRI = parameters used to print information if NPRI = 1
c     NPRI1 -- Print experimental data
c     NPRII -- Print calculated integral values
c              in experimental and extrapolated ranges
c     NPRIZ -- Print calculated polynomial fit Z-values
c     NPRIA -- Print calculated polynomial coefficients
c ***************************************************************
c
      implicit double precision (a-h,o-z)
      dimension zr(40),zi(40),zif(40),zrc(40),zic(40),
     1          zimfc(40),dzr(40),dzi(40),zrinf(40)
      common /most/n,f(40),npoly,norder,a(6,20),
```

```
     1            kfirst(20),klast(20)
      common /fcvari/nfc,fc(40),kfc(40),fc2(40),zrfc(40),zifc(40)
      common /fit/z(40),npriz,npria,zpoly(40),zzpoly(40),dzpoly(40)
      common /integr/zinteg(40),zfc(40)
      common /extr0/zire0(40),ziie0(40),zr0,zrl,zifl
      common /extrh/zireh(40),ziieh(40),fel,zrel,
     1            are,bre,aie,bie
      common /extrc/zirec(40),ziiec(40),zre2,zife2,fe2
      common /matrix/s(6,6),zm(6,13)
c ***********************************************************************
c
c Read some program parameters
      read(5,*)nac,n,nfc,zohm,nextr0,nextrh
      read(5,*)zr0,zrl,zrel,zre2
      read(5,*)fe2,aie,bie
      read(5,*)nprl1,nprii,npriz,npria
      write(6,115)nac,zohm
      write(6,116)nextr0,nextrh
      write(6,117)zr0,zrl,zrel,zre2
c
c Read and print experimental data
      if(nprl1.eq.1)write(6,101)
      do 2 k=1,n
      read(5,*)f(k),zr(k),zi(k)
c calculate  ZIF
      zif(k)=zi(k)*f(k)*6.2831853d00
      if(nprl1.eq.0)go to 2
      write(6,102)k,f(k),zr(k),zi(k),zif(k)
  2   continue
c
c Read frequencies  FC(I) and set  FC-variables
c All  FC values are taken at experimental points
c that are not endpoints of segments
c
      do 3 i=1,nfc
      read(5,*)kfc(i)
      fc(i)=f(kfc(i))
      zrfc(i)=zr(kfc(i))
      zimfc(i)=zi(kfc(i))
      zifc(i)=zif(kfc(i))
  3   fc2(i)=fc(i)**2
c ********************************************
c
c   Polynomial fit for  ZR (F)
c
      read(5,*)norder,npoly
      write(6,103)norder,npoly
      do 4 k=1,n
  4   z(k)=zr(k)
c Read endpoints of segments
      do 5 i=1,npoly
```

```
  5   read(5,*)kfirst(i),klast(i)
c
      call POLY
c ********************
c
c   Integrate  ZR(F) according to K-K relations to calculate ZIC
c
c Set values for subroutine  IPOLY
      do 6 i=1,nfc
  6   zfc(i)=zrfc(i)
c
      call IPOLY
c
      do 7 i=1,nfc
  7   zic(i)=zinteg(i)
c ****************************************
c
c   Polynomial fit for  ZIF(F)
c
c      read(5,*)norder,npoly
      write(6,104)norder,npoly
      do 8 k=1,n
  8   z(k)=zif(k)
c read endpoints of segments if they are different from  ZR(F)
c      do 9 i=1,npoly
c  9   read(5,*)kfirst(i),klast(i)
c
      call POLY
c ****************
c
c   Integrate ZIF(F) to calculate ZRC according to the K-K relations
c
c Set values for subroutine   IPOLY
      do 12 i=1,nfc
  12  zfc(i)=zifc(i)
c
      call IPOLY
c
      do 13 i=1,nfc
  13  zrc(i)=zinteg(i)
c ****************************************************
c
c Set all extrapolated integral values to zero
c for the case of no extrapolation
      nextra=nextr0*nextrh
      if(nextra.eq.0) then
       do i=1,nfc
       zire0(i)=0.0d00
       ziie0(i)=0.0d00
       zireh(i)=0.0d00
       ziieh(i)=0.0d00
```

```
      end do
     end if
c ***************************************************
c
c   Extrapolation to   F = 0
c
      zif1=zif(1)
      if(nextr0.eq.1) call EXTRA0
c
c ***************************************************
c
c   Extrapolation to  F = INFINITY
c
c The high frequency range is divided into  2  regions:
c  1 st region: FE1 to FE2  -- ZR and  ZIF changing with Frequency
c       subroutine  EXTRA1
c  2 nd region: FE2 to INFINITY  -- ZR and ZIF assumed constant
c       subroutine  EXTRAC
c
      if(nextrh.eq.0)go to 14
      fe1=f(n)
      write(6,113)fe1,fe2
c
      call EXTRA1
c
      write(6,114)are,bre,aie,bie,zife2
      call EXTRAC
c
c calculated integral values
      do 14 i=1,nfc
      zireh(i)=zireh(i)+zirec(i)
      ziieh(i)=ziieh(i)+ziiec(i)
  14  continue
c ***************************************************
c Print calculated integral values
      if(nprii.eq.1) then
       write(6,110)
       do i=1,nfc
       write(6,112)fc(i),zrc(i),zire0(i),zireh(i)
       end do
       write(6,111)
       do i=1,nfc
       write(6,112)fc(i),zic(i),ziie0(i),ziieh(i)
       end do
      end if
c ***************************************************
c
c  Finally calculate  ZR and ZI from K-K relations
c
      do 15 i=1,nfc
c
```

```
      zrc(i)=(zrc(i)+zire0(i)+zireh(i))/9.8696044d00
      zic(i)=(zic(i)+ziie0(i)+ziieh(i))*fc(i)*0.636619772d00
c
c Calculate fractional difference between calculated and
c experimental  Z  values
c ZR - difference assuming  ZRINF = Zohm
      dzr(i)=(zrc(i)+zohm-zrfc(i))/zrfc(i)
      dzi(i)=-(zic(i)+zimfc(i))/zimfc(i)
c calculated value for  ZRINF .  This should be a constant
  15  zrinf(i)=zrfc(i)-zrc(i)
c
c ***********************************************
c Print results for  ZRC
      write(6,106)
      do 18 i=1,nfc
  18  write(6,108)kfc(i),fc(i),zrc(i),zrinf(i),dzr(i)
c
c Print results for  ZIC
      write(6,107)
      do 19 i=1,nfc
      zic(i)=-zic(i)
  19  write(6,108)kfc(i),fc(i),zimfc(i),zic(i),dzi(i)
c
c ************************************************************
  101 format(//7x,'EXPERIMENTAL  DATA'/7x,'K',5x,'F(K)  Hz',12x,
     1      'ZR(K)     (ohm)',3x,'-ZI(K)',9x,'ZIF(K)'/)
  102 format(5x,i3,4x,e12.5,7x,e12.5,4x,e12.5,3x,e15.7)
  103 format(//7x,'POLYNOMIAL FIT FOR  ZR (F)',5x,
     1  'POLYNOMIAL ORDER =  ',i2/7x,'## SEGMENTS =  ',i3)
  104 format(//7x,'POLYNOMIAL FIT FOR  ZIF (K)',5x,
     1  'POLYNOMIAL ORDER =  ',i2/7x,'## SEGMENTS =  ',i3)
  105 format(/9x,'FC =    ',e12.5)
  106 format(//10x,'CALCULATED  VALUES'//7x,'K',5x,'FC(K)  Hz',
     1   10x,'ZRC - ZRINF  (ohm)',3x,'ZRINF',11x,'DZR'/)
  107 format(//10x,'CALCULATED  VALUES'//7x,'K',5x,'FC(K)  Hz',
     1     13x,'-ZI(K)    (ohm)',3x,'-ZIC',9x,'-DZI'/)
  108 format(5x,i3,4x,e12.5,7x,e13.6,4x,e13.6,3x,e15.7,3x,e13.6)
  110 format(//7x,'INTEGRAL  VALUES'/6x,
     1        'FC  (Hz)',10x,'ZIRPOLY',12x,'ZIRE0',13x,'ZIREH'/)
  111 format(//6x,'FC  (Hz)',10x,'ZIIPOLY',12x,'ZIIE0',13x,'ZIIEH'/)
  112 format(5x,e12.6,3x,e15.7,3x,e15.7,3x,e15.7)
  113 format(/10x,'EXTRAPOLATION   TO   F = INFINITY'/
     1       5x,'FE1 = ',e12.5,5x,'FE2 = ',e12.5)
  114 format(/5x,'ARE =',e15.7,3x,'BRE =',e15.7/
     1        5x,'AIE =',e15.7,3x,'BIE =',e15.7,2x,'ZIFE2 =',e15.7)
  115 format(//10x,'AC  EXPERIMENT  ##   'i4,10x,'Zohm = ',f8.5)
  116 format(/6x,'NEXTR0 ='i2,3x,'NEXTRH =',i2)
  117 format(/6x,'ZR0 =',f10.4,3x,'ZR1 =',f10.4/
     1        6x,'ZRE1 =',f8.4,4x,'ZRE2 =',f8.4)
c ******************************************************************
      stop
```

```
      end
c
c ***********************************************************************
      SUBROUTINE POLY
c ***********************************************************************
c   Fit Polynomials to data points  Z (X)
c   The data points can be divided in segments
c   A polynomial is determined for each segment
c   Least - Squares  method
c   MATINV  is used to solve the matrix equation
c ***********************************************
c   [A] = matrix of polynomial coefficients
c   [S] = matrix of sums of  X-powers   (X**L)
c   [ZM] = matrix of sums  Z(X)*(X**L)
c   Matrix equation  [S] [A] = [ZM]
c   Solution             [A] = [ZM] [S inverse]
c ***********************************************
c   N = # data points
c   NORDER = order of polynomial  (highest X-power)
c   NPOLY = # segments of data points
c   NA = # coefficients  A  to be determined
c   NA = NORDER + 1 = # linear equations = # rows in matrices
c   IP = segment index #
c   A (L,IP) = polynomial coefficient of  X**(L-1)
c   X (K,L) = X to the L power at data point (K)
c   I = matrix row index #
c   J = matrix column index #
c   NPRIZ -- print polynomial Z(K) if  npriz = 1
c   NPRIA -- print polynomial coefficients  A  if npria = 1
c ***********************************************************
c
      implicit double precision (a-h,o-z)
      dimension x(40,10),sumx(10),sumz(6)
      common /most/n,f(40),npoly,norder,a(6,20),
     1            kfirst(20),klast(20)
      common /fit/z(40),npriz,npria,zpoly(40),zzpoly(40),dzpoly(40)
      common /matrix/s(6,6),zm(6,13)
c ************************************************************
c
c Subroutine Matinv requires matrix [ZM] to be a 2-dimensional array
c Here, [ZM] is a 1-column matrix
c Initially set all [ZM] elements to zero
      na=norder+1
      m=na*2+1
      do 2 i=1,na
      do 2 j=1,m
  2   zm(i,j)=0.0d00
c
c highest power of  X  involved in the matrix equation
      np2=norder*2
c ******************************
```

```
c
c Determine polynomials for each data segment
c
      if(npriz.eq.1)write(6,201)
      do 15 ip=1,npoly
      if(npriz.eq.1)write(6,202)ip
c endpoints of segment
      k1=kfirst(ip)
      k2=klast(ip)
c ## data points in segment
      nk=k2-k1+1
c
c Evaluate sums  -- SUMX (L) = sum of  X**L
c First, sums with X to the 1st power,  and sum of Z
      sumx(1)=0.0d00
      sumz(1)=0.0d00
      do 3 k=k1,k2
      x(k,1)=f(k)
      sumx(1)=x(k,1)+sumx(1)
  3   sumz(1)=z(k)+sumz(1)
c Now, higher power sums
      do 4 l=2,np2
      sumx(1)=0.0d00
      do 4 k=k1,k2
      x(k,l)=x(k,l-1)*x(k,1)
  4   sumx(1)=x(k,l)+sumx(1)
c remaining  Z-sums
      do 6 l=2,na
      sumz(1)=0.0d00
      do 5 k=k1,k2
  5   sumz(1)=z(k)*x(k,l-1)+sumz(1)
c
c Elements of 1-column [ZM] matrix
  6   zm(1,1)=sumz(1)
c first element
      zm(1,1)=sumz(1)
c
c Elements of [S] matrix
c first column
      s(1,1)=nk
      do 7 i=2,na
  7   s(i,1)=sumx(i-1)
c other elements of [S] matrix
      do 8 i=1,na
      do 8 j=2,na
  8   s(i,j)=sumx(i+j-2)
c ***********************************
c
c Solve matrix equation to obtain [A] coefficients
c
      call matinv(na,m,determ)
```

```
c
c Check if matrix is singular
      if(determ.ne.0.0d00)go to 9
      write(6,200)
  9   continue
c
c Matinv returns calculated variable in the [ZM] matrix
c calculated coefficients
      do 11 l=1,na
  11  a(l,ip)=zm(l,1)
c ************************************
c
c Calculate Z(F) given by polynomial fit at experimental points
c
      if(npriz.eq.0) go to 15
      do 13 k=kl,k2
      zpoly(k)=a(1,ip)
      do 12 l=2,na
  12  zpoly(k)=a(l,ip)*x(k,l-1)+zpoly(k)
c Calculate error in polynomial fit -- fractional difference
      zzpoly(k)=zpoly(k)-z(k)
      dzpoly(k)=zzpoly(k)/z(k)
  13  write(6,203)k,f(k),zpoly(k),zzpoly(k),dzpoly(k)
c
  15  continue
c ****************************
c
c Print polynomial coefficients
      if(npria.eq.0)go to 22
      write(6,204)
      do 21 ip=1,npoly
  21  write(6,205)ip,(a(l,ip),l=1,na)
c
c ************************************************************
  200 format(//5x,'MATRIX IS SINGULAR TO WORKING PRECISION')
  201 format(/6x,'K',5x,'F(K)  HZ',10x,'ZPOLY(K)',
     1       9x,'ZZPOLY(K)',9x,'DZPOLY(K)'/)
  202 format(9x,'POLYNOMIAL  ## ',i3)
  203 format(4x,i3,4x,e12.5,4x,e13.6,2x,e16.8,2x,e16.8)
  204 format(//7x,'POLYNOMIAL COEFFICIENTS'/5x,'IP',7x,'A1',
     1      15x,'A2',15x,'A3',15x,'A4',15x,'A5',15x,'A6'/)
  205 format(4x,i3,3x,e15.7,2x,e15.7,2x,e15.7,2x,e15.7,2x,
     1                e15.7,2x,e15.7)
c ***************
  22  return
      end
c
c ***********************************************************************
      SUBROUTINE IPOLY
c ***********************************************************************
c   Analytic  integration  of  polynomial fit functions
```

```
c   Integration  segment by segment, for each  FC  value
c   ZINTEG = calculated value of integral over experimental range
c   SEGMEN (IP) = integral value over segment  IP
c ****************************************************
c
      implicit double precision (a-h,o-z)
      dimension segmen(20)
      common /most/n,f(40),npoly,norder,a(6,20),
     1            kfirst(20),klast(20)
      common /fcvari/nfc,fc(40),kfc(40),fc2(40),zrfc(40),zifc(40)
      common /integr/zinteg(40),zfc(40)
c ****************************************************
c
      do 5 i=1,nfc
      zint=0.0d00
      do 4 ip=1,npoly
c
c Evaluate integral terms at the 2 endpoints of each segment
c
      k=kfirst(ip)
c
  2   clog1=0.5d00*(dlog(dabs(f(k)-fc(i)))-dlog(f(k)+fc(i)))
      clog2=0.5d00*dlog(dabs(f(k)**2-fc2(i)))
      term=f(k)*(a(3,ip)+a(4,ip)*f(k)/2.0d00)
      c1=(a(1,ip)-zfc(i))/fc(i)+a(3,ip)*fc(i)
      c2=a(2,ip)+a(4,ip)*fc2(i)
      term=term+clog1*c1+clog2*c2
c
      if(k.eq.klast(ip))go to 3
      term1=term
      k=klast(ip)
      go to 2
c
  3   segmen(ip)=term-term1
c
  4   zint=segmen(ip)+zint
c
  5   zinteg(i)=zint
c ********************
      return
      end
c
c ***********************************************************************
c    SUBROUTINE    EXTRA0      **   From   FMIN  to  F = 0
c ***********************************************************************
c Extrapolate experimental data from the minimum experimental frequency
c   Calculate integrals   ZIRE0 and ZIIE0  in extrapolated region
c   First approximation :
c   Straight line quadratic extrapolation for  ZR(F)  and  ZIF(F)
c     ZR = ZR0  at  F = 0    and   ZR  = ZR1        at  F = FMIN
c     ZIF = 0  at   F = 0    and   ZIF = ZIF1       at  F = FMIN
```

```
c     ZR (F) = AR0*F**2 + ZR0      from  FMIN  to  F = 0
c     ZIF(F) = AI0*F**2            from  FMIN  to  F = 0
c   Then we can integrate analytically
c ******************************************************
      subroutine extra0
      implicit double precision (a-h,o-z)
      common /most/n,f(40),npoly,norder,a(6,20),
     1             kfirst(20),klast(20)
      common /fcvari/nfc,fc(40),kfc(40),fc2(40),zrfc(40),zifc(40)
      common /extr0/zire0(40),ziie0(40),zr0,zrl,zifl
c ******************************************************
c
      fmin=f(1)
c Calculate straight line equation coefficients
      ar0=(zrl-zr0)/fmin**2
      ai0=zifl/fmin**2
c
c Calculate integrals  ZIIE0 and ZIRE0  for each  FC
      do 2 i=1,nfc
      cfl=0.5d00*dlog((fc(i)-fmin)/(fc(i)+fmin))
      ziie0(i)=ar0*(fc(i)*cfl+fmin)+(zr0-zrfc(i))*cfl/fc(i)
  2   zire0(i)=ai0*(fc(i)*cfl+fmin)-zifc(i)*cfl/fc(i)
c **************
      return
      end
c
c ********************************************************************
c    SUBROUTINE   EXTRA1      **   From   FE1  to  FE2
c ********************************************************************
c Extrapolate experimental data from the maximum experimental frequency
c   FE1 to a chosen higher frequency  FE2
c   Calculate integrals in extrapolated region : ZIREH and ZIIEH
c   First approximation :
c   Straight line extrapolation for  ZR (F)  and  ZIF (F)
c     ZR = ZRE1   at  F = FE1
c     ZR = ZRE2   at  F = FE2
c     ZR (F)  = ARE*F + BRE
c     ZIF (F) = AIE*F + BIE
c   For  ZR  specify both ZRE1 and ZRE2 and calculate line coefficients
c   For  ZIF specify line coefficients
c   Then integrate analytically
c ************************************************
c
      subroutine extra1
      implicit double precision (a-h,o-z)
      common /fcvari/nfc,fc(40),kfc(40),fc2(40),zrfc(40),zifc(40)
      common /extrh/zireh(40),ziieh(40),fe1,zre1,
     1              are,bre,aie,bie
      common /extrc/zirec(40),ziiec(40),zre2,zife2,fe2
c ************************************************
c
```

```
      fel2=fel**2
      fe22=fe2**2
c Calculate straight line coefficient for  ZR (F)
      are=(zre2-zrel)/(fe2-fel)
      bre=zrel-are*fel
c
c Calculate integrals  ZIREH and ZIIEH  for each  FC
      do 2 i=1,nfc
      fll=(fe2-fc(i))*(fel+fc(i))/((fe2+fc(i))*(fel-fc(i)))
      cll=0.5d00*dlog(fll)/fc(i)
      cl2=0.5d00*dlog((fe22-fc2(i))/(fel2-fc2(i)))
      ziieh(i)=cll*(bre-zrfc(i))+cl2*are
  2   zireh(i)=cll*(bie-zifc(i))+cl2*aie
c
c Calculate  ZIFE2  for subroutine  EXTRAC
      zife2=aie*fe2+bie
c *********************
      return
      end
c
c ***********************************************************************
c    SUBROUTINE   EXTRAC      **   From   FE2  to  F = INFINITY
c ***********************************************************************
c   Extrapolate data from the chosen frequency  FE2  to infinity
c   Calculate integrals in extrapolated region : ZIREC  and  ZIIEC
c   In this region, assume :
c     ZR (F)  = ZRE2  = CONSTANT
c     ZIF (F) = ZIFE2 = CONSTANT
c   Then integrate analytically
c ***********************************************
      subroutine extrac
      implicit double precision (a-h,o-z)
      common /fcvari/nfc,fc(40),kfc(40),fc2(40),zrfc(40),zifc(40)
      common /extrc/zirec(40),ziiec(40),zre2,zife2,fe2
c ***********************************************
c
      do 2 i=1,nfc
      clog=0.5d00*dlog((fe2-fc(i))/(fe2+fc(i)))/fc(i)
      ziiec(i)=clog*(zrfc(i)-zre2)
  2   zirec(i)=clog*(zifc(i)-zife2)
c
      return
      end
c
c ***********************************************************************
      SUBROUTINE MATINV(N,M,DETERM)
c ***********************************************************************
c   MATINV  solves a matrix equation of the form
c       [B] [X] = [D]
c   The answer (X) is put into the first column of [D]
c   Matrix [D] should be dimensioned  (N x M),  where
```

```
c       M = (2*N + 1)
c    All columns of [D], except the first, should be initiallized with
c    zeros (0)
c ************************************************************
c
      implicit double precision (a-h,o-z)
      dimension ID(6)
c
      common /matrix/B(6,6),D(6,13)
c
      DETERM=1.0D+00
      DO 1 I=1,N
    1 ID(I)=0
      DO 18 NN=1,N
      BMAX=1.1D+00
      DO 6 I=1,N
      IF(ID(I).NE.0) GOTO 6
      BNEXT=0.0D+00
      BTRY=0.0D+00
      DO 5 J=1,N
      IF(ID(J).NE.0) GOTO 5
      IF(DABS(B(I,J)).LE.BNEXT) GOTO 5
      BNEXT=DABS(B(I,J))
      IF(BNEXT.LE.BTRY) GOTO 5
      BNEXT=BTRY
      BTRY=DABS(B(I,J))
      JC=J
    5 CONTINUE
      IF(BNEXT.GE.BMAX*BTRY) GOTO 6
      BMAX=BNEXT/BTRY
      IROW=I
      JCOL=JC
    6 CONTINUE
      IF(ID(JC).EQ.0) GOTO 8
      DETERM=0.0D+00
      RETURN
    8 ID(JCOL)=1
      IF(JCOL.EQ.IROW) GOTO 12
      DO 10 J=1,N
      SAVE=B(IROW,J)
      B(IROW,J)=B(JCOL,J)
   10 B(JCOL,J)=SAVE
      DO 11 K=1,M
      SAVE=D(IROW,K)
      D(IROW,K)=D(JCOL,K)
   11 D(JCOL,K)=SAVE
   12 F=1.0D+00/B(JCOL,JCOL)
      DO 13 J=1,N
   13 B(JCOL,J)=B(JCOL,J)*F
      DO 14 K=1,M
   14 D(JCOL,K)=D(JCOL,K)*F
```

```
      DO 18 I=1,N
      IF(I.EQ.JCOL) GO TO 18
      F=B(I,JCOL)
      DO 16 J=1,N
16    B(I,J)=B(I,J)-F*B(JCOL,J)
      DO 17 K=1,M
17    D(I,K)=D(I,K)-F*D(JCOL,K)
18    CONTINUE
      RETURN
      END
```

LAWRENCE BERKELEY LABORATORY
TECHNICAL INFORMATION DEPARTMENT
UNIVERSITY OF CALIFORNIA
BERKELEY, CALIFORNIA 94720